

Imperial College London

The Imperial College of Science, Technology and Medicine
Department of Physics

Towards Sideband Cooling of a Single $^{40}\text{Ca}^+$ Ion in a Penning Trap

Sean Donnellan

Submitted in part fulfilment of the requirements for the degree of
Doctor of Philosophy in Physics of Imperial College, London,
21/11/2011

Declaration

I declare that this thesis is my own work. Where I have used the work of others the sources are appropriately referenced and acknowledged.

Abstract

This thesis presents work aimed towards achieving sideband cooling of $^{40}\text{Ca}^+$ ions in a Penning trap.

The observation of an increase in the number of quantum jumps as a function of the trapping magnetic field is first presented. This observation is explained by the ion falling into a long-lived $D_{\frac{5}{2}}$ state, out of which the ion is not being re-pumped. The ion can fall into this state due to mixing of the fine structure components with the same m_J quantum number induced by the applied magnetic field. A calculation of the mixing and shelving rate as a function of magnetic field strength is presented. This theory matches well with the experimental results observed. This work has been presented in a publication in which a perturbative analysis was used. An alternative analysis is presented here in which the full Hamiltonian is diagonalised. The essential conclusions however remain unchanged.

This ‘J-state mixing’ effect means re-pumping from each of the six $D_{\frac{5}{2}}$ state sub-levels of our ion is required for efficient laser cooling. This is achieved by the addition of a system comprising an 854 nm laser and a fibre EOM to provide the radiation required to re-pump these levels. The same EOM is then used to re-pump out of the four sub-levels of the $D_{\frac{3}{2}}$ state using a single 866 nm laser. This is a great simplification of the experimental setup required to cool a $^{40}\text{Ca}^+$ ion in a Penning trap which would otherwise require ten separate lasers to independently address each of the D sub-states.

Achieving efficient repumping leads to the ability to perform pulsed spectroscopy on the quadrupole $S_{\frac{1}{2}} \rightarrow D_{\frac{5}{2}}$ transition in $^{40}\text{Ca}^+$. Preliminary results of this spectroscopy in a radio-frequency trap are presented.

Acknowledgements

Firstly I would like to thank all of the people I have worked with in the Ion Trapping Lab; from Dan, Shailen and Sandeep with whom I have spent the majority of my time to Joe, Graham and Danni who have joined more recently. Special thanks goes to Dan. Without his knowledge and incredible knack for making things work the results in this thesis would not be possible. Special thanks also goes to Sandeep. I don't think I will ever forget 'those' few months.

A big thank you to my supervisors Danny and Richard. It is difficult to imagine supervisors who are more encouraging and kind. I consider myself very lucky to have worked in your group.

Thanks as well to all the CCMers. It has been great feeling part of a bigger group and Friday nights down the pub would have been far less fun without you.

Finally thanks to my friends outside of Imperial College, especially Justin, Aldrin and Grace whom I have often neglected due to late nights in the lab. The existence of this thesis would be much less probable without you.

Contents

1	Introduction and Motivation	11
1.1	My Role in the Work Presented	13
1.2	Introduction to Quantum Computation	14
1.2.1	Quantum Gates	16
1.2.2	Quantum Algorithms	19
2	How to Trap an Ion	21
2.1	Penning Trap	24
2.2	Paul Trap	28
2.3	Combined Trap	31
3	Interaction of light with a trapped Ion - Coherent Dynamics and Laser Cooling	32
3.1	Doppler Cooling	32
3.1.1	Doppler Cooling in the Penning Trap	34
3.1.2	Axialisation	34
3.2	Coherent Dynamics	35
3.3	Sideband Cooling	41
3.4	Quantum Computation in Ion Traps	47
3.4.1	Cirac-Zoller C-NOT Gate Protocol	47
3.4.2	Geometrical-Phase Gate	50
3.4.3	Decoherence and Recent Advances	51
3.5	Quantum Simulation in Penning Traps	52
4	Experimental Setup	55
4.1	Electronic Energy Levels of a $^{40}\text{Ca}^+$ Ion	55

4.2	Laser Systems and Optical Setup	58
4.2.1	Diode Lasers	58
4.2.2	Laser Wavelength Measurement	62
4.2.3	Scanning Cavity Lock	63
4.2.4	Acousto-Optic Modulators	73
4.2.5	Optical Table Setup	73
4.2.6	729 nm Laser System Overview	78
4.2.7	Pound-Drever-Hall Locking Scheme - Theory	78
4.2.8	PDH Lock - Experimental Implementation	81
4.3	Ion Traps	85
4.3.1	Split Ring Trap	85
4.3.2	PCB Trap	85
4.4	Other Experimental Considerations	86
4.4.1	Magnetic Field Generation and Vacuum System	86
4.4.2	Photon Detection	87
4.4.3	Ion Creation	88
5	J-State Mixing	93
5.1	Calculation of the Energy Eigenvalues and Eigenstates of a $^{40}\text{Ca}^+$ Ion as a Function of Magnetic Field Strength	94
5.2	J-State Mixing - An Observable Effect	106
5.3	J-State Mixing - Experiment	110
6	D-State Re-pumping	116
6.1	Multiple transition repumping scheme using a single fibre EOM.	118
6.2	Numerical calculation of RF power required	121
6.3	Experimental Setup and Calibration of Fibre EOM	122
6.4	Repumping Results	128
6.4.1	$\mathbf{D}_{\frac{5}{2}} \rightarrow \mathbf{P}_{\frac{3}{2}}$ Transitions	128
6.4.2	$\mathbf{D}_{\frac{3}{2}} \rightarrow \mathbf{P}_{\frac{1}{2}}$ Transitions	135
7	Pulsed Spectroscopy of the $S_{\frac{1}{2}} \rightarrow D_{\frac{5}{2}}$ Electric Quadrupole Transition in $^{40}\text{Ca}^+$	140
7.1	Electronic Setup	142
7.2	Trap and Optical Setup	145
7.3	Initial Experimental Results and Analysis	148
7.3.1	Tentative Attribution of Spectral Features	152

8	Conclusions and Future Outlook	158
8.1	Conclusion	158
8.2	Future Outlook	159
A	Details of the $P_{\frac{1}{2}} \rightarrow D_{\frac{5}{2}}$ Transition Rate Calculation	162
B	Analytical Expressions for the RF powers required on the fibre EOM	165

List of Figures

1.1	The Bloch sphere representation of a qubit.	16
1.2	Representation of a $\pi/2$ rotation around the x axis and a Hadamard gate.	17
1.3	Representation of a Controlled-Not gate.	17
1.4	A schematic of the Deutsch algorithm.	18
2.1	Quadratic electrostatic trap potential.	22
2.2	Hyperbolic trap electrodes.	23
2.3	Origin of the $\mathbf{E} \times \mathbf{B}$ drift.	24
2.4	The origin of the magnetron motion in a Penning trap.	25
2.5	Circular coordinate system.	26
2.6	The motion of an ion in a Penning trap.	27
2.7	Stability diagram for the Paul and combined traps.	30
3.1	Description of axialisation.	35
3.2	Rabi oscillations for a detuned laser.	37
3.3	Simplified $^{40}\text{Ca}^+$ electronic energy levels.	40
3.4	Rabi frequencies as a function of the ion's motional state.	42
3.5	Rabi oscillations of an ion in a thermal state.	43
3.6	Transitions used in the sideband cooling model.	45
3.7	Zig-zag configurations for 3 ions.	53
4.1	$^{40}\text{Ca}^+$ electronic energy levels.	56
4.2	Gain profiles involved in a ECDL.	60
4.3	Schematic of the scanning cavity.	66
4.4	Scanning cavity optics.	67
4.5	Scanning cavity drive voltage and transmission pulses.	68

4.6	Scanning cavity lock electronics.	69
4.7	Scanning cavity peak detector.	70
4.8	AOM electronics.	74
4.9	Optical setup of the infra-red lasers.	75
4.10	Optical setup of the 397 nm lasers.	76
4.11	Optical setup of the trap breadboard.	77
4.12	Example PDH error signal.	81
4.13	Optical setup of the 729 nm laser system.	82
4.14	Ringdown spectroscopy of the 729 nm locking cavity.	83
4.15	Cavity transmission with a locked and scanning 729 nm laser.	84
4.16	Split-Ring trap electrodes.	85
4.17	Imaging system used for both the Split-Ring and PCB traps.	88
4.18	Electronic energy levels of a calcium atom.	90
4.19	Loading a small ion cloud with the YAG.	91
5.1	Spin-orbit perturbation.	97
5.2	Spin-orbit and Zeeman matrix operator ($L = 1$).	98
5.3	Spin-orbit and Zeeman matrix operator ($L = 2$).	99
5.4	D orbital wavefunction amplitudes after J-state mixing.	102
5.5	P orbital wavefunction amplitudes after J-state mixing.	103
5.6	P and D state eigenvalues as a function of magnetic field strength.	105
5.7	PMT signal when there is no 854 nm beam to repump the $D_{\frac{5}{2}}$ state.	107
5.8	n^{-1} as a function of applied magnetic field.	110
5.9	n_{detected}^{-1} as a function of magnetic field strength - theoretical and experimental results.	113
6.1	Fibre EOM travelling wave electrodes.	118
6.2	850 nm, 854 nm and 866 nm repumping transitions.	119
6.3	850 nm, 854 nm and 866 nm repumping scheme.	120
6.4	Numerically optimised EOM modulation strengths.	123
6.5	Numerically optimised EOM modulation strengths for a scrambled phase.	124
6.6	Fibre EOM electronic setup.	125
6.7	VCO frequency calibration.	126
6.8	EOM modulation index calibration.	127
6.9	Histogram of PMT counts with no 854 nm beam to repump the $D_{\frac{5}{2}}$ state.	129
6.10	Ion signal with a 1 μW 854 nm beam repumping the $D_{\frac{5}{2}}$ state.	130
6.11	Histogram of PMT counts with (1.0 ± 0.1) μW of 854 nm power.	132

6.12	Histogram of quantum jump lengths with (1.0 ± 0.1) μW of 854 nm power.	133
6.13	Histogram of PMT counts with (40 ± 20) nW of 854 nm power.	134
6.14	Histogram of quantum jump lengths with (40 ± 20) nW of 854 nm power. .	135
6.15	Histogram of PMT counts with (10.0 ± 0.5) μW of 854 nm power.	136
6.16	Histogram of PMT counts with (120.0 ± 10) μW of 854 nm power.	137
6.17	Saturation of the $D_{\frac{3}{2}} \rightarrow P_{\frac{1}{2}}$ 866 nm σ repumping transitions. Sideband power is changed via the low frequency RF on the EOM.	138
6.18	Saturation of the $D_{\frac{3}{2}} \rightarrow P_{\frac{1}{2}}$ 866 nm σ repumping transitions. Sideband power is changed via the high frequency RF on the EOM.	139
7.1	Pulsed spectroscopy sequence.	141
7.2	Pulse spectroscopy electronic setup.	143
7.3	Electronic state detecting circuit.	144
7.4	Power loss of the 729 nm beam as its AOM is scanned.	147
7.5	Pulsed spectroscopy on the 729 nm transition while the laser is locked to two separate transverse modes of its reference cavity.	149
7.6	Pulsed spectroscopy of the 729 nm transitions as a function of magnetic field strength.	150
7.7	Zeeman splitting of the 729 nm transitions.	151
7.8	Fitting 729 nm transitions as a function of magnetic field strength.	151
7.9	729 nm laser propagation and polarisation directions used when pulsed spectroscopy is performed.	152
7.10	$S_{\frac{1}{2}} \rightarrow D_{\frac{5}{2}}$ quadrupole transition probabilities as a function of laser polarisation and direction.	153
7.11	Detailed 729 nm pulsed spectroscopy scan.	154
7.12	The $S_{\frac{1}{2}} \rightarrow D_{\frac{5}{2}}$ transitions at a magnetic field of 10 gauss and at a finite temperature.	156
7.13	Spread of an electronic transition due to micromotion.	156
7.14	Simulated spectrum of a single $S_{\frac{1}{2}} \rightarrow D_{\frac{5}{2}}$ transition. The temperature of the ion is 0.34 mK. The trap frequency is 100 kHz.	157

Chapter 1

Introduction and Motivation

In 1995 Cirac and Zoller proposed performing quantum computations in ion traps [1]. The ideas presented in this seminal paper have since developed into a major research area. The goal is to create a quantum computer which has both enough quantum bits (qubits) and small enough computational errors such that it could perform computations which even the most powerful classical computer could not achieve within a reasonable period of time.

The vast majority of this work has been focused on linear chains of ions in Paul traps. These traps use a combination of static and RF electric fields to confine the ions. Penning traps which use a combination of static electric and magnetic fields have not been used for this purposeⁱ (see chapter 2 for a description of ion traps). One of the reasons for Penning traps having been neglected is the more complex ion motion which leads to difficulties in cooling the ions. There are also larger experimental overheads leading to greater expense. Generally more lasers are required (due to the Zeeman splitting of the energy levels) as well as a magnet with a large and stable field. The magnet causes spatial restrictions affecting the imaging of the ions and the paths which the laser beams can take. It will be seen that higher trap frequencies are advantageous (§ 3.2). In the Penning trap these are limited by the magnetic field strength. As fields of greater than ≈ 10 tesla are very difficult and expensive to create this sets an upper limit to the trap frequencies achievable.

On the other hand an advantage of the Penning trap is the lack of large RF voltages applied to the trap electrodes. These may cause heating of the ions which we will see would lead to computational errors (§ 3.4.3). The aim of the Ion trapping group at Imperial College when I joined was to try to measure heating and decoherence rates in a Penning trap and compare them to those seen in a Paul trap. The most sensitive method

ⁱExperiments in Penning traps have in general focused on precision mass [2] and g-factor [3] measurements. There has however been some work towards quantum computation and simulation experiments using large crystals of ions in a Penning trap [4].

to measure heating rates requires the ion to be cooled near to the ground state of its motionⁱⁱ. The first step in performing heating and decoherence rate measurements is thus to cool the ion to its ground state. This has not been achieved in a Penning trap by any group at the time of writing. The work described in this thesis will describe progress towards this end.

In parallel to this goal other work has been performed by the group to demonstrate the suitability of a Penning trap for quantum computation with small numbers of ions. Before I joined the group a single $^{40}\text{Ca}^+$ ion had been trapped and observed. Doppler cooling (§ 3.1) had been performed and axialisation (§ 3.1.2) was used to cool the magnetron motion. Work had been conducted to manipulate 2-ion crystals [6]. Using axialisation the 2-ions could be aligned along the axis of the magnetic field.

During my first year in the group I worked on the controlled movement of ions perpendicular to the trapping magnetic field [7]. The movement of ions between different trapping regions (in at least 2 dimensions) has developed into a major field in the Paul trap community and is seen as a necessity in most scalable quantum computation schemes in ion traps [8]. A proton has been moved between trapping zones along the magnetic field in a Penning trap [9]. Our work was the first to move ions between trapping regions perpendicular to the magnetic field. Though I was involved in this work it formed the basis of another student's PhD (D.Crick) and so is not included in this thesis.

There has been great progress towards performing useful quantum computations in Paul traps (see § 3.4). Theoretical work has estimated the maximal computational error allowed while experimental work has been performed to assess the size and source of the current computational errors. Since our group has embarked on this work it has become clear that the heating rate is not the factor which causes the largest errors (§ 3.4.3). Methods have been found which could be used to reduce the heating rate further such that the error caused is below the maximum allowed computational error (§ 3.4.3).

With these developments in mind the Imperial College Ion Trapping group's focus has shifted to other applications of small numbers of ions cooled to the motional ground state in a Penning trap. These will be discussed in § 3.5.

The focus of the remainder of this chapter will be the general idea of quantum computation. This will not be specific to ion traps. Its purpose is to provide an idea of its power and so provide a motivation for achieving it experimentally. It will also contribute to providing a framework in which the quantum computation experiments in ion traps can be discussed.

ⁱⁱThis method uses the difference in the absorption strength on the first red and blue motional sidebands. See § 3.2 for a calculation of the Rabi frequency as a function of the motional states on these sidebands. See reference [5] for an example of an experimental implementation.

Chapter 2 will provide details of how Paul, Penning and combined traps can confine ions. In chapter 3 the methods of Doppler and sideband cooling will be described. These are the processes by which an ion can be cooled to the ground state of its motion. Also in this chapter the methods by which the electronic and motional state of a trapped ion can be manipulated using lasers will be presented. This will be required for the subsequent review of quantum computation in ion traps and allows the experiments described in later chapters to be placed in context. Some other uses of ions in the motional ground state in Penning traps will then be described.

Chapter 4 will provide an overview of the current state of the Imperial College setup focusing on the equipment used for the experiments described in chapters 5, 6 and 7. Chapter 8 will give a conclusion and future outlook.

Chapter 5 describes the observation of magnetic field induced J-state mixing in our system. It will be shown that an otherwise forbidden transition becomes weakly allowed at our trapping magnetic field strength. The effect on the Doppler cooling efficiency as well as the read-out fidelity of our electronic qubit is discussed. Chapter 6 describes the use of a high bandwidth fibre electro-optic modulator (EOM) to generate the laser frequencies required to repump out of the $D_{\frac{5}{2}}$ and $D_{\frac{3}{2}}$ sub-levels of a $^{40}\text{Ca}^+$ ion. This technique is used to see a quantum jump free signal of a $^{40}\text{Ca}^+$ ion in a Penning trap at 1 tesla for the first time. The $D_{\frac{3}{2}}$ state repumping is performed with a single 866 nm laser instead of the four 866 nm lasers previously used. This greatly simplifies the experimental setup. The $D_{\frac{5}{2}}$ state repumping provides the possibility to perform pulsed spectroscopy on the $S_{\frac{1}{2}} \rightarrow D_{\frac{5}{2}}$ quadrupole transition in $^{40}\text{Ca}^+$. Preliminary results of this spectroscopy are provided in chapter 7.

1.1 My Role in the Work Presented

An overview of my role in the work presented in this thesis will be given. During the majority of my time in the group there were two or more people working on the experiment and so many tasks were shared.

Another student (D.Crick) and I took the data presented in chapter 5 where the effect of J-mixing in our system is detailed. To observe this effect an ion was confined in one of the three trapping zones of a trap designed to transport ions perpendicular to the trapping magnetic field [7]. I was involved in the process from initial trap construction to trapping a single ion in it for the first time. The program used for the data analysis described in this chapter was written by D.Crick. He also did the original theoretical work (published with the experiment in reference [10]) to find the expected shelving rate using perturbation theory. In this thesis I have detailed another method to calculate the mixings and shelving

rate which is valid at higher magnetic field strengths.

I led the inception of the scheme detailed in chapter 6 to repump out of the ten sub-levels of the D states (at 850 nm, 854 nm and 866 nm) using four lasers and a single fibre EOM with two RF frequencies applied. I ran simulations to find the optimal RF powers to put on the EOM with and without a controllable phase between the two applied signals. I performed the work detailed to calibrate the EOM and RF sources. I led the repumping experiments where the 854 nm and 866 nm laser powers required were found. I wrote the program to perform the data analysis in this chapter.

The narrow-linewidth 729 nm laser used to perform pulsed spectroscopy on the $S_{\frac{1}{2}} \rightarrow D_{\frac{5}{2}}$ quadrupole transition described in chapter 7 was developed by D.Crick. I worked on the digital electronics required to obtain the presented spectra. This included writing the software which the microcontroller uses to perform the pulse sequence. S.Mavadia, D.Crick and I performed the experiment on a single trapped ion in an RF trap.

A number of improvements to the experiment are described in chapter 4. This included the introduction of a scanning cavity to lock the 397 nm Doppler cooling lasers. A number of people worked on this project. The cavity itself was designed and developed by another student (J.Goodwin). The majority of my input was developing the digital electronics and writing the software to lock both the cavity and the 397 nm lasers to the HeNe reference laser.

Much of my time was spent making improvements to the experimental setup. This included creating a more optimised layout of the optical table such that less laser power is lost. This also included the addition of acousto-optic modulators (AOMs) and an electro-optic modulator (EOM) as well as a 60 m fibre link to another laboratory so as their wavemeter could be used.

1.2 Introduction to Quantum Computation

A classical bit can have a value of either 0 or 1. There is a lot more scope for a qubit. The system could either be in the $|0\rangle$ or $|1\rangle$ state or in a superposition of these states written as

$$\psi = a|0\rangle + b|1\rangle. \quad (1.1)$$

The coefficients a and b are complex and can take any value as long as they satisfy the normalisation condition $|a|^2 + |b|^2 = 1$.

Now let us compare two qubits with two classical bits. The classical bits can take the

values 00, 01, 10, 11. The state of the qubits however is

$$\begin{aligned}\psi &= (a|0\rangle_x + b|1\rangle_x)(c|0\rangle_y + d|1\rangle_y) \\ &= ac|0\rangle_x|0\rangle_y + ad|0\rangle_x|1\rangle_y + bc|1\rangle_x|0\rangle_y + bd|1\rangle_x|1\rangle_y.\end{aligned}\tag{1.2}$$

In the classical case two binary digits are required to specify the state while 4 complex amplitudes are required to specify the 2 qubit state. In the general case of n bits or qubits, n binary digits are required to specify the classical system while to specify a quantum system would require 2^n complex amplitudes. There is thus a lot more information contained in a quantum system of the same size. This would suggest that a computation with the quantum system could be more efficient.

The phases in the complex amplitudes a and b rotate at the frequencies corresponding to the energies of their respective eigenstates. Factoring out the phase of a we find that there is a phase difference between the two states which rotates at a frequency corresponding to their energy difference. The global phase has no observable effect as we measure the modular square of the wavefunction and can thus be disregarded. As the only condition on the amplitudes is that they obey the normalisation condition we can write the qubit in the form

$$\psi(t) = \cos\left(\frac{\theta}{2}\right)|0\rangle + e^{-i\phi}\sin\left(\frac{\theta}{2}\right)|1\rangle.\tag{1.3}$$

The angle $\phi = \omega_0 t$, where $\hbar\omega_0$ is the energy difference between the state $|0\rangle$ and $|1\rangle$.

Writing the qubit in this way lends itself to being displayed as a vector which points to the surface of a sphere. This sphere is called the Bloch sphere and is used extensively to keep track of the state of a qubit as it is manipulated during a quantum computation. The Bloch sphere is shown in figure 1.1. In this picture the $\psi = |0\rangle$ state will be represented by a vector (the Bloch vector) touching the sphere at the north pole ($\theta = 0$) while $\psi = |1\rangle$ will be denoted by a vector that touches the sphere at the south pole ($\theta = \pi$). When $\theta = \pi/2$ the qubit is an equal superposition. The Bloch vector will quickly rotate around the z axis of the Bloch sphere at the frequency corresponding to the energy difference of the two states. We will consider the Bloch sphere in a frame rotating at this frequency, this is useful as the external interaction will also be rotating at this frequency. A change in the angle ϕ will then correspond to a phase change between the external interaction and the qubit.

A rotation in the θ direction requires an external influence. We will see in § 3.2 when we introduce Rabi oscillations that the rotation can be caused by a laser beam which for a constant intensity produces a rotation θ which is linear with time. It is noticed that it

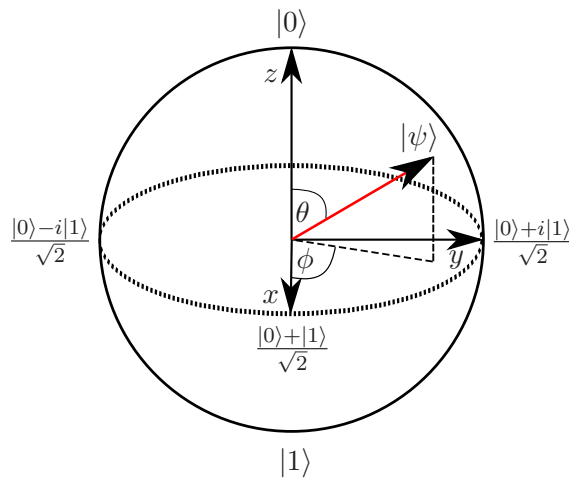


Figure 1.1: The Bloch sphere representation of a qubit. The angles θ and ϕ are required to represent the state up to a global phase.

takes two rotations around the sphere to obtain the original state with the same phase. This is not evident in the Bloch sphere picture and needs to be added in by hand.

1.2.1 Quantum Gates

In theory to perform any quantum computation it should be possible to subject the qubits to a time varying interaction whose Hamiltonian will evolve them into the final states which can then be read out. However the required interaction would be very difficult to engineer in practice. Instead a computation is broken down into a series of operations called gates analogous to the gates of classical computation. If a ‘universal set’ of gates is available any possible computation can be done. There are a number of known universal sets of quantum gates. One such set consists of an arbitrary rotation around any axis of the Bloch sphere together with the Controlled-Not (C-NOT) gate [11].

A single-qubit rotation gate performs a rotation around the x , y or z axis of the Bloch sphere. The rotation can be of any angle. A rotation is drawn schematically in figure 1.2. The input to the gate is on the left and the output is on the right. One can imagine a series of gates drawn like this which are then combined to produce the whole computation.

The Hadamard gate is a very useful gate in quantum computation. It is often used in quantum algorithms to create a superposition of states. Its action is

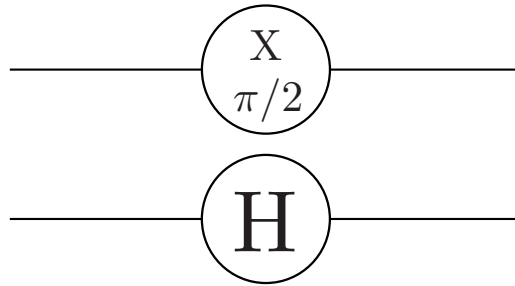


Figure 1.2: Representation of a $\pi/2$ rotation around the x axis and a Hadamard gate. This representation is used in diagrams of quantum algorithms.

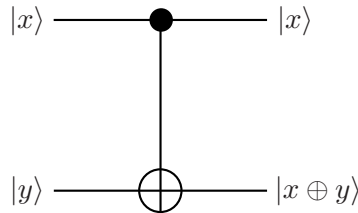


Figure 1.3: Representation of a Controlled-Not gate. $|x\rangle$ is the control qubit and $|y\rangle$ is the target qubit.

$$|0\rangle \rightarrow \frac{|0\rangle + |1\rangle}{\sqrt{2}}, \quad \frac{|0\rangle + |1\rangle}{\sqrt{2}} \rightarrow |0\rangle \quad (1.4)$$

$$|1\rangle \rightarrow \frac{|0\rangle - |1\rangle}{\sqrt{2}}, \quad \frac{|0\rangle - |1\rangle}{\sqrt{2}} \rightarrow |1\rangle \quad (1.5)$$

The Hadamard gate can be thought of as a $\pi/2$ rotation around the y -axis of the Bloch sphere followed by a π rotation around the x -axis. In a quantum circuit the Hadamard gate is represented as in figure 1.2.

The C-NOT gate has two qubits as both the input and output. The input qubits are called the ‘control’ and ‘target’ qubits. The state of the control qubit does not change during the operation. The target qubit is flipped if the control qubit is in state $|1\rangle$; if it is in the state $|0\rangle$ then it is left alone. The truth table for the C-NOT gate is shown in table 1.1. It can be represented schematically as in figure 1.3. The implementation of this gate using trapped ions will be described in detail in § 3.4.1.

Initial State	Final State
$ 0\rangle_x 0\rangle_y$	$ 0\rangle_x 0\rangle_y$
$ 0\rangle_x 1\rangle_y$	$ 0\rangle_x 1\rangle_y$
$ 1\rangle_x 0\rangle_y$	$ 1\rangle_x 1\rangle_y$
$ 1\rangle_x 1\rangle_y$	$ 1\rangle_x 0\rangle_y$

Table 1.1: Truth Table for the C-NOT Gate. x is the control qubit and y is the target qubit. The target is flipped only if the control is in the $|1\rangle$ state.

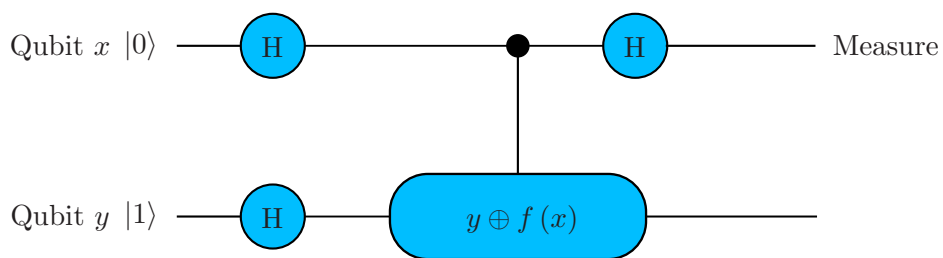


Figure 1.4: A schematic of the Deutsch algorithm. The ‘oracle’ is shown as $y \oplus f(x)$. Only the top qubit is measured.

1.2.2 Quantum Algorithms

The first quantum algorithm was proposed by Deutsch in 1985 [12]. The algorithm involves testing the action of a function, f which has a single bit as both its input and output. The function could obey four different equations,

$$\begin{aligned} f_1(\alpha) &= 0 \\ f_2(\alpha) &= 1 \\ f_3(\alpha) &= \alpha \\ f_4(\alpha) &= 1 \oplus \alpha, \end{aligned} \tag{1.6}$$

where \oplus represents addition modulo 2. The first two functions obey $f(0) = f(1)$ (f is constant) while the last two do not. The algorithm tells us whether the function is constant by evaluating the function only once. It will not tell us the exact form of the function, only whether it is constant. A classical algorithm could only ever obtain this information with a minimum of two function calls.

The algorithm is displayed schematically in figure 1.4. The inputs are shown on the left. The qubits are then put through a number of gates before a measurement is made on one of the qubits. For 2-qubit gates a solid circle signifies that that qubit is the control which controls the outcome of the target qubit (as in the C-NOT gate).

The part of the circuit which calculates the value of the function is called a standard quantum oracle. Quantum processes must be reversible. The function f cannot be evaluated directly on a single qubit as the value of the input cannot be known with certainty from the value of the output. By using two qubits there is enough information to reverse the procedure. It has been shown that the evaluation of a function can be done at least as efficiently using a quantum computer as a classical computer [11]. So without worrying how the function is evaluated we can see how efficient the algorithm is by how many times the oracle is called.

We can now go through the Deutsch algorithm and look at the wavefunction of the qubits after each gate to see how we can find out if the function is constant. First the qubits are prepared in the state $|\psi\rangle = |0\rangle_x |1\rangle_y$. Both qubits are then put through a Hadamard gate to create the state

$$\begin{aligned} |\psi\rangle &= \left[\frac{|0\rangle_x + |1\rangle_x}{\sqrt{2}} \right] \left[\frac{|0\rangle_y - |1\rangle_y}{\sqrt{2}} \right] \\ &= \frac{1}{2} \left[|0\rangle_x |0\rangle_y - |0\rangle_x |1\rangle_y + |1\rangle_x |0\rangle_y - |1\rangle_x |1\rangle_y \right]. \end{aligned} \tag{1.7}$$

The oracle is then consulted. Qubit x is not changed while qubit y is added modulo 2 to

the function call of x obtaining

$$|\psi\rangle = \frac{1}{2} \left[|0\rangle_x \left(|0\rangle_y \oplus f(0) \right) - |0\rangle_x \left(|1\rangle_y \oplus f(0) \right) + |1\rangle_x \left(|0\rangle_y \oplus f(1) \right) - |1\rangle_x \left(|1\rangle_y \oplus f(1) \right) \right]. \quad (1.8)$$

By evaluating the state at this point for each of the possible functions of equation 1.6. It is seen that the wavefunctions in the two cases where the function is constant only differ by a global phase. This is also the case for the two cases when the function is not constant. There is however a relative phase in the x qubit which is flipped if the function is balanced to if it is not

$$|\psi\rangle_{f(0)=f(1)} = \pm \left[\frac{|0\rangle_x + |1\rangle_x}{\sqrt{2}} \right] \left[\frac{|0\rangle_y - |1\rangle_y}{\sqrt{2}} \right] \quad (1.9)$$

$$|\psi\rangle_{f(0)\neq f(1)} = \pm \left[\frac{|0\rangle_x - |1\rangle_x}{\sqrt{2}} \right] \left[\frac{|0\rangle_y - |1\rangle_y}{\sqrt{2}} \right]. \quad (1.10)$$

Finally a Hadamard gate is applied to the first qubit to obtain either

$$|\psi\rangle_{f(0)=f(1)} = \pm |0\rangle_x \left[\frac{|0\rangle_y - |1\rangle_y}{\sqrt{2}} \right], \quad (1.11)$$

or

$$|\psi\rangle_{f(0)\neq f(1)} = \pm |1\rangle_x \left[\frac{|0\rangle_y - |1\rangle_y}{\sqrt{2}} \right]. \quad (1.12)$$

Measuring the first qubit will now tell us whether the function is constant. We have only evaluated the function once to obtain this result.

In practice Deutsch's algorithm isn't very useful as it only provides a factor of 2 speedup of a classical algorithm. In any case the classical algorithm only requires 2 function calls which would be performed very quickly on a classical computer.

Shor's algorithm [13] in contrast is one of the main reasons there is now so much interest in quantum computation. It is used to find the prime factors of a number. It provides an exponential decrease in computation time compared to classical algorithms.

Chapter 2

How to Trap an Ion

The operation of the different types of trap used for the results in this thesis will be described. Much of the general theory is based on that of references [14] and [15]. First a description of the electrostatic potential and its creation which is common to all the trap types will be detailed.

It is optimal to create a purely quadrupole potential well to trap ions. This would result in a force towards the centre of the trap which is proportional to the ion's distance from the centre and hence leads to harmonic motion. The general form for a three dimensional quadrupole potential is

$$\phi = V_{\text{scaled}}(ax^2 + by^2 + cz^2). \quad (2.1)$$

V_{scaled} will be defined for real traps later. For now it is considered as a proportionality constant.

It would be ideal to use an electrostatic field to create a 3D potential well to trap ions. This however can not be achieved as stated in Earnshaw's theorem [16]. For zero charge in the field the above potential must obey the Laplace equation,

$$\Delta^2\phi = 0 = 2V_{\text{scaled}}(a + b + c). \quad (2.2)$$

To satisfy the above equation it is required that the sum of the constants a , b and c must equal zero. Thus if a potential minimum is achieved in two dimensions then it is required that there be a maximum in the third direction as adding three numbers of the same sign cannot equal zero.

The shape of the quadratic potential that is achievable using static electric fields is known as a 'saddle point'. This is shown in figure 2.1 and is achieved by setting $(a, b, c) =$

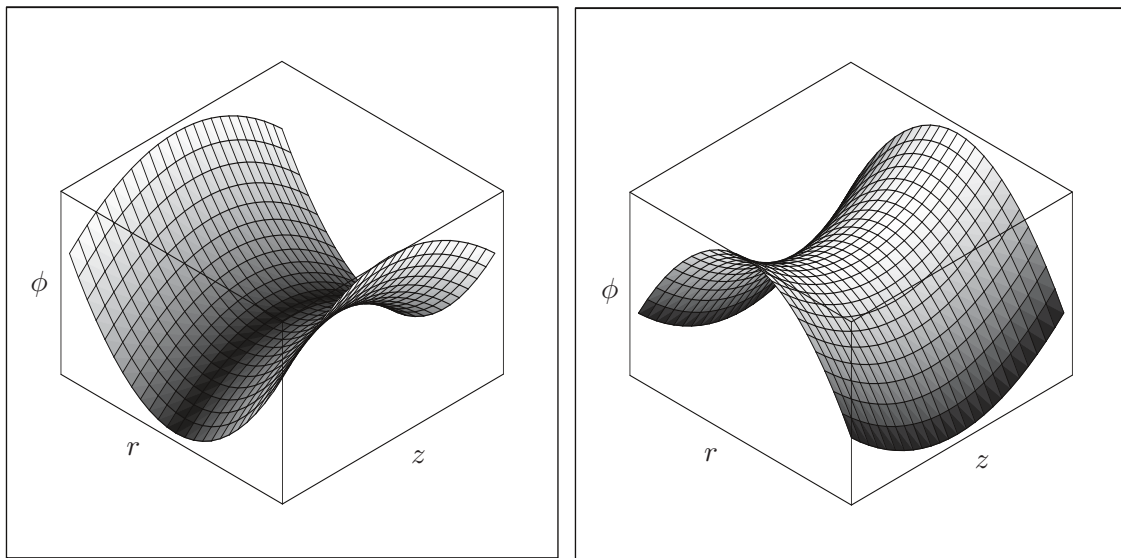


Figure 2.1: Trap potential achievable using a static electric field. There is a potential hill in either the radial or axial directions depending on the sign of the potential applied.

$(-1, -1, 2)$ giving

$$\begin{aligned}\phi &= V_{\text{scaled}}(2z^2 - y^2 - x^2) \\ &= V_{\text{scaled}}(2z^2 - r^2),\end{aligned}\tag{2.3}$$

where $r^2 = x^2 + y^2$. The potential varies quadratically in both the axial and radial directions but in one of the directions it must be a potential hill. Although this only constitutes a trap in either the radial or axial directions it turns out to be a good starting point. Strategies for 3D trapping based on a quadrupole potential will be discussed in the next section. To create such a potential, electrodes must be constructed which follow the equipotential surfaces. These surfaces are hyperboloids of revolution which obey

$$\frac{r^2}{r_0^2} - \frac{z^2}{z_0^2} = \pm 1,\tag{2.4}$$

where the positive and negative sign refer to the ‘ring’ and ‘endcap’ electrodes respectively. A diagram of the electrodes is shown in figure 2.2. It is impossible to create electrodes of infinite size and so the potential created is always an approximation to a true quadrupole. Many electrode geometries differ wildly from that shown in figure 2.2. It turns out that by careful optimisation of the electrode geometry or the voltage on extra ‘compensation’ electrodes the potential can be made to be very close to quadratic near the centre of the trap where the ions will be once they have been cooled. See reference [17] for examples of

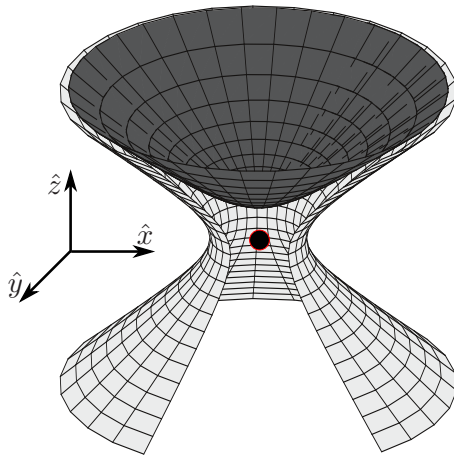


Figure 2.2: Hyperbolic trap electrodes used to produce a 3D quadrupole potential. Part of the ring electrode (light grey) has been removed so that the trap centre can be seen. Only one of the endcaps has been drawn (dark grey). The constants z_0 and r_0 are from the centre of the trap to the nearest point of the endcap and ring respectively. To create a perfectly quadrupole potential the electrodes would have to extend to infinity.

traps with electrodes very unlike the hyperbolic ones shown.

We can now define V_{scaled} in terms of the potential applied to the trap electrodes as

$$\begin{aligned} V_{\text{scaled}} &= \frac{V}{2z_0^2 + r_0^2} \\ &= \frac{V}{R_0^2}, \end{aligned} \tag{2.5}$$

where $R_0^2 = 2z_0^2 + r_0^2$ and V is the endcap voltage w.r.t the ring voltage.

A positive ion will feel a potential well in the axial direction and a potential hill in the radial plane if V is made positive. Defining V_{scaled} removes the dependency of the potential curvature on the trap size. Note that it has units of Vm^{-2} .

We have seen that it is impossible to create a static electric field which gives a potential well in all three dimensions. It is however still possible to trap ions. Penning trap uses an additional magnetic field to confine the ions in the radial plane. Alternatively the

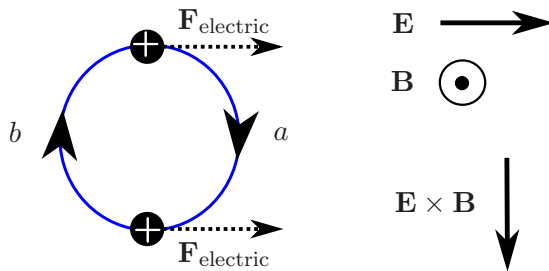


Figure 2.3: The origin of the $\mathbf{E} \times \mathbf{B}$ drift in uniform \mathbf{E} and \mathbf{B} fields. In the radial plane the ion feels a force in the $Q(\mathbf{v} \times \mathbf{B})$ direction resulting in a cyclotron orbit with a rotational direction which obeys a right-hand or left-hand rule for a positively or negatively charged ion respectively. During this orbit the ion feels a force due to the trapping electric field $\mathbf{F}_{\text{electric}} = Q\mathbf{E}$. For a uniform electric field pointing in a single direction as shown the positive ion is accelerated between b and a and then decelerated between a and b . It is thus moving faster at point a than point b and so drifts in the $\mathbf{E} \times \mathbf{B}$ direction.

Paul trap oscillates the confining axis of the saddle potential between the axial and radial directions at a frequency Ω . For ions with charge-to-mass ratios similar to $^{40}\text{Ca}^+$ this oscillation turns out to be at a radio frequency.

2.1 Penning Trap

The Penning trap uses both static electric and magnetic fields to confine an ion. The same electrode geometry is used (that of figure 2.2). Trapping in the axial direction is achieved via the electric field by putting a bias on the endcaps relative to the ring of the same sign as the ion's charge. The magnetic field is applied in the z direction. The Lorentz force on the ion due the electric and magnetic fields is written as

$$\begin{aligned} \mathbf{F} &= \mathbf{F}_{\text{electric}} + \mathbf{F}_{\text{magnetic}} \\ &= Q\mathbf{E} + Q(\mathbf{v} \times \mathbf{B}). \end{aligned} \quad (2.6)$$

The magnetic field thus does not affect the motion in the z direction ($\mathbf{v} \times \mathbf{B} = 0$). The axial motion is therefore just due to the quadratic potential and so the ion undergoes harmonic motion with frequency

$$\omega_z = 2\sqrt{\frac{Q}{m}V_{\text{scaled}}}. \quad (2.7)$$

The applied bias results in the same saddle shaped potential in the radial plane as seen previously in figure 2.1 and so the ion will begin to move outwards from the centre of the trap in the radial direction. Thus as the ion gains a velocity in the radial direction

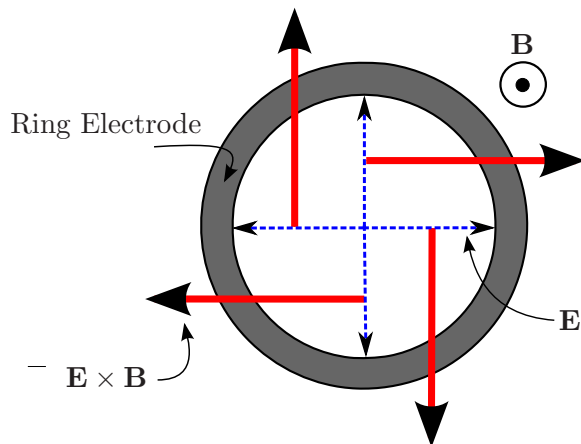


Figure 2.4: The origin of the magnetron motion in a Penning trap. The direction of the $\mathbf{E} \times \mathbf{B}$ drift at different points shows that the ion will travel in an orbit. The diagram is for a positive ion and so the ring is negatively biased. The $\mathbf{E} \times \mathbf{B}$ motion has the same rotation direction as the cyclotron motion.

it will experience a force perpendicular to this direction and the magnetic field. The ion will begin to move around the magnetic field lines in a cyclotron orbit (with frequency $\omega_c = QB/m$ in the absence of an electric field). The force on the ion due to the B field, $Q(\mathbf{v} \times \mathbf{B})$ is directed towards the centre of the cyclotron orbit. The motion is however complicated by the fact there is an electric field present. There is a drift of the centre of the cyclotron orbit around the trap centre. This is called the $\mathbf{E} \times \mathbf{B}$ drift. This drift is explained for a uniform, unidirectional electric field in figure 2.3. The electric field exerts a force, which for a positive ion is in the direction of the field. This results in a positive ion moving faster at point a than at point b . There is thus a net movement in the $\mathbf{E} \times \mathbf{B}$ direction.

In the Penning trap the electric field is not uniform. In the radial plane it points out from the trap centre to the ring. The $\mathbf{E} \times \mathbf{B}$ drift is thus not always in the same direction. Its direction at four points is shown in figure 2.4. It is seen that the drift results in a circular motion around the centre of the trap with the same rotation direction as the cyclotron orbit.

From these simple arguments we would expect the radial motion to consist of two circular orbits. One due to the cyclotron orbit and one due to the $\mathbf{E} \times \mathbf{B}$ drift. The presence of an electric field also modifies the frequency of the cyclotron motion. To find the radial motional frequencies we substitute the radial electric and magnetic fields into the equation for the Lorentz force (equation 2.6) assuming circular motion at a frequency ω as suggested in [18]. Figure 2.5 gives the coordinate system used.

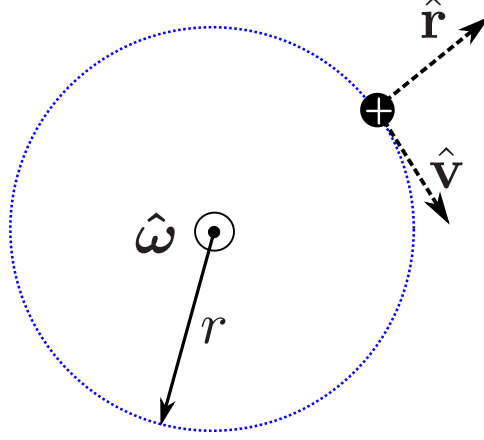


Figure 2.5: The coordinate system used in the derivation of equation 2.8. Circular motion is assumed. Three unit vectors are displayed. $\hat{\mathbf{v}}$ is in the direction of the ion's velocity (i.e. a tangent to the circle). $\hat{\mathbf{r}}$ is a unit vector from the ion to the centre of the orbit. $\hat{\boldsymbol{\omega}}$ is a unit vector coming out of the page in the diagram. It obeys a left-hand-rule w.r.t the positive ion's motion.

The total force on the positive ion is $\mathbf{F} = -mr\omega^2\hat{\mathbf{r}}$. The force due to the magnetic field is $Q(\mathbf{v} \times \mathbf{B}) = QB\omega r(\hat{\boldsymbol{\omega}} \times \hat{\mathbf{r}} \times \hat{\boldsymbol{\omega}}) = -QB\omega r\hat{\mathbf{r}}$. The radial electric field, $\mathbf{E}_r = -\frac{\partial}{\partial r}\phi\hat{\mathbf{r}} = \frac{\partial}{\partial r}V_{\text{scaled}}(r^2 - 2z^2)\hat{\mathbf{r}} = 2V_{\text{scaled}}r\hat{\mathbf{r}}$. Substituting these parts into the Lorentz equation we obtain a quadratic equation,

$$m\omega^2 - QB\omega + 2V_{\text{scaled}}Q = 0. \quad (2.8)$$

Which has two solutions for the frequency which we can write as

$$\omega'_c = \frac{\omega_c}{2} + \sqrt{\frac{\omega_c^2}{4} - \frac{\omega_z^2}{2}} \quad (2.9)$$

$$\omega_m = \frac{\omega_c}{2} - \sqrt{\frac{\omega_c^2}{4} - \frac{\omega_z^2}{2}}. \quad (2.10)$$

We now call ω_m the magnetron frequency and ω'_c the modified cyclotron frequency.

These expressions for the magnetron and modified cyclotron frequencies introduce a trapping condition. The expression in the square root should be positive so that the frequencies remain real. The consequences of a violation of this inequality will be described below. We have

$$\omega_c^2 - 2\omega_z^2 \geq 0. \quad (2.11)$$

Or substituting in for the cyclotron frequency or both the cyclotron and axial frequencies

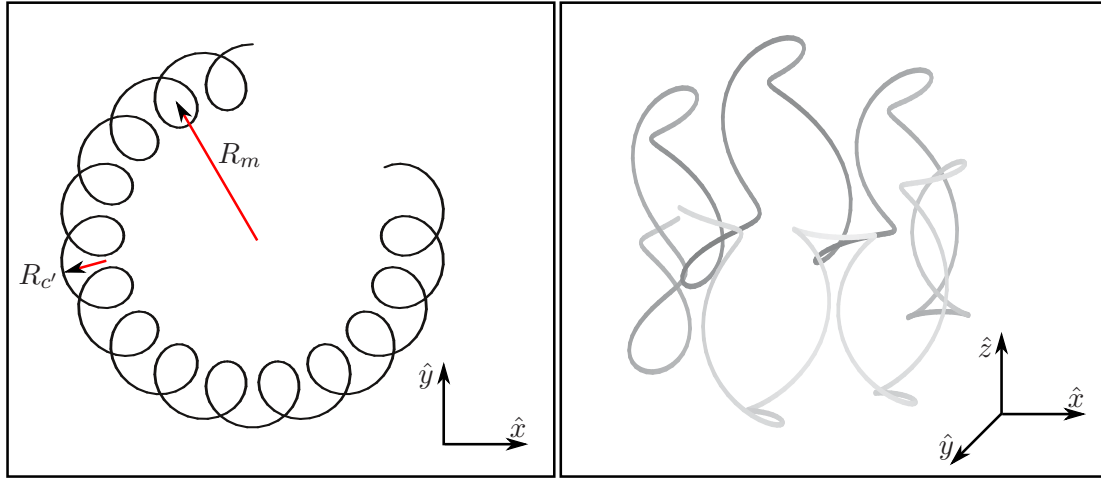


Figure 2.6: The motion of an ion in a Penning trap. The left plot shows the magnetron and modified cyclotron motions in the radial plane. The plot on the right shows the 3 dimensional motion. The modified cyclotron frequency was set to $\omega'_c = 0.95\omega_c$ (i.e. typical working conditions). The magnetron and axial frequencies were then calculated using equations 2.14 and 2.15.

we can write a condition for the axial frequency or the scaled trap voltage as

$$\omega_z \leq \frac{QB}{\sqrt{2}m} \quad (2.12)$$

$$V_{\text{scaled}} \leq \frac{QB^2}{8m}. \quad (2.13)$$

As the trap voltage is increased the curvature of the potential is increased in the axial direction resulting in a larger force towards the centre of the trap in that direction and a higher axial frequency. To obey Gauss' law the potential hill in the radial direction must also become steeper. There is thus a greater outwards force in the radial plane which has to be overcome by the magnetic force inwards. For a fixed magnetic field, when the trap voltage is increased so that equality is reached in equation 2.13, the inward and outward forces balance and the ion is no longer trapped.

By substitution into equations 2.9 and 2.10 it can be shown that

$$\omega_c = \omega'_c + \omega_m \quad (2.14)$$

$$\omega_c^2 = \omega'_c{}^2 + \omega_m^2 + \omega_z^2. \quad (2.15)$$

In typical working conditions we have $\omega_c > \omega'_c > \omega_z > \omega_m$. The typical trajectory in the radial plane of an ion in this situation is shown in figure 2.6.

The energies of the modified cyclotron and magnetron orbits are given by the sum of

their respective kinetic and potential energies,

$$\begin{aligned} E_{\text{total}} &= E_{\text{kinetic}} + E_{\text{potential}} \\ &= \frac{1}{2}m\omega^2 r^2 - Qr^2 V_{\text{scaled}}. \end{aligned} \quad (2.16)$$

E_{kinetic} is of course always positive and as there is a potential hill in the radial plane $E_{\text{potential}}$ is always negative. From equations 2.9 and 2.10 the maximum ω'_c and the minimum ω_m for stable trapping is $\frac{\omega_c}{2}$. It can be seen from equation 2.16 that when $\omega = \frac{\omega_c}{2}$ the total energy is zero. This means that for stable trapping parameters the energy of the modified cyclotron orbit is always positive while the energy of the magnetron orbit is always negative. This has to be considered when performing laser cooling in a Penning trap. To reduce the radius of the respective orbits, energy must be taken out of the cyclotron motion but put into the magnetron motion. This can be achieved by correct positioning and detuning of the laser beam or by using a technique called axialisation (§ 3.1).

2.2 Paul Trap

The other method to trap ions is in a Paul trap. Here both DC and AC voltages are put on the electrodes of figure 2.2. To find the equations of motion of ions in a trap where both a DC and AC voltage is applied, we first find the force on the ion in the axial and radial direction due to a potential of the form of equation 2.3 and substitute in for V_{scaled} using equation 2.5. For example in the axial direction we have $F_z = -Q \frac{\partial \phi}{\partial z} \hat{z} = -4 \frac{Q}{R_0^2} V z \hat{z}$. Equating this force to the ion's mass times its acceleration we find

$$\begin{aligned} \frac{d^2 z}{dz^2} + 4 \frac{Q}{MR_0^2} [V_{\text{DC}} + V_{\text{AC}} \cos(\Omega t)] z &= 0 \\ \frac{d^2 r}{dr^2} - 2 \frac{Q}{MR_0^2} [V_{\text{DC}} + V_{\text{AC}} \cos(\Omega t)] r &= 0, \end{aligned} \quad (2.17)$$

where the same method has been used in the radial direction. We now follow the example of references [14] and [15] and make a change of variables to convert the differential equations into a solvable form. We make the definitions

$$\begin{aligned} a_z &= \frac{4QV_{\text{DC}}}{MR_0^2 \Omega^2} = -2a_r \\ q_z &= -\frac{2QV_{\text{AC}}}{MR_0^2 \Omega^2} = -2q_r \\ \tau &= \frac{\Omega}{2} t. \end{aligned} \quad (2.18)$$

Here a_z and a_r are dimensionless parameters proportional to V_{DC} while q_z and q_r are dimensionless parameters proportional to V_{AC} . These definitions allow us to write equations for the radial and axial motion in the form of Mathieu equations as

$$\frac{d^2(r, z)}{d\tau^2} + [a_{r,z} - 2q_{r,z} \cos(2\tau)](r, z) = 0. \quad (2.19)$$

The equation has stable solutionsⁱ for certain combinations of $a_{r,z}$ and $q_{r,z}$. When the ion is stable its motion can be described by a sum of motions at different frequencies as

$$(r, z) = A_{r,z} \sum_{n=-\infty}^{\infty} C_{2n} \cos \left[(\beta_{r,z} + 2n) \frac{\Omega}{2} t \right] + B_{r,z} \sum_{n=-\infty}^{\infty} C_{2n} \sin \left[(\beta_{r,z} + 2n) \frac{\Omega}{2} t \right]. \quad (2.20)$$

So $\beta_{r,z}$ is a number which defines the set of frequencies which the ion can have,

$\sum_{n=-\infty}^{\infty} (\beta_{r,z} + 2n) \frac{\Omega}{2}$. It is a function of $a_{r,z}$ and $q_{r,z}$ and can be written to a good approximation as [19]

$$\beta_{r,z}^2 = a_{r,z} - \frac{a_{r,z} - 1}{2(a_{r,z} - 1)^2 - q_{r,z}^2} q_{r,z}^2 - \frac{5a_{r,z} + 7}{32(a_{r,z} - 1)^3(a_{r,z} - 4)} q_{r,z}^4. \quad (2.21)$$

When $|a|, q \ll 1$ a simpler approximation can be used,

$$\beta_{r,z}^2 = a_{r,z} + \frac{q_{r,z}^2}{2}. \quad (2.22)$$

The combinations of $a_{r,z}$ and $q_{r,z}$ which are stable are also governed by $\beta_{r,z}$. The stability region with the lowest $a_{r,z}$ and $q_{r,z}$ values is defined by $0 < \beta_{r,z} < 1$. This region is shown in figure 2.7.

When the approximation given in equation 2.22 is valid the ion's position can be written as

$$(r, z) = C_0 \sqrt{A_{r,z} + B_{r,z}} \left(1 - \frac{q_{r,z}}{2} \cos(\Omega t) \right) \cos \left(\beta_{r,z} \frac{\Omega}{2} t \right), \quad (2.23)$$

where $\frac{C_2}{C_0} = \frac{C_{-2}}{C_0} = -\frac{q_{r,z}}{4}$ has been used which is valid in the limit of equation 2.22 [15].

So the motion is a combination of oscillations at $\beta_{r,z} \frac{\Omega}{2}$ which we call the secular frequency and Ω which we call the micromotion frequency. We are considering the limit of small $\beta_{r,z}$ and so the secular frequency is much lower than the micromotion frequency. Let us thus examine the micromotion by approximating the ion's position in its secular

ⁱA solution is defined as stable if it results in a periodic motion in both the axial and radial directions. The ion has a maximum displacement from the trap center when parameters corresponding to these solutions are used.

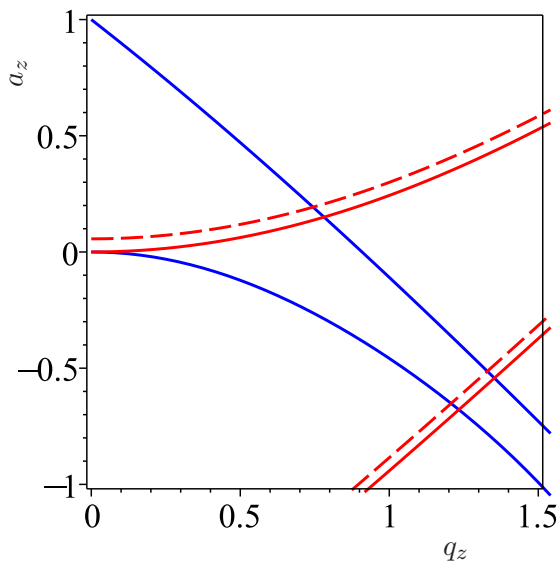


Figure 2.7: Stability diagram for the Paul and combined traps. The blue and red lines define the boundary of stability for the axial and radial directions respectively. The dashed line shows the new radial boundaries for the case of a combined trap for a $^{40}\text{Ca}^+$ ion with $B = 1$ tesla and the RF applied, $\Omega = 2.27$ MHz.

oscillation to remain constant during a single micromotion oscillation. Considering just the axial motion we can write

$$z = G - H \cos(\Omega t), \quad (2.24)$$

where G and H are constant on the timescale of the micromotion. We define H as the amplitude of the micromotion. The force on the ion can be found via the second derivative of z time its mass or from the trap potential. In the absence of a DC field we have

$$F_z = M \frac{d^2 z}{dt^2} = MH\Omega^2 \cos(\Omega t) = 4 \frac{Q}{R_0^2} V_{\text{AC}} \cos(\Omega t) z. \quad (2.25)$$

Rearranging for the micromotion amplitude we find

$$H = \frac{4QV_{\text{AC}}}{\Omega^2 M R_0^2} z. \quad (2.26)$$

So the amplitude of the micromotion increases linearly with the distance from the trap centre. The micromotion is generally something which adds complication to experiments and so is to be minimised. The ion's equilibrium position can be moved away from the trap centre by stray electric fields and so extra compensation voltages are usually applied

on the trap and/or extra electrodes installed near the trap electrodes to move the ion back to the trap centre and hence minimise the micromotion.

Let us try and obtain a better physical understanding of the trapping action of a Paul trap. If F_z at a single position z is considered then the time averaged force over one RF period is equal to zero. However F_z has the action of moving the ion. We can think of the ion's micromotion sampling the trapping field. As the force exerted on the ion is larger the further the ion is from the trap centre there is a time averaged force towards the trap centre.

We can find this time averaged force by integrating F_z over a single RF period using equation 2.24 for the ion's position (with the micromotion amplitude substituted from equation 2.26). We find a force directed towards the trap centre which is proportional to z . Simple harmonic motion (SHM) thus results. The frequency of which given by [18]

$$\omega_z = \frac{2\sqrt{2}QV_{AC}}{m\Omega R_0^2}z = \frac{\Omega}{2\sqrt{2}}q_z. \quad (2.27)$$

This is the same frequency found when using the small q_z approximation for β_z (equation 2.22 with $a_z = 0$). The effective potential which creates this SHM is called the pseudopotential.

2.3 Combined Trap

A combined trap results when both an AC electric field and a static magnetic field (applied in the axial direction as in the Penning trap) are used trap ions with the option of also applying a static electric field. The force due to the magnetic field acts perpendicular to the magnetic field direction and so does not affect the ion's motion in the axial direction. The magnetic field acts like an extra DC trapping force in the radial plane and can be included in the above analysis for a Paul trap by increasing the a_r parameter by a factor $(\frac{\omega_c}{\Omega})^2$ [20]. The shift in the stability diagram (figure 2.7) has been shown for the parameters used in an experiment in this thesis (§ 5.3). In the experiment an ion is trapped at different magnetic field strengths (from 0 tesla up to ≈ 1 tesla). It is important to note the combined trap is stable for all these fields.

Interaction of light with a trapped Ion - Coherent Dynamics and Laser Cooling

3.1 Doppler Cooling

Doppler cooling was first proposed in 1975 by Wineland and Dehmelt [21] and Hansch and Schawlow [22]. It is now used extensively to cool atoms and ions. A simple overview will be given here to find an approximate rate and final temperature of a trapped ion. The motional frequency of the ion will be assumed low enough such that it can be ignored. The fact that the ion is already trapped by non-optical means does however result in only a single laser being required as the ion will keep coming into resonance as it oscillates.

The idea is to use the momentum transfer from photons to the ion when absorption occurs to reduce the ion's temperature. Reducing the temperature of an ion means to reduce the spread of its Maxwell-Boltzmann distribution. This requires a velocity dependent absorption. We will see that this is achieved via the Doppler effect.

First let us note that there is also a heating effect. Before a second photon can be absorbed a photon has to be emitted. This can occur via stimulated or spontaneous emission. A photon emitted via stimulated emission will have a velocity in the same direction as the absorbed photon. There will thus be no net momentum transfer and thus no cooling. A spontaneously emitted photon's direction however is uncorrelated to the absorbed photon's direction. It is governed by the transition's radiation pattern which has the same emission probability for a direction, \hat{r} as $-\hat{r}$. For a finite number of emissions there is however a momentum increase which causes a heating effect which we shall discuss.

Following reference [23] let us first consider the cooling force, $F_{\text{cooling}} = \frac{dp_{ab}}{dt}$ where p_{ab} is the momentum gained from absorbing photons. This force is equal to the rate of

absorption, R multiplied by the momentum gained by an absorption, $\hbar k$ (where $k = \frac{2\pi}{\lambda}$ is the magnitude of the photon's wavevector). The rate can be broken down into the probability of being in the upper electronic level, P_e times the spontaneous emission rate, Γ . The probability of being in the upper level is a tradeoff between the rates of absorption, spontaneous emission and stimulated emission and can be written as

$$P_e = \frac{\Omega_R^2}{2\Omega_R^2 + 4\Delta^2 + \Gamma^2}, \quad (3.1)$$

where Ω_R is the on-resonant Rabi frequency and Δ is the laser detuning. The ion moving towards the laser with velocity, v will see a different detuning due to the Doppler effect given by $\Delta \rightarrow \Delta - kv$. Expanding the expression for F_{cooling} and looking at the term proportional to v we see that a friction force results for a negative detuning,

$$F_{\text{cooling}} = \frac{8\hbar k^2 \Gamma \Omega_R^2 \Delta}{(2\Omega_R^2 + 4\Delta^2 + \Gamma^2)^2} v. \quad (3.2)$$

This force is maximal for $\Delta = -\frac{\Gamma}{2}$ and $\Omega_R = \Gamma$. The rate that energy is removed, $\frac{dE}{dt}_{\text{cooling}} = -F_{\text{cooling}}v$ so the maximum energy reduction isⁱ

$$\frac{dE}{dt}_{\text{cooling}} = \frac{1}{4} \hbar k^2 v^2. \quad (3.3)$$

We have noted that there is a heating effect via the momentum gained by the recoil from spontaneous emission. The ion can be thought of as taking a random walk through momentum space with a step size given by $\hbar k$. The average momentum increase after N scattering events is $\sqrt{N}\hbar k$. The number of spontaneous emissions is Rt so that the average momentum increase is $\hbar k\sqrt{Rt}$. Converting this momentum into an energy and differentiating we find

$$\frac{dE}{dt}_{\text{heating}} = \frac{\hbar^2 k^2}{8m} \Gamma. \quad (3.4)$$

The rate of cooling is thus $\frac{\hbar k^2}{8} (2v^2 - \frac{\hbar}{m}\Gamma)$ and when equilibrium is reached the ion should have a final temperature of

$$T_{\text{Doppler}} = \frac{\hbar\Gamma}{2k_B}. \quad (3.5)$$

This is the Doppler limit temperature and shows that the narrower the transition used

ⁱThe reader might expect that this cooling force should depend on Γ . Taking the Taylor expansion assumes $v \ll \frac{\Delta}{k} = \frac{\Gamma}{2k}$. So it is assumed that the ion's Doppler spread is small compared with the transition linewidth. Thus the rate is only achieved when Γ is large enough.

the lower is the temperature that can be reached.

3.1.1 Doppler Cooling in the Penning Trap

In a Paul trap the Doppler cooling laser is set red-detuned from the transition frequency. This results in the ion being more likely to absorb a photon when it is travelling towards the laser as required. As the ion oscillates back and forth in the trap it will keep coming in resonance with the laser. Having a red-detuned laser with a component in both the axial and radial directions is therefore enough to cool an ion in a Paul trap. In a Penning trap the axial motion is harmonic and thus can be cooled in the same way with a component of a red-detuned laser beam along that direction. The situation in the radial plane is complicated by the magnetron motion. Energy must be put in to this motion to reduce the radius of the magnetron orbit. The cyclotron motion on the other hand behaves normally requiring a reduction in its energy to reduce its orbit size. It is impossible to meet both of these criteria via a choice of laser frequency alone.

The typical motion in a Penning trap is shown in figure 2.6. The magnetron orbit is generally much larger than the cyclotron. The laser beam can be offset such that it points in the same direction as the magnetron motion but still covers the whole of the cyclotron orbit. If the laser is red-detuned absorption is most likely to occur on the part of the cyclotron orbit where the ion is moving towards the laser. Due to the spatial offset absorption is more likely to occur during the part of the magnetron orbit when the ion is moving away from the laser. This meets the criteria to cool the ion towards the centre of a Penning trap.

3.1.2 Axialisation

It is not ideal to require the cooling laser to be spatially offset to Doppler cool in a Penning trap. The laser spot size would limit the minimum magnetron orbit radius and the lowest temperatures would not be achievable. A method called axialisation has been developed which can be used. This involves using a small amplitude rotating quadrupole drive to mix the magnetron and cyclotron motions. A simple picture of axialisation can be obtained by considering the quantised cyclotron and magnetron orbits. The ion can have an integer number of phonons of each of these motions. The ion's energy due to its radial motion is shown in figure 3.1. The energies associated with the cyclotron and magnetron motions increase and decrease respectively as the phonon numbers are increased. As shown in the diagram if an RF photon is absorbed at the sum of the magnetron and cyclotron frequencies then the cyclotron phonon number will increase by 1 while the magnetron phonon number will decrease by 1. A red-detuned laser can then cool the cyclotron motion. If this laser is

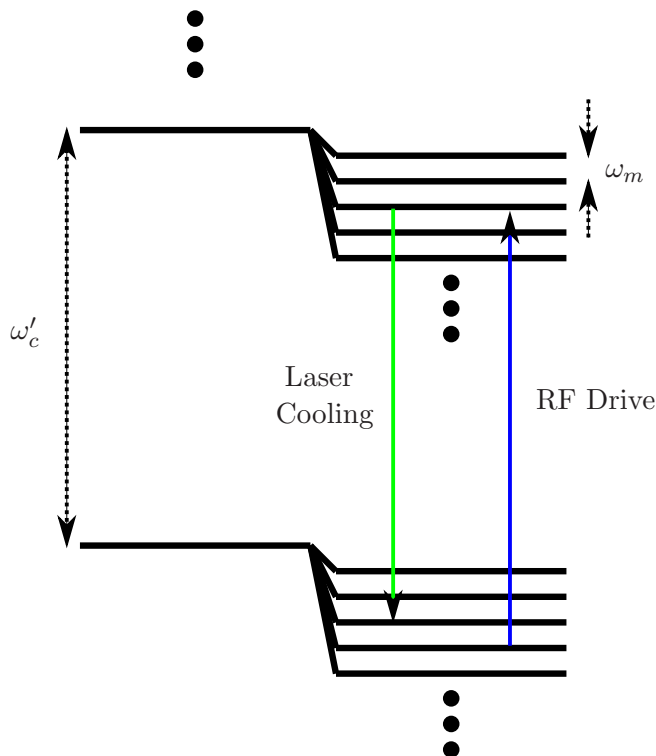


Figure 3.1: Axialisation description in terms of quantised cyclotron and magnetron motions.

not spatially offset it will have a relatively small effect on the lower frequency magnetron motion. The net effect of the RF drive and Doppler cooling laser is thus to increase the magnetron energy while reducing the cyclotron energy and so the ion will be cooled towards the centre of the trap.

3.2 Coherent Dynamics

Trapped ions have both electronic and vibrational states. We will see in § 3.4 that quantum computation schemes use both of these sets of states. We need to investigate the dynamics of a trapped ion's electronic and motional wavefunction as it interacts with a laser pulse. The analysis in this chapter is applicable to any trapped ion with two electronic states. In § 4 the actual states of a $^{40}\text{Ca}^+$ ion used throughout this thesis will be described.

First let us consider a simplification where an ion is not trapped and so only has a set of electronic states. Let us also ignore all other electronic states apart from the two which we are coupling with the laser. We will also make the assumption throughout this section

that the electronic excited state is long lived compared with the dynamics described. Note that these states are not linked to the Doppler cooling transition described in the previous section but are associated with a much narrower ‘forbidden’ transition which can nonetheless be driven coherently with a laser. The interaction of a classical oscillating electric field interacting with a 2-level system can be solved exactly for the time dependence of the amplitude in each state. The total state of this system $|\psi\rangle$, can be written at a time t , as a superposition of the individual electronic states which we label as the ground $|g\rangle$, and excited $|e\rangle$, states with amplitudes A_g and A_e respectively and a relative phase between the states rotating at the transition frequency, ω_E as

$$|\psi\rangle = A_g |g\rangle + e^{-i\omega_E t} A_e |e\rangle. \quad (3.6)$$

This is the state introduced in the introduction when describing a qubit, the quantum analog of a classical bit. If at $t = 0$ the amplitude is entirely in the ground state then it can be shown that the laser causes the amplitude to oscillate as [24]

$$A_e = \frac{\Omega_R}{\Omega} \sin\left(\frac{\Omega t}{2}\right) \quad A_g = \frac{\Omega_R}{\Omega} \cos\left(\frac{\Omega t}{2}\right), \quad (3.7)$$

where Ω_R is the Rabi frequency for a laser on resonance. It depends on the matrix element of the interaction between the ion (an electric quadrupole transition is used in $^{40}\text{Ca}^+$) and the electric field of the laser between the ground and excited electronic states. Ω is generalised for a laser with a detuning from the transition $\Delta = \omega_L - \omega_E$ such that $\Omega = \sqrt{\Omega_R^2 + \Delta^2}$. It is therefore noted that the Rabi frequency of a transition is increased as the laser is detuned. The evolution of the state under the interaction of the laser is equivalent to the evolution of the qubit of equation 1.3 with $\theta = \Omega t$ and with $\Delta = 0$. Thus a laser can rotate the state around the Bloch sphere at a frequency given by Ω .

The probability of being in the ground or excited state is the square of the corresponding amplitude,

$$P_e = \left(\frac{\Omega_R}{\Omega}\right)^2 \sin^2\left(\frac{\Omega t}{2}\right) \quad P_g = \left(\frac{\Omega_R}{\Omega}\right)^2 \cos^2\left(\frac{\Omega t}{2}\right). \quad (3.8)$$

The probability of being in either the ground or excited state at any time is always equal to 1. It is noted that when the laser is detuned it is not possible to achieve a 100% population transfer to the excited state (see figure 3.2).

So far we have considered a classical electric field interacting with a two level system. An ion trapped in a harmonic potential has a set of motional states as well as the 2 electronic states. We will now consider this case, following the treatment of reference [25]. The Hamiltonian, $H = H_0 + H_1$ for a classical, single mode laser of wavevector k and

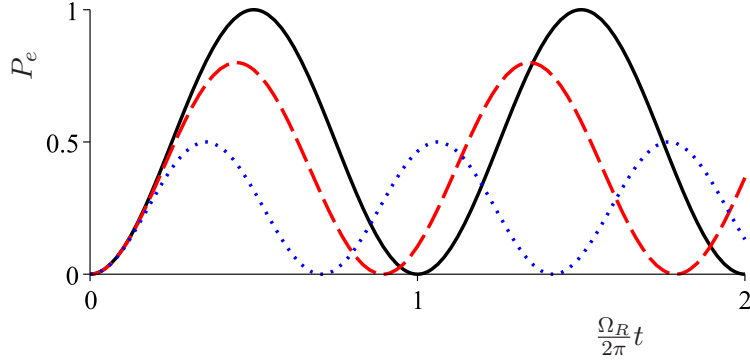


Figure 3.2: Rabi oscillations for different laser detunings. The plots are for $\Delta = 0$ (black, solid), $\Delta = \frac{\Omega_R}{2}$ (red, dash) and $\Delta = \Omega_R$ (blue, dot). It is noted that Ω is defined as the frequency at which the population oscillates so $\frac{\Omega}{2}$ is the frequency at which the amplitude oscillates.

angular frequency ω_L interacting with an ion of mass m trapped in a harmonic potential with an oscillation frequency ω_T is given by

$$H_0 = \frac{p^2}{2m} + \frac{1}{2}m\omega_T^2 x^2 + \frac{1}{2}\hbar\omega_E \hat{\sigma}_z \quad (3.9)$$

$$H_1 = \frac{1}{2}\hbar\Omega \left[e^{i(kx - \omega_L t + \phi)} \sigma^+ + e^{-i(kx - \omega_L t + \phi)} \sigma^- \right], \quad (3.10)$$

where $\hat{\sigma}_z = |e\rangle\langle e| - |g\rangle\langle g|$, $\sigma^+ = |e\rangle\langle g|$ and $\sigma^- = |g\rangle\langle e|$. H_0 gives the energy of the trapped ion with no laser field present. The three terms in H_0 correspond to the kinetic, potential and electronic energy of the ion. H_1 is the interaction energy between the laser and ion. Now Ω has been defined to be a measure of the strength of the interaction. We will see that this definition leads to Ω governing the frequency of the oscillation between the states but the frequency is only the same (and only to first order) for transitions which do not change the phonon number.

The position and momentum can be written in terms of creation and annihilation operators which operate on a motional state of the ion with n phonons and create a normalised state with one extra or one less phonon respectively $\hat{a}^\dagger |n\rangle = \sqrt{n+1} |n+1\rangle$ and $\hat{a} |n\rangle = \sqrt{n} |n-1\rangle$,

$$\hat{x} = \sqrt{\frac{\hbar}{2\omega_T m}} (\hat{a} + \hat{a}^\dagger) \quad (3.11)$$

$$\hat{p} = i\sqrt{\frac{\hbar m \omega_T}{2}} (\hat{a} - \hat{a}^\dagger). \quad (3.12)$$

Substituting these into the Hamiltonian and using $[\hat{a}, \hat{a}^\dagger] = 1$ we obtain

$$H_0 = \hbar\omega_T \left(\hat{a}^\dagger \hat{a} + \frac{1}{2} \right) + \frac{1}{2} \hbar\omega_E \hat{\sigma}_z \quad (3.13)$$

$$H_1 = \frac{1}{2} \hbar\Omega \left[e^{i\eta(\hat{a}+\hat{a}^\dagger)} e^{-i(\omega_L t + \phi)} \sigma^+ + e^{-i\eta(\hat{a}+\hat{a}^\dagger)} e^{i(\omega_L t + \phi)} \sigma^- \right], \quad (3.14)$$

where $\eta = k\sqrt{\frac{\hbar}{2m\omega_T}}$ is the Lamb-Dicke parameter and can be shown to be given by the extent of the motional ground state wavefunction of the ion relative to the wavelength of light projected along the axis of the ion's motion. It is noted that even when the ion has no phonons it still has a motional energy given by $\frac{1}{2}\hbar\omega_T$. It is instructive to now go into the interaction picture where the interaction Hamiltonian is defined as $H_I = U^\dagger H U$ where $U = e^{\frac{iH_0 t}{\hbar}}$ and we move some of the time dependence into the creation and annihilation operators $a^\dagger = \hat{a}^\dagger e^{i\omega_T t}$ and $a = \hat{a} e^{-i\omega_T t}$. We find

$$H_I = \frac{1}{2} \hbar\Omega \left[e^{i\eta(a+a^\dagger)} \sigma^+ e^{-i\Delta t} e^{i\phi} + e^{-i\eta(a+a^\dagger)} \sigma^- e^{i\Delta t} e^{-i\phi} \right]. \quad (3.15)$$

Substituting this into the Schroedinger equation, $i\hbar \frac{d\psi}{dt} = H_I \psi$ and solving the resulting equations we can find the time dependence of the amplitude in the ground and excited states. We find a sinusoidal oscillation when the ion is initially in a state with a definite number of phonons and the laser couples to an excited electronic state, again with a set phonon number. This oscillation is similar to that described by equations 3.7 and 3.8. The Rabi frequency is now however a function of the initial and final motional states which the laser is coupling. By detuning the laser from the carrier transition by $\pm m\omega_T$ (where m is an integer) it can couple to states with m more or less phonons. The ion's spectrum thus has gained a set of sidebands separated by the trap frequency. The Rabi frequency for a given sideband is changed by a matrix element between the motional states which are being addressed by the laser,

$$\Omega_{n+m,n} = \Omega \left| \langle n+m | e^{i\eta(\hat{a}^\dagger + \hat{a})} | n \rangle \right|. \quad (3.16)$$

Note that if Ω is to be modified by a detuning then the detuning should be relative to the sideband. This Rabi frequency between any two motional states for any value of the Lamb-Dicke parameter can be calculated in full using the expression

$$\Omega_{n+m,n} = \Omega \left[\frac{n!}{(n+m)!} \right]^{\frac{\text{sign}(m)}{2}} \eta^{|m|} e^{-\frac{\eta^2}{2}} L_n^{|m|}(\eta^2), \quad (3.17)$$

where $L_n^{|m|}(\eta^2)$ are the associated Laguerre polynomials. An important situation is when $\eta \ll 1$. It will be explained that in conventional sideband cooling which is used to put the

ion in the motional ground state with high probability uses this condition. If η is small then we can expand the exponential in equation 3.16,

$$\begin{aligned} e^{i\eta(\hat{a}^\dagger + \hat{a})} &= 1 + i\eta(\hat{a}^\dagger + \hat{a}) - \frac{1}{2}\eta^2(\hat{a}^\dagger + \hat{a})^2 + \dots \\ &= 1 - \frac{1}{2}\eta^2(\hat{a}^\dagger\hat{a} + \hat{a}\hat{a}^\dagger) + i\eta(\hat{a}^\dagger + \hat{a}) - \frac{1}{2}\eta^2(\hat{a}^\dagger\hat{a}^\dagger + \hat{a}\hat{a}). \end{aligned} \quad (3.18)$$

Using the parts of equation 3.18 that lead to a non-zero matrix element by changing the motional state by the correct number of phonons we can find simple expressions for the Rabi frequencies. We find to terms in η^2 ,

$$\begin{aligned} \Omega_{n,n} &= \Omega \left[1 - \frac{1}{2}\eta^2(n+1) \right] \\ \Omega_{n+1,n} &= \Omega\eta\sqrt{n+1} \\ \Omega_{n-1,n} &= \Omega\eta\sqrt{n} \\ \Omega_{n+2,n} &= -\frac{1}{2}\Omega\eta^2\sqrt{(n+2)(n+1)} \\ \Omega_{n-2,n} &= -\frac{1}{2}\Omega\eta^2\sqrt{n(n-1)}. \end{aligned} \quad (3.19)$$

The probability of a transition is proportional to the square of the relevant Rabi frequency. From now on we will assume that η is small enough so that we can ignore the terms in η^2 which would lead to transition probabilities proportional to η^4 . The Rabi frequency is now only non-zero for transitions on the carrier or those which increase or decrease the motional state by one phonon which we will call the first blue and red sidebands respectfully. On the carrier transition we have $\Omega_{n,n} = \Omega$.

Now let us look at the interaction Hamiltonian of the system when $\eta \ll 1$. We expand the exponential containing η in equation 3.15. If we look at the three cases when the detuning is such that we are resonant with the carrier and first red and blue sidebands and we neglect the terms which are oscillating at ω or 2ω we find

$$H_{I,\text{carrier}} = \frac{1}{2}\hbar\Omega(\sigma^+ + \sigma^-) \quad (3.20)$$

$$H_{I,\text{red}} = \frac{1}{2}i\hbar\eta\Omega(\hat{a}\sigma^+ - \hat{a}^\dagger\sigma^-) \quad (3.21)$$

$$H_{I,\text{blue}} = \frac{1}{2}i\hbar\eta\Omega(\hat{a}^\dagger\sigma^+ - \hat{a}\sigma^-). \quad (3.22)$$

On the carrier there is no interaction which changes the motional state as would be expected. On the red sideband the terms describe the amplitude moving from the state with n phonons to that with $n-1$ phonons as the excited electronic state amplitude is increased. On the blue sideband the amplitude moves from the state with n phonons to

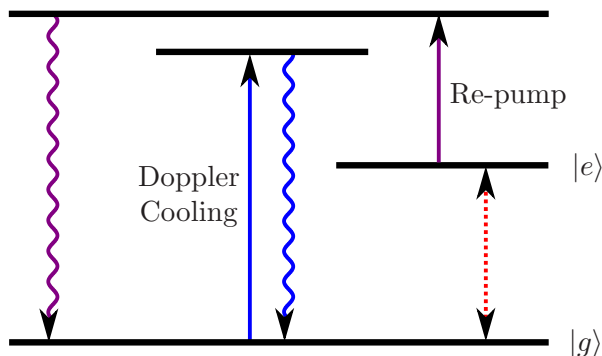


Figure 3.3: Simplified $^{40}\text{Ca}^+$ electronic energy levels. The red dashed arrow shows the quadrupole transition to be used for sideband cooling and coherent dynamics. The blue arrows indicate the dipole-allowed transition used for Doppler cooling. This is also used to detect whether the ion is in the ground, $|g\rangle$ or excited, $|e\rangle$ state. As it does not couple to $|e\rangle$ the ion will only scatter photons on this transition if it is in the ground state. The transition shown in purple is used to repump the ion from $|e\rangle$ back to the ground state.

that with $n + 1$ phonons as the excited electronic state amplitude is increased. The interaction on the red sideband is called the Jaynes-Cummings interaction while on the blue it is called the anti-Jaynes-Cummings. The Jaynes-Cummings interaction has been much studied in the context of cavity QED where \hat{a}^\dagger and \hat{a} create and destroy photons of the electromagnetic field [24]. An experiment has been conducted [26] where the predictions of the anti-Jaynes-Cummings interaction have been demonstrated on the first blue sideband of a trapped ion which was in number, thermal, coherent and squeezed states. After Doppler cooling the ion is in a thermal state, we will thus concentrate at the dynamics of this state. We wish to look at the dynamics via the probability of being in the excited electronic state as a function of the interaction time with the laser. This is done experimentally using pulsed spectroscopy which will be described in detail later when initial results are given in chapter 7.

The $^{40}\text{Ca}^+$ ion has an electric-dipole allowed transition which is used for Doppler cooling and detection of the ion's state after coherent manipulation. There is also an electric-quadrupole allowed transition that is to be used for sideband cooling (see § 3.3) and performing the coherent dynamics described in this section. These two transitions share the same ground state, $|g\rangle$ which is the lowest electronic state of the ion. A simplified electronic energy level diagram of $^{40}\text{Ca}^+$ is shown in figure 3.3. The ion is first pumped out of the excited state of the quadrupole transition, $|e\rangle$ into the ground state via a higher lying state. A laser can then address the quadrupole transition for a given interaction time. The laser addressing the Doppler cooling transition is then switched on and it is

noted if the ion emits photons. If it emits a number of photons above a set thresholdⁱⁱ then it can be concluded that the ion was in the ground state after the interaction period. If it does not then the ion must have been in the excited state of the quadrupole transition to which the laser cannot couple. To find the probability of excitation for a given interaction time the experiment is repeated a number of times after which the interaction time is stepped and the process is repeated. If the ion is initially in the state with n phonons with 100% probability then the probability of being in the excited state as a function of the interaction time should be sinusoidal with a Rabi frequency given by equation 3.17. A thermal state is however a mixed state with a probability of being in a range of states with different phonon numbers. The full probability is thus weighted by the thermal probability distribution defined by the average number of phonons \bar{n} . We have

$$P(e) = \sum_{n=0}^{\infty} P(n) \sin^2\left(\frac{\Omega_{n+m,nt}}{2}\right) = \sum_{n=0}^{\infty} \left(\frac{\bar{n}}{1+\bar{n}}\right)^n \sin^2\left(\frac{\Omega_{n+m,nt}}{2}\right), \quad (3.23)$$

where the probability distribution has not been normalised. Instead of seeing pure Rabi oscillations a thermal state will thus be the sum of Rabi oscillations at lots of different frequencies. The range of different Rabi frequencies included depends both on \bar{n} and η . Figure 3.4 is a plot of the Rabi frequency on the carrier and first red and blue sidebands as a function of the number of phonons the ion has. This has been drawn for three different trap frequencies. Namely an estimated modified cyclotron frequency for a magnetic field of 1 tesla (in which the Penning trap experiments in this thesis were conducted) and 2.5 tesla (in which future experiments in the group will be done) and also the estimated frequency in a RF trap where some preliminary pulsed spectroscopy results were taken (100 kHz).

Using equation 3.23 the predicted oscillations of the amplitude in the excited state when the laser is interacting on the carrier and first red and blue sidebands can be plotted (3.5). It is seen that on the carrier transition when most of the thermal distribution is below the point when the Rabi frequency goes to zero the oscillations last longer the lower n is. It is also noted that as the carrier Rabi frequency is maximised when $n = 0$ the oscillation period is therefore longer for any other n or distribution of n .

3.3 Sideband Cooling

It was discussed in the introduction that to measure the temperature of an ion and hence its heating or decoherence rate it first needs to be cooled to close to its ground state of motion. Many quantum computation implementations also require ground-state cooled

ⁱⁱA threshold is required as there is a background photon count, predominately from laser scatter from the trap electrodes.

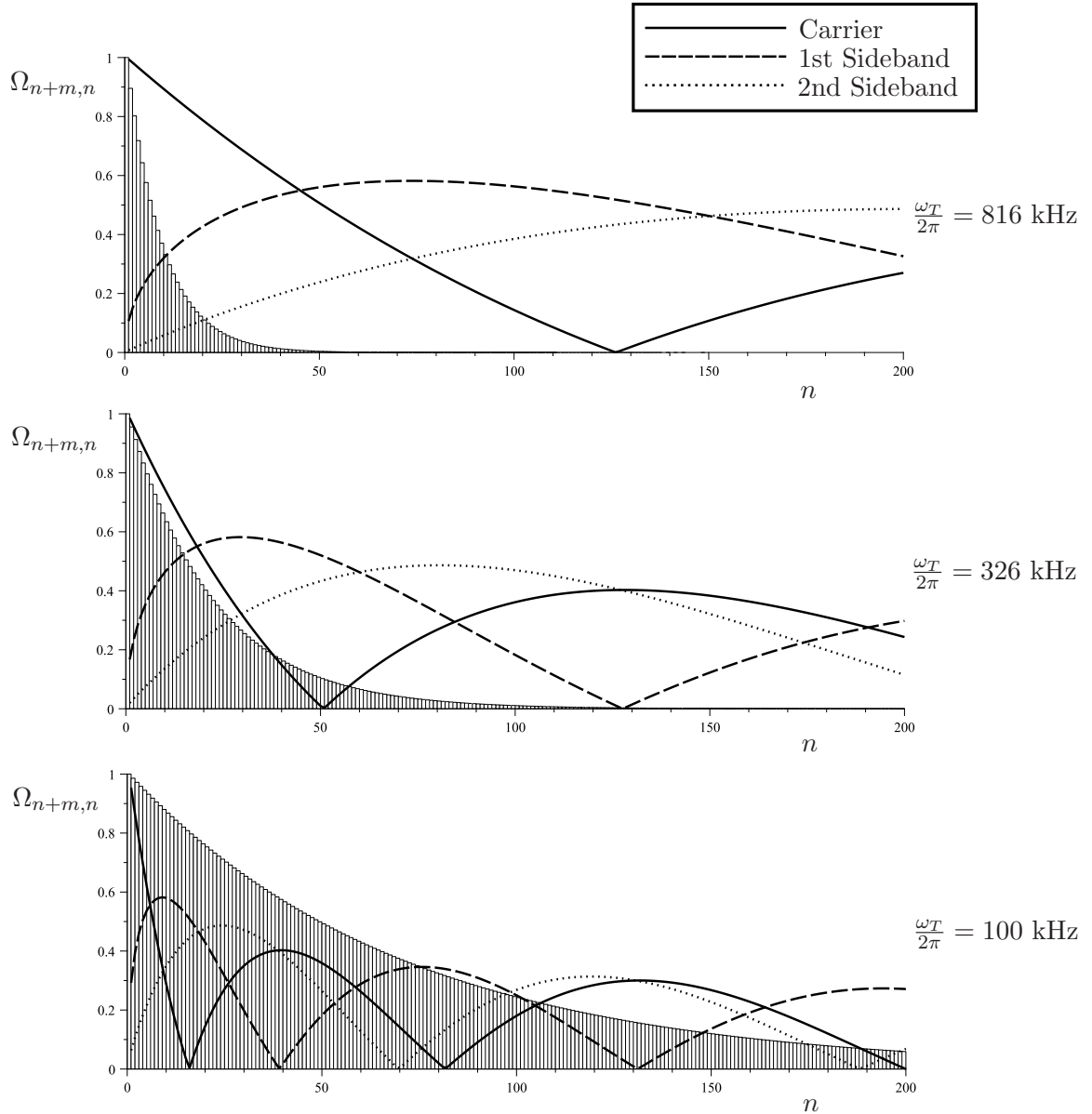


Figure 3.4: Rabi frequencies as a function of the ion's motional state on the carrier and the first and second sidebands. The red and blue sidebands of the same order are very similar on this scale and so only the blue have been displayed. The bar charts are unnormalised thermal state distributions at the respective Doppler limits. The plots are for $\frac{1}{2\pi}\omega_T$ of 816 kHz, 326 kHz and 100 kHz. This results in Lamb-Dicke parameters of 0.11, 0.17 and 0.31 and thermal states with \bar{n} at the Doppler cooling limit of 8.6, 21.5 and 70.0.

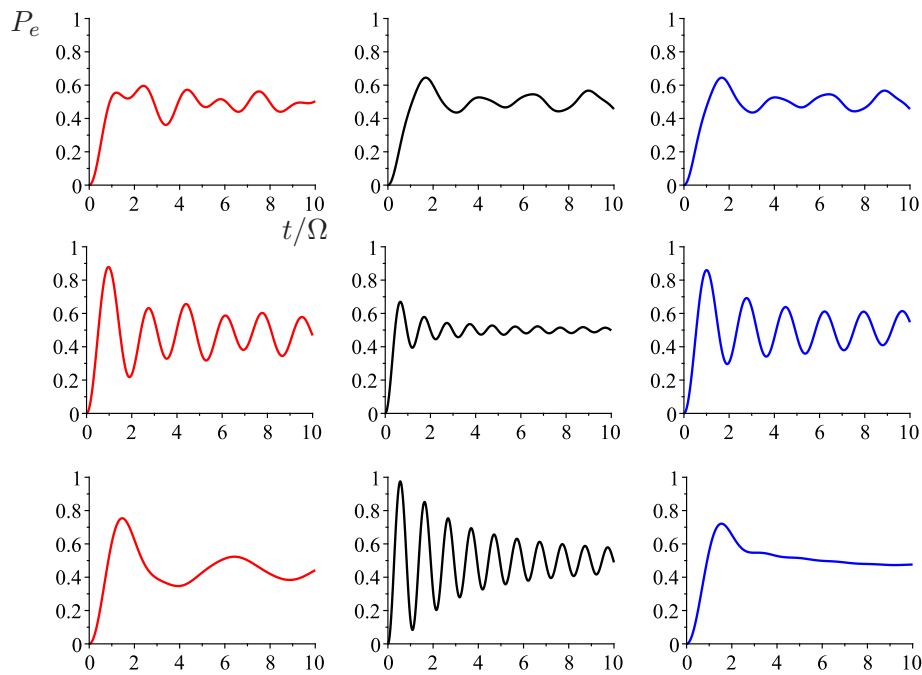


Figure 3.5: The predicted probability of being in the excited state as a function of the laser interaction time. The trap frequencies for the top to bottom rows of plots are 100 kHz, 326 kHz and 816 kHz respectively. These frequencies result in the same parameters as those in figure 3.4. Plots are shown for the laser interacting with the first red sideband (red), the carrier (black) and the first blue sideband (blue).

ions. Sideband cooling is the technique most often used to put a trapped ion into its motional ground state with a high probability. Its first implementation was in 1989 [5]. Conventional sideband cooling requires the Rabi frequency on the carrier to be larger than that on the first order sidebands and much larger than that on the second order sidebands. From figure 3.4 this requires both \bar{n} and η to be small. This is called the Lamb-Dicke regime. Sideband cooling outside of this regime has been studied theoretically [27] but has not been done experimentally. Cooling close to the Doppler limit with high trap frequencies is thus a prerequisite for this technique. The analysis in this section is valid in the Lamb-Dicke regime and is based on that of reference [28].

When a change in the motional quantum number accompanies excitation or spontaneous emission, matrix elements of the form in equation 3.16 are involved. In the Lamb-Dicke regime these result in the factors of equation 3.19 which are a function of the ion's motional state. The probability of a transition is proportional to the square of the relevant factor. To include the fact that an off-resonant photon can be absorbed the lineshape of the transition is included in any absorption process. We write this as

$$P(\Delta) = \frac{\Omega^2}{2\Gamma^2} \frac{(\Gamma/2)^2}{(\Gamma/2)^2 + \Delta^2}. \quad (3.24)$$

When a photon is emitted via spontaneous emission the probability that it is emitted in a given direction is dependent on the radiation pattern of the transition involved. The recoil momentum on the ion is more likely to excite a phonon if it has a larger component along the mode of motion under question. For instance if the photon is always emitted perpendicular to the motion being cooled a phonon can never be lost or gained. The radiation pattern is included in this analysis as α . For $\alpha = 0$ the photon is always emitted perpendicular to the motion while for $\alpha = 1$ the photon is emitted along the axis of the motion.

The transitions shown in figure 3.6 have rates given by

$$\begin{aligned} T_1 &= \eta^2 n P(\Delta - \nu) \times \Gamma \\ T_2 &= \eta^2 (n + 1) P(\Delta + \nu) \times \Gamma \\ T_3 &= P(\Delta) \times \eta^2 n \alpha \Gamma \\ T_4 &= P(\Delta) \times \eta^2 (n + 1) \alpha \Gamma \\ T_5 &= \eta^2 n P(\Delta + \nu) \times \Gamma \\ T_6 &= \eta^2 (n + 1) P(\Delta - \nu) \times \Gamma \\ T_7 &= P(\Delta) \times \eta^2 n \alpha \Gamma \\ T_8 &= P(\Delta) \times \eta^2 (n + 1) \alpha \Gamma, \end{aligned} \quad (3.25)$$

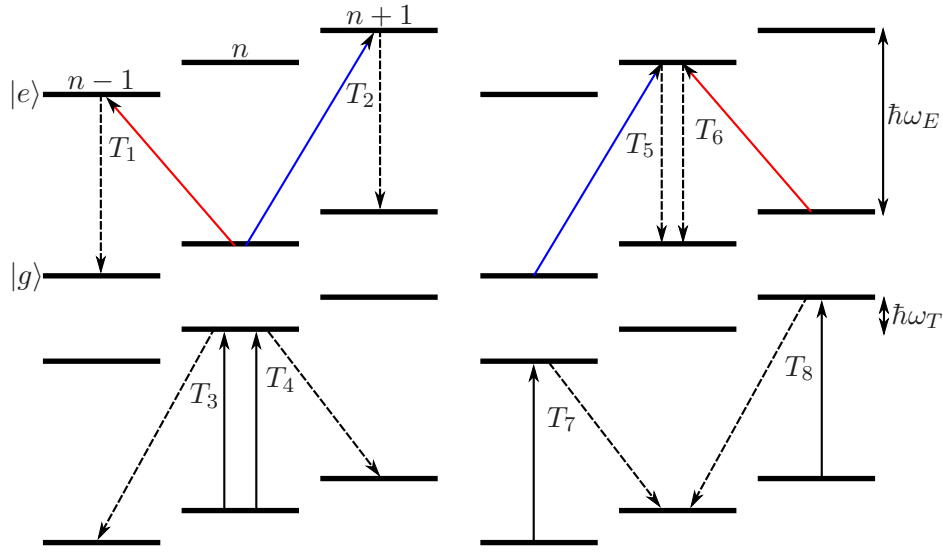


Figure 3.6: The possible transitions in sideband cooling to terms in η^2 in the Lamb-Dicke regime. The solid lines represent absorption from the laser on the carrier (black), the first blue sideband (blue) and the first red sideband (red). The dashed lines represent spontaneous emission processes.

where we have included the factors discussed. Γ is the spontaneous emission rate on the carrier.

Let us now set up an equation governing the probability that the ion is in the state n , $P(n)$. Contained in this equation will be the transitions T_1 to T_8 . Writing the probability that the ion is in the state $n+1$ or $n-1$ as $P(n+1)$ and $P(n-1)$ we multiply by the rate of the transitions which would move the ion into the n state. These are thus terms describing the increase in $P(n)$. Similarly we get terms describing the decrease in $P(n)$ by multiplying by the probability of being in the n state by the rate of the transitions out of this state. We obtain

$$\begin{aligned} \frac{d}{dt}P(n) = (n+1)A_-P(n+1) - [(n+1)A_+ + nA_-]P(n) \\ + nA_+P(n-1), \end{aligned} \quad (3.26)$$

where we have defined $A_{\pm} = \Gamma\eta^2[\alpha P(\Delta) + P(\Delta \pm \nu)]$.

The aim of sideband cooling is to reach the ground motional state with as high a probability as possible. We are thus interested in the final state reached after a long time, once the system has reached equilibrium. Here there is no probability transfer between

any of the motional states. Setting $\frac{d}{dt}P(n) = 0$ we find

$$\begin{aligned} A_+P(n-1) &= A_-P(n) \\ A_+P(n) &= A_-P(n+1). \end{aligned} \quad (3.27)$$

The solution of this is a thermal state, $P(n) = \left(1 - \frac{A_+}{A_-}\right) \left(\frac{A_+}{A_-}\right)^n$ which has been normalised so that $\sum_{n=0}^{\infty} P(n) = 1$. We are interested in the average motional state occupation, $\langle n \rangle = \sum_{n=0}^{\infty} nP(n)$ which can be shown to be, in the equilibrium situation,

$$\langle n \rangle_{\text{final}} = \frac{A_+/A_-}{1 - A_+/A_-} = \frac{\alpha P(\Delta) + P(\Delta + \nu)}{P(\Delta - \nu) - P(\Delta + \nu)}. \quad (3.28)$$

So we see that the final state achieved is higher the greater the probability of an off-resonant photon being absorbed on the carrier or blue sideband relative to that on the red sideband. There is also the factor α on the carrier as would be expected. In the limit that the transition and laser linewidths are much smaller than the trap frequency the probability of exciting on the carrier or blue sideband tends to zero and the ground state population after sideband cooling tends to 100%. Another important factor is the rate at which cooling occurs. The sideband cooling rate must be significantly bigger than the rate of any heating processes. The rate of change of the average motional state is given by $\frac{d}{dt}\langle n \rangle = \sum_{n=0}^{\infty} n \frac{d}{dt}P(n)$. Substituting equation 3.26 into this it can be shown that

$$\frac{d}{dt}\langle n \rangle = -[\langle n \rangle (A_- - A_+) - A_+]. \quad (3.29)$$

So for large $\langle n \rangle$ we can approximate the cooling rate by

$$A_- - A_+ = \Gamma\eta^2 [P(\Delta - \nu) - P(\Delta + \nu)]. \quad (3.30)$$

A high sideband cooling rate thus requires fast scattering on the red sideband as would be expected. In practice the final temperature reached will only follow equation 3.28 if the cooling rate is faster than the heating rate in the trap. For a negligible heating rate the final temperature will be limited by the amount of coupling to the carrier and blue sideband. This means low transition and laser linewidths and high trap frequencies are ideal.

An effective transition rate of the sideband cooling transition can be chosen by using a laser to couple its upper state to another level which quickly decays to the ground state. The detuning and intensity of this laser can be used to set the rate [29].

3.4 Quantum Computation in Ion Traps

Quantum computation with trapped ions was first proposed by J.I Cirac and P. Zoller in 1995 [1]. They envisaged a chain of ions along the axis of a linear Paul trap. The ions would first be laser cooled to the ground state of motion. Their electronic and motional state would be manipulated by individually addressing, focused laser beams.

Pulses from the laser beams are used to implement rotations around the Bloch sphere (see figure 1.1). The interaction time and Rabi frequency define the rotation θ while the phase of the laser relative to the ion's polarisation defines ϕ .

Each ion in the trap has an internal qubit consisting of two long lived electronic states, $|0\rangle$ and $|1\rangle$. There is also a common qubit which is the motion of the center of mass of the trapped ions. The first two quanta of this motion ($|n=0\rangle$ and $|n=1\rangle$) are used as the lower and upper levels of the qubit. We will see how this additional qubit can be used to let the ions talk to each other and hence create operations on one ion conditional on another ion's electronic state.

To perform a computation the data needs to be input into the computer and the results need to be read out. The qubits can be initialised using optical pumping. When the result of the computation needs to be read out a laser is used to drive an allowed dipole transition between one of the qubit states and another level. If the ion is in this qubit state then light will be seen which can be viewed using a photo-multiplier tube or a CCD camera. If the ion is in the other qubit level then it will remain dark.

3.4.1 Cirac-Zoller C-NOT Gate Protocol

We will now see how to perform a C-NOT gate using trapped ions. In the original Cirac and Zoller proposal the control and target qubits were the electronic energy levels of two separate ions in a trap. It is however possible to perform a C-NOT gate on a single ion where the control and target qubits are its vibrational and electronic levels respectively.

Firstly we will look at the procedure using a single ion. This was performed experimentally by the Wineland group at NIST in 1995 [30]. The resulting wavefunctions after each operation are shown in table 3.1. Comparing this to the truth table for a C-NOT gate (table 1.1) we see that the motional qubit is the control and the electronic qubit is the target.

The two $\pi/2$ pulses do not change the state unless there is an interaction occurring between them. The control procedure works by only interacting with the 2π pulse if the ion is in the excited motional state.

We can see how the state changes in each step by looking at the rotations on the Bloch

Initial State	$\frac{\pi}{2}$ Pulse on Carrier	2π Pulse on BSB of $ 1\rangle \rightarrow \text{aux}\rangle$ transition	$\frac{\pi}{2}$ Pulse on Carrier (dephased by π)
$ 0\rangle n=0\rangle$	$\frac{ 0\rangle - i 1\rangle}{\sqrt{2}} n=0\rangle$	$\frac{ 0\rangle - i 1\rangle}{\sqrt{2}} n=0\rangle$	$ 0\rangle n=0\rangle$
$ 1\rangle n=0\rangle$	$\frac{ 0\rangle + i 1\rangle}{\sqrt{2}} n=0\rangle$	$\frac{ 0\rangle + i 1\rangle}{\sqrt{2}} n=0\rangle$	$ 1\rangle n=0\rangle$
$ 0\rangle n=1\rangle$	$\frac{ 0\rangle - i 1\rangle}{\sqrt{2}} n=1\rangle$	$\frac{ 0\rangle + i 1\rangle}{\sqrt{2}} n=1\rangle$	$ 1\rangle n=1\rangle$
$ 1\rangle n=1\rangle$	$\frac{ 0\rangle + i 1\rangle}{\sqrt{2}} n=1\rangle$	$\frac{ 0\rangle - i 1\rangle}{\sqrt{2}} n=1\rangle$	$ 0\rangle n=1\rangle$

Table 3.1: The laser pulses required to perform the C-NOT gate on a single ion.

sphere (figure 1.1). The first $\pi/2$ pulse acts to rotate the Bloch vector down to the x - y plane from the north pole around the x -axis if the ion is initially in the $|0\rangle$ state ending up in the $\frac{|0\rangle - i|1\rangle}{\sqrt{2}}$ state. If the ion is initially in the $|1\rangle$ state it moves up to the x - y plane (again around the x -axis) ending up in the $\frac{|0\rangle + i|1\rangle}{\sqrt{2}}$ state. Next a 2π pulse is implemented between the $|1\rangle$ and $|\text{aux}\rangle$ states. This is on the blue sideband (BSB) and so only affects the states which are motionally excitedⁱⁱⁱ. The result of a 2π pulse is to change the sign and so the $|1\rangle$ components of the superpositions have their sign swapped. The final pulse is applied when the laser is π out of phase with ion relative to the original pulse. This phase can be thought of as a $\phi = \pi$ rotation on the Bloch sphere. The $\pi/2$ pulse then leads to the final states shown in table 3.1.

The two-ion C-NOT gate was first implemented in 2003 by the Blatt group in Innsbruck [31]. The group held two $^{40}\text{Ca}^+$ ions in a linear Paul trap. The electronic transition used as the internal qubit was the same quadrupole $D_{\frac{5}{2}} \rightarrow S_{\frac{1}{2}}$ transition discussed in this thesis (see § 4.1). The transition was addressed using a laser at ≈ 729 nm which could be individually focused onto each of the ions. The laser pulses used to implement the gate are shown in table 3.2. Initially the common motional state of the ions is in the ground state. The laser is focused onto one of the ions (ion a) and a π pulse on the first blue sideband is performed. This effectively maps the internal state of the ion onto the motional state. If ion a is in the ground state then the motional mode of the two ions is excited while if the ion is in the excited state the motional state is left in the ground level. The laser is

ⁱⁱⁱIt is the blue and not the red sideband as the auxiliary state used has a lower energy than the electronic states used for the qubit.

Initial State	π Pulse on the Blue Sideband of Ion a	Single Ion C-NOT Gate (Ion b)	π Pulse on the Blue Sideband of Ion a ($\phi = \pi$)
$ 0\rangle_a 0\rangle_b n=0\rangle$	$ 1\rangle_a 0\rangle_b n=1\rangle$	$ 1\rangle_a 1\rangle_b n=1\rangle$	$ 0\rangle_a 1\rangle_b n=0\rangle$
$ 0\rangle_a 1\rangle_b n=0\rangle$	$ 1\rangle_a 1\rangle_b n=1\rangle$	$ 1\rangle_a 0\rangle_b n=1\rangle$	$ 0\rangle_a 0\rangle_b n=0\rangle$
$ 1\rangle_a 0\rangle_b n=0\rangle$	$ 1\rangle_a 0\rangle_b n=0\rangle$	$ 1\rangle_a 0\rangle_b n=0\rangle$	$ 1\rangle_a 0\rangle_b n=0\rangle$
$ 1\rangle_a 1\rangle_b n=0\rangle$	$ 1\rangle_a 1\rangle_b n=0\rangle$	$ 1\rangle_a 1\rangle_b n=0\rangle$	$ 1\rangle_a 1\rangle_b n=0\rangle$

Table 3.2: The laser pulses required to perform the C-NOT gate on a two ions. Note that the target qubit is flipped if the control qubit is initially in the ground $|0\rangle$ state.

then directed onto the other ion (ion b) and a single ion C-Not gate between the ion and the motional state is then performed. Finally a π pulse on the BSB of ion a maps the motional state back onto the internal state.

Looking at the truth table that this process performs we see that ion a is the control and ion b is the target qubit. The control qubit however becomes the motional state after the first mapping pulse. In the experiment performed in 2003 by the Blatt group the 2π BSB pulse to an auxiliary state used in the single ion C-NOT gate at NIST was replaced by four separate pulses on the BSB of the same $D_{\frac{5}{2}} \rightarrow S_{\frac{1}{2}}$ transition^{iv}.

The Blatt group has also implemented the Deutsch algorithm using a pair of ions [32].

^{iv}A single 2π BSB pulse cannot be used on the $D_{\frac{5}{2}} \rightarrow S_{\frac{1}{2}}$ transition as there would be coupling from the $|0\rangle |n=1\rangle$ state to the $|1\rangle |n=2\rangle$ state. This would mean the 2π BSB pulse would act on both the $|0\rangle |n=1\rangle$ and $|1\rangle |n=1\rangle$ states and so only a global phase shift would result which would not have an observable affect. The solution NIST employs is to use a transition to an additional state whose frequency only matches the $|1\rangle |n=1\rangle \rightarrow |\text{aux}\rangle$ transition. Innsbruck does not use an additional state. Instead they take advantage of the motional state dependence of the Rabi frequency. From equation 3.19 there is a factor of $\sqrt{2}$ difference between the two Rabi frequencies. Using a composite pulse sequence it is possible to selectively perform the 2π pulse on the $|1\rangle |n=1\rangle$ population. The $|0\rangle |n=1\rangle$ population is returned to its original state.

3.4.2 Geometrical-Phase Gate

A set of possible ion trap, two-qubit gates different to the Cirac-Zoller 1995 scheme were discussed around the year 2000. The two most widely used gates are those proposed by Molmer and Sorensen [33] and Milburn [34]. The geometric phase gate discussed by Milburn and implemented by the group at NIST [35] will be described here.

Two ions are trapped along the axis of a linear Paul trap. In the NIST implementation these were ${}^9\text{Be}^+$ ions with two ground state hyperfine levels split by ω_q as the internal qubit. Transitions between the two levels of the qubit could be driven by 2-photon Raman transitions. The two lasers had a frequency difference of close to $\omega_q + \omega_T$ where ω_T is the frequency of the ‘breathing’ mode. This is a motional mode of the ions where the ions move in opposite directions. The lasers were detuned from the $P_{1/2}$ and $P_{3/2}$ levels which mediated the transition. The lasers create a ‘walking’ wave at their difference frequency.

The axial trap potential was changed such that the equilibrium distance between the two ions is equal to a multiple of the wavelength of the walking wave. This results in each ion feeling the same phase of the laser field.

There is an AC Stark shift and associated dipole force on each ion due to the Raman lasers. The direction, polarisation and detuning of the Raman lasers was chosen such that the dipole force on the ion is in a different direction dependent on its electronic state and is twice as large if the ion is in the upper electronic state. To excite the breathing motional mode, a force is required which has an opposite direction for each ion. Thus it can only be excited via the Raman lasers if the ions are in different levels of the electronic qubit.

Excitation of the breathing mode leads to a time dependent Coulomb potential between the two ions as their separation is changed. An energy change results in a phase change of the ion’s wavefunction. Thus a phase has been introduced which depends on the electronic states of both ions.

The frequency difference of the Raman lasers is not chosen to exactly hit the breathing mode sideband but is offset slightly by δ . By choosing a pulse time of $\frac{1}{\delta}$ the driving of the ions during the second half of the pulse will cancel that of the first half. The motional state is thus left unchanged by the operation. The motional excitation of the ions can be described by a closed loop in phase space. It can be shown that the phase introduced is independent of the path taken by the ion and only depends on the area of the loop. This makes the gate more robust to intensity noise of the laser beams. There are also less stringent conditions placed on the ion temperature compared to the Cirac-Zoller scheme. No longer must the motional state be cooled to the ground state but only into the Lamb-Dicke regime.

3.4.3 Decoherence and Recent Advances

A quantum computer would ideally provide the correct answer to a computation 100% of the time. Errors can be generated via the ions interacting with their environment in an uncontrolled way thereby changing the state of the qubit. This is called decoherence. There will always be some small unknown interaction occurring and so a perfect quantum computation would seem impossible. The invention of quantum error correction schemes in the mid-1990s changed this [36] [37]. In the schemes a number of extra qubits are required per logical qubit. The number of extra qubits required depends on the fidelity of the gate operations. The fidelity is a measure of the overlap of the obtained state with that of the expected state. It is a number between 0 and 1 where 1 means there is no error. Infidelities of towards 10^{-4} are required for reasonable qubit numbers [38].

In ion traps the major reduction in fidelity is due to the two-qubit gates. In the geometrical-phase gate by the NIST group the largest error was due to spontaneous emission from the P states used for the Raman transition leading to a fidelity of 0.97(2). While in Cirac-Zoller type gates off-resonant excitations on the incorrect sideband, laser intensity and frequency noise, stray magnetic fields and unwanted AC stark shifts all contribute. The 2-qubit C-NOT gate had a fidelity of 0.71(3).

In the introduction, ground-state cooling of an ion in a Penning trap was motivated by measuring its heating rate. However at the moment heating rates have a small contribution to the gate fidelity. The heating rate would still have to be reduced before fidelities of 10^{-4} could be obtained. However experiments have shown a reduction in the heating rate by 6 orders of magnitude by cooling down the trap electrodes from room temperature to 6 K [39]. This would provide a solution to the motional heating issue and thus makes a Penning trap quantum computer less desirable.

There have also been advances in reducing the decoherence due to the other factors other than the motional heating. One of these is the demonstration of microwave gates by the group at NIST [40]. Here the electronic qubit consists of two hyperfine levels of the ground state of $^{25}\text{Mg}^+$ and is manipulated directly using microwaves instead of lasers via a Raman transition. The type of gate used is similar to the geometrical phase gate described previously. The small Lamb-Dicke factors inherent to using long wavelength microwaves leads to a small coupling between the electronic and motional states of the ion. This can be overcome by using magnetically sensitive states and applying a magnetic field gradient [41] or using the oscillating magnetic field gradients in the near-field of microwave currents [42]. Decoherence due to the spontaneous emission from the upper state mediating the Raman transition is removed using this method. Frequency stability is easier for a microwave source than it is for lasers and so decoherence due to this error

will also be reduced.

Equivalently to reducing the decoherence rate, the time taken to perform the gate can be reduced. This was the approach taken by the group of Monroe which has used a fast laser pulse to implement a π pulse on a single ion in less than 50 ps [43]. It has been shown theoretically that 2-qubit gates can be performed using a sequence of fast laser pulses [44].

So far we have discussed performing gates with two ions in a trap. To perform useful quantum computations many more ions are required. In the Cirac-Zoller scheme one could imagine many ions being trapped in a line along the axis and gates between any two could be achieved via the centre of mass motional mode of the ions using focused laser beams. This however becomes more difficult the more ions there are in the trap. The more ions the more motional modes exist and so the sideband spectrum can become very complex. Also the ions equilibrium positions in the trap get closer to each other as the number of ions increases making it difficult to individually address them using laser beams. To date a maximum of 14 ions have been entangled in a single trap [45]. To overcome this problem a scheme has been invented which consists of multiple trapping zones. Ions are held in many separate memory regions. Voltages are applied to electrode segments to move any two ions from the memory regions to a trap in which the gate is implemented. The ions are then separated and moved back to a memory region. Much progress has been made in this technology, with very low heating introduced during the ion transport. Arrays of up to 150 trapping zones have been created [8]. One of the most difficult steps in this procedure is the separation of ions in the same trap. This requires very small electrodes and high voltages to create a potential between the ions. Recent work has reported the coupling of the motional state of ions in separate traps [46] [47]. This could remove the need for the tricky ion separation procedure.

3.5 Quantum Simulation in Penning Traps

The possible advantages of using a Penning trap over a Paul trap for building a universal quantum computer are no longer clear. With this in mind some other examples of using ground-state cooled ions in a Penning trap will be provided. These involve quantum simulation experiments. A universal quantum computer calculates what any given quantum system would do. Instead in a quantum simulator a quantum system is created which can simulate a specific system or set of systems. Ideally this created system will have well controlled parameters and the behavior of the system as a function of these parameters can be experimentally found.

The first example is the creation of a double well potential from different spatial configurations of a chain of ions. This is based on the proposal of reference [48]. With

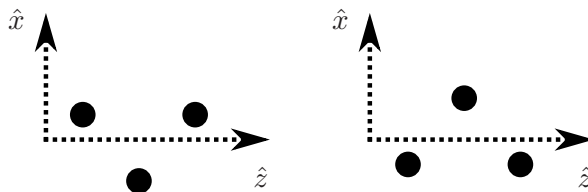


Figure 3.7: The two different possible zigzag configurations for 3 ions.

strong radial confinement the ions can be made to lie in a line along the axial trap axis. If the confinement along one axis (\hat{x}) in the radial direction is decreased below a critical value then another spatial configuration becomes more energetically favorable. This is the so called ‘zigzag’ configuration (see figure 3.7). It is seen that at least 3 ions are required to make this configuration. There are two different configurations depending if the direction of the ‘kink’ is in the \hat{x} or $-\hat{x}$ direction. The two configurations have the same energy but the ions cannot readily flip between the configurations as they have to pass through the higher energy state of the linear chain. This results in a double-well potential. Symmetric and anti-symmetric combinations of the ion being in each configuration are the eigenstates of the system; the symmetric combination having the lower energy. Investigations into tunneling rates between the two eigenstates as a function of the barrier height could be conducted.

To create the symmetric or anti-symmetric wavefunctions first a linear chain with either 0 or 1 phonons in the radial direction is created. The confinement in the x direction is then decreased to adiabatically move to the symmetric or anti-symmetric case (for zero or one phonon respectively).

To move between the symmetric and anti-symmetric wavefunctions, sidebands at their frequency difference on an electronic transition can be addressed. The transition could also be addressed directly with resonant RF. Another option is to adiabatically move the ions back to a linear chain and then address sidebands on the electronic transition at the trap motional frequency^v before moving back to the double-well potential.

This experiment could be performed in either a Paul or Penning trap and each has advantages and disadvantages. In a Paul trap there will certainly be micromotion as the scheme requires the ions to be displaced from the axial trap axis. This will lead to higher decoherence effects. In a Penning trap there is no micromotion and so this source of decoherence will not be present. However the experiment is made more complex. The asymmetrical potential in the radial plane must be achieved with an axialisation drive

^vThese sidebands are more easily resolvable from the carrier transition as the trap frequency is higher than the frequency corresponding to the difference between the symmetric and anti-symmetric eigenstates.

(see § 3.1.2) instead of a simple DC potential. The crystal will also be rotating at close to the magnetron frequency. The difference of the two zigzag configurations can only be easily observed by a camera observing the crystal in the axial direction which is triggered at the rotation frequency.

The double well potential is a paradigm in quantum mechanics. It has been studied in other systems [49] but this ion trap realisation may prove to be a particularly clean system in which to explore the relevant physics.

Another proposal is to create an effective molecule in a Penning trap using Rydberg ions [50]. First two ions of the same species are trapped along the magnetic field axis of a Penning trap. Removing an extra electron from one of the ions results in a crystal made from one singly and one doubly charged ion. An electron from the singly charged ion is then excited into a Rydberg state. If the trap parameters are such that the inter-ion distance is comparable to the size of the Rydberg orbit then there will be some overlap of the electron's wavefunction with the available Rydberg state of the other ion. It is shown that it is possible to create states where the electron is delocalised between the two ions.

Imagine the situation from the viewpoint of the electron in the Rydberg state. It will feel the attraction of the two doubly positively charged ions as well as the anti-trapping potential of the trap (as the trap is set up to trap positively charged ions). If the electron is in too high a Rydberg state then the magnitude of the trap potential at the electron will be greater than that from the ions and the electron will be lost. If the electron is in too low a Rydberg state then it will not feel the potential from the second ion. Calculations show that with reasonable trap parameters there are a range of Rydberg states which create a delocalised electron.

The potential which the electron sees is similar to that of a double well. The eigenstates are symmetric and anti-symmetric pairs which have slightly different energies. An electron which is definitely in one of the wells has a wavefunction which is a superposition of a symmetric and anti-symmetric pair. As the two parts of the wavefunction do not have the same energy there will be an oscillation in the amplitudes at a frequency corresponding to the energy difference. By coupling the Rydberg state of the singly ionised ion to a fast transition the probability of the electron being in one of the ions can be observed as a function of time.

An advantage of conducting this experiment in a Penning trap is the absence of the strong RF fields used for confinement in a Paul trap. These can result in ionisation of the Rydberg electron. Therefore higher lying Rydberg states can be used in the Penning trap.

This effective molecule can be used as a clean way to implement simulations of Hubbard models.

Chapter 4

Experimental Setup

This chapter will describe the setup used for the experiments presented in this thesis. The experiments investigating the J-mixing effect described in chapter 5 were conducted towards the beginning of the author's work while those showing new repumping schemes (chapter 6) and pulsed spectroscopy of the $S_{\frac{1}{2}} \rightarrow D_{\frac{3}{2}}$ quadrupole transition (chapter 7) were done towards the end. A lot of the experimental setup was improved during this time. The setup for the early work has been described extensively elsewhere [51] [52] and so will only briefly be described here. Attention will mostly be given to the new equipment and improvements that have been made.

4.1 Electronic Energy Levels of a $^{40}\text{Ca}^+$ Ion

First we will consider the $^{40}\text{Ca}^+$ ions that are to be trapped. The parameters of the laser systems required are specified by the available electronic states that the ion possesses. The low energy states of a $^{40}\text{Ca}^+$ ion are shown in figure 4.1.

The states are labeled by the orbital, L and total angular momentum, J as L_J . As there is only 1 electron in the ion's outer shell the total spin angular momentum, $S = \frac{1}{2}$ for all states and is not noted. The transitions indicated by the solid arrows in figure 4.1 are all electric-dipole allowed resulting in transition linewidths of 0.2 - 24 MHz. First let us consider the transitions before a magnetic field is applied. The $S_{\frac{1}{2}} \rightarrow P_{\frac{1}{2}}$ 397 nm transition is used for Doppler cooling. After the ion is excited up to the $P_{\frac{1}{2}}$ state it can spontaneously emit down to the $S_{\frac{1}{2}}$ or $D_{\frac{3}{2}}$ states. The branching ratio for going to the $D_{\frac{3}{2}}$ state is ≈ 0.065 [53]. This means an average of only 15.4 photons are scattered on the Doppler cooling transition before the ion is shelved in the $D_{\frac{3}{2}}$ state which has a lifetime of ≈ 1 s. It is obviously unacceptable for the ion to be out of the cooling cycle for this time

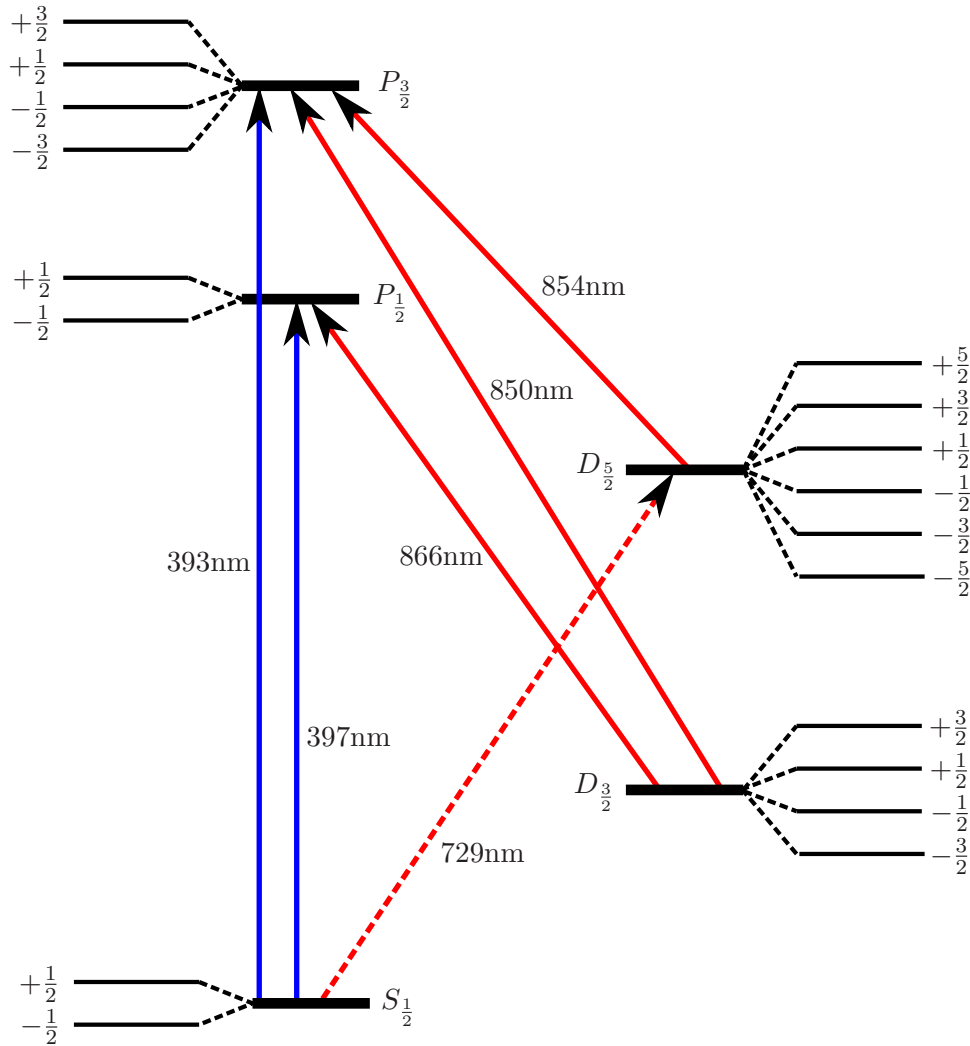


Figure 4.1: Low energy states of a $^{40}\text{Ca}^+$ ion. The states are shown before (bold lines) and after an external magnetic field is applied. The numbers labelling the states indicate the projection of J along the quantisation axis, m_J . The solid arrows indicate electric-dipole allowed transitions while the dashed arrow shows the electric-quadrupole transition which is to be used as a qubit.

State	g_J	$\Delta\nu$ (GHz T $^{-1}$)
$S_{\frac{1}{2}}$	2	27.99
$P_{\frac{1}{2}}$	2/3	9.33
$P_{\frac{3}{2}}$	4/3	18.66
$D_{\frac{3}{2}}$	4/5	11.20
$D_{\frac{5}{2}}$	6/5	16.80

Table 4.1: The g_J factors and splittings of the low energy electronic states in $^{40}\text{Ca}^+$. The splittings are between states with a difference of 1 in their m_J quantum number.

resulting in it scattering only ≈ 15 photons per second. The solution is to have a 866 nm repumping laser addressing the $D_{\frac{3}{2}} \rightarrow P_{\frac{1}{2}}$ transition to move the ion back into the cooling cycle.

When an external magnetic field, B_0 is applied the orientation of J can take $2J + 1$ values whose energies relative to the zero field case obey

$$\Delta E_{\text{Zeeman}} = \mu_B g_J m_J B_0, \quad (4.1)$$

where $\mu_B = \frac{e\hbar}{2m_e}$ is the Bohr Magnetron, $g_J = 1 + \frac{j(j+1) - l(l+1) + s(s+1)}{2j(j+1)}$ is the Landé g-factor and m_J is the projection of J along the magnetic field axis. The g_J factors and resulting splittings are shown in table ??.

In the case of a Penning Trap the magnitude of the applied magnetic field is such that the splitting of the individual m_J states is larger than the laser and transition linewidths and so separate lasers are required to excite the ion out of each individual m_J state. Thus two separate frequencies near 397 nm and four near 866 nm are required. In the present setup the π ($\Delta m_J = 0$) transitions are used at 397 nm while the σ ($\Delta m_J = \pm 1$) transitions are used at 866 nm.

Although the $P_{\frac{1}{2}} \rightarrow D_{\frac{5}{2}}$ transition is strongly forbidden it is still possible for the ion to end up in this state at high magnetic fields due to the $D_{\frac{3}{2}}$ state mixing with the $D_{\frac{5}{2}}$ state and the $P_{\frac{1}{2}}$ state mixing with the $P_{\frac{3}{2}}$ state. This is explained and experimentally investigated in chapter 5. Repumping out of the $D_{\frac{5}{2}}$ states is thus required. It is shown in chapter 6 that this can be achieved using a fibre EOM to create sidebands on a single 854 nm laser at the required transitions. It is also demonstrated that repumping without

the EOM is achievable with enough laser power.

The dashed red arrow in figure 4.1 indicates the transition to be used for coherent manipulation (§ 3.2) and for sideband cooling (§ 3.3). The $S_{\frac{1}{2}} \rightarrow D_{\frac{5}{2}}$ transition is electric-dipole forbidden and has a natural linewidth of 0.14 Hz. It has a lifetime of 1.17 s and is electric-quadrupole allowed. The narrow linewidth is required so motional sidebands at the trap frequency can be resolved as described in chapter 3.3. The transition frequency has been measured to be 411 042 129 776 393.2(1.0) Hz using a trapped $^{40}\text{Ca}^+$ ion [54]. The first step to using this transition for the applications described in chapter 3 is to perform pulsed spectroscopy on it. The results of this are presented in chapter 7. The use of this quadrupole transition creates a need for another laser at 854 nm. This laser is used to repump out of this excited state when performing pulsed spectroscopy on the quadrupole transition. It will also be used in future experiments to shorten the $D_{\frac{5}{2}}$ state lifetime during sideband cooling (§ 3.3).

4.2 Laser Systems and Optical Setup

4.2.1 Diode Lasers

We have seen that two lasers are required to address the two Doppler cooling transitions at ≈ 397 nm. Four repumping lasers are required at ≈ 866 nm and one is required to repump at ≈ 854 nm. Another laser is required to address the quadrupole $S_{\frac{1}{2}} \rightarrow D_{\frac{5}{2}}$ transition at 729 nm.

A simple and relatively inexpensive method to derive the light required at 397 nm, 729 nm, 854 nm and 866 nm is via laser diodes. Here a p-n junction is created in a semiconductor. A current source is used to inject electrons and holes into the depletion region at the junction. When the electrons and holes recombine a photon is emitted which is designed to be at the required wavelength. To produce coherent laser light the electron and hole recombination needs to be stimulated by one of the created photons rather than by simply being in the vicinity of each other. To do this the laser diode needs to be in a cavity where a percentage of the created photons are directed back into the diode. As the laser diode current is increased more holes and electrons are moved into the depletion region and both the spontaneous and stimulated recombination rate is increased. The stimulated rate however increases more quickly and so at a high enough current the stimulated rate dominates and when the gain in a round trip of the cavity is greater than unity the diode will lase. The back facet of the diode acts like a mirror, the front facet is often anti-reflection coated to varying degrees. Depending on the percentage of light reflected from this surface the diode may or may not lase when it is not in an extended

cavity.

The diode lasers used in the experiment are all placed in extended cavities. They are described as ‘extended’ as they extend the cavity created between the diode’s facets. The extended cavity serves two purposes; to reduce the laser linewidth and to help to tune the wavelength of the light emitted. The cavity design is based on a grating in the Littrow configuration [55]. The idea is to have the grating at an angle such that the first order diffracted light will be directed back into the laser diode. The zeroth order light from the grating will then be emitted and can be used for the experiment. The grating angle required depends on the wavelength of light and the density of the lines ruled on the grating. The grating angle and the distance from the back facet of the diode to the grating are both tunable. The tuning is achieved via a stable optical mount with manual control of the grating angle and a piezo-electric transducer (PZT) respectively. There are a number of different factors that affect the output frequency in this setup. First there is the gain spectrum of the laser diode itself. This spectrum depends on the particular diode used but can extend over 80 nm in the case of the infra-red diodes. There is then the spread of frequencies which the grating directs back into the laser diode. This generally has a width of a couple of nm. The back facet of the diode and the grating then define a cavity which produces a set of longitudinal modes separated by the cavity FSR, determined by the cavity length, $L \approx 15$ mm to be $\frac{c}{2L} \approx 10$ GHz. There may also be a set of modes due to the cavity created between the two facets of the diode. As this is within the extended cavity the frequency separation between the modes is always greater than for the extended cavity modes. The influence of this cavity will depend on the quality of the anti-reflection coating on the front surface of the diode. Each of these considerations leads to a characteristic ‘gain curve’ as shown in figure 4.2. All of these different gain curves are required to line up in frequency space such that one of the grating-diode cavity modes has significantly more gain and so will be the only one to lase. There are a variety of controllable parameters that can move each of these gain curves. The temperature of the diode can be changed via a peltier heater which creates a temperature differential between the mount and the optical table. This moves the gain curve of the diode. The grating is on a stable optical mount which allows the vertical angle to be manually varied for alignment and the horizontal angle to be adjusted to move the grating gain curve. There is a PZT on the back of the grating which changes the length of the diode-grating cavity moving its modes. The amount of current supplied to the diode has the effect of changing the refractive index of the diode via the number of electrons and holes created and so changes the optical length of both the diode and the diode-grating cavities. As the PZT is scanned the grating-diode longitudinal modes (bottom of figure 4.2) move relative

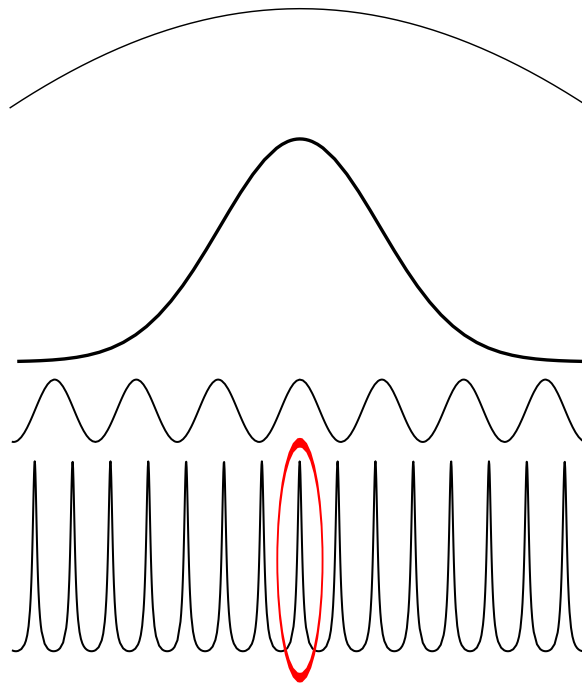


Figure 4.2: Gain profiles involved in a ECDL. Top is the curve corresponding to the gain of the diode itself. Next is the frequency spread directed back into the diode from the grating. Next is the longitudinal modes between the two facets of the diode. Finally at the bottom are the longitudinal modes between the back facet of the diode and the grating. The longitudinal mode which would lase in this case has been marked.

to the other gain curves. Eventually the next longitudinal mode will have enough gain to lase in preference to the original mode. The laser will ‘mode-hop’ to this other mode. To increase the frequency range which the laser can be scanned the diode current can be changed in conjunction with the grating PZT. With the correct current tuning rate the diode’s internal modes can be made to move at the same rate as the diode-grating modes resulting in a greater mode-hop free frequency range.

Each grating has a blaze angle which is the angle of the sawtooth pattern on the grating relative to the surface. In the Littrow configuration the grating is most efficient at diffracting light into the 1st order when the angle between the laser beam and the normal to the grating surface is equal to the blaze angle. Choosing a blaze angle thus amounts to choosing a percentage of the light that is fed back to the laser diode. In practice as much usable laser power as possible is desired while keeping it lasing in a single mode. For diodes which have good anti-reflection coatings, blaze angles designed for very different wavelengths compared to the desired lasing wavelength are used so only a small amount

of power is fed back to the diode. This is the case with the 866 nm and 854 nm repumping lasers where a grating designed for maximum feedback at 300 nm is used leading to a feedback fraction of $< 10\%$. It is noted that the laser linewidth will increase the smaller the amount of feedback. This is due to the effective finesse of the cavity decreasing. This however is quite a small effect [56] and the extra laser power achieved is deemed more important.

Extended-cavity diode laser (ECDL) setups are relatively cheap, simple to use and require little maintenance. They are unfortunately however only available at certain wavelengths. Diode lasers at 854 nm and 866 nm are now readily available and are used in the experiment. It is trickier to find diodes at 397 nm. There are however a few available and we use these for the Doppler cooling transitions in our experiment. There are also now diodes available for the 729 nm transition, one of which we use. These were however not available until recently. It is testament to the advantages of laser diodes over other systems that the group at Osaka university has previously cooled down a 743 nm diode to ≈ -50 °C to convince it to lase at 729 nm to address the same $S_{\frac{1}{2}} \rightarrow D_{\frac{5}{2}}$ transition [57]. This required the complication of putting the diode in a vacuum system to avoid condensation.

The linewidths of the infra-red ECDL systems in our experiment have not been measured but have been found in other groups to be less than 1 MHz [56]. This is adequate to address the electric-dipole transitions. The 729 nm laser requires a much smaller linewidth as it is addressing a transition with a linewidth of 0.14 Hz. This laser must also be significantly narrower than the trap frequency (≈ 100 kHz - 1 MHz) to see motional sidebands as described in § 3. The linewidth of our 729 nm diode laser was narrowed via a Pound-Drever-Hall (PDH) lock described in § 4.2.7. The linewidth of the 397 nm lasers was estimated to be > 10 MHz via the transmission of the scanning cavity described in § 4.2.3. This is not ideal when trying to reach the Doppler limit since the laser linewidth is a sizable fraction of the natural linewidth of the transition. Work is currently underway to reduce the linewidth of these lasers via a PDH lock similar to that of the 729 nm laser but using a lower finesse cavity and modulating the current of the laser itself rather than using an EOM.

It is noted that the beam shape of a laser diode is elongated in one direction with an aspect ratio of anything from 1:2 to 1:6. This shape is due to the active region in the diode being of a rectangular shape. There are therefore different divergences in each direction which leads to different beam sizes in each direction at the collimating lens. The beam shape and astigmatism are manipulated using optical components described in § 4.2.5.

4.2.2 Laser Wavelength Measurement

The most precise measurement that we have of the laser wavelengths is via the light emitted from a cold, trapped single ion. The transition frequencies have been measured previously to very high accuracies by other groups [58]. Our laser wavelengths can be optimised using the light from the ion. However to initially obtain a signal from the ion, the two 397 nm and the four 866 nm lasers need to be close enough to the correct wavelengths such that they are within the ion's Doppler width. Thus a method is required to initially measure these wavelengths. Until recently there was only one way to do this in our group - via a home built wavemeter based on an Michelson interferometer. This has been described extensively elsewhere [51] and so will only briefly be described here. The wavelength is measured relative to a stabilised Helium-Neon laser (HeNe). A HeNe will lase on two longitudinal modes of its cavity at any given time. The modes are both linearly polarised but the polarisation angle of one mode is 90 degrees from the other. The HeNe is stabilised by putting the light emitted through the back of the laser into a polarising beam splitter so each of the polarisations is separately measured on photodiodes. Equalising the power of the two different polarisations the HeNe is kept at a constant frequency. Its stability is found to be better than 1 MHz/day [59]. The stabilised HeNe laser and the laser to be measured take separate paths around the interferometer and are measured on separate photodiodes. A cart moves up and down an air track to change the path length difference between the two arms of the interferometer resulting in fringes when they are combined onto a photodiode. The number of fringes are counted for both lasers and the ratio once calibrated gives the wavelength of the laser measured. The laser wavelengths can be measured to an accuracy of less than < 500 MHz.

This wavemeter has many disadvantages. Only one laser can be measured at any time, during which the laser has to be directed away from the ions as a lot of power is required. The movement of the cart also causes vibrations which can interfere with other apparatus on the table. Also different alignments of the lasers through the wavemeter can affect its reading. Recently we had the opportunity to use a commercial (High Finesse WS-6) wavemeter from another laboratory. An optional add-on (High Finesse MC8) allows eight laser wavelengths to be measured simultaneously. A precision of 200 MHz is achievable with this wavemeter. Unfortunately the wavemeter was approximately 60 metres away and so optical fibres of this length were required to transmit the light. One fibre is used to transmit both the 397 nm beams, one fibre transmits the 866 nm and 854 nm beams and a final fibre transmits the 729 nm beam. A lot less optical power is required for this wavemeter and so only a fraction of the light can be sent to the wavemeter while still performing experiments with the trapped ions.

4.2.3 Scanning Cavity Lock

Experiments with a trapped ion can take hours to complete. Over this time the laser frequencies can drift out of resonance with the ion. This could be due to the angle of the extended cavity grating drifting or possibly long-term drifts in temperature if the PID system used for stabilisation is not optimised. Ideally the 866 nm and 397 nm lasers used for repumping and Doppler cooling respectively should not drift by more than a fraction of the ≈ 20 MHz transition linewidth on the timescale of the experiment.

The solution is to create a signal for each laser which is linearly dependent on the laser's frequency and then feed back to the laser to keep this signal constant. When I first joined the group the method used was to lock the lasers to stable, tunable reference cavities. This was the method used when conducting the experiment of chapter 5. The method has been described extensively in reference [51] and so only an overview will be provided here. The idea is to measure the cavity transmission which has a maximum in frequency space for each cavity mode. The cavity length is tuned via PZTs on one of the cavity mirrors until a TEM_{00} mode is found via a CCD camera monitoring the cavity transmission. A setpoint is used which corresponds to approximately half the maximum cavity transmission. This corresponds to the side of a fringe which has an approximately linear gradient and is an odd function such that positive and negative frequency shifts can be differentiated. The difference between the cavity transmission and the setpoint is then used as an error signal which is sent to PID electronics to create a signal which is fed back to the PZT on the external cavity grating of the laser, altering the length of the extended cavity. A separate cavity was used to individually lock each 397 nm laser. Only one of the 866 nm lasers however was locked to a cavity. The other three 866 nm lasers were locked to this master laser by directing some of the light from each laser into a commercial scanning cavity (TecOptic SA-7.5) which we will label as a spectrum analyser. As the length of the spectrum analyser was scanned over a FSR (7.5 GHz) all four 866 nm laser peaks could be seen via a photodiode measuring the transmission. This signal was sent into a Labview program which digitally measured the position of the peaks. With this information the program could calculate the frequency difference between each peak and the master laser and create an error signal to feed back to the PZT of each laser to keep this frequency offset constant. The lock was very slow - the frequency of updating the voltages being fed back being only ≈ 1 Hz. The stable cavities had a finesse of ≈ 60 and a free-spectral-range of ≈ 1.5 GHz resulting in a transmission peak width of ≈ 25 MHz. The lasers could be thus locked well within the ≈ 20 MHz transition natural linewidths.

This was a reasonably robust lock but the laser frequency stability depends on the stability of the reference cavity length. The cavities were kept under vacuum to reduce

changes in pressure and temperature. The temperature was stabilised and the spacer was made out of a low-expansion glass (Zerodur). To reduce changes in the cavity length due to the relatively high thermal coefficient of expansion of the PZTs another set of PZTs was attached which move the opposing mirror by the same amount (this re-entrant design is described in [60]). However there were still large drifts in the PZT lengths after the voltage on them were changed. Another problem was that using this lock would translate laser power instability into frequency instability. This is due to the setpoint being on the side of the transmission peak, a change in the peak's size will result in the setpoint at a given intensity moving in frequency. The signal level from the ion could be seen to change due to the instability of the lock. The feedback bandwidth achieved was very low and it would be advantageous to feedback more quickly, possibly reducing some of the laser acoustic noise.

A new locking system was developed which was used to lock the 397 nm lasers in the experiments detailed in chapters 6 and 7. The fundamental difference in the locking schemes is that an atomic transition was used for the frequency measurement rather than a cavity length. The transition used is the $3s \rightarrow 2p$ transition in Neon at ≈ 633 nm. This is the lasing transition in a HeNe laser. The HeNe was locked using the same method used in the Michelson interferometer wavemeter described in § 4.2.2 achieving a similar stability of < 1 MHz/day.

The method to lock the 397 nm lasers to the HeNe is to use a scanning cavity. A similar method is used to that of the spectrum analyser used to lock three 866 nm lasers to a master 866 nm laser described earlier. The length of the cavity is scanned. As the lasers are of different wavelengths they will become resonant with a mode of the cavity at different parts of the scan and so separate peaks will be seen on the cavity transmission spectrum. The frequency difference between each 397 nm laser peak and the HeNe peak is detected and used as an error signal which is then sent through PID electronics and fed back to the external cavity grating PZT of each 397 nm laser. The system is designed to have as high a feedback bandwidth as possible. This is achieved by using a fast scan (≈ 2 kHz) and using fast electronics such that the feedback value can be updated every cavity scan. A similar laser lock to a fast scanning cavity was developed in the group of Wolfgang Lange in Sussex [61].

First let us consider the design of the cavity itself. The design and construction was led by J. Goodwin, a PhD student in our group [59]. Only an overview of the cavity design will be given here. I was responsible for programming the microcontrollers used and designing and building some of the electronics and so more details of this aspect will be given below.

It was decided to use a confocal cavity for which the radius of curvature of the mirrors

is equal to the cavity length. In this configuration the transverse cavity mode frequencies overlap such that modes are only seen every FSR/2. This should reduce the mode-matching requirementⁱ. One cavity mirror is mounted on a small PZT to allow rapid scanning of the cavity length. Although the laser stability depends on the HeNe frequency stability and not the cavity length it is still important that the cavity does not drift by too large an amount as the transmission peaks could move out of the range of the scan and the lasers would then become unlocked. It was chosen to compensate for a drift in the cavity length by using a second PZT stack on the other cavity mirror instead of using a low expansion material to try to make the cavity length stable. This opens the choice of materials that can be used. Brass was chosen as it is easy to work with. The mirrors must be highly reflective at both 397 nm and 633 nm and so a special double stacked coating was used. It was shown in [59] that the effects due to dispersion in the air between the mirrors were important as this resulted in a movement of the HeNe and 397 nm peaks relative to each other which could not be differentiated from a drift in the laser frequency. It was decided to allow the cavity to be placed under vacuum ($\approx 10^{-2}$ mbar) to reduce this unwanted effect. For the experiments described in this thesis the cavity was left at atmospheric pressure. It has been calculated [59] that laboratory temperature changes of 4 K would require the cavity length to be compensated by 12 μm . It was thus decided to use a PZT stack with a throw of 13.3 μm (Noliac SCMAR03-12). For a given cavity finesse choosing a FSR is a compromise between how much the laser frequency can be scanned while locked and how accurately the frequency of each peak can be detected. The cavity length was chosen to be 15 cm resulting in a FSR of 1 GHz.

Figure 4.3 shows a schematic of the scanning cavity. The main brass body is in three separate pieces. The mirrors and PZTs are held in the endpieces which are screwed into the central piece. The amount which these are screwed in determines the length of the cavity and are optimised for confocality. Windows at the input and output and a sleeve glued over the screw threads fully seal the cavity which can then be pumped from the vacuum inlet which is then valved off.

The optics used to couple into the cavity and detect the transmitted light are shown in figure 4.4. It is noted that a photomultiplier tube (PMT) has been used instead of a photodiode to detect the 397 nm light. This is due to the small amount of 397 nm light which is transmitted through the cavity. The reason for this has been attributed to a large effective linewidthⁱⁱ of the 397 nm lasers compared with the cavity linewidth resulting in

ⁱIn practice the cavity was usually used away from the confocal position. A slight misalignment from confocality results in the spreading out of the transmission peak due to the transverse modes having slightly different frequencies leading to a reduction in the finesse. The TEM₀₀ mode was mode-matched and used to lock to.

ⁱⁱThis effective linewidth is due to the laser jitter during the time the cavity takes to scan past the

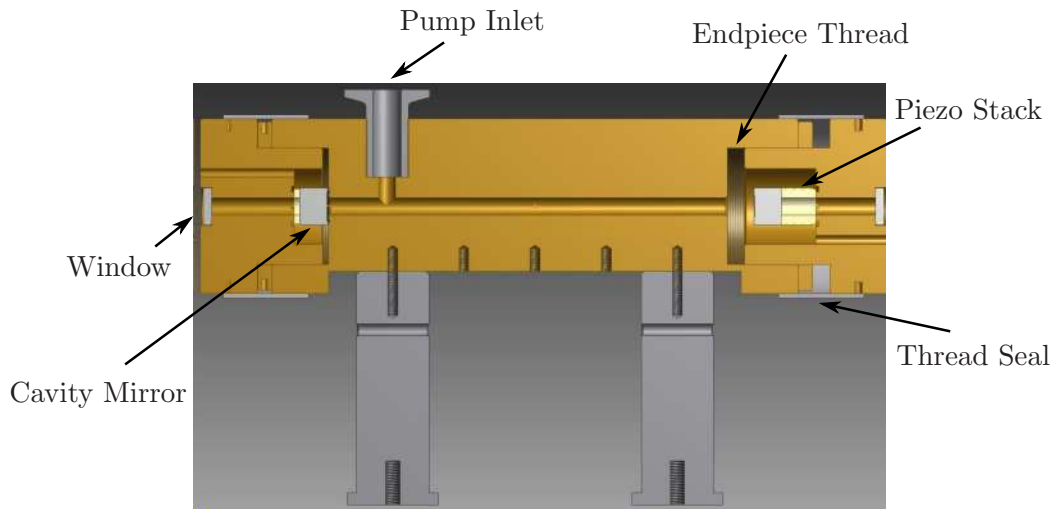


Figure 4.3: Schematic of the scanning cavity. Adapted with permission from [59]

only a small fraction of the light being resonant with the cavity at any given moment of time as the cavity is scanned. To test this theory the effective finesse at 397 nm and 633 nm with cavity lengths of 15 cm and 2 cm, corresponding to FSRs of 1 GHz and 7.5 GHz respectively was measured. The finesse at 633 nm was measured to be 1000 and 2000 at FSRs of 1 GHz and 7.5 GHz respectively. A factor of 2 increase in the finesse for a cavity linewidth increase by a factor of 7.5 suggests that the finesse measurement of 2000 at a FSR of 7.5 GHz is not limited by the laser linewidth and is the actual finesse of the cavity at 633 nm. In contrast the effective finesse at 397 nm was 83 and 600 at FSRs of 1 GHz and 7.5 GHz respectively [59]. This suggests that the laser linewidth is limiting the effective finesse at both of these FSRs. The linewidth of the 397 nm lasers is thus estimated to be on the order of 10 MHz on the timescale of the cavity scanⁱⁱⁱ.

The sensitivity of the PMT is adequate to see a peak over the background with $\approx 50 \mu\text{W}$ of light from each 397 nm laser through the input fibre in figure 4.4. The waveplate is included to rotate the axis of the linearly polarised 397 nm light. It was found that unless the polarisation was aligned with a certain axis of the cavity two overlapping peaks would be seen on the cavity transmission. This is attributed to birefringence in the dielectric coatings of the mirrors.

The voltage applied to the scanning PZT and the position of the detected transmission peaks are shown in figure 4.5. A sinusoidal scan was applied to the PZT. This was chosen

resonance.

ⁱⁱⁱIt has since been concluded that although the relatively large laser linewidth does reduce the cavity transmission a larger effect is due to loss within the cavity. A cavity with a lower finesse would improve the transmission due to both of these effects.

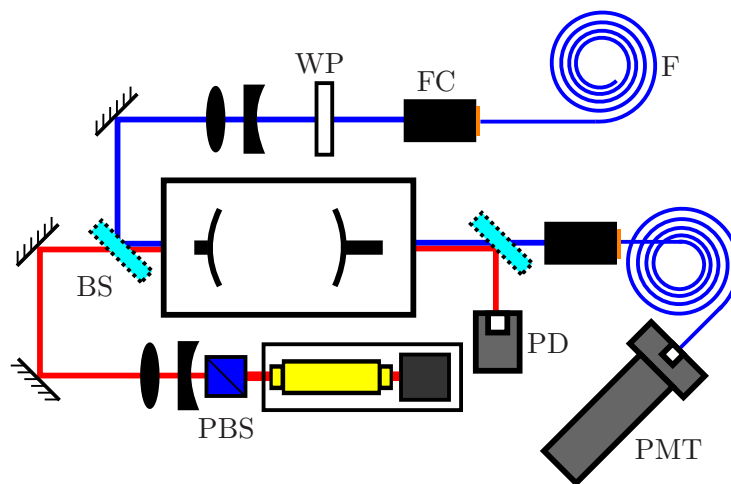


Figure 4.4: Schematic of the optics used for the scanning cavity lock. Some light from the 397 nm lasers (FC = fibre coupler) is picked off and transmitted through the optical fibre (F) shown to the cavity optics. It is then put through a $\frac{\lambda}{2}$ waveplate (WP) and then two lenses are used to couple to the cavity mode. One of the polarisation modes from the HeNe laser (shown in yellow) is chosen via a polarising beam splitter (PBS). This is then sent through two lenses to couple to the cavity mode and then combined on a dichroic beamsplitter (BS) with the 397 nm lasers. The transmitted light is split into the 397 nm and HeNe beams using another beamsplitter. The HeNe light is detected on a photodiode (PD) while the 397 nm light is viewed using a fibre-coupled PMT.

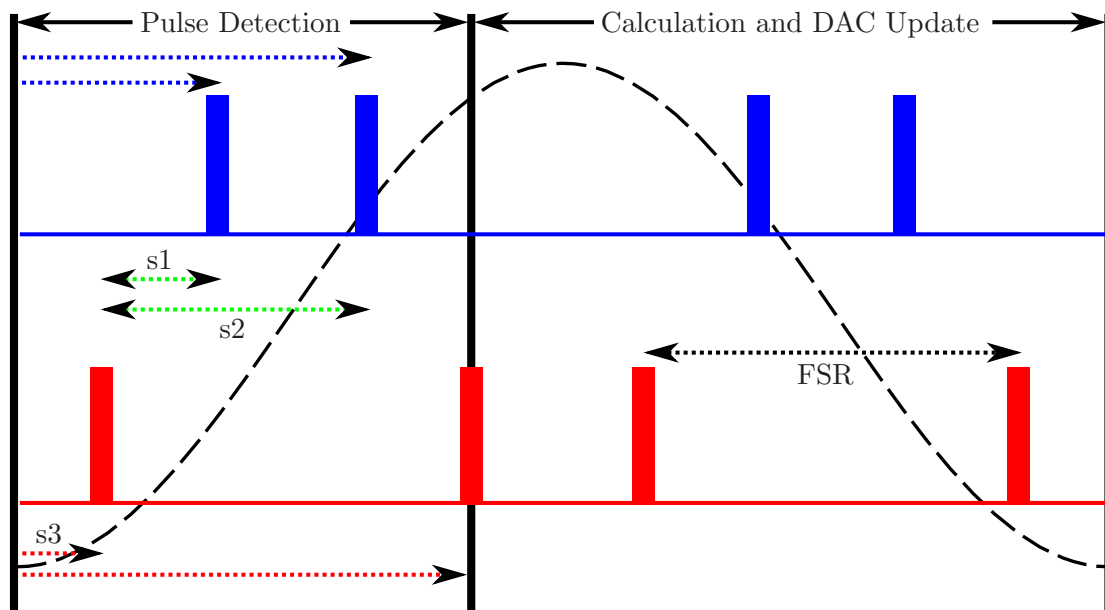


Figure 4.5: Schematic of the scanning cavity drive voltage and transmission pulses. The pulses from the two 397 nm lasers are shown in blue while those from the HeNe are shown in red. The pulses seen are mirrored after the maximum voltage applied to the piezo as the scan is symmetrical. The AC voltage applied to the short piezo is set such that the scan range is just longer than one free spectral range. The DC bias on the long piezo is adjusted so that the HeNe mode appears near the beginning and end of the scan range. The two different blue laser frequencies then give a pair of peaks somewhere within the scan range.

over a triangular scan as higher frequency fourier components could have been resonant with the cavities vibrational modes and caused unwanted effects. The frequency separation between the first two HeNe peaks detected represents the cavity FSR. The lock aims to keep the frequency separation between each 397 nm laser pulse and the first HeNe pulse constant (shown as $s1$ and $s2$ in the diagram). The cavity lock is implemented by keeping the frequency separation between the start of the cavity scan and the first HeNe pulse constant ($s3$ in the diagram). Calculating the voltage to output and updating the voltage on the DACs begins after the second HeNe pulse to maximise the time available.

Figure 4.6 provides a high level view of the electronics used in the system. The currents produced by the light hitting the photodiode and PMT are sent through transimpedance amplifiers and then into analog peak detector electronics. The 5 V pulses representing the peaks are then sent into microcontrollers (Arduino Mega) which are used to detect the pulse times and calculate error signals. A voltage-controlled oscillator (VCO) (XR-2206) is the source used to scan the cavity. It is sent through a high power amplifier (based on

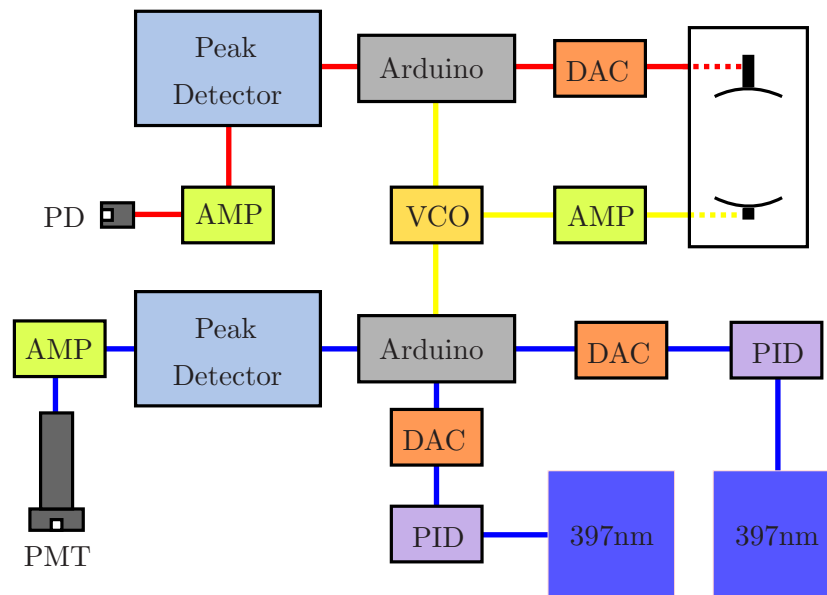


Figure 4.6: Schematic of the electronics used for the scanning cavity lock.

two high current OPA 547 op-amps) and is then connected to the short PZT. A trigger from the VCO is sent to the microcontroller to let it know when the scan begins. The microcontrollers output in parallel to three 8-bit digital to analog converters (DACs - LTC1597). The error signals for the 397 nm lasers are sent to analog PID (proportional-integral-derivative) electronics to produce a voltage to feedback to the ECDL cavity piezos. The feedback voltage for the cavity is instead calculated by the microcontroller^{iv}.

The stages performed in the peak detector are shown in figure 4.7. As explained in the caption the signal is differentiated, compared with ground and then sent through an AND gate with a threshold detection of the original signal. This produces a very short 5 V pulse. This is sent through a monostable multivibrator to extend the pulse duration to $\approx 2 \mu\text{s}$ so it can be easily detected by the microcontroller.

The microcontroller used is an Arduino Mega which is based on a ATmega1280 chip. The Arduino board has connections for 54 digital input/output pins and a USB connection so it can easily be connected to a computer to upload programs. Programs are written in a specifically designed language based on C. The clock speed is 16 MHz.

When each peak is detected a 5 V pulse is sent to a pin of the Arduino which has been configured as an input. Three pins are used, one for the HeNe peaks, one for the peaks

^{iv}It was chosen to use the microcontroller to calculate the feedback to the cavity as there are less stringent time constraints. It is not required to feedback every cavity scan as this lock is to only stop a slow drift of the cavity length. In practice for a 2 kHz scan frequency there is enough time to perform the calculation every scan.

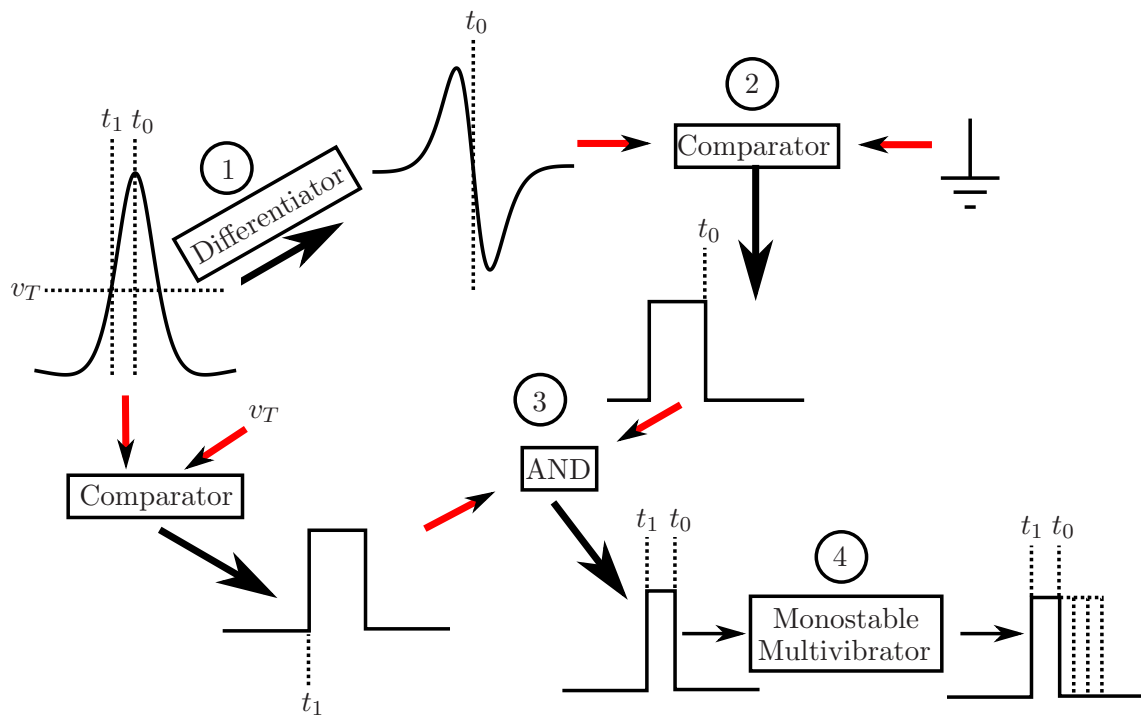


Figure 4.7: Schematic of the peak detector used for the scanning cavity lock. First the cavity transmission signal is differentiated to create a signal with a zero crossing at the peak maximum. This signal is put through a comparator with the other input grounded to produce a positive pulse which stops at this zero crossing. There will however be many more zero crossings originating from small spurious noise spikes in the input signal (not shown in the figure) and so to remove these the signal is put through an AND gate with a threshold detection of the original signal. Finally a monostable multivibrator is used to extend the pulse length to $\approx 2 \mu\text{s}$ so it can be easily detected by the microcontroller.

corresponding to both 397 nm lasers and one for a trigger indicating that the scan has started from the VCO. The pins used are those which can be configured as interrupt pins. An interrupt is hardware configured such that it interrupts whatever the microprocessor is doing and forces it to begin a function created by the user. The program was written such that a rising edge on an interrupt pin triggers a function to be called. The interrupt function corresponding to the VCO trigger resets a variable which counts the number of clock cycles that have passed. The ones attached to the transmission peaks read the clock times at which the peaks were detected and assigns them to variables. Interrupts have been used as they will minimise any variation in the delay between detecting a pulse and setting the relevant variable. It is important to turn off automatic timer interrupts which are used by the Arduino for some timing functions^v. These cause $\approx 4 \mu\text{s}$ glitches which repeat on the order of 1 s. Directly counting the clock cycle number bypasses the need for these timer interrupts^{vi}.

As the cavity is being scanned with a sinusoidal voltage a particular time difference in different parts of the scan will not correspond to the same cavity length difference and hence not the same frequency difference. The time at which a pulse is detected thus needs to be converted to be proportional to the PZT extension. The voltage applied is shown in figure 4.5. It is biased such that it is always positive. Considering half an oscillation for a given cavity scan frequency, Ω and clock speed, C_s the number of clock cycles in the half oscillation, N is given by $\frac{C_s}{2\Omega}$. A pulse which is detected i clock cycles from the beginning of the scan is thus proportional to an extension and is thus proportional to the required voltage to be output to the DAC if

$$V_{\text{out}} = \frac{A}{2} \left[1 - \cos \left(\pi \frac{i}{N} \right) \right]. \quad (4.2)$$

This has been calibrated such that V_{out} covers the whole range of the DAC if A is the maximum number that can be output. To speed up the computation time required by the DAC a lookup table is created by the program for V_{out} for a given number of clock cycles. The conversion is done within the interrupt functions.

To actually tell the DAC a voltage to which it should be updated a 16-bit number is required. The Arduino has a number of ports consisting of a set of 8 pins. The ports are hard-wired such that their voltages can be set simultaneously using a single command. Using the calibration of equation 4.2 it is assured that the maximum number sent to the ports is the maximum number that can be processed by a 16 bit counter ($2^{16} - 1$). The 8 most and least significant bits of the number are then separated and sent to the separate

^vUsing the command 'TIMSK0=0'.

^{vi}Using the timer variable 'TCNT1'.

ports of the Arduino. Triggers are then sent to the DAC to tell it to update the voltage it is outputting.

Due to the low 397 nm power transmitted through the cavity the threshold on the peak detector must be set close to the background level and so spurious peaks can sometimes be mistakenly detected. These peaks could occur anywhere in the scan and will cause problems if they result in a radically different voltage being sent to the extended cavity grating piezo. It was thus decided to include windows around the 397 nm peaks. If from one scan to the next a detected peak appears to have moved by more than the window then it will be ignored and the DAC voltage will not be updated.

After the lasers have been locked a voltage is output to each DAC equal to the relevant 397 nm peak position frequency difference from the first HeNe peak minus the same frequency difference measured when the locking began (plus an offset to keep the voltage away from the DAC rails). We will call this original frequency difference the setpoint. The laser frequencies can be scanned by changing the value of this setpoint. This is achieved via a Labview interface which sends digital signals to the Arduino. Three digital signals are required, one specifies which laser to move, the second says whether to increase or decrease the setpoint and the third performs the action every time a pulse is provided.

For the 397 nm lasers the signal from each DAC is sent into commercial analog PID (proportional-integral-derivative) electronics (TuiOptics P100) to create the voltages to be applied to the PZTs. The scanning cavity is locked by keeping the first HeNe pulse time the same time from the beginning of the scan. This lock is required to keep the HeNe and 397 nm pulses within the range of the scan. It was decided to calculate the proportional and integral feedback for this lock digitally^{vii}. The integral is calculated using the formula ‘integral = integral + error’ where ‘error = setpoint - pulse position’. This results in the integral being updated every cavity scan. The output to the cavity piezo, V_{piezo} is thus

$$V_{\text{piezo}} = \frac{A}{2} + P \times \text{error} + I \times \text{integral}. \quad (4.3)$$

The lock has been found to be successful in stopping the lasers from drifting. No reduction in the signal from the ion is seen over a timescale of hours due to a drift the frequency of the 397 nm lasers. A second scanning cavity is under construction to lock the infra-red lasers via the same method. For the results of chapters 6 and 7 the lengths of the extended cavities of the infra-red lasers are manually adjusted (via the voltage on their respective PZTs) if a reduction in the signal from the ion is witnessed. No reduction

^{vii}It was originally decided to perform the cavity feedback calculation digitally as it was not necessary to feedback every scan and so there was plenty of time to perform the computation. In practice at a cavity scan speed of 2 kHz there was enough time to feedback every scan.

in the linewidths of the 397 nm lasers is seen via the cavity transmission when the lock is activated.

4.2.4 Acousto-Optic Modulators

Each laser is pulsed using a commercial acousto-optic-modulator (AOM) to select temporal slices from the continuous wave laser output. This is required for creating laser pulses used for the pulsed spectroscopy of chapter 7. The crystal is bonded to a piezo transducer. The piezo is driven at an RF frequency of ≈ 100 MHz launching an acoustic travelling wave into the crystal. Light diffracts from the resulting compressions and rarefactions of the crystal. The first order diffracted light is at the frequency of the laser plus the RF frequency. The zeroth order light is blocked and the first order is directed towards the ions. Thus ideally only when the AOM is switched on will the ions see the laser beam. Figure 4.8 shows a schematic of the electronic components used for the AOMs. The voltage-controlled-oscillator (VCO) outputs a radio frequency which is dependent on the voltage supplied. The frequency is optimised to obtain the highest 1st order diffracted efficiency. The RF is then passed through a switch which is controlled via a TTL input. A variable attenuator is then used which has a gain dependent on an input voltage. Currently this is used to optimise the AOM efficiency but in the future a signal from a photodiode will be fed back to this to reduce the amplitude noise of the laser (forming a ‘noise-eater’). A final amplifier is used before the signal is sent to the AOM. The laser beam must either be collimated or be within the Rayleigh range of a focus (so the divergence is small) when it passes through the AOM. The beam size at the AOM is a tradeoff between switching speed and diffraction efficiency. The switching (≈ 10 ns) is much quicker than our current requirements (≈ 10 ms pulses) and so the beam is made as large as possible (≈ 300 μm). Up to 80% of the light passed into the AOM is diffracted into the 1st order.

4.2.5 Optical Table Setup

We have seen many of the optical components required for the experiment. Now let us look at how the lasers are maneuvered through them before being focused onto the trapped ions. All the lasers except for the 729 nm (§ 4.2.6) are on a single optical table. For clarity the layouts of the infra-red (IR) and 397 nm lasers have been shown on separate figures. This is the optical layout at the time of writing where the scanning cavity lock is being used for the 397 nm lasers and the AOMs and fibre EOM (§ 6.3) have been included. The paths of the 866 nm and 854 nm beams are shown in figure 4.9 while that of the 397 nm is shown in figure 4.10. The 866 nm beams are first combined and then sent through an anamorphic prism pair to partially circularise the initially elongated beam shape (§ 4.2.1).

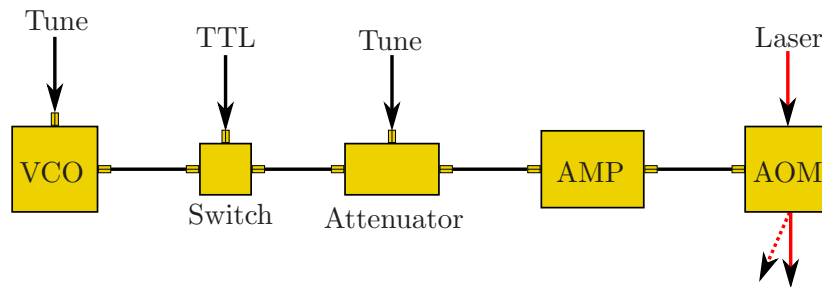


Figure 4.8: Schematic of electronics used for AOMs. The 397 nm AOMs are centered at 110 MHz (Isomet 1206C-833), the 729 nm at 250 MHz (Isle Optics LM250) and the 854 nm at 80 MHz (Brimrose 80-20). VCOs are used at all of these frequencies (110 MHz: ZX95-200-S+, 250 MHz: ZX73-2500-S+, 80 MHz: ZOS-100). The variable attenuators are based on variable amplifiers (LMH6505MA). The Amplifiers for the 397 nm and 854 nm AOMs are based on a ASC2832 chip. The 729 nm AOM amplifier is a Mini Circuits ZHL-1-2W.

The combined beam is then put through a Faraday isolator to reduce reflections back into the lasers which could disrupt the wavelength and single mode operation. A $\lambda/2$ waveplate is then used to rotate the polarisation such that it is vertical so it does not become elliptical after reflecting off the many mirrors it encounters further along the path. The 854 nm and 397 nm lasers have a similar arrangement, however the beam shaping is performed using a cylindrical lens pair. Pick-offs are placed after the waveplates to send light to the wavemeter (High Finesse) and the scanning cavity in the case of the IR and 397 nm lasers respectively. This is done as early as possible so the lock and wavemeter reading will not be interrupted if the beam is blocked further down the line. Flipping mirrors are used to direct the light to the Michelson wavemeter if it is required since it requires a lot of light. The spectrum analyser shown in figure 4.9 is that used for the old 866 nm lock (§ 4.2.3) and is used in chapter 6 to look at the sidebands generated by the fibre EOM.

The electromagnet used to generate the magnetic field for Penning trap operation (§ 4.4.1) sits on the optical table such that the trap itself is 325 mm above the table. A breadboard with components at this height is used for combining the beams and changing the beam polarisation. Single-mode, polarisation-maintaining optical fibres are used to send the light up to this breadboard. Two single-mode fibres are used, one for the 397 nm beams and one for the 854 nm, 866 nm and 729 nm beams. As the lasers have traveled through the same fibre they will automatically be spatially overlapped. It only remains to overlap the output of the 397 nm fibre with that of the infra-red fibre at the centre of the trap using a single lens external to the trap vacuum system. A 250 mm focal length lens is used to produce spot sizes at the ions of 90-100 μm . Figure 4.11 shows the components used on the breadboard.

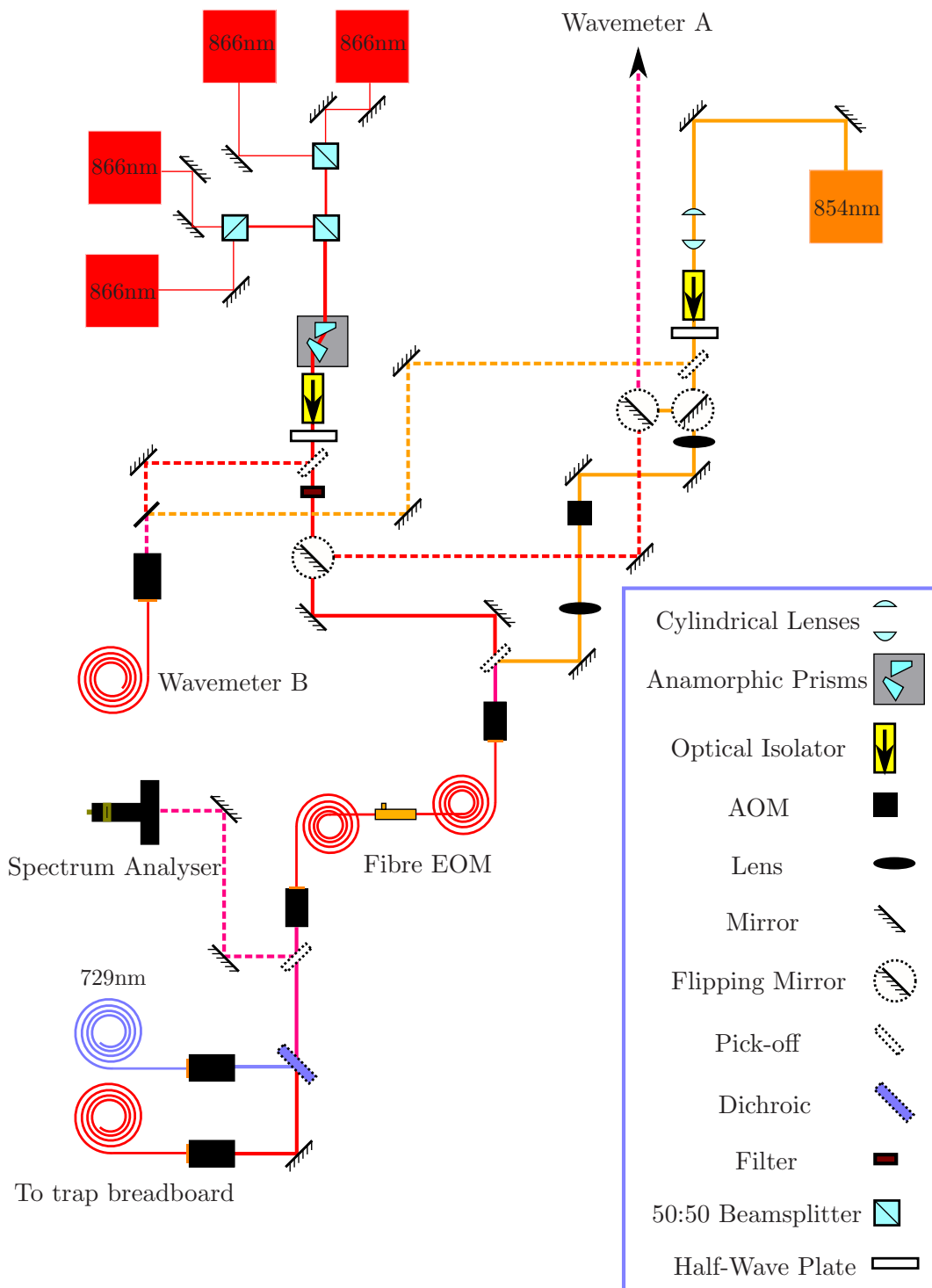


Figure 4.9: Optical Setup of the 854 nm and 866 nm lasers. The optical setup of the 397 nm lasers is shown separately in figure 4.10 and how they are combined is shown in figure 4.11. Wavemeter A is the Michelson interferometer described in the text. Wavemeter B is the commercial High Finesse wavemeter (see text). The fibre EOM will be detailed in chapter 6.

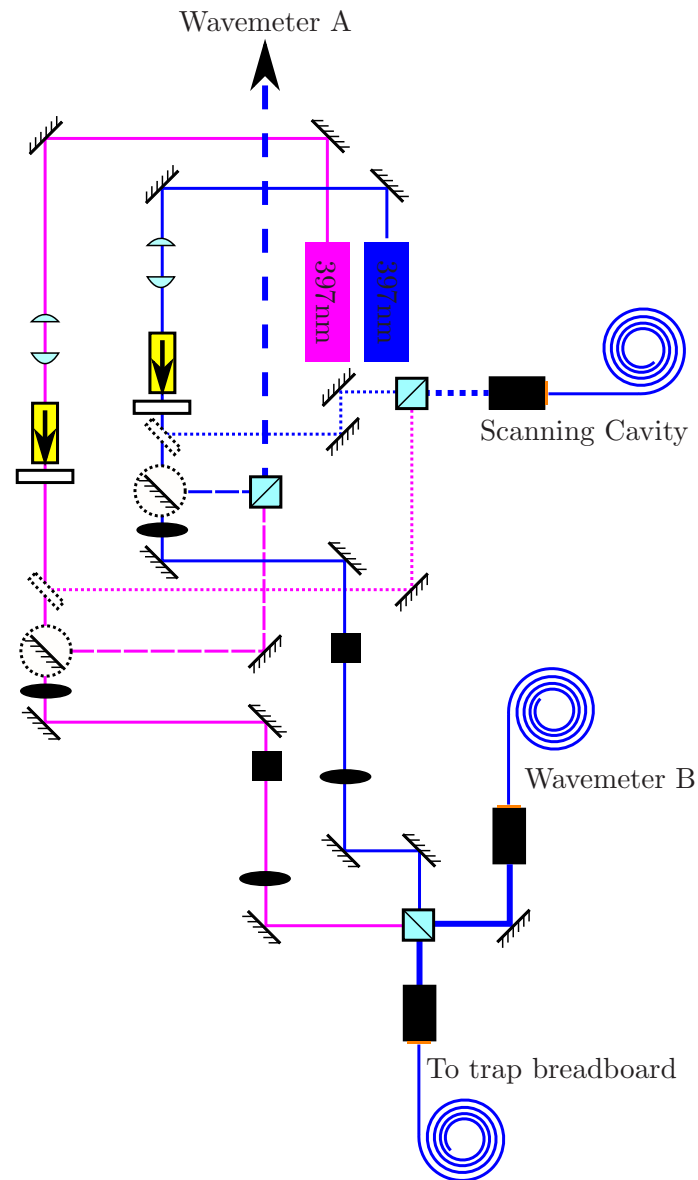


Figure 4.10: Optical Setup of the 397 nm lasers. The optical setup of the infra-red lasers is shown separately in figure 4.9 and how they are combined is shown in figure 4.11. Wavemeter A is the Michelson interferometer described in the text. Wavemeter B is the commercial High Finesse wavemeter (see text).

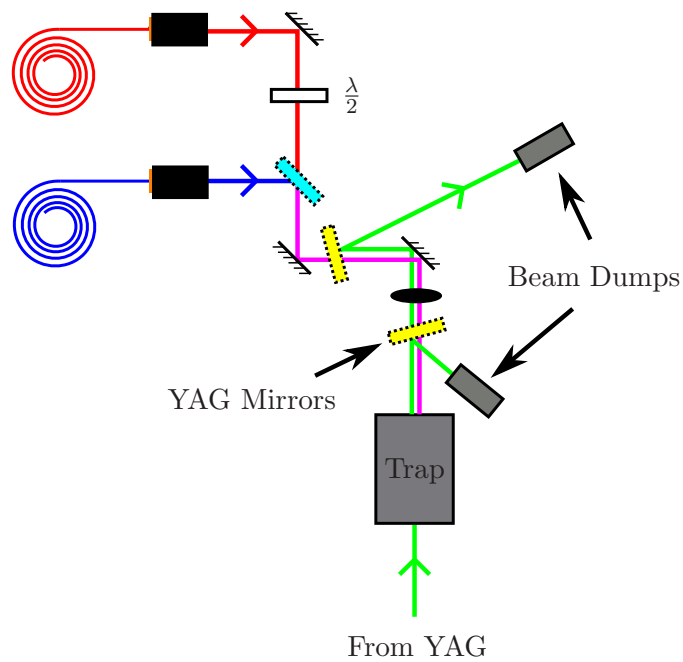


Figure 4.11: Optical Setup before the trap where the IR and UV beams are combined. The YAG beam shown is used for photoionisation and is discussed in § 4.4.3. It is sent through the trap in the opposite direction to the other beams. Two YAG mirrors ($> 90\%$ transmission at IR and UV) are used to stop damage to the IR and UV fibres. The polarisation of the 854 nm, 866 nm and 729 nm lasers can be rotated using the $\lambda/2$ waveplate. The 397 nm polarisation is set by the angle of the output fibre coupler. A 250 mm focal length lens is used to focus all of the beams into the trap.

4.2.6 729 nm Laser System Overview

The $S_{\frac{1}{2}} \rightarrow D_{\frac{5}{2}}$ quadrupole transition needs to be addressed with a narrow linewidth laser to resolve individual sidebands of the ion's motion. This is required for sideband cooling (§ 3.3) and for quantum computation schemes discussed in § 3.4. The coherent dynamics which occur are described in § 3.2.

Originally the 729 nm source was a commercial Verdi pumped Titanium-Sapphire laser. The linewidth of the laser was narrowed using a Pound-Drever-Hall (PDH) lock to an external cavity. The scheme used is described in reference [52]. The linewidth achieved was estimated to be ≈ 1.7 kHz. The lock however was not very robust. When the laser head of the Verdi became faulty it was decided to develop a new system based on the newly available 730 nm diodes instead of maintaining the Titanium-Sapphire laser system. The new system was developed by a Post-Doc in our group (D.Crick). The system uses the external cavity used for the Titanium-Sapphire system to produce a PDH lock. The electronics and optics have however been improved to produce a very robust lock. An overview of the PDH locking scheme will be given together with an overview of the optics and electronics used.

4.2.7 Pound-Drever-Hall Locking Scheme - Theory

The Pound-Drever-Hall (PDH) technique was first implemented in the microwave regime by R. Pound in 1946 [62] and then in the optical regime by R. Drever and J. Hall in 1983 [63]. In this technique the laser is locked using the reflected light from a stable external cavity. The set point used is a position where there is a narrow dip in reflected light detected. As will be shown below, the error signal produced is essentially dispersion shaped, with a zero crossing at the centre of the intensity dip. This is advantageous as the laser's intensity noise does not generate frequency noise. The fraction of light reflected from the cavity is an even function of the laser frequency. If this is directly used as an error signal the laser cannot be locked to the central point because it is impossible to differentiate between a positive or negative frequency shift. To circumvent this problem the error signal used is related to the derivative of the cavity's Airy function. The derivative is an odd function and so the laser can be locked to the central point. Another advantage of the more complicated PDH lock is due to the fact that the error signal is derived from the light from the input cavity mirror rather than the light transmitted through the cavity. A fraction of the light used is that which has been instantly reflected from the first mirror. The light used has two components - a promptly reflected component at the actual laser frequency, and a delayed component at the cavity resonance frequency leaking from the cavity mode. The PDH scheme essentially compares these two components so that very

rapid deviations of the input frequency from the desired cavity frequency can be detected and ultimately removed in a feedback loop. The PDH technique can thus cope with faster frequency fluctuations than the side-of-fringe technique, resulting in a tighter lock.

To physically obtain the derivative of the cavity's Airy function the laser frequency is modulated. The laser intensity measured will either vary in phase with the modulation applied (for a positive gradient) or out of phase (for a negative gradient). This is the method used for a 'dither lock'. The PDH lock can be thought of as the high modulation frequency limit of this technique. The error signal acquired permits a tighter lock and will work at a higher maximum frequency jitter of the laser.

The mathematical form of the PDH error signal will be derived using a standard treatment similar to that adopted in reference [64]. First the reflected power of a phase modulated laser beam from a reference cavity is calculated. It is the light intensity that is required rather than the electric field as a photodiode cannot directly see the field. The electric field of a phase modulated laser beam can be expressed as

$$E_{\text{incident}} = E_0 e^{i[\omega t + \beta \sin(\Omega t)]}, \quad (4.4)$$

where β is the magnitude of the modulation and Ω is the modulation frequency.

It is intuitively more favorable to express the incident field as a sum of Bessel functions. For a small modulation we can approximate the field as zeroth and first order Bessel functions (§ 6 for a more complete description at higher modulation amplitudes). We obtain

$$E_{\text{incident}} \approx E_0 \left[J_0(\beta) e^{i\omega t} + J_1(\beta) e^{i(\omega+\Omega)t} - J_1(\beta) e^{i(\omega-\Omega)t} \right], \quad (4.5)$$

where $J_0(\beta)$ and $J_1(\beta)$ are the zeroth and first order Bessel functions respectively.

There are now three terms in the expression representing waves at three different frequencies. It is seen that the magnitudes of these frequency components depend on the magnitude of the modulation. There is one component at the frequency of the original, unmodulated wave (carrier) while the others have frequencies separated from the original by $\pm\Omega$ (sidebands).

The PDH error signal is derived from the signal coming from the input cavity mirror. A reflection coefficient as a function of frequency is thus required. It is a standard result

that for a symmetric cavity with mirrors of reflectivity r , the reflection coefficient is^{viii} [65]

$$F(\omega) = \frac{E_{\text{reflected}}}{E_{\text{incident}}} = r \left[\frac{e^{i\omega/\Delta\nu_{fsr}} - 1}{1 - r^2 e^{i\omega/\Delta\nu_{fsr}}} \right]. \quad (4.6)$$

The reflected electric field from the cavity is thus

$$E_{\text{reflected}} = E_0 \left[F(\omega) J_0(\beta) e^{i\omega t} + F(\omega + \Omega) J_1(\beta) e^{i(\omega + \Omega)t} - F(\omega - \Omega) J_1(\beta) e^{i(\omega - \Omega)t} \right]. \quad (4.7)$$

The reflected power is then obtained by finding the modulus squared of the field

$$\begin{aligned} P_{\text{reflected}} = & P_c |F(\omega)|^2 + P_s \left[|F(\omega + \Omega)|^2 + |F(\omega - \Omega)|^2 \right] \\ & + 2\sqrt{P_c P_s} [\text{Re} [F(\omega) F^*(\omega + \Omega) \\ & - F^*(\omega) F(\omega - \Omega)] \cos(\Omega t) + \text{Im} [F(\omega) F^*(\omega + \Omega) \\ & - F^*(\omega) F(\omega - \Omega)] \sin(\Omega t)] + (2\Omega \text{ terms}), \end{aligned} \quad (4.8)$$

where P_c and P_s are the reflected carrier and sideband powers from the cavity respectively.

The terms in which we are interested for our error signal are those containing information about both the carrier and sidebands ($F(\omega) F^*(\omega + \Omega) - F^*(\omega) F(\omega - \Omega)$). The 2Ω terms are easily discarded using a low-pass filter. The constant terms are removed by capacitively coupling the photodiode. We are left with a term varying as $\cos(\omega t)$ and a term varying as $\sin(\omega t)$. The frequency of the modulation decides which of these terms is significant. The PDH technique operates in the high frequency regime. The higher the modulation frequency the further the sidebands are from the carrier in frequency space. In the high modulation frequency limit we can assume all the power of the sidebands is reflected ($F(\omega + \Omega) = F(\omega - \Omega) = -1$). In this case the real part of equation 4.8 is negligible and so we neglect the $\cos(\omega t)$ term obtaining

$$P_{\text{reflected}} = 2\sqrt{P_c P_s} \text{Im} [F(\omega) F^*(\omega + \Omega) - F^*(\omega) F(\omega - \Omega)] \sin(\Omega t). \quad (4.9)$$

We would like to measure a DC signal. To get rid of the sinusoidal variation with time the signal is mixed with the original modulation signal. This creates a DC term and a AC term with a frequency of 2Ω (using $\sin^2(\Omega t) = \frac{1}{2} [1 - \cos(2\Omega t)]$).

The 2Ω term can be removed using a low-pass filter and we finally have our error signal

$$\epsilon = \sqrt{P_c P_s} \text{Im} [F(\omega) F^*(\omega + \Omega) - F^*(\omega) F(\omega - \Omega)]. \quad (4.10)$$

^{viii}Note that this expression contains both a immediately reflected component as well as a component which leaks out of the cavity.

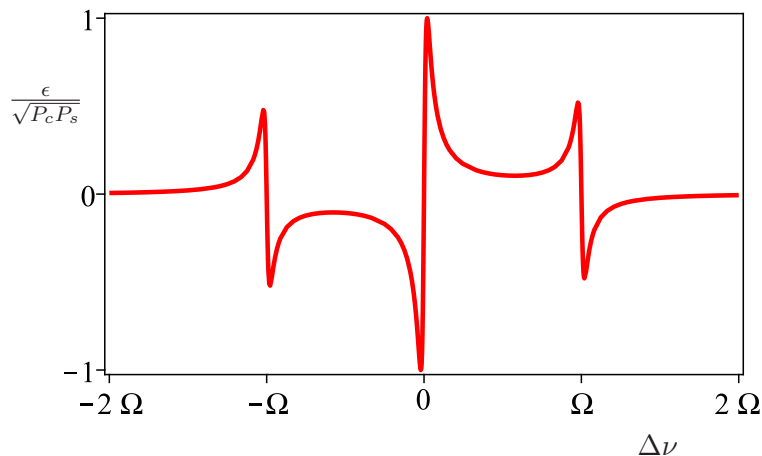


Figure 4.12: Example PDH error signal. A relatively low finesse of ≈ 300 has been used so the structure can easily be seen. The frequency of the laser modulation is Ω .

Figure 4.12 shows an example of the form of this error signal.

4.2.8 PDH Lock - Experimental Implementation

The optical setup is shown in figure 4.13. The initially elongated beam shape of the diode laser is partially circularised using an amorphous prism pair. Two Faraday isolators were required to reduce feedback from the external cavity so that it did not interfere with the lock. The rest of the optics is very similar to that used for the old Titanium-Sapphire laser system described in [52]. Polarising beam splitters (PBS) and wave plates are used to direct the light around the different sections. The first $\lambda/2$ and PBS determine the fraction of light directed towards the external cavity to produce the required error signal. The remainder of the light goes through a second $\lambda/2$ and PBS to choose the fraction of light double-passed through a AOM and then sent through a fibre to the trap. The $\lambda/4$ waveplate is also double passed so that the light's polarisation is changed from vertical to horizontal so it then passes through the PBS. The other portion of the light goes straight through the PBS through a fibre to either of the wavemeters described in § 4.2.2. It is noted that the wavemeter reading does not include the frequency shift imparted by the AOM.

The fraction of the light sent towards the cavity is first sent through an EOM to modulate the laser's phase as required to create the PDH error signal. It is then mode matched with two lenses into the cavity. The light transmitted through the cavity is measured on a photodiode and observed on a CCD camera to check the mode which is being coupled. The reflected light from the cavity passes twice through the $\lambda/4$ waveplate

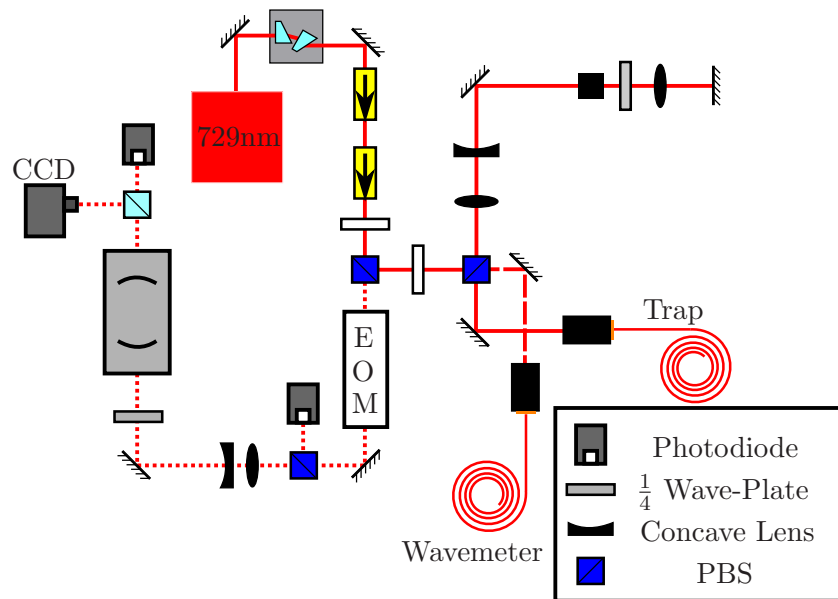


Figure 4.13: Optical Setup of the 729 nm Laser System. The EOM (Linios PM25) is used to generate sidebands on the laser required for the PDH error signal. The cavity has a FSR of 1.5 GHz

and so is reflected off the PBS onto a photodiode. It is the electronic signal from this reflected light which is used to create the PDH error signal. The signal is first sent through a DC blocking capacitor to remove the DC terms of equation 4.8. It is then mixed with the original oscillator signal, the phase lag of which is optimised to create the required error signal.

The error signal is sent into a loop filter to create the required feedback signal to the laser diode current. A loop filter has been chosen rather than conventional PID electronics as its gain curve can be made to more closely match the optical characteristics of the system. Loop filter design is discussed at length in references [52] and [66]. Low frequency feedback is also provided to the piezo attached to the grating of the laser's extended cavity via an Arduino (§ 4.2.3). The Arduino samples the error signal and then outputs via a DAC to the piezo. Additional features which help the robustness of the lock are also implemented with this Arduino. When the laser is locked the cavity transmission should be high. If a sudden jolt knocks the laser far enough in frequency such that it is no longer within the capture range of the error signal then the high gain at low frequency will quickly move the feedback to a rail of the voltage. This is undesirable as the laser then has no chance of re-locking to the correct cavity mode. To overcome this the Arduino freezes the piezo feedback value if the cavity transmission falls below a certain value (the assumption being the laser has become unlocked or the light to the cavity has been blocked). This

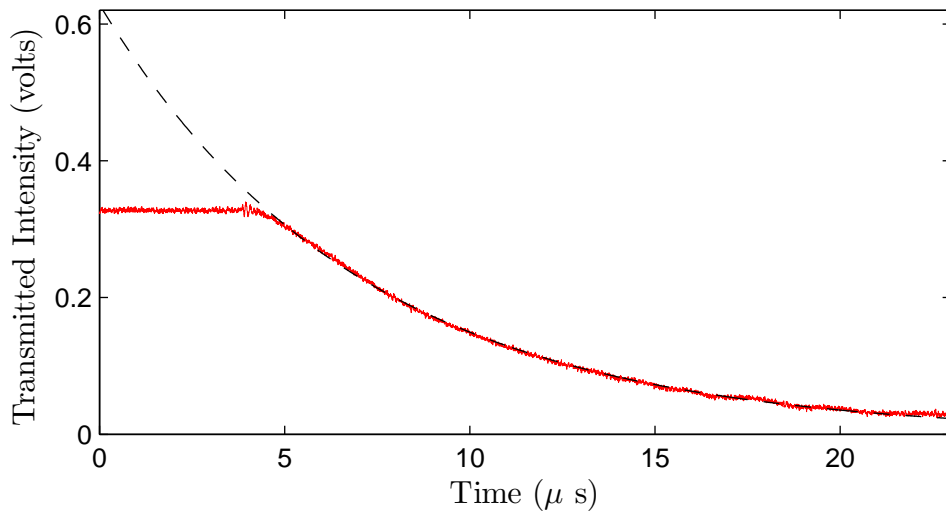


Figure 4.14: Ringdown spectroscopy on the 729 nm locking cavity. The red plot shows the detected cavity transmission. The initially locked laser is unlocked and quickly moves from the cavity resonance. The cavity transmission then exponentially decays. The fit gives a time constant of $6.33 \mu\text{s}$ which results in an estimated finesse of $\approx 60\,000$. Courtesy of D.Crick.

has worked well to produce a robust lock.

The cavity finesse has been measured to be $\approx 60\,000$ using ring-down spectroscopy (see figure 4.14). Figure 4.15 shows the cavity transmission when the laser is locked and is scanned. The extent of the cavity transmission jitter when the laser is locked is much smaller than the cavity linewidth ($\approx 25 \text{ kHz}$). However the cavity acts as a low-pass filter and jitter above the cavity linewidth is attenuated so this is not an accurate measure of the laser linewidth relative to the cavity^{ix}. With difficulty and many assumptions a rough estimate of the laser linewidth relative to the cavity has been calculated from the error signal to be of order 10 Hz (performed by D.Crick). To achieve an accurate measure of the laser linewidth a similar laser system is required and the stability of the beatnote between the two systems is measured.

^{ix}Also as the laser is locked to the peak of the cavity transmission there is no change in the transmission for a frequency change of the laser to first order.

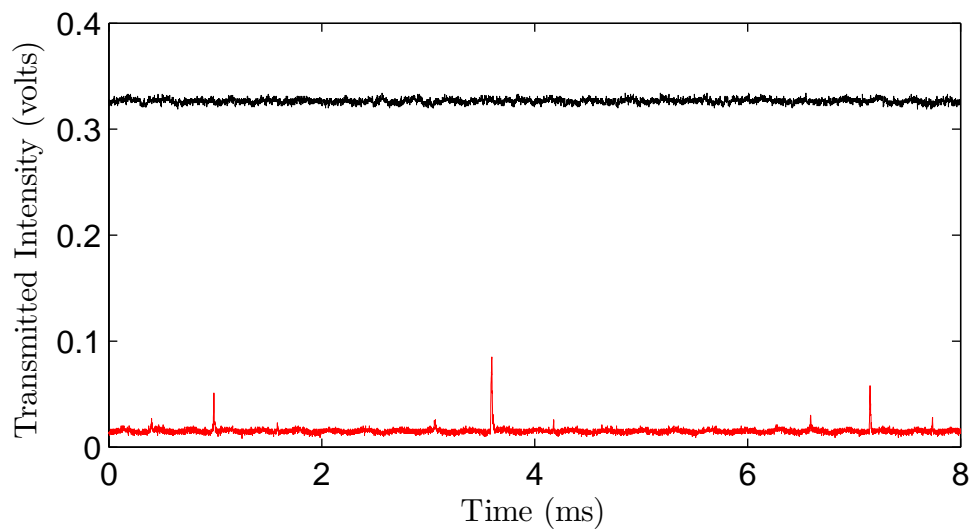


Figure 4.15: 729 nm locking cavity transmission with laser locked (black) and scanning (red). The sidebands on the laser can just be made out in the plot where the laser is scanning. It is noted that much more light is transmitted through the cavity when the laser is locked. One reason for this is due to there being a greater amount of time for light to build up in the cavity. Another reason is that the laser linewidth is smaller when it is locked and so a greater percentage of the light can be resonant with the cavity at any time. Courtesy of D.Crick.

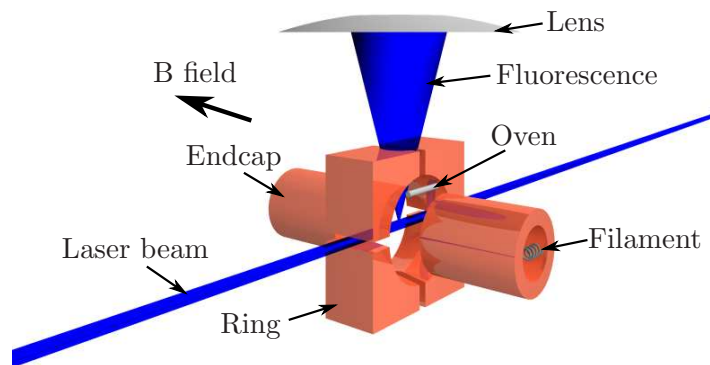


Figure 4.16: Split-Ring trap electrodes. Adapted with permission from [52].

4.3 Ion Traps

4.3.1 Split Ring Trap

The split-ring trap was used in the repumping and pulsed spectroscopy experiments of chapters 6 and 7. It was made by Martijn Van Eijkelenborg and is detailed in reference [67]. Figure 4.16 is a diagram of the trap electrodes. Although the electrodes are very different from the ideal hyperbolic ones described in figure 2.2 the potential is close to harmonic at the centre of the trap. The ring electrode is split into four sections so that axialisation (§ 3.1.2) can be applied. The endcaps are hollow so that a filament can be housed in each one. A hole in the endcap allows electrons to move along the magnetic field direction to the trap centre for ionisation of calcium atoms (§ 4.4.3). A calcium oven is between the ring and endcaps on each side. Each oven has a hole pointing towards the trap centre which the atoms can come out of.

The laser and fluorescence detection directions are shown in figure 4.16. Note that there are no laser beams along the magnetic field direction and so Doppler cooling cannot be performed along this axis. The first imaging lens is shown. This is inside the vacuum chamber. See § 4.4.2 for a description of the imaging system.

4.3.2 PCB Trap

The PCB trap is used in the J-mixing experiment of § 5.3. It is made out of two pieces of circuit board (FR4) facing each other. The trap electrodes are milled onto the boards. The trap actually has 3 trapping regions. It was designed for moving ions between these trapping zones perpendicular to the magnetic field. The experiments where this is performed and the details of the trap have been described extensively elsewhere (see references [51]

and [7]) and so will not be described here. Although the electrodes are vastly different from the ideal theoretical shape the distance between the two boards is optimised such that the potential is again almost harmonic at the trap centre. The lasers pass between the two boards and imaging is perpendicular to this as in the case of the Split-Ring trap.

4.4 Other Experimental Considerations

4.4.1 Magnetic Field Generation and Vacuum System

The magnetic field was generated by a conventional electromagnet (Oxford Instruments - Newport Series N100). Up to 15 amps is sent through each of the two coils of the electromagnet in parallel to produce a magnetic field strength at the ion of up to 1 tesla. A movable iron pole piece is in the centre of each coil. These clamp the vacuum can of the trap in the magnet. The current source used is a Danfysik - System 8000 - 853. This is specified to a drift of ± 3 ppm over 30 minutes and ± 10 ppm over 8 hours. Using a Hall probe the the magnetic field at the ions has been calibrated for a given current through the coils [51]. The coils saturate at high current. At ≈ 1 tesla the increase in the current required to produce an increase in the magnitude of the magnetic field is 100 ampere tesla⁻¹ while at < 0.5 tesla this gradient is 18.8 ampere tesla⁻¹. The 30 minute drift when a field of ≈ 1 tesla is generated is expected to be $\pm 9 \times 10^{-7}$ tesla. This drift is insignificant for the dipole transitions. It is however important for the $S_{\frac{1}{2}} \rightarrow D_{\frac{5}{2}}$ transition. The transition with the largest Zeeman shift is the $m_J = -\frac{1}{2} \rightarrow +\frac{3}{2}$. The magnetic field drift results in a drift in the frequency of this transition of ± 35 kHz. This suggests that the magnetic field stability should be good enough to see motional sidebands at the trap frequency (§ 3.2) when pulsed spectroscopy is performed (chapter 7). This is however a lower limit on the magnetic field stability.

Connecting the magnets in parallel is not ideal for magnetic field stability. A change in the relative resistance of the two coils will result in a change in the current passing through each coil which will change the magnetic field at the ions. If the coils are instead connected in series then a resistance change will change the voltage drop across the coil but the current should stay constant and thus the magnetic field should stay constant. Unfortunately the current source is not able to produce the voltage required to connect the coils in series.

Ultra-high vacuum conditions are required to trap ions in a Penning trap for extended periods of time. A pressure of $< 10^{-9}$ mbar is achieved for the experiments described in this thesis. The vacuum system is heated to ≈ 120 °C in a bakeout oven for ≈ 2 weeks while it is pumped by a turbopump. An ion pump is then permanently switched on and

the chamber is valved off from the turbo pump to achieve the lowest pressures. The trap chamber can then be removed from the bakeout oven and installed on the optical table. The PCB trap's vacuum system has an extra pump attached. This is a getter pump (Capacitorr - D400-2). It is made up of a material with a large surface area which gases stick to. The Split-Ring trap has a ion-gauge to measure the pressure. The PCB trap relies on the ion pump current to give a rough measurement of the pressure.

4.4.2 Photon Detection

For all of the experiments described in this thesis the light from the ions is detected using a photomultiplier tube (PMT). This device is affected by magnetic fields and so is kept 510 mm away from the ions. The same symmetric three-lens system is used as the imaging system for both the Split-Ring and PCB traps described earlier (see figure 4.17). The first lens (l_1) is held in the vacuum chamber ≈ 19 mm from the trap centre and has a focal length of ≈ 40 mm. The second lens (l_2) has a focal length of ≈ 155 mm and the third is a copy of the first. The system is designed to be as symmetrical as possible so as to reduce aberrations and keep the magnification close to 1. The light is focussed through a pinhole to remove background light. The size of this pinhole is as large as 1 mm when trapping large clouds of ions but is reduced to ≈ 200 μm when a single ion is trapped.

A band-pass filter (Semrock FF01-406/15-25) was placed before the PMT to block out background light at other frequencies (transmission of $\approx 90\%$ at 397 nm). This was used for the experiments described in chapters 6 and 7. Previously a combination of a low-pass (Comar 435IK25) and band-pass (Comar 395GB25) filters were used. These were still in place for the experiment described in chapter 5. The transmissions of these filters were 70% and 80%. The detection efficiency is important for the experiment in chapter 5. The transmission of the trap window and each lens is 90%. At the time the solid angle of light detected was limited by the diameter of the second lens to a fraction of 0.0087 of 4π . The quantum efficiency of the PMT is ≈ 0.2 so in total the detection efficiency is calculated as $\approx 6 \times 10^{-4}$. However we can also define an effective detection efficiency as the ratio of the rate of photons we detect over the number we should theoretically be scattering. The theoretical scattering rate is approximated by $\Gamma/8$. There are 8 states which are coupled to the cooling transition; two $S_{\frac{1}{2}}$, four $D_{\frac{3}{2}}$ and two $P_{\frac{1}{2}}$. If these transitions are saturated then the ion will spend approximately a quarter of its time in the $P_{\frac{1}{2}}$ states. For efficient Doppler cooling the lasers are detuned by half the transition linewidth leading to a factor of two reduction in the time spent in the $P_{\frac{1}{2}}$ states. The expected scattering rate is thus $\Gamma/8 = 1.7 \times 10^7$ photons s^{-1} . We detect a maximum of 7000 photons s^{-1} leading to an effective detection efficiency of 4×10^{-4} . This is the value used in chapter 5 to compare

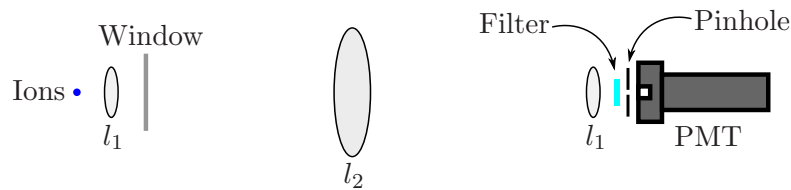


Figure 4.17: Imaging system used for both the Split-Ring and PCB traps. The focal length of lenses l_1 is 40 mm while lens l_2 has a focal length of 155 mm. The first lens is inside the vacuum chamber. See the text for a description of the other components.

the experimental results with theory.

The signal from the PMT is sent through a discriminating amplifier and then converted to TTL pulses. The pulses are counted on an multi-channel-scaler card (EG and G-Ortec). This has 8000 time bins whose width can be manually set or controlled via an external trigger. The bin width can be set as low as $2 \mu\text{s}$ but generally a width of 10 ms is used.

4.4.3 Ion Creation

The trap potential is always present. This means that the ions must be created inside the trap if they are to remain confined since they find themselves in a conservative field. The idea is to send a ^{40}Ca atom into the trap and then convert it into an ion so it suddenly begins to feel the trapping potential. The atoms are produced by passing a current through a tantalum wire which is spot welded to a tantalum tube which has been filled with calcium shavings and crimped at both ends (a calcium oven). Natural abundance calcium can be used as ^{40}Ca is the most abundant isotope (96.9% abundance [68]). A small hole is made in the middle of this tube using a pin. When the temperature of the oven is high enough some calcium atoms will travel out of the hole and will head towards the trap. An aperture is generally used to only pass atoms which are directed towards the central region of the trap stopping calcium from hitting electrodes and causing possible shorts and contact potentials. The method used to ionise the atoms when I joined the group (and used in obtaining the results of chapter 5) was to create a beam of electrons by heating up a short section of thoriated tungsten wire (a filament). The wire is placed such that the electrons would travel along the magnetic field direction to the trap centre. By setting the potential on the wire relative to the trap centre to be above the ionisation energy (6.1 eV) but below the energy required to doubly ionise the calcium atoms (11.9 eV) [58] Ca^+ ions will be created in the trap. There are many problems using this ionisation method. The electron beam can charge up any resistive materials which are near the trap and so alter the trap potential which the ion sees. The filament positioning requirements can be restrictive for electrode design and laser and imaging access. The filament also gets very hot and so can

cause outgassing of material near it which can raise the pressure in the trap. The method is also inefficient which means the oven has to be heated to a high temperature as well so that a large flux of neutral atoms is generated. The light from the filament can also cause a lot of background light which can reduce the chance of observing the ions while they are being loaded.

A better approach which circumvents many of these problems is to use photoionisation. Here the atoms are created in the same way but a laser is used to provide the energy required to excite an electron above the ionisation threshold. The relevant electronic energy levels of the calcium atom are shown in figure 4.18. A common method to photoionise calcium ions is using a 423 nm laser diode to excite an electron to the $4s4p\ ^1P_1$ state and then another laser diode near 389 nm to excite it up to the continuum [69] [70]. The isotope shift of the 423 nm transition between ^{40}Ca and ^{43}Ca is ≈ 600 MHz while the transition linewidth is ≈ 35 MHz. It is therefore possible to selectively ionise one isotope of Ca. This approach has allowed the Oxford group to load pure crystals of $^{43}\text{Ca}^+$ using an oven filled with natural abundance calcium [71]. Another method is to use a 272 nm laser as the first step to excite an electron up to the $4s5p\ ^1P_1$ [72]. A second photon from the same laser can then ionise the ion. A photon from the 397 nm cooling laser also has enough energy to perform this second step. If a second photon is not absorbed quickly enough then the ion may spontaneously emit down to the $4s3d\ ^1D_2$ state. A 272 nm photon can also excite the electron up to the continuum from this state. The drawback of this scheme is that it requires the use of an expensive dye laser system.

The photoionisation method which we have deployed is to use a short-pulse frequency doubled Nd-YAG laser (Continuum SureLite II) which via a 3 photon transition ionises the atom. The maximum energy per pulse that the laser can produce is ≈ 300 mJ at 532 nm. The pulse length is ≈ 5 ns with a repetition rate of 10 Hz. This leads to a power during the pulse of 60 MW and an average power of 3 W. Dichroic mirrors (Coma 555 IM25) are used to maneuver the beam. Approximately 650 mJ of the fundamental 1064 nm is produced. The majority of the power at this wavelength passes through the first dichroic mirror into a beam dump. A periscope is used to send the beam up to the height of the trap. It is then sent through a focusing lens ($f \approx 800$ mm) into the trap (spot size $\approx 200\ \mu\text{m}$) in the opposite direction to the other lasers. On the other side of the trap two dichroic mirrors are placed in the beam to direct the laser away from the fibres which could be damaged by the high power pulses (figure 4.11).

The YAG power can be crudely changed by altering the Q-switch delay and it is found that this is adequate for our requirements. A $\lambda/2$ waveplate and polariser have previously been used to finely adjust the power but they have now been taken out of the beam.

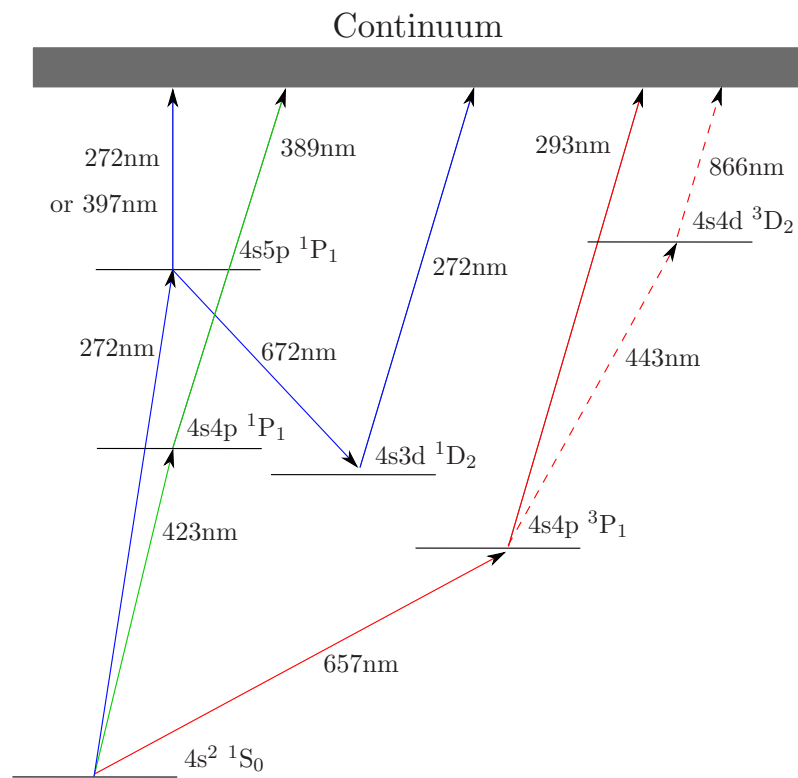


Figure 4.18: Electronic energy levels of a calcium atom. Reproduced with permission from [73].

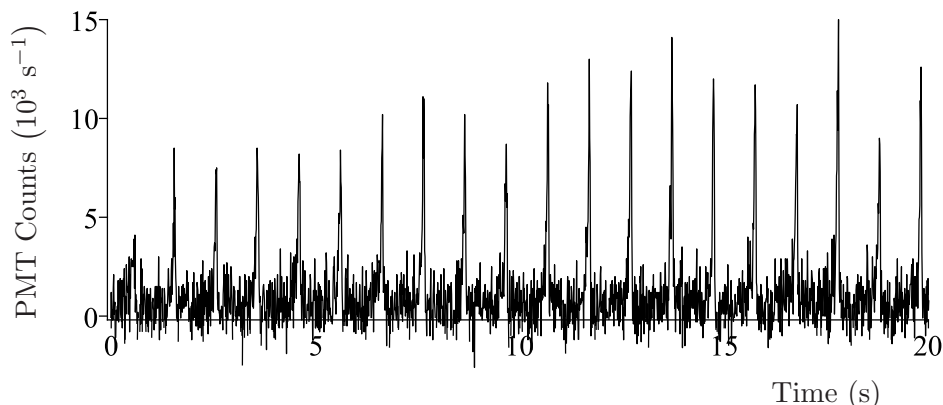


Figure 4.19: Loading a small ion cloud with the YAG

Figure 4.19 shows a PMT trace of ions being loaded into a Penning trap at ≈ 1 tesla using the YAG laser for photoionisation. The Split-Ring trap was used for this experiment. A current of 1.7 amps was passed through the oven for ≈ 30 s and then the YAG was fired for 10 pulses. A Q-switch delay of $160 \mu\text{s}$ was used which gives a measured average power of ≈ 100 mW and so an energy per pulse of 10 mJ. One of the 397 nm lasers was repetitively scanned by ≈ 1 GHz from an initial red detuning up towards resonance with a period of 1 s. This helps to cool in any very hot ions more quickly. It is noticed that compared to previous loads where a filament was used [51] [52] the ions seem to be cold as soon as signal from them is seen as evidenced by the narrowness of the peaks. Previously the peaks would first be wide and then get taller and thinner as the ions cooled. Now the signal still increases as more ions are loaded but even the small peaks are thin. This is attributed to the ions being colder due to a lower background pressure at the trap. This could be caused by a reduction in outgassing due to hot filament not being required.

Once the experimental parameters have been optimised for single ions they can be loaded with a $1 \mu\text{J}$ pulse. It is noted that if the YAG alignment is not optimal it can take up to 30 s for an ion to cool in to the trap centre such that a signal can be seen. If good alignment is achieved then the loading can be instantaneous.

Whilst once readily available, laser diodes at 423 nm are now rare and so a relatively complex and expensive doubling system is required to create this light. As an alternative for isotope selective loading an attempt was made to excite an electron to the $4s4p \ ^3P_1$ state and then ionise the atom with a 2 photon transition from the YAG. A 657 nm diode in a ECDL setup was used. The power of the YAG was reduced such that it was on the border of being able to ionise atoms. The 657 nm laser frequency was scanned and loading was attempted at each frequency, separated by 50 MHz. The power of the 657 nm laser

was ≈ 6 mW at the trap. No enhancement in loading was seen. This was attributed to both the Doppler width and the narrow linewidth of the transition (≈ 400 Hz). Only a fraction of the 657 nm laser power is resonant with transition as the laser linewidth is much greater than the transition linewidth. The YAG is able to ionise all of the atoms it interacts with no matter what their frequency shift due to the Doppler effect is. The 657 nm laser linewidth is much less than the Doppler width of the atomic beam (≈ 1 GHz) and so can only interact with a fraction of the beam. To be able to ionise via this transition (and hence obtain isotope selective loading) a locked, narrow linewidth laser would be ideal. A well collimated atomic beam perpendicular to the laser beam direction would also improve the probability of exciting a higher proportion of the atoms. If this method were to be employed a CW laser at 443 nm or < 293 nm would be required.

J-State Mixing

An energy level diagram has been presented for a $^{40}\text{Ca}^+$ ion in the presence of an applied magnetic field (see figure 4.1). It was implied that these states, written in the $|L, S, J, m_J\rangle$ basis were the energy eigenstates of the system. The applied magnetic field B , would cause a linear shift of these energy levels given by

$$\Delta E_{\text{Zeeman}} = \mu_B g_J m_J B, \quad (5.1)$$

where $\mu_B = \frac{e\hbar}{2m_e}$ is the Bohr Magnetron and $g_J = 1 + \frac{J(J+1) - L(L+1) + S(S+1)}{2J(J+1)}$ is the Landé g-factor. Implicit in this treatment is the notion that the spin-orbit interaction causes L and S to couple to form J and whereas m_L and m_S are not good quantum numbers, m_J is. In terms of a hierarchy of perturbation the spin-orbit interaction is seen as strong and is treated first. The interaction with the B field is treated as a secondary, smaller perturbation.

However when the applied magnetic field is large a different coupling scheme is appropriate. Now L and S couple individually to the B field and m_L and m_S are good quantum numbers. In this scheme it is the spin-orbit interaction that must be treated as a smaller, secondary perturbation. The energy eigenstates of the system can then be written independently in the $|L, S, m_L, m_S\rangle$ basis and the field causes a linear shift of the energy levels given by

$$\Delta E_{\text{Paschen-Back}} = \mu_B (m_L + 2m_S) B. \quad (5.2)$$

We can always write $m_J = m_L + m_S$ as the components are all defined along the same axis so there is an inconsistency between equation 5.1 and equation 5.2. The energy eigenstates presented earlier must obviously be an approximation at low field. The energy of the states

must also not exactly follow equation 5.1. In this chapter a solution will be shown for the energy eigenvalues and eigenvectors of a $^{40}\text{Ca}^+$ ion for an applied magnetic field following the methods used in [74] and [75]. The solution is valid while the resulting splitting is much less than the energy difference between the S, P or D orbitals. We will then look at experimentally observable effects due to this change in eigenvalues and eigenvectors.

5.1 Calculation of the Energy Eigenvalues and Eigenstates of a $^{40}\text{Ca}^+$ Ion as a Function of Magnetic Field Strength

The outer electron in a $^{40}\text{Ca}^+$ ion has both an orbital and spin angular momentum and associated magnetic moments. These magnetic moments can interact with each other via the spin-orbit effect or they can each interact with an applied magnetic field via the Zeeman effect. The spin-orbit interaction can be thought of as the spin angular momentum of the electron interacting with the magnetic field created by the nucleus orbiting the electron (in the frame of the electron). This created magnetic field is proportional to the electron's orbital angular momentum so we have a term proportional to $\hat{L} \cdot \hat{S}$ which we write as

$$\begin{aligned}\hat{H}_{\text{Spin-Orbit}} &= f(r) \hat{L} \cdot \hat{S} \\ &= f(r) (\hat{J}^2 - \hat{L}^2 - \hat{S}^2),\end{aligned}\tag{5.3}$$

where $f(r)$ is dependent on the principle quantum number and orbital angular momentum quantum number (via the quantum defect) and can be found experimentally by measuring the fine-structure splitting at $B = 0$ if L , S and J are known.

The applied magnetic field does not interact equally with the electron's spin and orbital angular momentum. Relativistic quantum field theory can be used to show the interaction is approximately twice as strong in the case of the electron's spin. The interaction with the external magnetic field can be written as

$$\hat{H}_{\text{Zeeman}} = \frac{\mu_B}{\hbar} B (\hat{L}_z + 2\hat{S}_z),\tag{5.4}$$

where the magnetic field is applied along the z axis. The reason a single set of eigenfunctions cannot exist independently of B is related to this factor of 2. If the magnetic field interacted equally with the orbital and intrinsic angular momenta then we could write $\hat{J}_z = \hat{L}_z + \hat{S}_z$. As \hat{J}_z commutes with \hat{J}^2 , \hat{L}^2 and \hat{S}^2 the spin-orbit and Zeeman Hamiltonians would share a common set of eigenfunctions for all B . Instead we find that the eigenfunctions and corresponding eigenvalues are a function of B . We must find the

eigenfunctions, Ψ and eigenvalues, q that satisfy

$$\hat{H}\Psi = q\Psi, \quad (5.5)$$

where

$$\begin{aligned} \hat{H} &= \hat{H}_{\text{Spin-Orbit}} + \hat{H}_{\text{Zeeman}} \\ &= f(r) \left(\hat{J}^2 - \hat{L}^2 - \hat{S}^2 \right) + \frac{\mu_B}{\hbar} B \left(\hat{L}_z + 2\hat{S}_z \right). \end{aligned} \quad (5.6)$$

When an operator has a finite number of eigenfunctions it is often easier to use matrix notation. Here we write the eigenfunction of equation 5.5 as a vector, $[\Psi]$ whose elements, Ψ_n give the amplitudes of the states of a particular, chosen basis. The operator then becomes a matrix, $[H]$ whose elements, H_{nm} are

$$H_{nm} = \langle \Psi_n | \hat{H} | \Psi_m \rangle. \quad (5.7)$$

Our first task is thus to choose a basis and calculate the matrix elements using the Hamiltonian of equation 5.6 in this basis. There are two obvious choices for our basis states; either the eigenstates at zero applied field $|L, S, J, m_J\rangle$ or those in the limit of high applied field $|L, S, m_L, m_S\rangle$. In our system we are much closer to the zero field limit and so we will use the $|L, S, J, m_J\rangle$ states as shown in figure 4.1 as our basis states.

For the $L = 0$ states there is no spin-orbit interaction term in the Hamiltonian and the states will be pure eigenstates for all applied magnetic fields with energies given by equation 5.1. We will treat the $L = 1$ (P states) and $L = 2$ (D states) in separate eigenvalue equations.

Due to our choice of basis the spin-orbit part of the matrix elements is very easy to calculate. We can simply let the operators act and then use orthonormality. For clarity we shall drop the L and S quantum numbers when specifying the states but it is implied. We obtain

$$\begin{aligned} H_{(J,m_J),(J',m'_J),\text{spin-orbit}} &= \langle J, m_J | f(r) \left(\hat{J}^2 - \hat{L}^2 - \hat{S}^2 \right) | J', m'_J \rangle \\ &= \langle f(r) \rangle \hbar^2 \left[J'(J'+1) - L(L+1) - S(S+1) \right] \langle J, m_J | J', m'_J \rangle \\ &= \langle f(r) \rangle \hbar^2 \left[J'(J'+1) - l(l+1) - S(S+1) \right] \delta_{JJ'} \delta_{m_J m'_J}. \end{aligned} \quad (5.8)$$

The spin-orbit terms thus only contribute to the diagonal elements of the matrix and can be found by simple substitution of J , L and S . The natural basis to calculate the part of the matrix elements belonging to the Zeeman effect is $|m_L, m_S\rangle$. We must first transform into this basis before the matrix elements can be calculated. This is possible

via the Clebsch-Gordon coefficients, C_{J,m_J,m_L,m_S} which are defined as

$$|J, m_J\rangle = \sum_{m_L=-L, L} \sum_{m_S=-S, S} C_{J,m_J,m_L,m_S} |m_L, m_S\rangle. \quad (5.9)$$

The states $|m_L, m_S\rangle$ are eigenstates of the operators \hat{L}^2 , \hat{S}^2 , \hat{L}_z and \hat{S}_z . They are also obviously eigenstates of $\hat{J}_z = \hat{L}_z + \hat{S}_z$ with an eigenvalue $m_J = m_L + m_S$. For a given combination of L and S there are different combinations of m_L and m_S which add to give the required m_J . These different combinations will all be degenerate eigenstates of the system. By simple substitution into the eigenvalue equation (equation 5.5) it can be seen that any state that is a linear combination of degenerate eigenstates is also an eigenstate of the system. This linear combination is what is shown in equation 5.9. The job of the Clebsch-Gordon coefficients is to create a linear combination which is also an eigenstate of \hat{J}^2 . The sum is taken over all m_L and m_S , however the terms will only be non-zero for those combinations which sum to m_J . The Clebsch-Gordon coefficients can be readily calculated or are widely available in tables. So armed with our new tool we will seek to calculate the Zeeman part of the matrix elements. This is done by first applying the Clebsch-Gordon coefficients, then letting the operators \hat{L}_z and \hat{S}_z act and finally using orthonormality to obtain

$$\begin{aligned} H_{(J,m_J),(J',m'_J),\text{Zeeman}} &= \langle J, m_J | \frac{\mu_B}{\hbar} B (\hat{L}_z + 2\hat{S}_z) | J', m'_J \rangle \\ &= \frac{\mu_B}{\hbar} B \sum_{m_L, m_S} \sum_{m'_L, m'_S} C_{J,m_J,m_L,m_S}^* C_{J',m'_J,m'_L,m'_S} \\ &\quad * \langle m_L, m_S | (\hat{L}_z + 2\hat{S}_z) | m'_L, m'_S \rangle \\ &= \mu_B B \sum_{m_L, m_S} \sum_{m'_L, m'_S} C_{J,m_J,m_L,m_S}^* C_{J',m'_J,m'_L,m'_S} \\ &\quad * \langle m_L, m_S | (m'_L + 2m'_S) | m'_L, m'_S \rangle \\ &= \mu_B B \sum_{m_L, m_S} C_{J,m_J,m_L,m_S}^* C_{J',m'_J,m_L,m_S} \\ &\quad * (m_L + 2m_S). \end{aligned} \quad (5.10)$$

So we can obtain these parts of the matrix elements by simple substitution of the Clebsch-Gordon coefficients and the m_L and m_S quantum numbers. For the $L = 1, S = \frac{1}{2}$ and $L = 2, S = \frac{1}{2}$ cases we have 6×6 and 10×10 matrices respectfully. Thankfully the majority of the elements are zero. The full matrices are shown in figures 5.2 and 5.3. The ϵ_1 and ϵ_2 introduced here are used to describe the energy splitting due to the spin-orbit effect for the $L = 1$ and $L = 2$ states respectively. The magnitude of the splittings are $3\epsilon_1$ and

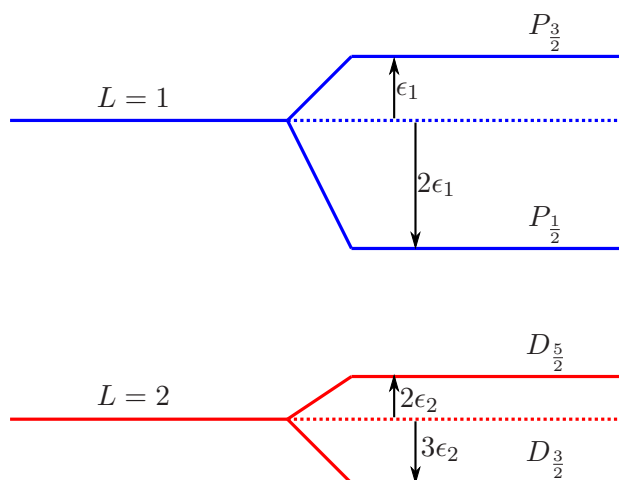


Figure 5.1: The P and D states prior and after the spin-orbit effect with $B = 0$.

$5\epsilon_2$ for the $L = 1$ and $L = 2$ states respectively. The splitting is however not symmetrical about the unperturbed state. The $P_{\frac{3}{2}}$ is ϵ_1 above the unperturbed state while the $P_{\frac{1}{2}}$ is $2\epsilon_1$ below the unperturbed state. The $D_{\frac{5}{2}}$ is $2\epsilon_2$ above the unperturbed state while the $D_{\frac{3}{2}}$ state is $3\epsilon_2$ below the unperturbed state. This is shown schematically in figure 5.1.

(J, m_J)	$(\frac{3}{2}, +\frac{3}{2})$	$(\frac{3}{2}, +\frac{1}{2})$	$(\frac{3}{2}, -\frac{1}{2})$	$(\frac{3}{2}, -\frac{3}{2})$	$(\frac{1}{2}, +\frac{1}{2})$	$(\frac{1}{2}, -\frac{1}{2})$
$(\frac{3}{2}, +\frac{3}{2})$	$\epsilon_1 + 2\mu_B B$	0	0	0	0	0
$(\frac{3}{2}, +\frac{1}{2})$	0	$\epsilon_1 + \frac{2}{3}\mu_B B$	0	0	$-\frac{\sqrt{2}}{3}\mu_B B$	0
$(\frac{3}{2}, -\frac{1}{2})$	0	0	$\epsilon_1 - \frac{2}{3}\mu_B B$	0	0	$-\frac{\sqrt{2}}{3}\mu_B B$
$(\frac{3}{2}, -\frac{3}{2})$	0	0	0	$\epsilon_1 - 2\mu_B B$	0	0
$(\frac{1}{2}, +\frac{1}{2})$	0	$-\frac{\sqrt{2}}{3}\mu_B B$	0	0	$-2\epsilon_1 + \frac{1}{3}\mu_B B$	0
$(\frac{1}{2}, -\frac{1}{2})$	0	0	$-\frac{\sqrt{2}}{3}\mu_B B$	0	0	$-2\epsilon_1 - \frac{1}{3}\mu_B B$

Figure 5.2: Operator in matrix notation for the spin-orbit and Zeeman Hamiltonian for $L = 1$ in the $|J, m_J\rangle$ basis states.

(J, m_J)	$(\frac{5}{2}, +\frac{5}{2})$	$(\frac{5}{2}, +\frac{3}{2})$	$(\frac{5}{2}, +\frac{1}{2})$	$(\frac{5}{2}, -\frac{1}{2})$	$(\frac{5}{2}, -\frac{3}{2})$	$(\frac{5}{2}, -\frac{5}{2})$	$(\frac{3}{2}, +\frac{3}{2})$	$(\frac{3}{2}, +\frac{1}{2})$	$(\frac{3}{2}, -\frac{1}{2})$	$(\frac{3}{2}, -\frac{3}{2})$
$(\frac{5}{2}, +\frac{5}{2})$	$2\epsilon_2 + 3\mu_B B$	0	0	0	0	0	0	0	0	0
$(\frac{5}{2}, +\frac{3}{2})$	0	$2\epsilon_2 + \frac{9}{5}\mu_B B$	0	0	0	0	$-\frac{2}{5}\mu_B B$	0	0	0
$(\frac{5}{2}, +\frac{1}{2})$	0	0	$2\epsilon_2 + \frac{3}{5}\mu_B B$	0	0	0	0	$-\frac{\sqrt{6}}{5}\mu_B B$	0	0
$(\frac{5}{2}, -\frac{1}{2})$	0	0	0	$2\epsilon_2 - \frac{3}{5}\mu_B B$	0	0	0	0	$-\frac{\sqrt{6}}{5}\mu_B B$	0
$(\frac{5}{2}, -\frac{3}{2})$	0	0	0	0	$2\epsilon_2 - \frac{9}{5}\mu_B B$	0	0	0	0	$-\frac{2}{5}\mu_B B$
$(\frac{5}{2}, -\frac{5}{2})$	0	0	0	0	0	$2\epsilon_2 - 3\mu_B B$	0	0	0	0
$(\frac{3}{2}, +\frac{3}{2})$	0	$-\frac{2}{5}\mu_B B$	0	0	0	0	$-3\epsilon_2 + \frac{6}{5}\mu_B B$	0	0	0
$(\frac{3}{2}, +\frac{1}{2})$	0	0	$-\frac{\sqrt{6}}{5}\mu_B B$	0	0	0	0	$-3\epsilon_2 + \frac{2}{5}\mu_B B$	0	0
$(\frac{3}{2}, -\frac{1}{2})$	0	0	0	$-\frac{\sqrt{6}}{5}\mu_B B$	0	0	0	0	$-3\epsilon_2 - \frac{2}{5}\mu_B B$	0
$(\frac{3}{2}, -\frac{3}{2})$	0	0	0	0	$-\frac{2}{5}\mu_B B$	0	0	0	0	$-3\epsilon_2 - \frac{6}{5}\mu_B B$

Figure 5.3: Operator in matrix notation for the spin-orbit and Zeeman Hamiltonian for $L = 2$ in the $|J, m_J\rangle$ basis states.

The eigenvalue equation (equation 5.5) needs to be solved using each of these matrices together with their corresponding eigenvectors in our chosen basis. It follows from the nature of the matrices that it is only pairs of levels are mixed. This means that each matrix can be broken down into a number of 2×2 matrices and solved for the eigenvalues and eigenvectors individually.

We find that states with the same L and m_J become mixed. The eigenstates are now superpositions of the two states. As would be expected the magnitude of the mixing of $|J, m_J\rangle$ into $|J \pm 1, m_J\rangle$ is the same as that from $|J \pm 1, m_J\rangle$ into $|J, m_J\rangle$. There is however a negative sign between the two different wavefunctions. This sign has been written explicitly in the following expressions so that A_{L, m_J} and B_{L, m_J} are positive for all B . The $L = 0$ states are unchanged,

$$\begin{aligned} \left| S_{\frac{1}{2}}, +\frac{1}{2} \right\rangle &\rightarrow S1_{+\frac{1}{2}} = \left| S_{\frac{1}{2}}, +\frac{1}{2} \right\rangle \\ \left| S_{\frac{1}{2}}, -\frac{1}{2} \right\rangle &\rightarrow S1_{-\frac{1}{2}} = \left| S_{\frac{1}{2}}, -\frac{1}{2} \right\rangle. \end{aligned} \quad (5.11)$$

The $L = 1$ states become

$$\begin{aligned} \left| P_{\frac{3}{2}}, +\frac{3}{2} \right\rangle &\rightarrow P2_{+\frac{3}{2}} = \left| P_{\frac{3}{2}}, +\frac{3}{2} \right\rangle \\ \left| P_{\frac{3}{2}}, +\frac{1}{2} \right\rangle &\rightarrow P2_{+\frac{1}{2}} = A_{1, +\frac{1}{2}} \left| P_{\frac{3}{2}}, +\frac{1}{2} \right\rangle - B_{1, +\frac{1}{2}} \left| P_{\frac{1}{2}}, +\frac{1}{2} \right\rangle \\ \left| P_{\frac{3}{2}}, -\frac{1}{2} \right\rangle &\rightarrow P2_{-\frac{1}{2}} = A_{1, -\frac{1}{2}} \left| P_{\frac{3}{2}}, -\frac{1}{2} \right\rangle - B_{1, -\frac{1}{2}} \left| P_{\frac{1}{2}}, -\frac{1}{2} \right\rangle \\ \left| P_{\frac{3}{2}}, -\frac{3}{2} \right\rangle &\rightarrow P2_{-\frac{3}{2}} = \left| P_{\frac{3}{2}}, -\frac{3}{2} \right\rangle \\ \\ \left| P_{\frac{1}{2}}, +\frac{1}{2} \right\rangle &\rightarrow P1_{+\frac{1}{2}} = A_{1, +\frac{1}{2}} \left| P_{\frac{1}{2}}, +\frac{1}{2} \right\rangle + B_{1, +\frac{1}{2}} \left| P_{\frac{3}{2}}, +\frac{1}{2} \right\rangle \\ \left| P_{\frac{1}{2}}, -\frac{1}{2} \right\rangle &\rightarrow P1_{-\frac{1}{2}} = A_{1, -\frac{1}{2}} \left| P_{\frac{1}{2}}, -\frac{1}{2} \right\rangle + B_{1, -\frac{1}{2}} \left| P_{\frac{3}{2}}, -\frac{1}{2} \right\rangle. \end{aligned} \quad (5.12)$$

The $L = 2$ states become

$$\begin{aligned}
\left| D_{\frac{5}{2}}, +\frac{5}{2} \right\rangle &\rightarrow D2_{+\frac{5}{2}} = \left| D_{\frac{5}{2}}, +\frac{5}{2} \right\rangle \\
\left| D_{\frac{5}{2}}, +\frac{3}{2} \right\rangle &\rightarrow D2_{+\frac{3}{2}} = A_{2,+\frac{3}{2}} \left| D_{\frac{5}{2}}, +\frac{3}{2} \right\rangle - B_{2,+\frac{3}{2}} \left| D_{\frac{3}{2}}, +\frac{3}{2} \right\rangle \\
\left| D_{\frac{5}{2}}, +\frac{1}{2} \right\rangle &\rightarrow D2_{+\frac{1}{2}} = A_{2,+\frac{1}{2}} \left| D_{\frac{5}{2}}, +\frac{1}{2} \right\rangle - B_{2,+\frac{1}{2}} \left| D_{\frac{3}{2}}, +\frac{1}{2} \right\rangle \\
\left| D_{\frac{5}{2}}, -\frac{1}{2} \right\rangle &\rightarrow D2_{-\frac{1}{2}} = A_{2,-\frac{1}{2}} \left| D_{\frac{5}{2}}, -\frac{1}{2} \right\rangle - B_{2,-\frac{1}{2}} \left| D_{\frac{3}{2}}, -\frac{1}{2} \right\rangle \\
\left| D_{\frac{5}{2}}, -\frac{3}{2} \right\rangle &\rightarrow D2_{-\frac{3}{2}} = A_{2,-\frac{3}{2}} \left| D_{\frac{5}{2}}, -\frac{3}{2} \right\rangle - B_{2,-\frac{3}{2}} \left| D_{\frac{3}{2}}, -\frac{3}{2} \right\rangle \\
\left| D_{\frac{5}{2}}, -\frac{5}{2} \right\rangle &\rightarrow D2_{-\frac{5}{2}} = \left| D_{\frac{5}{2}}, -\frac{5}{2} \right\rangle \\
\left| D_{\frac{3}{2}}, +\frac{3}{2} \right\rangle &\rightarrow D1_{+\frac{3}{2}} = A_{2,+\frac{3}{2}} \left| D_{\frac{3}{2}}, +\frac{3}{2} \right\rangle + B_{2,+\frac{3}{2}} \left| D_{\frac{5}{2}}, +\frac{3}{2} \right\rangle \\
\left| D_{\frac{3}{2}}, +\frac{1}{2} \right\rangle &\rightarrow D1_{+\frac{1}{2}} = A_{2,+\frac{1}{2}} \left| D_{\frac{3}{2}}, +\frac{1}{2} \right\rangle + B_{2,+\frac{1}{2}} \left| D_{\frac{5}{2}}, +\frac{1}{2} \right\rangle \\
\left| D_{\frac{3}{2}}, -\frac{1}{2} \right\rangle &\rightarrow D1_{-\frac{1}{2}} = A_{2,-\frac{1}{2}} \left| D_{\frac{3}{2}}, -\frac{1}{2} \right\rangle + B_{2,-\frac{1}{2}} \left| D_{\frac{5}{2}}, -\frac{1}{2} \right\rangle \\
\left| D_{\frac{3}{2}}, -\frac{3}{2} \right\rangle &\rightarrow D1_{-\frac{3}{2}} = A_{2,-\frac{3}{2}} \left| D_{\frac{3}{2}}, -\frac{3}{2} \right\rangle + B_{2,-\frac{3}{2}} \left| D_{\frac{5}{2}}, -\frac{3}{2} \right\rangle.
\end{aligned} \tag{5.13}$$

We have introduced the new notation $L\#_{m_J}$ to name the new states which don't have J as a good quantum number anymore. The number $\# = 1, 2$ is used to keep track of the value of J the state possesses at $B = 0$ and will be required later.

We can write these wavefunctions in the form

$$|J, m_J\rangle \rightarrow N_{L,m_J} (|J, m_J\rangle \pm M_{L,m_J} |J \pm 1, m_J\rangle), \tag{5.14}$$

where N_{L,m_J} and M_{L,m_J} are thought of as normalisation and mixing coefficients respectively and $N_{L,m_J} = \left(1 + M_{L,m_J}^2\right)^{-\frac{1}{2}}$. This has been done as A_{L,m_J} and B_{L,m_J} are reasonably complicated and for small B the normalisation coefficient, $N_{L,m_J} \approx 1$ and thus can

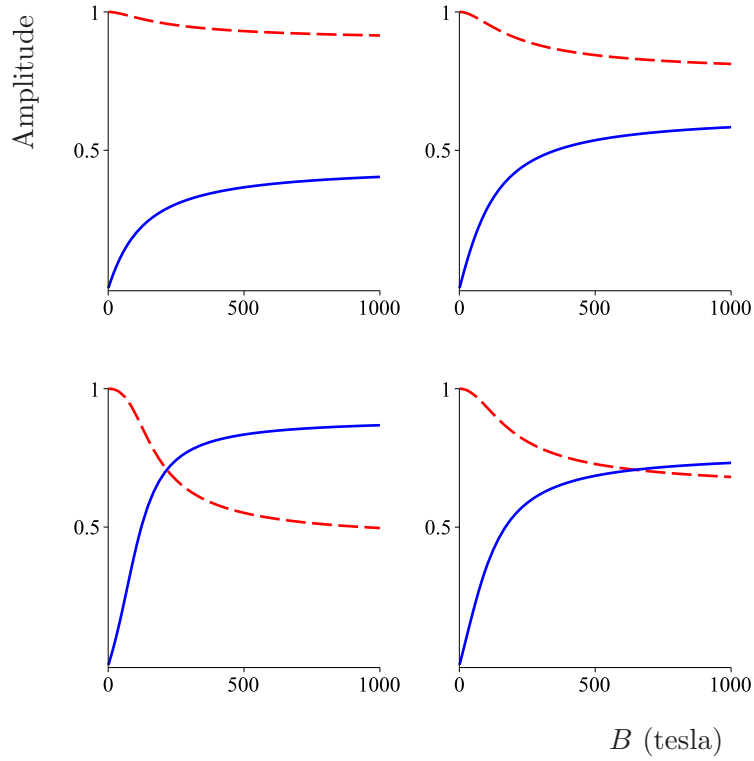


Figure 5.4: The amplitude of the original (N_{2,m_J}) and mixed ($N_{2,m_J}M_{2,m_J}$) parts of the wavefunctions of the D orbital states (dashed and solid lines respectively). Clockwise from top-left the plots correspond to $m_J = +\frac{3}{2}, +\frac{1}{2}, -\frac{1}{2}$ and $-\frac{3}{2}$.

be omitted. The mixing coefficients are

$$\begin{aligned}
 M_{1,\pm\frac{1}{2}} &= \frac{\pm 2\sqrt{2}\mu_B B}{\pm 9\epsilon_1 + \mu_B B \pm 3\sqrt{9\epsilon_1^2 \pm 2\epsilon_1\mu_B B + \mu_B^2 B^2}} \\
 M_{2,\pm\frac{1}{2}} &= \frac{\pm 2\sqrt{6}\mu_B B}{\pm 25\epsilon_2 + \mu_B B \pm 5\sqrt{25\epsilon_2^2 \pm 2\epsilon_2\mu_B B + \mu_B^2 B^2}} \\
 M_{2,\pm\frac{3}{2}} &= \frac{\pm 4\mu_B B}{\pm 25\epsilon_2 + 3\mu_B B \pm 5\sqrt{25\epsilon_2^2 \pm 6\epsilon_2\mu_B B + \mu_B^2 B^2}}.
 \end{aligned} \tag{5.15}$$

The equations for the mixings are quite complicated and so visual representation of the states is shown in figures 5.4 and 5.5 for the D and P states respectively.

We now wish to find the eigenvalues of the system. The S states do not have a spin-orbit term and so their energies evolve linearly with an applied magnetic field as given by

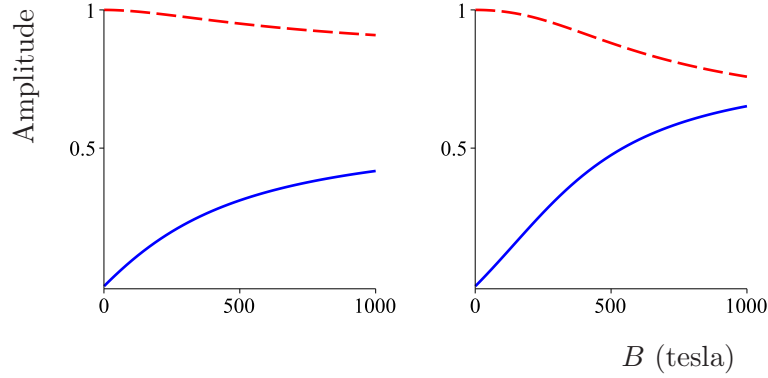


Figure 5.5: The amplitude of the original (N_{1,m_J}) and mixed ($N_{1,m_J}M_{1,m_J}$) parts of the wavefunctions of the P orbital states (dashed and solid lines respectively). The left, right plot is for the $m_J = +\frac{1}{2}$, $-\frac{1}{2}$ state respectively.

equation 5.1

$$\begin{aligned} E_{S1_{+\frac{1}{2}}} &= \mu_B B \\ E_{S1_{-\frac{1}{2}}} &= -\mu_B B. \end{aligned} \tag{5.16}$$

For the other states the eigenvalue equation (equation 5.5) needs to be solved for the eigenvalues corresponding to the eigenstates of equation 5.15. We find the P state eigenvalues to to be

$$\begin{aligned} E_{P2_{+\frac{3}{2}}} &= \epsilon_1 + 2\mu_B B \\ E_{P2_{+\frac{1}{2}}} &= -\frac{\epsilon_1}{2} + \frac{\mu_B B}{2} + \frac{1}{2}\sqrt{9\epsilon_1^2 + 2\epsilon_1\mu_B B + \mu_B^2 B^2} \\ E_{P2_{-\frac{1}{2}}} &= -\frac{\epsilon_1}{2} - \frac{\mu_B B}{2} + \frac{1}{2}\sqrt{9\epsilon_1^2 - 2\epsilon_1\mu_B B + \mu_B^2 B^2} \\ E_{P2_{-\frac{3}{2}}} &= \epsilon_1 - 2\mu_B B \\ E_{P1_{+\frac{1}{2}}} &= -\frac{\epsilon_1}{2} + \frac{\mu_B B}{2} - \frac{1}{2}\sqrt{9\epsilon_1^2 + 2\epsilon_1\mu_B B + \mu_B^2 B^2} \\ E_{P1_{-\frac{1}{2}}} &= -\frac{\epsilon_1}{2} - \frac{\mu_B B}{2} - \frac{1}{2}\sqrt{9\epsilon_1^2 - 2\epsilon_1\mu_B B + \mu_B^2 B^2}. \end{aligned} \tag{5.17}$$

The D state eigenvalues were found to be

$$\begin{aligned}
E_{D2+\frac{5}{2}} &= 2\epsilon_2 + 3\mu_B B \\
E_{D2+\frac{3}{2}} &= -\frac{\epsilon_2}{2} + \frac{3}{2}\mu_B B + \frac{1}{2}\sqrt{25\epsilon_2^2 + 6\epsilon_2\mu_B B + \mu_B^2 B^2} \\
E_{D2+\frac{1}{2}} &= -\frac{\epsilon_2}{2} + \frac{1}{2}\mu_B B + \frac{1}{2}\sqrt{25\epsilon_2^2 + 2\epsilon_2\mu_B B + \mu_B^2 B^2} \\
E_{D2-\frac{1}{2}} &= -\frac{\epsilon_2}{2} - \frac{1}{2}\mu_B B + \frac{1}{2}\sqrt{25\epsilon_2^2 - 2\epsilon_2\mu_B B + \mu_B^2 B^2} \\
E_{D2-\frac{3}{2}} &= -\frac{\epsilon_2}{2} - \frac{3}{2}\mu_B B + \frac{1}{2}\sqrt{25\epsilon_2^2 - 6\epsilon_2\mu_B B + \mu_B^2 B^2} \\
E_{D2-\frac{5}{2}} &= 2\epsilon_2 - 3\mu_B B \\
\\
E_{D1+\frac{3}{2}} &= -\frac{\epsilon_2}{2} + \frac{3}{2}\mu_B B - \frac{1}{2}\sqrt{25\epsilon_2^2 + 6\epsilon_2\mu_B B + \mu_B^2 B^2} \\
E_{D1+\frac{1}{2}} &= -\frac{\epsilon_2}{2} + \frac{1}{2}\mu_B B - \frac{1}{2}\sqrt{25\epsilon_2^2 + 2\epsilon_2\mu_B B + \mu_B^2 B^2} \\
E_{D1-\frac{1}{2}} &= -\frac{\epsilon_2}{2} - \frac{1}{2}\mu_B B - \frac{1}{2}\sqrt{25\epsilon_2^2 - 2\epsilon_2\mu_B B + \mu_B^2 B^2} \\
E_{D1-\frac{3}{2}} &= -\frac{\epsilon_2}{2} - \frac{3}{2}\mu_B B - \frac{1}{2}\sqrt{25\epsilon_2^2 - 6\epsilon_2\mu_B B + \mu_B^2 B^2}.
\end{aligned} \tag{5.18}$$

The energies of the states as a function of B are plotted in figure 5.6. At a magnetic field of 1000 tesla the system is effectively in the high field limit. Here some of the states become degenerate such that there are 5 different state energies in the P orbital and 7 in the D orbital. Equation 5.2 shows the energy of the states have a factor $m_L + 2m_S$. Using this we can write down the states. From the top to bottom in the high field limit of figure 5.6 the P states are (m_L, m_S) : $(1, \frac{1}{2})$, $(0, \frac{1}{2})$, $\{(1, -\frac{1}{2}), (-1, \frac{1}{2})\}$ (degenerate), $(0, -\frac{1}{2})$ and $(-1, -\frac{1}{2})$. The D states are $(2, \frac{1}{2})$, $(1, \frac{1}{2})$, $\{(0, \frac{1}{2}), (2, -\frac{1}{2})\}$, $\{(1, -\frac{1}{2}), (-1, \frac{1}{2})\}$, $\{(-2, \frac{1}{2}), (0, -\frac{1}{2})\}$, $(-1, -\frac{1}{2})$ and $(-2, -\frac{1}{2})$.

The expressions for the eigenvalues given in equations 5.17 and 5.18 provide the energy of a state relative to the energy the state would have prior to spin-orbit coupling at $B = 0$. Ideally we would like all of the ion's energy levels relative to one reference point which we will choose as the $S_{\frac{1}{2}}$ state energy at $B = 0$ ⁱ. The link between the different L states is the experimentally measured $B = 0$ energy states. The state energies relative to the

ⁱThese energies will be required in the calculation of the $D_{\frac{5}{2}}$ shelving rate in the next section.

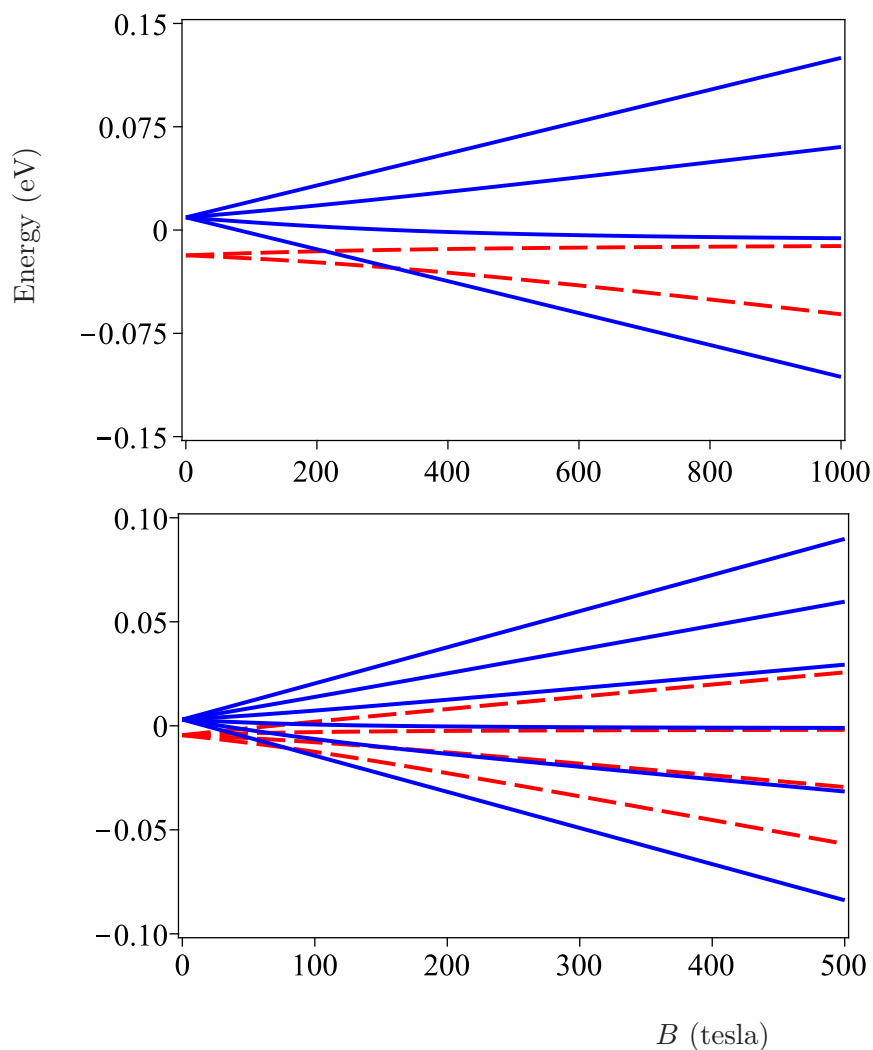


Figure 5.6: The eigenvalues of the P (top) and D (bottom) states as a function of applied field. The energy plotted is relative to the $B = 0$ situation, with no spin-orbit coupling. Note the different scale for B in the two plots. In the case of the P states the blue, solid lines and the red, dashed lines represent the states with $J = 3/2$ and $J = 1/2$ at $B = 0$ respectively. In the case of the D states the blue, solid lines and the red, dashed lines represent the states with $J = 5/2$ and $J = 3/2$ at $B = 0$ respectively.

$S_{\frac{1}{2}}$ state ($B = 0$) are (via figure 5.1)

$$\begin{aligned}
E'_{S1m_J} &= E_{S1m_J} \\
E'_{P1m_J} &= E_{P_{\frac{1}{2}}}(B = 0) + 2\epsilon_1 + E_{P1m_J} \\
E'_{P2m_J} &= E_{P_{\frac{3}{2}}}(B = 0) - \epsilon_1 + E_{P2m_J} \\
E'_{D1m_J} &= E_{D_{\frac{3}{2}}}(B = 0) + 3\epsilon_2 + E_{D1m_J} \\
E'_{D2m_J} &= E_{D_{\frac{5}{2}}}(B = 0) - 2\epsilon_2 + E_{D2m_J},
\end{aligned} \tag{5.19}$$

where $E_{Lm_J}(B = 0)$ are the experimentally determined energies of the ion's states at zero applied magnetic field.

5.2 J-State Mixing - An Observable Effect

We have seen how the states shown in figure 4.1 were only low magnetic field approximations of the actual electronic states of our ion. The approximation is however a very good one. At our trapping field of ≈ 1 tesla the maximum amplitude of the mixing is only 0.0038. The eigenvalues are different from those caused by a linear Zeeman shift by < 300 kHz at 1 tesla. This small shift would not be noticed on the dipole transitions which have linewidths of ≈ 20 MHz. It would be possible to see a shift in principle on the $S_{\frac{1}{2}} \rightarrow D_{\frac{5}{2}}$ quadrupole transition but it would have no experimental consequences once the transition had been found. There is however a remarkably clear effect of the J-state mixing which will now be described.

Quantum jumps occur when the ion goes into a metastable state which is not part of the cycle from which the signal is being observed. No light is observed until it is repumped back out of the state or if it finally spontaneously decays. There are two possible metastable states in the $^{40}\text{Ca}^+$ ion. These are the two D states - $D_{\frac{3}{2}}$ and $D_{\frac{5}{2}}$ which have lifetimes of ~ 1 s. During Doppler cooling the ion can readily spontaneously decay into the $D_{\frac{3}{2}}$ state from the $P_{\frac{1}{2}}$ state with a probability of $\approx \frac{1}{15.4}$ [53]. Thus to be able to Doppler cool (scattering more than ≈ 15 photons) efficient repumping from the $D_{\frac{3}{2}}$ level is required. This is achieved with a single 866 nm laser in an RF trap and four 866 nm lasers in a Penning trap to address each of the m_J sub-levels. The ion cannot get into the $D_{\frac{5}{2}}$ level during the cooling cycle as the $P_{\frac{1}{2}} \rightarrow D_{\frac{5}{2}}$ transition is strongly forbidden. The only way the ion could possibly get into this state is from spontaneous emission via the $P_{\frac{3}{2}}$ state. There is no laser to resonantly excite the ion up into the $P_{\frac{3}{2}}$ state. The gain profile of the 866 nm lasers does however extend down to the 850 nm required to excite up to the $P_{\frac{3}{2}}$ state and so amplified-spontaneous-emission at this wavelength will

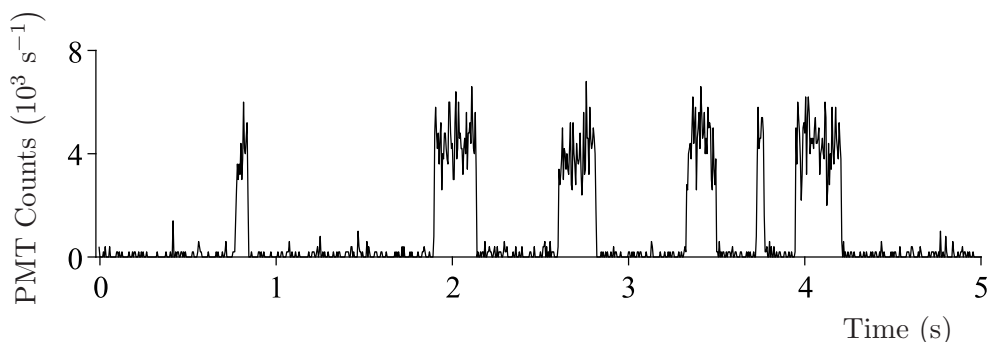


Figure 5.7: PMT signal when there is no 854 nm beam to repump the $D_{\frac{5}{2}}$ state.

be present. A filter (Thorlabs FB870-10) has been placed in the beam to remove more than 99% of this light. The filter also removes $\approx 99\%$ of any 854 nm light which would repump the $D_{\frac{5}{2}}$ state. A filter (Semrock FF01-406/15-25) was also placed in the 397 nm beam to remove light at 393 nm which could excite the ion up to the $D_{\frac{3}{2}}$ state. So during our standard Doppler cooling process we would expect not to see any quantum jumps in our system and in the case of the RF trap this is indeed the case. There is however a marked difference when we move to the Penning trap. An example of the signal seen from the ion at 1 tesla is shown in figure 5.7. It is seen that the ion is dark the majority of the time, staying bright for periods < 1 sⁱⁱ. When B was decreased fewer quantum jumps were seen.

As the $D_{\frac{5}{2}}$ state is the only metastable state which we are not repumping, the ion must be getting into this state. So how is our ion getting shelved? The clue is the increase in quantum jumps as the applied magnetic field increases and the answer lies within the J-state mixing which we have described. Using our calculated states we will solve for the probability of decaying from the $P_{\frac{1}{2}}$ to the $D_{\frac{5}{2}}$ as a function of magnetic field strength.

The number of 397 nm photons emitted during the cooling cycle before the ion is shelved into the metastable state at a certain magnetic field is given by

$$n = \frac{\Gamma(P1 \rightarrow S1)}{\Gamma(P1 \rightarrow D2)}, \quad (5.20)$$

where Γ is a transition rate - a probability per unit time of the transition occurring. We ignore transitions down to the $D_{\frac{3}{2}}$ states as these are being efficiently repumped. We are expecting the number of photons emitted to decrease as B increases so a more natural

ⁱⁱWhen the filters are not used quantum jumps are seen even in both the RF and Penning traps. The jumps are shorter than the $D_{\frac{5}{2}}$ state lifetime due to the 854 nm light which repumps out of the state.

variable to calculate would be the inverse of this given by

$$n^{-1} = \frac{\Gamma(P1 \rightarrow D2)}{\Gamma(P1 \rightarrow S1)}. \quad (5.21)$$

In the first stage of the cooling cycle the ion is excited up to either the $P1_{+\frac{1}{2}}$ or $P1_{-\frac{1}{2}}$ state with equal probability. We thus average over these initial states as the ion will be in each of these states half the time

$$n^{-1} = \frac{\Gamma\left(P1_{+\frac{1}{2}} \rightarrow D2\right) + \Gamma\left(P1_{-\frac{1}{2}} \rightarrow D2\right)}{\Gamma\left(P1_{+\frac{1}{2}} \rightarrow S1\right) + \Gamma\left(P1_{-\frac{1}{2}} \rightarrow S1\right)}. \quad (5.22)$$

The total transition rate is the sum over the transition rates to the individual m_J sub-levels. Using the selection rule $\Delta m_J = 0, \pm 1$ we obtain

$$n^{-1} = \frac{\sum_{m_J=-\frac{1}{2}}^{+\frac{3}{2}} \Gamma\left(P1_{+\frac{1}{2}} \rightarrow D2_{m_J}\right) + \sum_{m_J=-\frac{3}{2}}^{+\frac{1}{2}} \Gamma\left(P1_{-\frac{1}{2}} \rightarrow D2_{m_J}\right)}{\sum_{m_J=-\frac{1}{2}}^{+\frac{1}{2}} \Gamma\left(P1_{+\frac{1}{2}} \rightarrow S1_{m_J}\right) + \sum_{m_J=-\frac{1}{2}}^{+\frac{1}{2}} \Gamma\left(P1_{-\frac{1}{2}} \rightarrow S1_{m_J}\right)}. \quad (5.23)$$

We can write Fermi's golden rule for an atomic dipole transition from state ψ_1 to state ψ_2 as [76]

$$\Gamma(\psi_1 \rightarrow \psi_2) = \frac{4}{3\hbar c^3} \omega_{\psi_1 \rightarrow \psi_2}^3 |\langle \psi_2 | \underline{d} | \psi_1 \rangle|^2. \quad (5.24)$$

If we apply this to each of the terms individually in equation 5.23 we obtain

$$n^{-1} = \frac{\sum_{m_J=-\frac{1}{2}}^{+\frac{3}{2}} \omega_{\left(P1_{+\frac{1}{2}} \rightarrow D2_{m_J}\right)}^3 \left| \langle D2_{m_J} | \underline{d} | P1_{+\frac{1}{2}} \rangle \right|^2 + \sum_{m_J=-\frac{3}{2}}^{+\frac{1}{2}} \omega_{\left(P1_{-\frac{1}{2}} \rightarrow D2_{m_J}\right)}^3 \left| \langle D2_{m_J} | \underline{d} | P1_{-\frac{1}{2}} \rangle \right|^2}{\sum_{m_J=-\frac{1}{2}}^{+\frac{1}{2}} \omega_{\left(P1_{+\frac{1}{2}} \rightarrow S1_{m_J}\right)}^3 \left| \langle S1_{m_J} | \underline{d} | P1_{+\frac{1}{2}} \rangle \right|^2 + \sum_{m_J=-\frac{1}{2}}^{+\frac{1}{2}} \omega_{\left(P1_{-\frac{1}{2}} \rightarrow S1_{m_J}\right)}^3 \left| \langle S1_{m_J} | \underline{d} | P1_{-\frac{1}{2}} \rangle \right|^2}. \quad (5.25)$$

For each of the four terms in this equation we first substitute in the mixed states previously calculated and then multiply out. We neglect terms which are not dipole allowed transitions (where $\Delta J = 2$). The expressions are quite complicated and so are shown in an appendix (appendix A). For example the $P1_{+\frac{1}{2}} \rightarrow D2_{m_J}$ term becomes the first part of equation A.2 where the variables a_{m_J, m'_J} , b_{m_J, m'_J} and c_{m_J, m'_J} are products of the mixing and normalisations of equation 5.14 and are thus functions of the applied magnetic field.

These variables are defined in the appendix (equation A.1).

We now have non-zero electric dipole matrix elements and thus can readily see paths for which our ion can become shelved in the $D_{\frac{5}{2}}$ state. To calculate the shelving rate we must link to experimentally measured or theoretically calculated transition rates. Transition rates between individual sub-levels are rarely observed or calculated. It is more usual to find a total rate between levels. The Wigner-Eckart theorem enables these total transition rates to be calculated. The Wigner-Eckart theorem for an electric dipole transition can be stated as

$$\langle J, m_J | \underline{d} | J', m'_J \rangle = \langle J || \underline{d} || J' \rangle \frac{\langle J', 1, m'_J, \Delta m_J | J', 1, J, m_J \rangle}{\sqrt{2J+1}}. \quad (5.26)$$

On the left we have a full matrix element between fully specified states. On the right we have a reduced matrix element whose angular part has been absorbed into a Clebsch-Gordon coefficient divided by the number of sub-levels of the final state. We apply this to each term in the first part of equation A.2 to obtain the second part. Using the same method for the $P1_{-\frac{1}{2}} \rightarrow D2_{m_J}$ term we can obtain equation A.3. Similarly for the $P1_{+\frac{1}{2}} \rightarrow S_{m_J}$ and $P1_{-\frac{1}{2}} \rightarrow S_{m_J}$ terms we obtain equations A.4 and A.5 respectively.

The transition frequencies present in these equations are readily found from the eigenvalues calculated earlier (equations 5.16, 5.17 and 5.18) converting the energies to be relative to the ground state via equations 5.19. Fortunately the reduced matrix elements have been theoretically calculated using many-body perturbation theory [53]. Those which have had semi-empirical corrections made were used. They are (in arbitrary units)ⁱⁱⁱ

$$\begin{aligned} \langle S_{\frac{1}{2}} || \underline{d} || P_{\frac{1}{2}} \rangle &= 2.890 \\ \langle S_{\frac{1}{2}} || \underline{d} || P_{\frac{3}{2}} \rangle &= 4.088 \\ \langle D_{\frac{3}{2}} || \underline{d} || P_{\frac{1}{2}} \rangle &= 2.373 \\ \langle D_{\frac{3}{2}} || \underline{d} || P_{\frac{3}{2}} \rangle &= 1.059 \\ \langle D_{\frac{5}{2}} || \underline{d} || P_{\frac{3}{2}} \rangle &= 3.186. \end{aligned} \quad (5.27)$$

Calculating all of the terms we can plot n^{-1} as a function of magnetic field (figure 5.8). It is seen that the probability of the ion going into the $D_{\frac{5}{2}}$ state increases until $B \approx 300$ tesla when the probability decreases and then levels off. This leveling off is expected as the probability of spontaneous emission to the $D_{\frac{5}{2}}$ state should never be higher than the

ⁱⁱⁱNote that these reduced matrix elements can be used to find the P state to D state branching ratios. The reduced matrix elements are substituted into Fermi's golden rule together with the relevant transition frequency ratios.

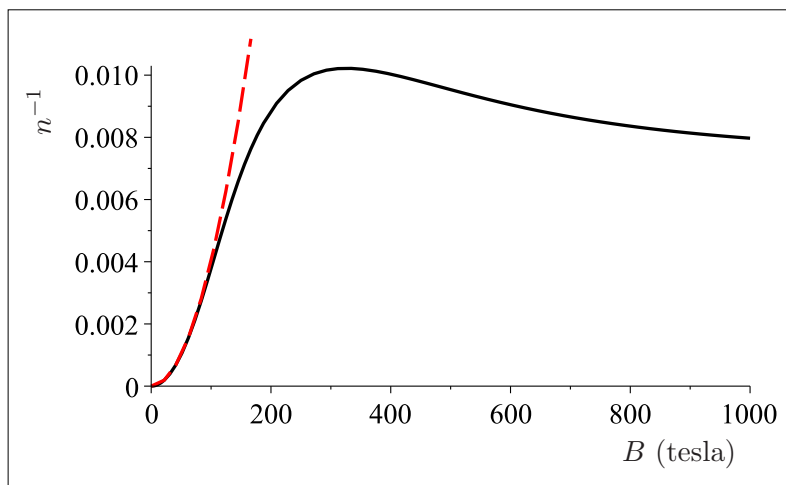


Figure 5.8: n^{-1} as a function of applied magnetic field. The red dashed line is a fit at low fields, $n^{-1} = 4.03 \times 10^{-7} B^2$.

branching ratio to the $D_{\frac{3}{2}}$ state at zero magnetic field. A fit performed shows that $n^{-1} = 4.03 \times 10^{-7} B^2$ is a good approximation at low fields.

It will be seen that this theoretical dependency on B is in agreement with what we see experimentally. The approach taken here to calculate the dependence differs from that used in the publication of the following experiment [10]. First-order perturbation theory was used to calculate the mixing which was found to be linear with B . This then led to finding the $n_{\text{detected}}^{-1} \propto B^2$ dependence ^{iv}.

5.3 J-State Mixing - Experiment

An experiment was performed to observe the $D_{\frac{5}{2}}$ shelving rate of a single $^{40}\text{Ca}^+$ ion as a function of B to test the predicted B^2 dependence. The experiment was performed in the PCB trap described in § 4.3.2. The trap was run as a combined trap where both DC and RF voltages are placed on the trap electrodes as well as a trapping magnetic field (§ 2.3). A combined trap was used because our Penning trap has been found to only be stable above ≈ 0.6 tesla and so a larger range of magnetic fields could be achieved. The RF was always used at all B so any systematic effects due to it would not influence the resulting trend. Two 397 nm lasers were used for the Doppler cooling transition and four 866 nm lasers were used for repumping the $D_{\frac{3}{2}}$ state. Their laser wavelengths were

^{iv}There is $\approx 3\%$ discrepancy between the results. This is attributed to the approximations used in the calculation using perturbation theory including the fine structure frequency splitting being much smaller than the orbital splitting.

manually changed to follow the transitions as the magnetic field was stepped. Sometimes the same ion was trapped as the magnetic field was changed, occasionally however the ion was lost and another was reloaded. This experiment was conducted before the optical table was updated and before the new scanning cavity lock was introduced. The lasers were thus locked using side-of-fringe locks to reference cavities (§ 4.2.3 and reference [51]). Photoionisation (§ 4.4.3) was also not yet available and so the calcium atoms were ionised using a beam of electrons from a filament.

The magnetic field was generated using the electro-magnet that is generally used for Penning trap experiments 4.4.1. The magnetic field was calibrated using a Hall probe. First the magnetic field created at the maximum current of 15 A through each coil was accurately measured by finding the trap frequencies via RF-photon correlations from the ions. The magnetron and modified cyclotron frequencies were found to be 51 kHz and 291 kHz respectively leading to a magnetic field of 0.898 tesla. By calibrating the Hall probe at this magnetic field the current was then stepped and the magnetic field read. The error in this reading is estimated to be ± 0.005 tesla. The 397 nm photons emitted from the ion were detected via the imaging system described in § 4.4.2 on a PMT and were counted using the electronics and card described in the same section. The data were recorded for approximately 1000 seconds in 10 ms bins. This amounts to more than the 8000 bins available on the MCS card and so a number of successive runs were taken.

At each magnetic field a trace of the ion's signal is obtained. The measurement that is first made is the average time the ion stays bright. This can then be multiplied by the rate at which photons are detected to give the number of photons detected before the ion goes dark. This is linked to the theory of figure 5.8 via the detection efficiency (the fraction of photons emitted by the ion which are detected) estimated to be 4×10^{-4} (§ 4.4.2). So the inverse of the average number of photons detected before the ion goes dark will be plotted ($n_{\text{detected}}^{-1} = \frac{n^{-1}}{4 \times 10^{-4}}$) where we will use the low magnetic field approximation to give $n_{\text{detected}}^{-1} \approx 0.001B^2$. The detected number of photons is used as the signal level is different in each trace with a general trend of a lower signal level as the magnetic field is increased.

The scans were saved and then analysed using a Perl script written by a fellow student. The data analysis has been described in detail [51]. The script is similar to the C program used for the data analysis described in § 6.4.1. For each time-bin the decision must be made whether the ion was bright (in the cooling cycle) or dark (in the $D_{\frac{5}{2}}$ state). This requires a threshold number of counts to be set. If more than this number of counts were detected in the bin then it is labeled as bright. As the signal level is different in each scan

the optimal threshold is also different. The bright (S_b) and dark (S_d) signal levels^v were first found using an initial threshold. The threshold to be used is then calculated using the formula $\frac{2S_d+S_b}{3}$. The threshold level has thus been biased towards the dark signal level due to the nature of the Poissonian noise. This noise increases with the square-root of the number of counts so the bright level is more noisy and hence the threshold needs to be moved further from this.

The start of a quantum jump is defined as when the ion goes from bright to dark and its end is when it goes from dark to bright. It was decided to only define the start of a quantum jump when the ion is initially bright and then 5 successive 10 ms bins occur which have all been classified as dark. The end of a quantum jump was defined when the ion is initially dark and then 5 successive bins have all been classified as bright. This procedure was designed to bypass spurious bins in which the background level was higher than the threshold or when the ion was bright but not enough counts were achieved due to being in the lower tail of the count's Poissonian distribution. This did however have the effect of missing bright or dark periods which were less than 50 ms long. The effect of missing these bright periods is found to be insignificant on the scale of the statistical error which will shortly be discussed.

Figure 5.9 shows the n_{detected}^{-1} found experimentally together with the theoretical fit. The range of fits corresponding to the range of possible detection efficiencies is displayed. It is seen that the points clearly do have a B^2 dependence in agreement with theory. The data points fall within the 1σ bounds of a straight line fit in figure 5.9. The error of the detection efficiency (shown as the lighter red lines in figure 5.9) encompasses the results within their 1σ bounds.

The script produces a list of all the bright period lengths in the scan. This list is used to find the error on the average bright period length (shown as the error bars on the data points of figure 5.9). The method used is bootstrapping. The list is randomly sampled, replacing the chosen bright length each time such as to create a new data set. This procedure is repeated 10^4 times to produce the same number of data sets. The standard deviation of the average bright period length in the data sets is then found and is the error used.

The shelving into the $D_{\frac{5}{2}}$ state due to the J-mixing effect is disadvantageous for efficient Doppler cooling of $^{40}\text{Ca}^+$ ions in a Penning trap. At a magnetic field of 1 tesla the ion is in the $D_{\frac{5}{2}}$ state and is hence not being Doppler cooled the majority of the time. The situation will only get worse in future planned experiments at higher magnetic fields as the shelving rate increases as B^2 . The solution is to use lasers to repump out of the 6

^vThe majority of the (S_d) signal level is due to light scattered from the trap electrodes.

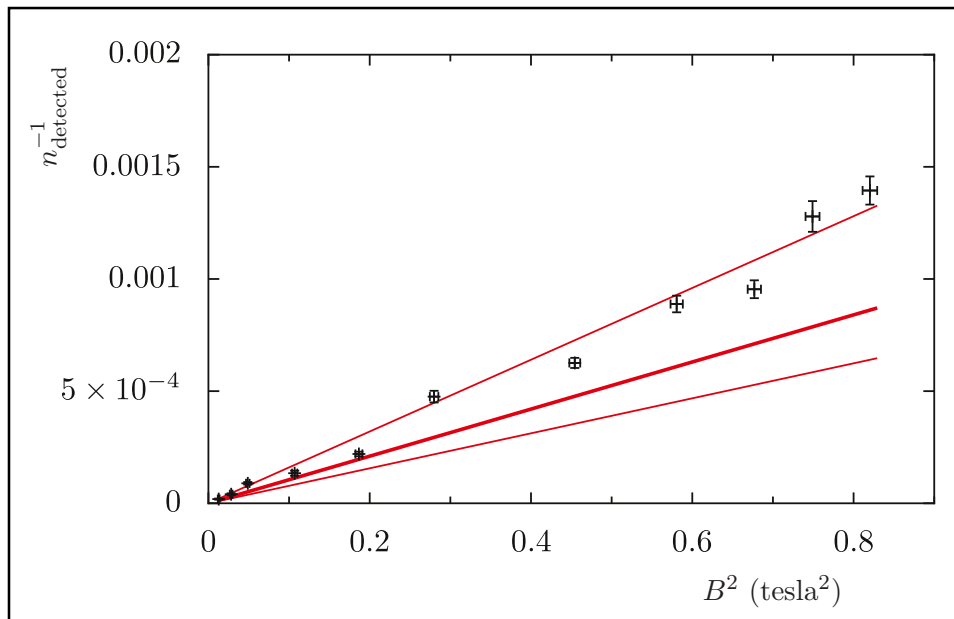


Figure 5.9: n_{detected}^{-1} as a function of magnetic field strength - theoretical and experimental results. The range of fits corresponding to the range of possible detection efficiencies is denoted by the two lighter red lines. The error in B is ± 0.005 tesla and is due to the error in the Hall Probe used. The error in n_{detected}^{-1} has been found using bootstrapping as detailed in the text [10].

$D_{\frac{5}{2}}$ states to move the ion back into the cooling cycle. The experimental demonstration of this is described in § 6.4.1.

Another issue is that of the readout fidelity when using the $S_{\frac{1}{2}} \rightarrow D_{\frac{5}{2}}$ transition as a qubit. To decide whether the ion is in the $S_{\frac{1}{2}}$ or $D_{\frac{5}{2}}$ state the 397 nm lasers are switched on together with the 866 nm lasers to repump the $D_{\frac{3}{2}}$ state. Photons at 397 nm should be emitted if the ion is in the $S_{\frac{1}{2}}$ state while they should not if the ion is in the $D_{\frac{5}{2}}$ state. Ideally we wish to decide which state the ion is in with the smallest error. A readout time is chosen which is a compromise between building up enough statistics to make the decision whilst not waiting too long so that the probability of the $D_{\frac{5}{2}}$ state spontaneously emitting becomes significant.

If the ion is in the $D_{\frac{5}{2}}$ state then the J-mixing effect will not cause any error. However if the ion is initially in the $S_{\frac{1}{2}}$ state the J-mixing adds the possibility of the ion decaying from the $P_{\frac{1}{2}}$ state to the $D_{\frac{5}{2}}$ state and thus becoming dark. If just the number of photons detected in the entire readout period is recorded then depending at which point the ion became dark, enough photons may not have been collected to decide the ion was bright and so the decision would be incorrect. This is similar to the case when an ion is in the $D_{\frac{5}{2}}$ state and then spontaneously emits. The earlier this occurs in the readout period the more likely the ion could be wrongly classified as being bright and hence in the $S_{\frac{1}{2}}$ state. Methods have been developed by the ‘Ion Trapping Quantum Computation’ group in Oxford to increase the readout fidelity by binning up the photons detected so that two detection periods with the same number of total counts can be differentiated if most of the counts occurred from a certain bin onwards. Using methods based on this, average readout fidelities of 99.991(1)% have been achieved using a $^{40}\text{Ca}^+$ ion [77]. A similar method could be used to detect (and then discard or correct) detection periods where the J-mixing effect has caused the ion to become dark after a certain bin.

The Oxford group requires 8.1 photons on average to decide with the above precision that the ion is in the $S_{\frac{1}{2}}$ state. Assuming a similar background count rate we can estimate that we would need a similar number in our setup. With our detection efficiency we would require 2 ms to detect on average 8.1 photons. In this time the probability of spontaneous emission from the $D_{\frac{5}{2}}$ state is $\approx 0.17\%$. The probability of the ion falling into the $D_{\frac{5}{2}}$ state before 8.1 photons are detected is 0.8% at 1 tesla. This increases to 5.1% at 2.5 tesla. The error in the readout fidelity is a small effect at the trapping magnetic field used. Analysis of the readout data to see the shelving events is required however to achieve readout fidelities similar to those obtained in Paul trap experiments.

We have discussed the effect J-mixing has on the readout fidelity of a $^{40}\text{Ca}^+$ ion in a Penning trap. There are however a number of other ions with similar D states below the

	ΔE_D (meV)	ΔE_P (meV)	$ \Delta E_D ^{-2}$ (arb. units)
Ca ⁺	7.5	27.6	1
Sr ⁺	34.8	99.4	0.046
Ba ⁺	99.3	209.6	0.0057
Yb ⁺	170.1	412.9	0.0019
Hg ⁺	1864.8	1131.0	0.000016
Ra ⁺	205.6	602.3	0.0013

Table 5.1: Fine structure splittings of other ions [10]. The approximate shelving rates relative to $^{40}\text{Ca}^+$ are shown.

$P_{\frac{1}{2}}$ level used for cooling and detection and they will experience a similar effect. In the small magnetic field approximation it can be seen by analysing equations 5.15 or can be seen directly if the mixings are calculated using first order perturbation theory that the mixing scales with the inverse of the fine structure splitting [51], [10]. It can also be seen from the calculated n^{-1} that the number of photons emitted before shelving occurs scales approximately with the inverse of the square of the fine structure splitting. Table 5.1 shows the fine structure splittings of the P and D states of a variety of ions together with approximate relative $D_{\frac{5}{2}}$ shelving rates. It is seen that the other ions have smaller rates and hence their readout fidelities would be affected to a lesser extent than Ca⁺.

D-State Re-pumping

The electronic energy diagram of a $^{40}\text{Ca}^+$ ion in the presence of a magnetic field together with the relevant transitions was shown as figure 4.1. In chapter 5 it was seen that at a magnetic field of 1 tesla the ion spends much of its time in the $D_{\frac{5}{2}}$ state due to the J-mixing process (see figure 5.7). The ion would spend an even greater fraction of the time out of the cooling cycle in future experiments in a 2.5 tesla magnet. For efficient Doppler cooling the ion needs to spend most of its time in the cooling cycle and so repumping out of the $D_{\frac{5}{2}}$ state using light at 854 nm is imperative. The rate at which the ion is repumped must be large compared to the shelving rate. Another constraint on the repumping rate occurs when pulsed spectroscopy is conducted on the $S_{\frac{1}{2}} \rightarrow D_{\frac{5}{2}}$ transition (see chapter 7). The quicker the repumping rate, the shorter the 854 nm pulse that can be used during the pulsed spectroscopy. There were no 850 nm lasers available in the experimental setup to address the $D_{\frac{3}{2}} \rightarrow P_{\frac{3}{2}}$ transitions. Although this is not required it would be useful to have the option to repump out of the $D_{\frac{3}{2}}$ state without coupling to the $S_{\frac{1}{2}} \rightarrow P_{\frac{1}{2}}$ Doppler cooling transition (as is the case when using 866 nm lasers). This should result in a greater rate of 397 nm photons emitted from the ionⁱ. It should be noted that even if 850 nm and 854 nm lasers were used for repumping during Doppler cooling then 866 nm lasers would still be required for state detection as there can be no coupling to the $D_{\frac{5}{2}}$ state during this period. Fourteen lasers would be required to individually address the required 850 nm, 854 nm and 866 nm transitions. This is not very practical. Another option would be to use fewer lasers and use an electro-optic modulator (EOM) to create sidebands at

ⁱUsing the 866 nm lasers the population is approximately equally spread amongst the two $S_{\frac{1}{2}}$, two $P_{\frac{1}{2}}$ and four $D_{\frac{3}{2}}$ levels resulting in the ion spending approximately half its time in the $S_{\frac{1}{2}} \rightarrow P_{\frac{1}{2}}$ cooling cycle.

Chapter 6

the desired frequenciesⁱⁱ.

Sidebands can be imposed on a laser by modulating the phase of its electric field. This can be achieved by sending the laser beam through a material with a time-varying refractive index. This modulation is achieved in an EOM via the Pockels effect. The refractive index change is proportional to the electric field applied to the crystal. If a sinusoidal voltage is applied to the EOM then the phase of the laser field will vary sinusoidally and the total electric field leaving the EOM is

$$E = E_0 e^{i(\omega_L t + \alpha \sin(\Omega_{\text{RF}} t))}, \quad (6.1)$$

where ω_L is the angular frequency of the laser, α is the depth of the RF phase modulation and Ω_{RF} is the angular frequency of the RF field. It is possible to write the part of this equation corresponding to the phase shift as an infinite sum of Bessel functions

$$e^{i\alpha \sin(\Omega_{\text{RF}} t)} \equiv \sum_{n=-\infty}^{\infty} i^n J_n(\alpha) e^{in\Omega_{\text{RF}} t}. \quad (6.2)$$

Using $J_{-n}(\alpha) \equiv (-1)^n J_n(\alpha)$ we can now write the total electric field as

$$E = E_0 e^{i\omega_L t} \left[J_0(\alpha) + \sum_{n=1}^{\infty} i^n J_n(\alpha) (e^{in\Omega_{\text{RF}} t} + e^{-in\Omega_{\text{RF}} t}) \right]. \quad (6.3)$$

This describes a field consisting of light at the carrier frequency of the laser and also at frequencies offset from the carrier by integer multiples of the RF frequency, $\omega_L \pm n\Omega_{\text{RF}}$. The light at each of these new frequencies is called a sideband. The frequencies with $n = 1, 2, \dots$ are the 1st, 2nd... order sidebands respectively. The amplitudes of the carrier and sidebands are controlled by the Bessel functions, $J_n(\alpha)$. Their intensities are given by

$$I = |E|^2 = I_0 J_n^2(\alpha), \quad (6.4)$$

where $I_0 = |E_0|^2$ is the intensity of the laser prior to any modulation. For small modulation depths the first sideband is appreciable but higher order sidebands become progressively smaller. Larger modulation depths can result in a spectrum where a large number of sidebands are of a similar height to the carrier.

In conventional ‘bulk’ free space EOMs the RF is applied to a pair of electrodes which sandwich the crystal through which the laser passes. The refractive index change is pro-

ⁱⁱAnother method is to modulate the current of the diode laser. This method has previously been used to put sidebands on the 866 nm repumping lasers [78]. It is difficult to put a high percentage of the carrier light into the first sidebands using this method and so a lot of laser power is lost.

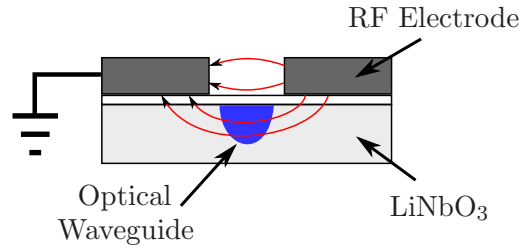


Figure 6.1: Cross-section of the fibre EOM travelling wave electrodes. The laser light is confined to the optical waveguide created by doping the crystal with transition metals.

portional to the electric field between these plates and so is inversely proportional to the distance between the electrodes. For a given refractive index change a larger phase modulation will result the longer the EOM is. The capacitance of the plates is also proportional to their length and inversely proportional to the distance between them. The bandwidth of the EOM can thus not be increased indefinitely. The sideband spacing required in our system is of the order of 10 GHz (approximately the size of the Zeeman splitting at 1 tesla). A significant phase modulation is difficult to achieve with this type of EOM above ≈ 1 GHz. Higher bandwidths are possible however using ‘travelling wave electrodes’ [79]. A schematic of the setup is shown in figure 6.1. The RF mode is travels partly through the air and partly through the LiNbO_3 crystal. The crystal is doped in a small region to create an optical waveguide. So the laser and the RF travel in the same direction. The dimensions are chosen so as to match the phase velocity of the RF and light waves in the crystal so that the interaction can occur over large distances. Optical fibres are used to deliver the light to and collect the light from the waveguide. This device will thus be described in the following as a ‘fibre EOM’.

This technology has recently been developed in the wavelength region of our repumper lasers. In the following sections a scheme is introduced whereby a single fibre EOM can be used to repump the required transitions using just 4 lasers. The optimal parameters required to do this are then deduced. The fiber EOM was subsequently calibrated and laser cooling results using it are presented.

6.1 Multiple transition repumping scheme using a single fibre EOM.

At low magnetic fields the Zeeman splitting of each m_J state is linear in B and depends on the g_J factors of each state. These were provided in table ???. They are all rational

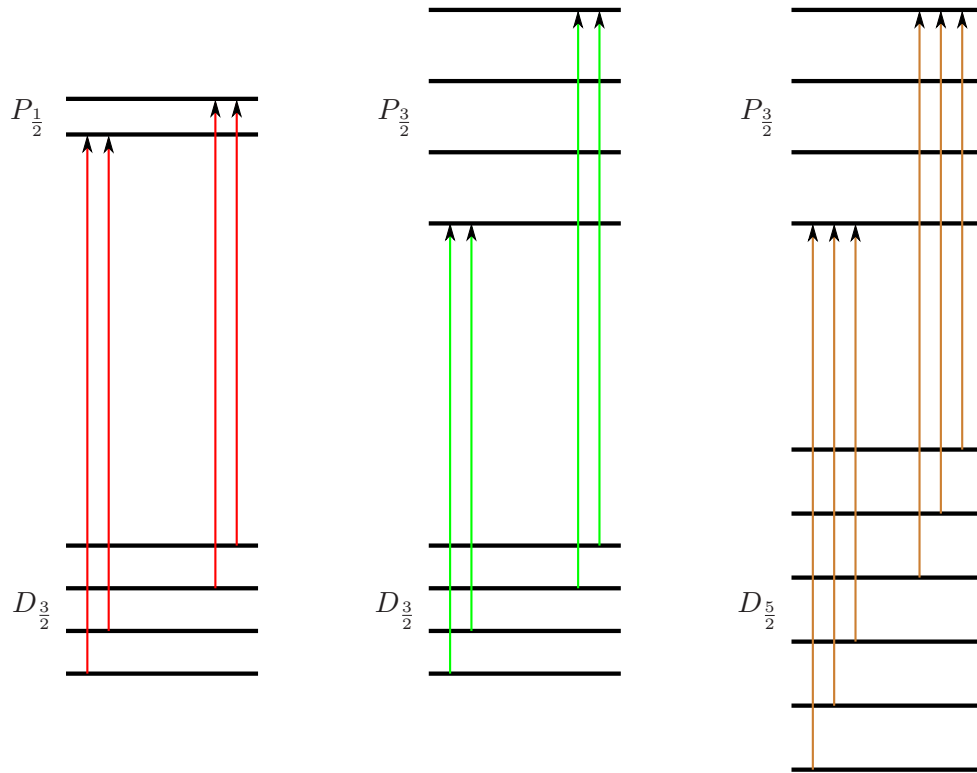


Figure 6.2: The transitions which the scheme of figure 6.3 uses. From left to right are the 866 nm, 850 nm and the 854 nm transitions. A similar pattern is seen in each case where the states are only repumped to the two outer P states. Both π , σ^+ and σ^- transitions are required. The relative Zeeman splitting is to scale.

numbers. The frequency of a transition depends on a linear combination of the two relevant g_J factors. The simple nature of these factors gives us a clue that putting the lasers at 850 nm, 854 nm and 866 nm through the same EOM with a judiciously selected set of RF frequencies applied to it could provide us with sidebands at the required frequencies. It turns out that it is possible to hit all 14 transitions required with one 850 nm laser, one 854 nm laser and two 866 nm lasers. The transitions which the proposed scheme addresses are shown in figure 6.2. The lasers and sidebands required are displayed in figure 6.3.

The figure shows a single set of sidebands at a spacing ν_a which is a linear function of magnetic field ν_a (GHz) = 5.5985 B (tesla) such that the frequency of a sideband is specified by $\nu_{\text{sideband}} = m\nu_a$ where m is the order of the sideband. The 850 nm laser is set at the transition frequency at $B = 0$ and so the transitions are symmetrical about zero in the diagram. The 854 nm and 866 nm lasers are offset to the outer π transitions.

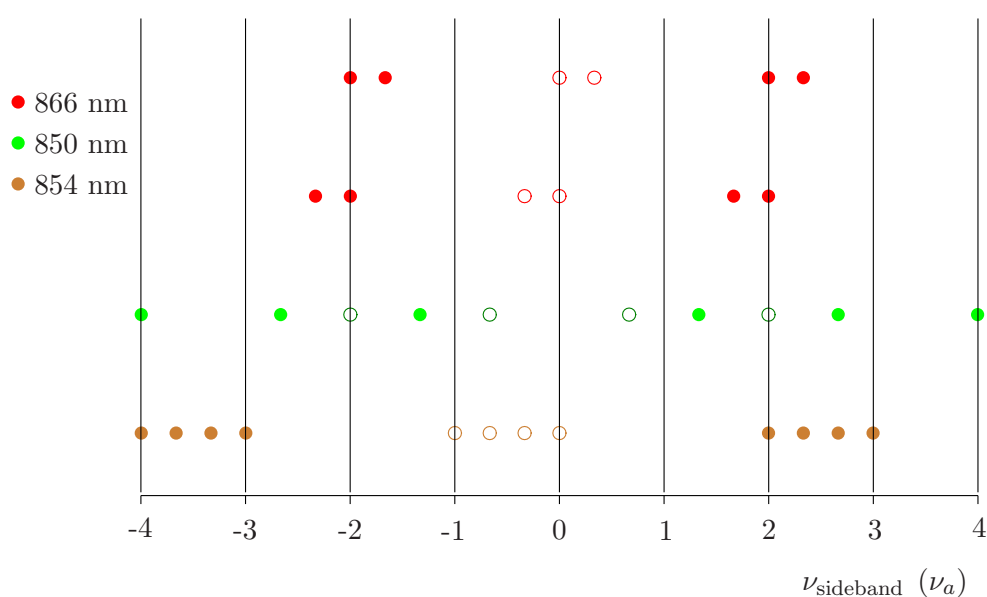


Figure 6.3: Visual representation of how a comb of sidebands with a spacing of ν_a (GHz) = $5.5985B$ (tesla) can hit enough transitions to re-pump out of all the sub-levels at 850 nm, 854 nm and 866 nm. The frequency of a given sideband is $\nu_{\text{sideband}} = m\nu_a$ where m is an integer which specifies the sideband. Each row of circles corresponds to a separate laser (note the two 866 nm lasers required). The solid and open circles represent σ and π transitions respectively. The carrier laser frequency is set to the zero position on the horizontal axis. The vertical lines then give the available frequencies.

6.2 Numerical calculation of RF power required

The scheme requires up to fourth order sidebands to address the required transitions. It will be seen that even the fibre EOM can't create large fourth order sidebands. Instead two RF frequencies, ν_a and $3\nu_a$ are applied to the fibre EOM. The nine frequencies in the comb can then be created by just the carrier and first order sidebands. Labelling the sidebands from -4 to $+4$ if we imagine the lower frequency RF acting first then sidebands are created at ± 1 . Then the high frequency RF acts on these sidebands creating sidebands at ± 4 and ± 2 ($-1 \rightarrow -4$, $+2$ and $+1 \rightarrow +4$, -2). If higher order sidebands are considered then the ± 2 sidebands can also be created by second order sidebands at the lower RF frequency. Interference will occur between the light created via these two different routes. We define a phase difference ϕ between the ν_a and $3\nu_a$ RF signals at $t = 0$ (which can be defined as one frequency is a harmonic of the other). The resulting electric field is

$$E = E_0 \sin [2\pi\nu_L t + \alpha \sin (2\pi\nu_a t) + \beta \sin (2\pi 3\nu_a t + \phi)], \quad (6.5)$$

where ν_L is the carrier frequency of the laser and α , β are the depths of the phase modulation produced via the RF applied at ν_a and $3\nu_a$ respectively. Depending on whether the phase between the two RF signals is controllable it will either be a variable which we can adjust to help us obtain the resulting electric field we desire or it will be averaged in time.

We wish to calculate the frequency spectrum created as a function of the amplitudes of the RF fields and the phase between them. This can be achieved by expanding both the phase modulation at ν_a and $3\nu_a$ in terms of Bessel functions. The resulting expressions are given in appendix B. Here we will sample equation 6.5 and then take the discrete Fourier transform. We can then optimise for the ideal parameters.

To do this E is calculated at each value of α , β and ϕ for a set of values of t . The discrete Fourier transform is then taken and then the modulus squared of this is calculated to give the light intensity as a function of frequency. The intensity at the carrier and each sideband is then saved for each set of α , β and ϕ .

First we have to put in values for the laser and RF frequencies. These two frequencies differ by a factor of $\approx 10^4$ and so it is difficult to see both these frequencies in a Fourier transform. Instead we set the ratio between these two frequencies large enough so that the results do not change if it is made larger. Setting $\nu_L = 10$ and $\nu_a = 1$ is adequate. The number of values of t was chosen to be 2000 and t was scaled by 100 so that 200 cycles, 20 cycles and 60 cycles are sampled for ν_L , ν_a and $3\nu_a$ respectively. α and β were scanned from 0 up to 2.5 with a step size of 0.05. ϕ was scanned from 0 to 2π with a step size of $\frac{\pi}{20}$.

Now we can search through our new data to find the optimal parameters that can be applied to the EOM to get the most light at the transition frequencies we desire. The resulting light field is a symmetrical comb at ν_a . The 850 nm, 854 nm and 866 nm transitions all require different components of this comb to hit the target transitions. The components required can be seen readily from figure 6.3. The optimal parameters will be found individually for each laser. A compromise will then need to be found if more than one of these lasers is being used at once. For each ϕ the amplitudes corresponding to each α and β are scanned and the parameters which maximise the power in the least powerful transition are found. The results of this procedure are shown in figure 6.4. Shown are optimal RF amplitudes and the resulting percentage of the initial laser intensity that is at the transition frequency with the smallest amplitude (%max). These are plotted as a function of the phase between the two RF signals. If the phase is not controllable and is jittering so rapidly that the ions will not respond to it then we must average over the phase at each α and β . Figure 6.5 displays contour plots of %max as a function of α and β . %max for each transition set is written in the caption.

6.3 Experimental Setup and Calibration of Fibre EOM

The fibre EOM used for the experiments in this chapter is a commercial 20 GHz phase modulator from EOSPACE. The two RF frequencies for the fibre EOM originate from different sources. For the experiment of § 6.4.1 where modulation at frequencies ν_a and $3\nu_a$ is applied to the EOM the setup of figure 6.6 was used. The two RF signals were combined using a splitter and then amplified before being applied to the EOM. The VCO described has a frequency range which corresponds to an operating region of the trapping magnetic field from 0.95 to 1.01 tesla. For other experiments where different frequencies were required, different VCOs and function generators were used to create the RF but the signals were combined in the same way. The EOM itself is rated to 20 GHz and has not been tested above this. This corresponds to a magnetic field of 1.2 tesla in the described scheme. One way to control the phase between the two RF signals ν_a and $3\nu_a$ is to have them originate from the same source. This can be achieved by using a VCO or function generator to produce ν_a which is then split into two signals. A 3x frequency multiplier can create the $3\nu_a$ on one of the signals which is then recombined with the other signal at ν_a .

The RF frequency produced by the VCO as a function on the voltage applied was calibrated by performing a beat-note measurement. The electronic setup was the same as in figure 6.6. The RF power from both the function generator and VCO was optimised to produce first order sidebands as large as possible as seen on the transmission of the optical

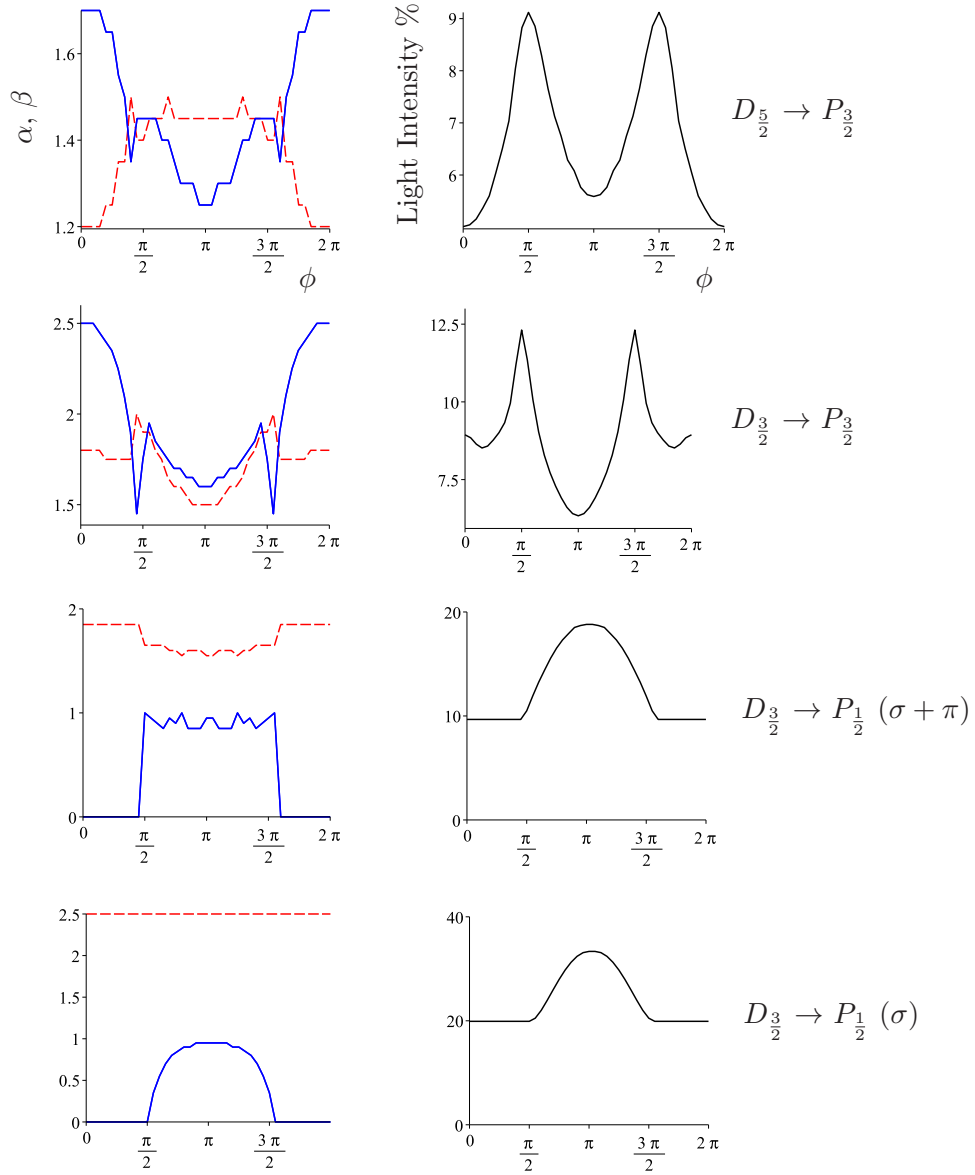


Figure 6.4: The optimised amplitudes of the phase modulation at ν_a and $3\nu_a$ (left) and the corresponding light intensity at the transition frequency with the lowest power (right) as a function of the phase between the two RF signals. The dashed and solid lines in the RF amplitude plots are for the α and β amplitudes respectively. Note that the transition frequency with the lowest power can be change for different values of ϕ .

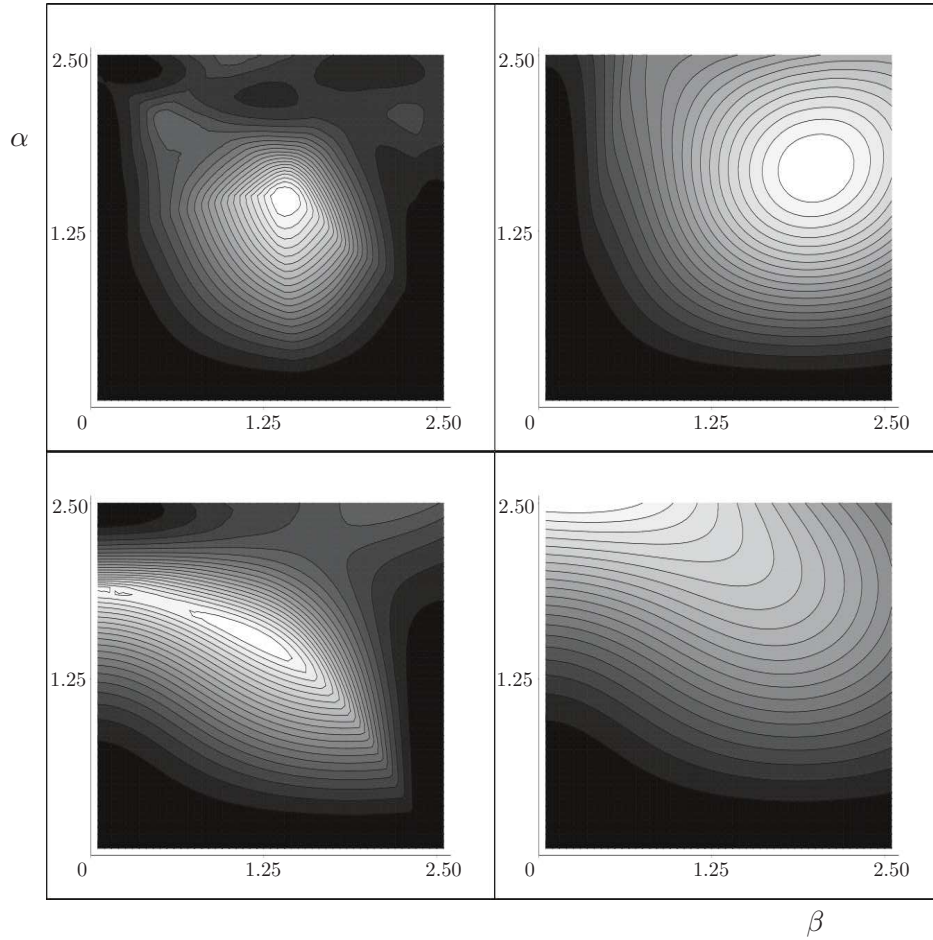


Figure 6.5: Numerically Optimised EOM modulation strengths (α and β) for a scrambled phase. Clockwise from the top-left are the $D_{\frac{5}{2}} \rightarrow P_{\frac{3}{2}}$, $D_{\frac{3}{2}} \rightarrow P_{\frac{3}{2}}$, $D_{\frac{3}{2}} \rightarrow P_{\frac{1}{2}}$ (σ) and $D_{\frac{3}{2}} \rightarrow P_{\frac{1}{2}}$ (σ and π) transitions. Each contour denotes a 5% change in intensity. Black indicates there is 0-5% of the maximum intensity (white). The maximum intensities are different for the different plots. They are (clockwise from top-left) 6.3%, 8.7%, 22.0% and 11.0%.

Note that the transition frequency with the lowest power can change for different values of α and β . To try and make sense of these plots let's look at the $\alpha = 0$ and $\beta = 0$ cases. Each set of transitions require the 2nd order sideband. As this sideband cannot be created via the high RF, when $\alpha = 0$ the power in the worst transition is always zero. When $\beta = 0$, sidebands are only created by the lower RF. In the bottom-right plot (866 σ transitions) the second order sideband is the only one required. This is thus always limiting and so the $\beta = 0$ line follows the square of a 2nd order Bessel function. In the top-right plot (850 transitions) the 4th order sideband is always limiting and so the $\beta = 0$ line follows the square of a 4th order Bessel function. In the other two plots different sidebands are limiting at different points along the $\beta = 0$ line. In the top-left plot (854 transitions) the 4th order sideband is limiting until $\alpha \approx 2.3$ when the carrier is limiting. In the bottom-left plot (866 $\sigma + \pi$ transitions) the 2nd order sideband is limiting until $\alpha \approx 1.8$ when the carrier falls below it and becomes limiting.

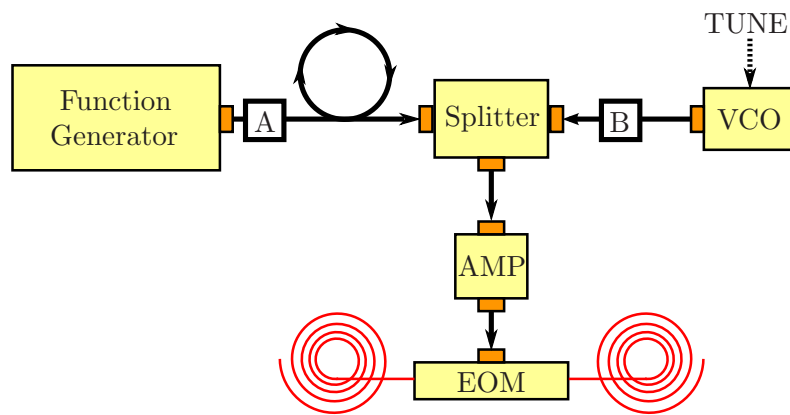


Figure 6.6: Diagram of the electronic setup for when RF at frequencies of ν_a and $3\nu_a$ are applied to the fibre EOM. The higher frequency was generated from a Agilent 83650L function generator which could be used from 10 MHz to 50 GHz producing up to ≈ 20 dBm of RF power. The VCO (ZX95-5580+) could be tuned from 5.33 to 5.63 GHz with an output power of ≈ -0.5 dBm. The high frequency RF from the function generator had to be transmitted by high frequency coaxial cable to reduce losses. The two signals were combined on a resistive splitter (ZFRSC-183-S+) with a loss of ≈ 3.5 dB. The combined signals were then amplified on a ZVA-213-S+ which has a gain of ≈ 26 dB between 0.8 and 21 GHz. The power of the two RF frequencies could be altered by inserting different fixed attenuators at A and B. These also help to stop any damage from reflections back into the RF sources.

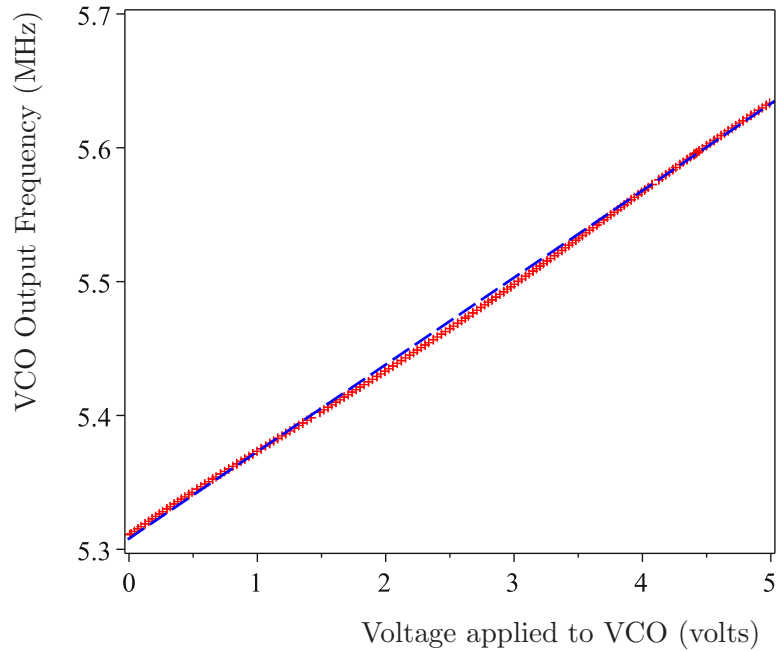


Figure 6.7: Calibration of the VCO (ZX95-5580+) output frequency as a function of the the tuning voltage on it. The calibration was relative to a function generator whose calibration had been checked relative to a counter. The beat note frequency between the first order sidebands created by the VCO and function generator RF signals on the fibre EOM was observed. A linear fit to the data is shown which has a y-intercept of 5.31 MHz and a gradient of 0.065 V/MHz

spectrum analyser as described in § 4.2.5. The sidebands were overlapped in frequency space. A photodiode was placed after the EOM, the signal from which was viewed using the Fourier transform mode of an oscilloscope (300 MHz, digital). The function generator frequency was scanned until a beatnote was seen in the Fourier transform. Noting both the RF frequency from the function generator and the beatnote frequency, the VCO frequency could be calculated. The voltage applied to the VCO was then stepped and the beatnote frequency noted. This was continued until the VCO was calibrated over its voltage range. The function generator frequency was moved to keep the beatnote under 100 kHz so it could be easily observed. The results of this calibration are shown as figure 6.7. It is seen that the frequency is an approximately linear function of the applied voltage.

Figure 6.8 displays the intensity of the sidebands produced by the EOM as a function of the amplitude of the RF applied. The sidebands were seen via the transmission of the same scanning cavity used for the beatnote measurement while the RF was applied to the EOM using the setup of figure 6.6. The RF power was measured at the EOM using an RF

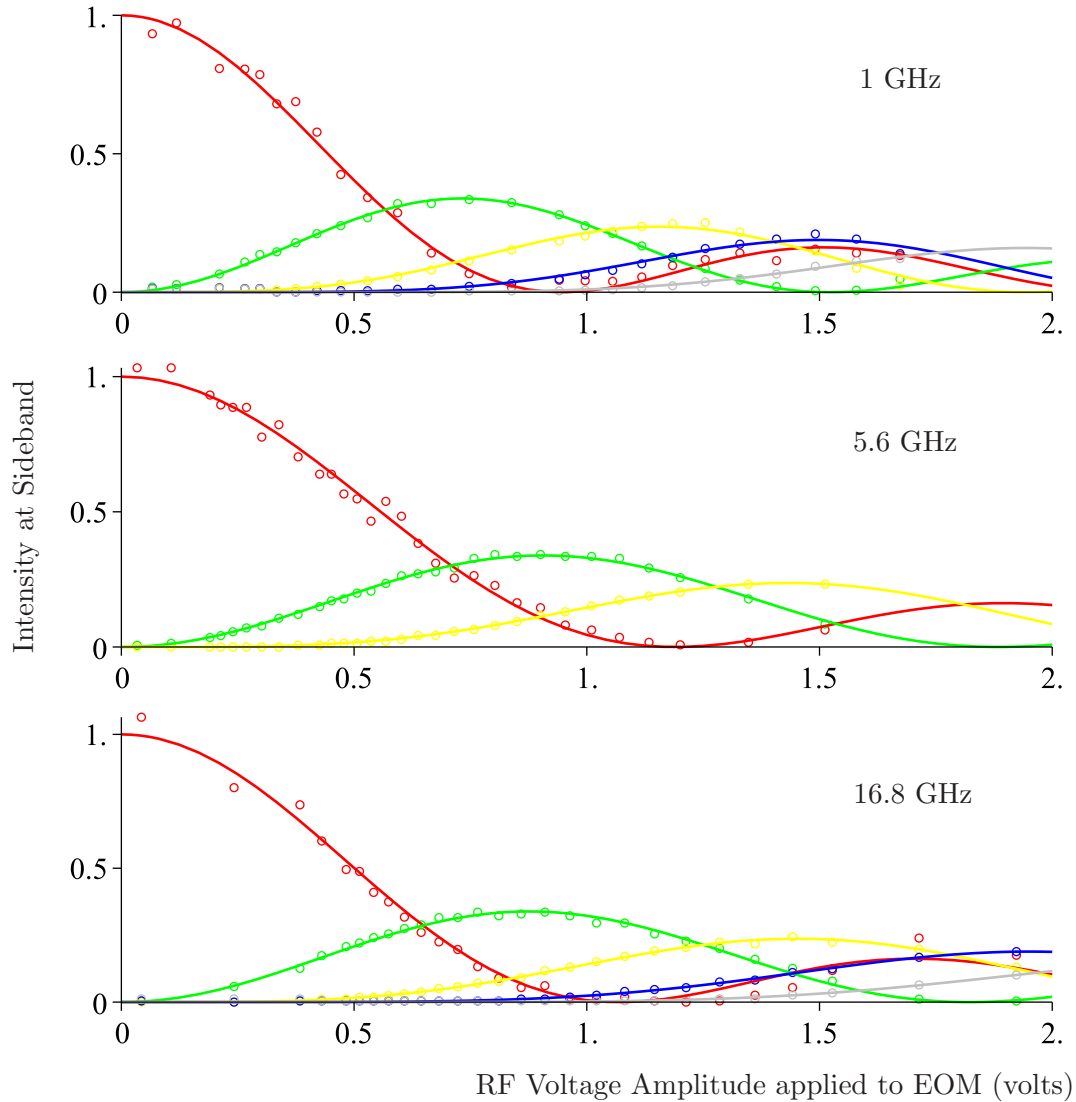


Figure 6.8: The intensity of the carrier and sidebands on the 854 nm laser seen via the transmission of a scanning cavity. The different plots are for different RF frequencies applied to the EOM. From top to bottom the frequency applied is 1 GHz, 5.6 GHz and 16.8 GHz. The fits are Bessel functions of the form $I_0 J_m(aV)$. Each sideband has been fitted individually to obtain a value of a . Averaging this value of the carrier, first and second sidebands we obtain $a = 2.57, 2.06$ and 2.15 for applied RF frequencies of 1 GHz, 5.6 GHz and 16.8 GHz respectively. The red, green, yellow, blue and grey data is that of the carrier, first, second, third and fourth order sidebands respectively.

power meter (Agilent U2000A). Each sideband of order m was fitted individually to the corresponding Bessel function $I_0 J_m(aV)$. The coefficient a , when multiplied by the voltage applied, gives the amplitude of the phase shift, α as defined in equation 6.1 (for a single applied frequency) and α and β of equation 6.5 (for the case of two applied frequencies). The averaged a coefficients found over the carrier, first and second sidebands are 2.57, 2.06 and 2.15 for applied RF frequencies of 1 GHz, 5.6 GHz and 16.8 GHz respectively. We see that significantly less RF power needs to be applied at 1 GHz than at 5.6 GHz or 16.8 GHz to achieve an identical phase shift depth.

6.4 Repumping Results

6.4.1 $D_{\frac{5}{2}} \rightarrow P_{\frac{3}{2}}$ Transitions

The first experiment that we consider was performed with a single 854 nm laser sent through the fibre EOM driven at RF frequencies of ν_a and $3\nu_a$ to create a comb of frequencies at ν_a (see figure 6.3) to repump the $D_{\frac{5}{2}}$ state via the six transitions as shown in figure 6.2. This laser was then combined with four separate 866 nm lasers to repump out of the four $D_{\frac{3}{2}}$ levels via the σ transitions. The optical setup is that of figure 4.9 except the combining with the 866 nm lasers is after the EOM, and not before as shown. The optical setup of the cooling lasers and the combining of the lasers before the trap is that of figures 4.10 and 4.11. The trap used was the Split Ring Trap (SRT) described in § 4.3.1. A magnetic field strength of ≈ 1 tesla was used with a single $^{40}\text{Ca}^+$ ion loaded into the trap. The 397 nm light emitted from the ion is observed on a PMT with the optics and electronic setup of § 4.4.2. Approximately 100 μW of laser power from each of the cooling lasers and the 866 nm repumping laser was focused at the ion with a spot size of 90-100 μm . Axialisation (§ 3.1.2) was used to help cool it. The polarisation of the 854 nm laser was set to approximately 45 degrees so it could hit both π and σ transitions as required in the scheme of figures 6.3 and 6.2. The wavelengths of all the lasers were set using the commercial wavemeter described in § 4.2.2. The tunings of the 397 nm and 866 nm lasers were then optimised to produce the largest signal from the ion. The filter used in § 5.2 was placed in the 866 nm beam to remove any 850 nm and 854 nm light so repumping of the $D_{\frac{5}{2}}$ state is only done by the 854 nm laser.

We wish to look at the percentage of time the ion is dark as well as the length of quantum jumps as a function of 854 nm power at the trap and whether the EOM RF is switched on or off. The percentage of time the ion is dark is important for efficient laser cooling as the ion is only being cooled when it is scattering 397 nm photons which obviously cannot happen when it is in the $D_{\frac{5}{2}}$ state. The quantum jump length is important as it

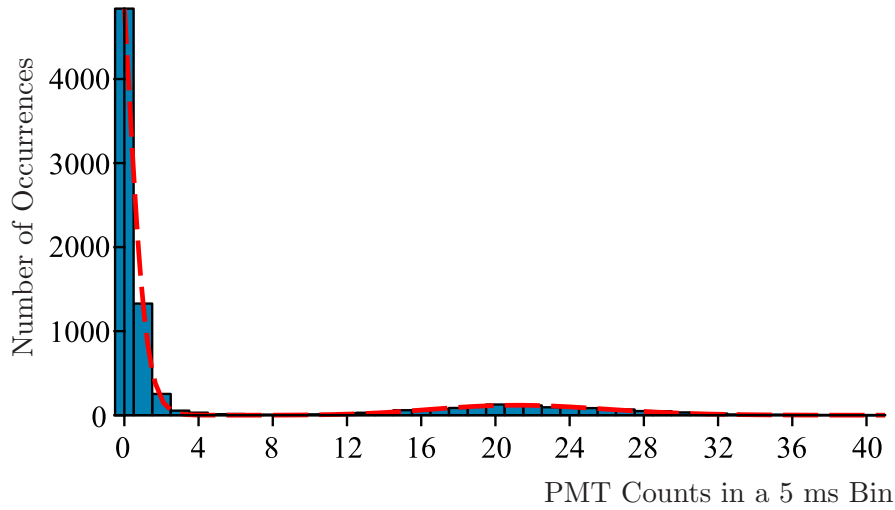


Figure 6.9: Histogram of the number of counts in each 5 ms bin. There is no 854 nm beam to repump the $D_{\frac{5}{2}}$ state. Summing up the number of bright and dark bins the ion is found to spend 82% of the time in the $D_{\frac{5}{2}}$ state. A small sample of the raw data is shown in figure 5.7.

gives an indication of the time the 854 nm laser takes to repump the ion out of the $D_{\frac{5}{2}}$ state. This is important when considering the required duration of the repumping pulse used when performing pulsed spectroscopy (see chapter 7). The power required is important as there is usually a compromise in power between different lasers when they are combined so a good understanding of this parameter allows a judicious choice to be made. A number of repumping experiments have thus been conducted at different 854 nm powers.

A typical trace is shown in figure 5.7 when there is no repumping from the $D_{\frac{5}{2}}$ state. In figure 6.9 the number of counts in each bin for the trace have been histogrammed for the data set of which figure 5.7 shows a sample. The histogram has been fitted to the sum of two Poissonian distributions

$$f(x) = A \left(\frac{a^x e^{-a}}{x!} \right) + B \left(\frac{b^x e^{-b}}{x!} \right), \quad (6.6)$$

where A , a , B and b are free variables.

The two distributions represent the two cases when either the ion is scattering 397 nm photons and so is ‘bright’ or it is in the $D_{\frac{5}{2}}$ state and is ‘dark’. Defining a bright bin as one in which more than 8 photons were detected we find that the ion was dark 82% of the time. This means that the ion would only be cooled 18% of the time at a magnetic field

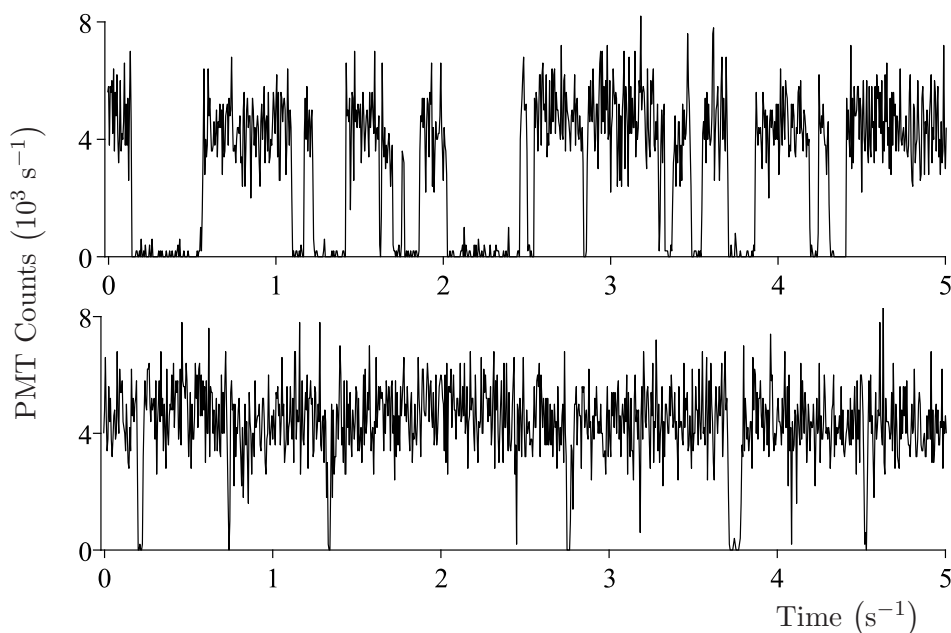


Figure 6.10: Ion signal recorded on a PMT with a $1 \mu\text{W}$ 854 nm beam for repumping the $D_{\frac{5}{2}}$ state. The upper and lower plots are for the EOM RF turned off and on respectively.

of 1 tesla and this time will decrease for higher fields.

Another consideration is the effect on the pulsed spectroscopy of the $S_{\frac{1}{2}} \rightarrow D_{\frac{5}{2}}$ transition discussed in the next chapter. Here the probability of shelving the ion in the $D_{\frac{5}{2}}$ state using a narrow linewidth 729 nm laser is measured as a function of the laser's frequency. To find the shelving probability the experiment must be performed many times. Before repeating the experiment the ion must be 'reset' back to the $S_{\frac{1}{2}}$ state. If a repumping 854 nm pulse is not used when performing pulsed spectroscopy then we must wait for the ion to spontaneously emit from the $D_{\frac{5}{2}}$ state. Using a larger data set (such as those used in § 5.3) the lifetime of the $D_{\frac{5}{2}}$ state has been measured in our group [51]. The most accurate measurement of this value performed by other groups is (1.168 ± 0.007) seconds [80]. To be sure that the ion has spontaneously emitted out of the $D_{\frac{5}{2}}$ state a time delay is required which is much longer than the lifetime of the $D_{\frac{5}{2}}$ state. This is a long time to wait and so a 854 nm repumping pulse is required.

First let us look at an experiment conducted with $(1.0 \pm 0.1) \mu\text{W}$ of 854 nm power at the trap. A single ion was trapped in the Split Ring Trap (§ 4.3.1). With the two 397 nm, four 866 nm and the single 854 nm laser directed at the ion the fluorescence was recorded for 40 s. This data set was split up into 8000 5 ms bins. There is ≈ 4400 counts per second from the ion when it is scattering which is enough signal to distinguish between

when the ion is bright (in the cooling cycle) or dark (in the $D_{\frac{5}{2}}$ state). This can easily be seen by histogramming the number of counts in each bin. Figure 6.10 shows traces for an experiment where the RF was applied to the EOM and one where it was not, with corresponding histograms in figure 6.11.

The histograms have again been fitted to the sum of two Poissonian distributions representing the dark and bright bins. The first thing to notice is that the ion spends much more time in the cooling cycle when the RF is applied to the EOM and so it has the desired effect. It can be seen however that quantum jumps do still occur. This shows that the rate of repumping is too small to be sure of emptying the $D_{\frac{5}{2}}$ state within a fraction of a 5 ms bin. The ion does however spend $\approx 97\%$ of the time in the cooling cycle and so efficient Doppler cooling is achievable with this 854 nm power. We can quantitatively look at the repumping rate by defining an effective lifetime of the $D_{\frac{5}{2}}$ state. A program was written which, given a threshold number of counts to distinguish between when the ion is bright and dark (set manually by looking at the relevant histogram), creates a new array of whether the ion is bright or dark in each bin. Scanning through this array the program labels the start of a jump when there is a dark bin following a bright bin. The number of bins in which the ion remains dark is then incremented until a bright bin is found defining the end of the jump. The process is repeated until the whole data set has been scanned. It then creates a histogram of the lengths of the quantum jumps. The result of this is shown in figure 6.12.

An exponential fit to this histogram gives effective $D_{\frac{5}{2}}$ state lifetimes of 160 ms and 16 ms when the RF to the EOM is off and on respectively. It is noted that the lifetime is shortened from the natural 1.17 s lifetime even without the EOM turned on but the EOM does help to significantly shorten the jump length. When the EOM is turned off the 854 nm laser is detuned by $4\nu_a$ from the furthest transition but it still has some effect through off-resonant repumpingⁱⁱⁱ. However, even with the EOM on, a 1 μW 854 nm pulse of ≈ 90 ms would be required to have a good repumping success rate. This will be seen to be a long time on the pulsed spectroscopy timescale and so an increase in 854 nm power is required. An experiment was also conducted with (40 ± 20) nW of 854 nm light. The histograms show a similar effect as the experiment with 1 μW of light however the repumping is less efficient as expected and the ion spends a greater fraction of its time in the $D_{\frac{5}{2}}$ state (see figure 6.13) and has a longer effective lifetime of 103 ms with the EOM on (see figure 6.14).

ⁱⁱⁱThis repumping could be due to laser noise or ASE. Another possibility is due to Johnson noise on the EOM. The RMS voltage on the amplifier per Hz of bandwidth is $4k_BTR$. At room temperature after being amplified this could result in 5 mV of noise on the EOM over a bandwidth of 100 MHz around each transition resulting in the observed repumping.

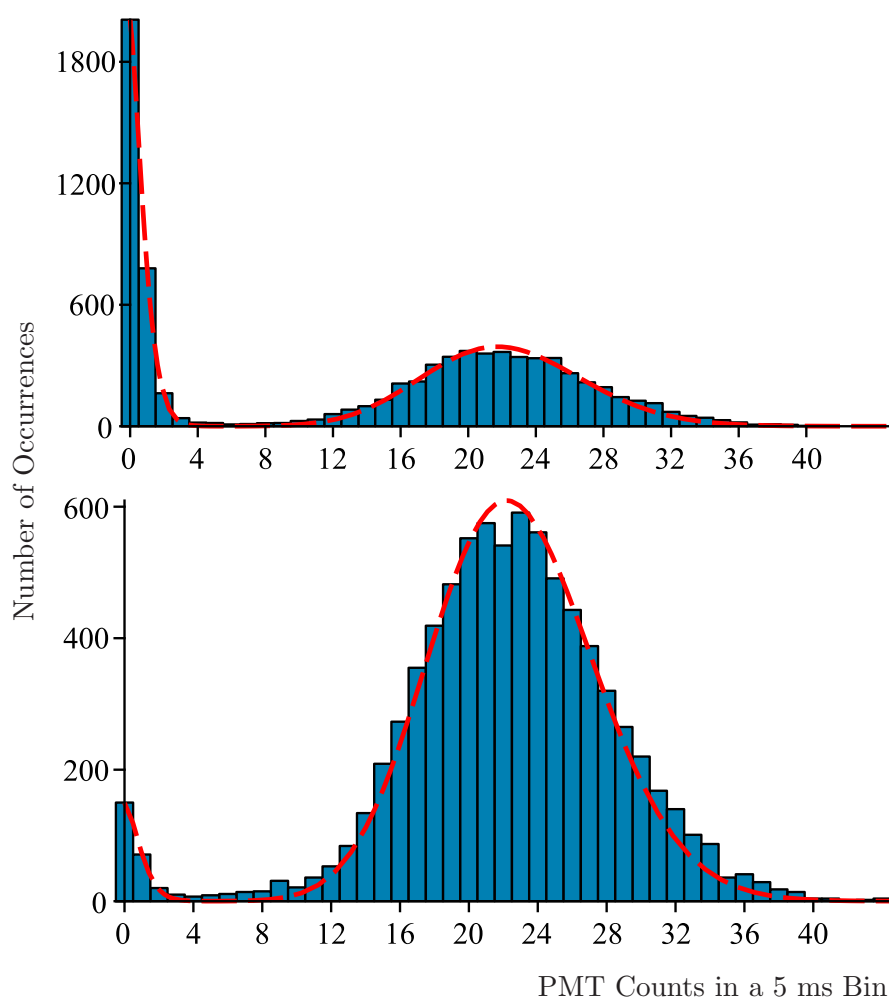


Figure 6.11: Histogram of the number of counts in each 5 ms bin. $(1.0 \pm 0.1) \mu\text{W}$ of 854 nm power is directed at the ion for repumping the $D_{\frac{5}{2}}$ state. The upper and lower plots show data collected with the EOM RF off and on respectively. Summing up the number of bright and dark bins the ion is found to spend 37.9% of the time in the $D_{\frac{5}{2}}$ state with the EOM off and 3.2% of the time with the RF on.

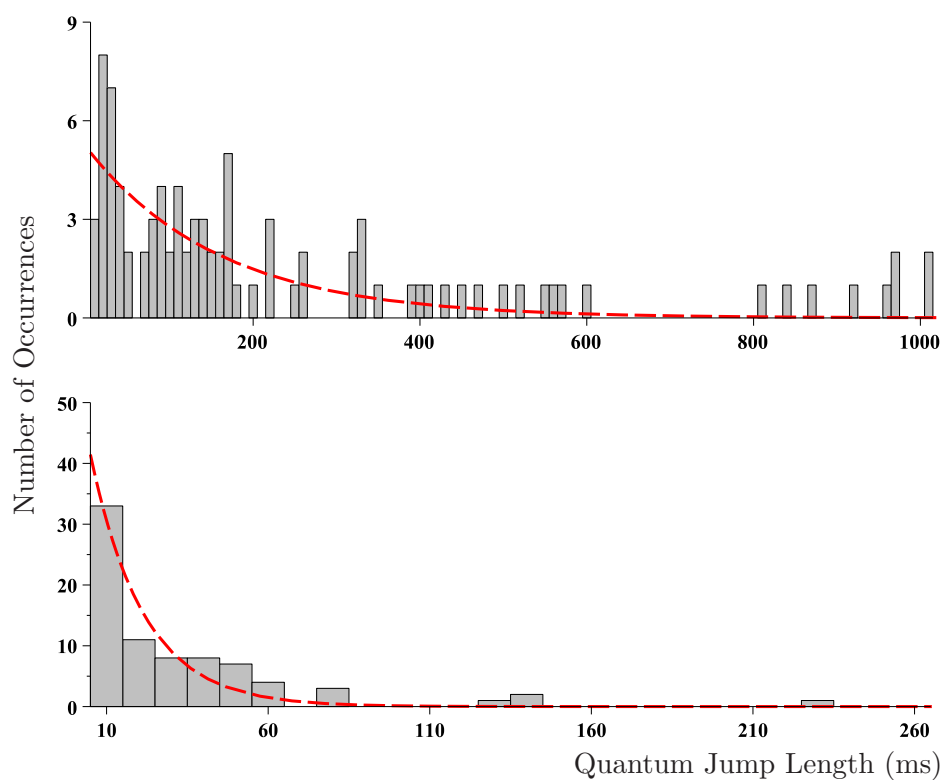


Figure 6.12: Histogram of the quantum jump lengths in the data set where $(1.0 \pm 0.1) \mu\text{W}$ of 854 nm power is directed at the ion for repumping the $D_{\frac{5}{2}}$ state. Samples of these data are shown in figure 6.10. The upper and lower plots show data collected with the EOM RF off and on respectively. From the exponential fit, effective lifetimes of 160 ms and 16 ms are found when the RF to the EOM is off and on respectively. This compares to the natural lifetime of 1.17 s.

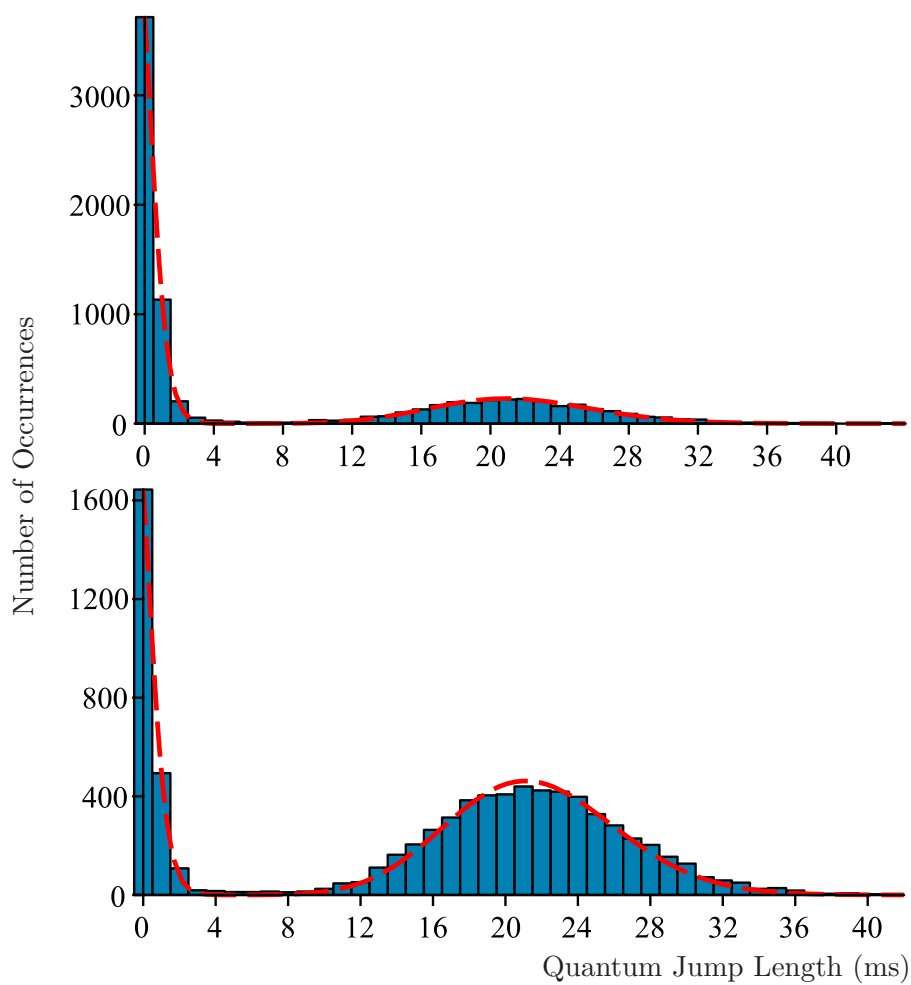


Figure 6.13: Histogram of the number of counts in each 5ms bin. (40 ± 20) nW of 854 nm power is directed at the ion for repumping the $D_{\frac{5}{2}}$ state. The top and bottom plots show data collected with the EOM RF off and on respectively. Summing up the number of bright and dark bins the ion is found to spend 64.6% of the time in the $D_{\frac{5}{2}}$ state with the EOM off and 28.8% of the time with the RF on.

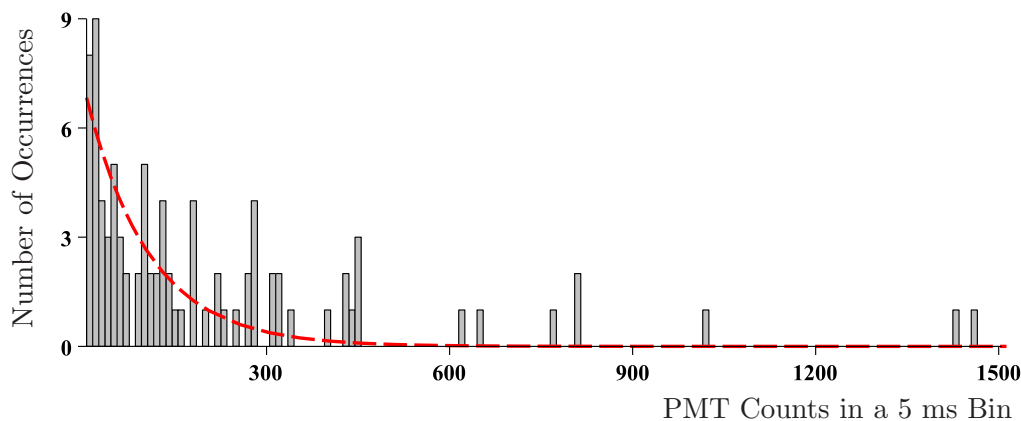


Figure 6.14: Histogram of the quantum jump lengths in the data sets where (40 ± 20) nW of 854 nm power is directed at the ion for repumping the $D_{\frac{5}{2}}$ state. The RF is being applied to the EOM. The exponential fit gives an effective lifetime of the $D_{\frac{5}{2}}$ state of 103 ms. This compares to the natural lifetime of 1.17 s.

We have seen that $1 \mu\text{W}$ of 854 nm light shortens the lifetime of the $D_{\frac{5}{2}}$ state to about 16.45 ms. Increasing the power to $10 \mu\text{W}$ the histograms shown in figure 6.15 are obtained. Note that only 8 seconds of data has been taken which is split into 8000 bins of 1 ms. When the EOM is turned on there is no evidence of the ion being in the $D_{\frac{5}{2}}$ state. We can conclude that the quantum jump length is less than on the order of 1 ms. For the histogram with the EOM turned off although the fit to two Poissonions gives a negligible coefficient for the one corresponding to the dark state there is quite a lot of bins with zero counts and so there is some evidence that there are still quantum jumps.

Figure 6.16 shows the histogram with the EOM turned off when $120 \mu\text{W}$ of 854 nm light is used. Here there is no evidence of quantum jumps and this shows that the EOM need not be used to repump from the $D_{\frac{5}{2}}$ state if enough 854 nm light is available.

In summary 40 nW of 854 nm light directed at the ion with the RF frequencies applied to the EOM does not provide adequate repumping. $10 \mu\text{W}$ of light with the RF on does provide the repumping rate required while if $120 \mu\text{W}$ of light is used then adequate repumping is achieved even without the RF applied to the EOM.

6.4.2 $D_{\frac{3}{2}} \rightarrow P_{\frac{1}{2}}$ Transitions

It was seen in the previous section that if the 854 nm laser has enough power then it is sufficient to repump the $D_{\frac{5}{2}}$ state without requiring sidebands to be put on it via the EOM. With this in mind an experiment was conducted to repump the $D_{\frac{5}{2}}$ state using a

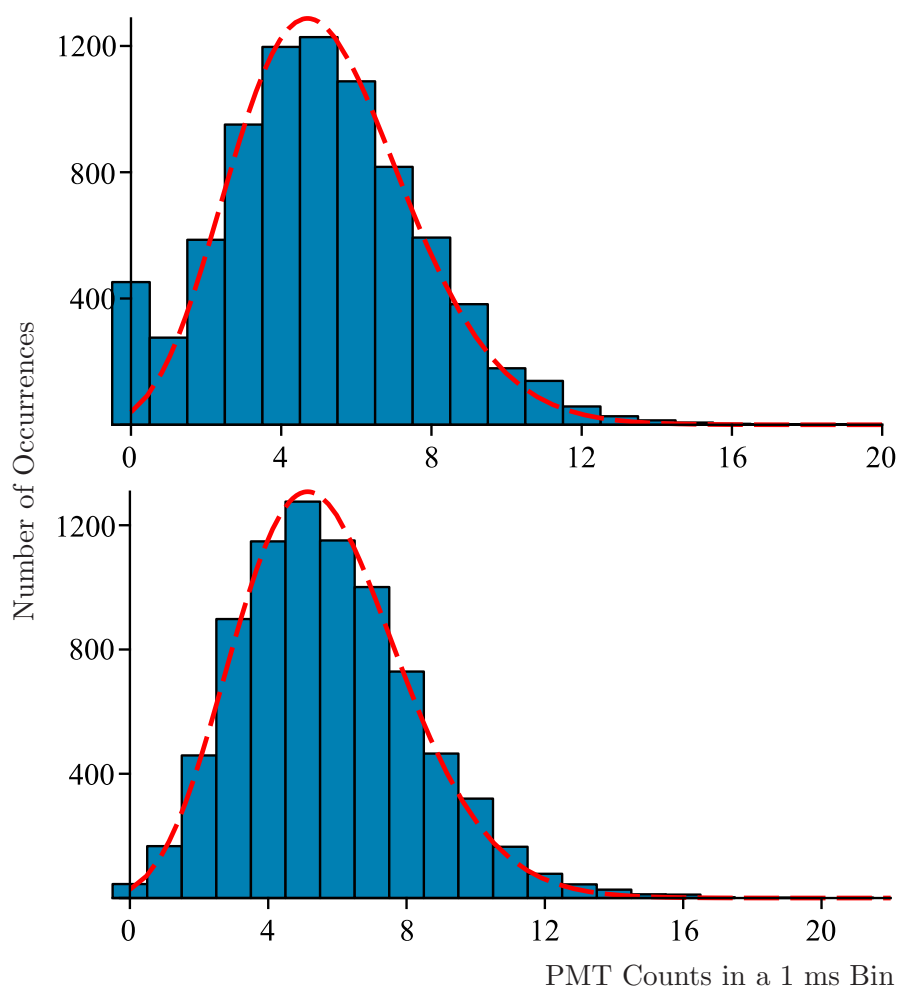


Figure 6.15: Histogram of the number of counts detected in each of 8000 5 ms bins. $(10.0 \pm 0.5) \mu\text{W}$ of 854 nm power was directed at the ion. The top plot is with the RF to the EOM off while the bottom plot is of data with the RF on. The fits to two Poissonians show the ion spends a negligible amount of time in the $D_{\frac{5}{2}}$ state. There is however a peak at 0 counts in the data with the RF off. This suggests quantum jumps of a length longer that ≈ 1 ms are still occurring with no RF present.

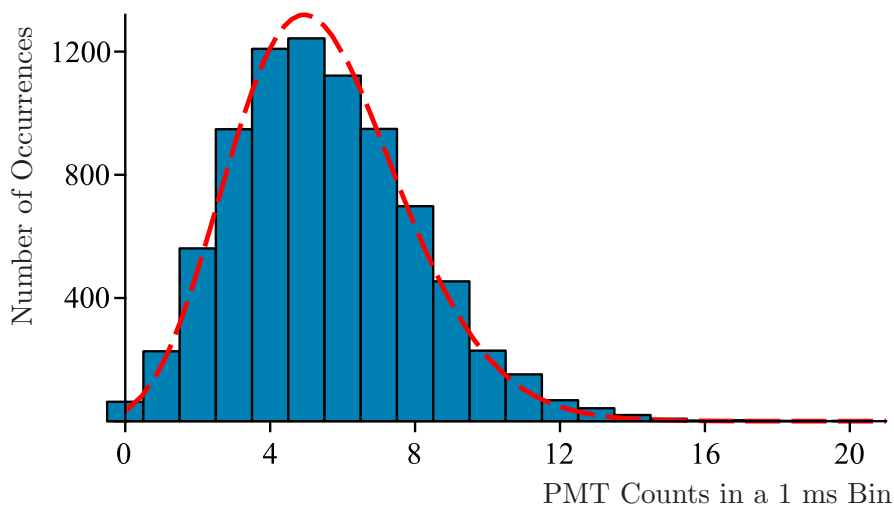


Figure 6.16: Histogram of PMT counts with (120.0 ± 10) μW of 854 nm power directed at the ion. The RF to the EOM was turned off for this data set. There is no evidence that quantum jumps of a length longer than ≈ 1 ms are occurring.

single 866 nm laser. This requires different RF frequencies to be put on the EOM than for the scheme described in figure 6.3. The EOM can thus not be used to put sidebands on a 854 nm laser as the sidebands will not be resonant with the required transitions. It was hoped that there would be enough 854 nm power to repump sufficiently anyway. The advantage of a single 866 nm laser was deemed greater than the disadvantage of requiring more 854 nm power. The 854 nm beam was thus combined with the 866 nm after the EOM. Another difference from the optical setup of figure 4.9 is the beamsplitters which were used to combine the 866 nm lasers were removed to maximise the 866 nm power available from the single laser.

The RF frequencies that must be applied to the EOM to address the $D_{\frac{3}{2}} \rightarrow P_{\frac{1}{2}} \sigma$ transitions are shown in figure 6.3. First order sidebands are required at $2\nu_a$ and $\frac{1}{6}\nu_a$. The higher frequency was created with the same function generator as used in the 854 nm repumping experiments. The lower frequency was created by a second function generator (Hewlett Packard 8643A) which is capable of providing signals between 0.02 and 1.03 GHz. The polarisation of the 866 nm light was set to hit the σ transitions (see the top row of figure 6.3). An experiment was conducted to see how much 866 nm light was required to repump a single ion's $D_{\frac{3}{2}}$ state sufficiently. A single ion was trapped and the signal obtained was optimised. The RF power to the fibre EOM was then decreased to various values and 10 seconds of data were recorded at each value. As the RF power was decreased the amount of light at the frequencies of the σ transitions decreased. The amount of light

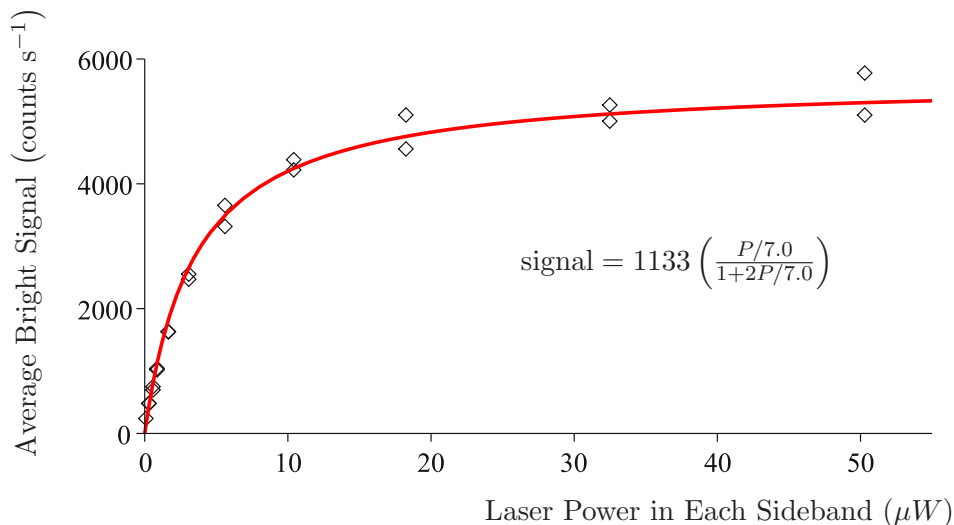


Figure 6.17: Saturation of the $D_{\frac{3}{2}} \rightarrow P_{\frac{1}{2}}$ 866 nm σ repumping transitions as the sideband power is changed via the LF RF ($\frac{1}{6}\nu_a$) on the EOM.

at the σ transitions was calibrated by looking at the various peaks on the same optical spectrum analyser described earlier. The height of the transmission peaks relative to the carrier transition when no RF was applied was noted. This ratio multiplied by the total 866 nm power at the trap, $(495 \pm 5) \mu\text{W}$ gives the power in the sideband. The experiment was conducted by changing the amplitude of the higher frequency (HF) or lower frequency (LF) phase modulation individually. When either frequency is switched off there is no sideband at any of the σ transitions. However when the HF is turned off there are sidebands resonant with the π transitions and so if there is an error in the polarisation then some repumping could occur. When the LF is off there are sidebands only ≈ 1 GHz away from all transitions. There could therefore be some significant repumping from the off-resonant light. Figures 6.17 and 6.18 show the saturation of the 866 nm transition via the scanning of the LF or HF respectively.

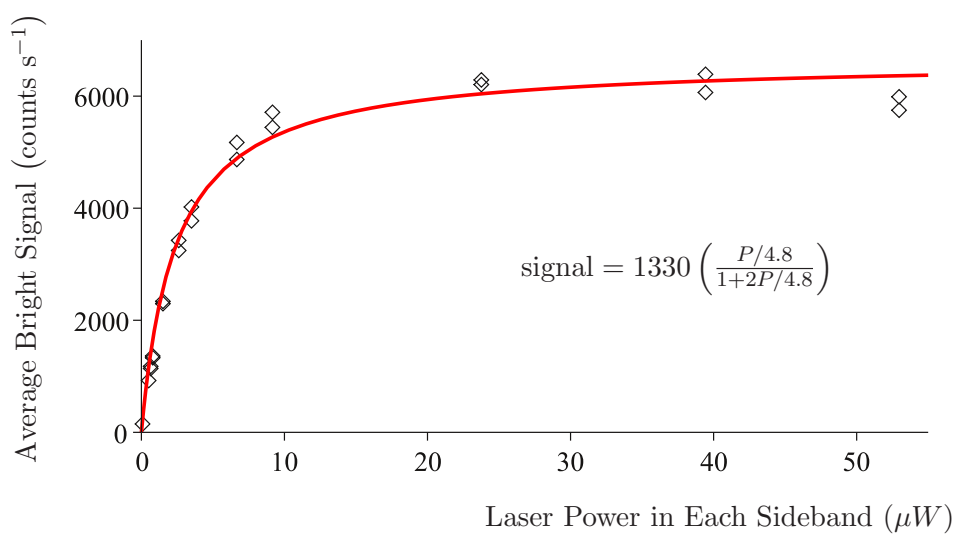


Figure 6.18: Saturation of the $D_{3/2} \rightarrow P_{1/2}$ 866 nm σ repumping transitions as the sideband power is changed via the HF RF ($2\nu_a$) on the EOM.

Pulsed Spectroscopy of the $S_{\frac{1}{2}} \rightarrow D_{\frac{5}{2}}$ Electric Quadrupole Transition in $^{40}\text{Ca}^+$

The first step to using the $S_{\frac{1}{2}} \rightarrow D_{\frac{5}{2}}$ transition for coherent manipulation and sideband cooling is to characterise the transition spectroscopically. In this chapter initial results performed in an RF trap will be presented. This constitutes a proof-of-principle experiment where the same techniques can be used in future experiments in a Penning trap. To perform spectroscopy on an electric-dipole allowed transition such as those used for Doppler cooling at 397 nm the laser frequency would be scanned and the rate of scattered photons from the ion would be measured. It would be very difficult to use this simple method on a quadrupole transition as the rate of photons emitted is simply too low to measure. Instead we indirectly observe if the ion has been excited into the $D_{\frac{5}{2}}$ state using Dehmelt's electron shelving technique (quantum jumps) [81]. This entails observing the plentiful number of photons scattered on the $S_{\frac{1}{2}} \rightarrow P_{\frac{1}{2}}$ transition. This is achieved using a series of laser pulses shown in figure 7.1.

First the ion is Doppler cooled and then optically pumped into one of the $S_{\frac{1}{2}}$ states. The 729 nm laser is then switched on for a set time after which the ion should be in the $S_{\frac{1}{2}}$ or $D_{\frac{5}{2}}$ state (or in a superposition state of the twoⁱ). The 397 nm lasers are then switched on to make a measurement (collapsing any superposition state). If photons are detected from the ion then it must be in the $S_{\frac{1}{2}}$ state as the 397 nm lasers do not couple to

ⁱAs the time required for the $D_{\frac{5}{2}}$ state to spontaneously emit a photon is much longer than the 729 nm pulse time and the detection period it is assumed that only absorption and stimulated emission occurs. In this regime the coherent dynamics analysis of § 3.2 is applicable.

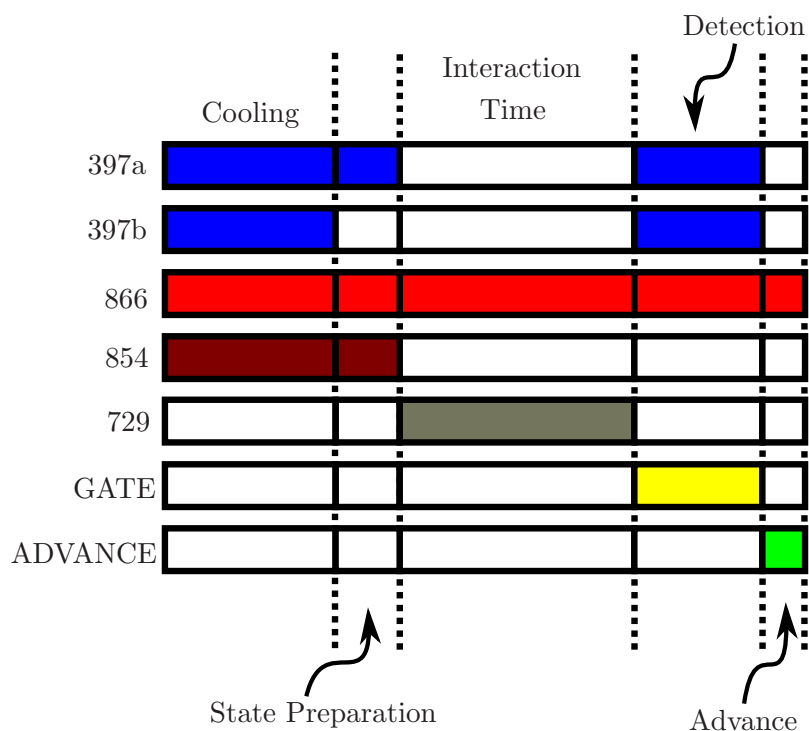


Figure 7.1: The full sequence to be used in the future to perform pulsed spectroscopy on the 729 nm transition. First the ion is Doppler cooled. This is required as it will heat up if the pulse sequence is repeated a large number of times. A cooling time of 5 ms seems to be adequate. State preparation is then performed. This differs for Penning and Paul traps as explained in the text. A simplified sequence omitting the state preparation pulse has been employed for the results presented here. The 729 nm transition is then addressed using a 5-10 ms pulse. A 10 ms pulse is then used to detect the ion’s state. Triggers are sent to both step the bin number and gate the counters as well as to change the 729 nm frequency as explained in the electronic schematic of figure 7.2.

the $D_{\frac{5}{2}}$ state. The 854 nm and 397 nm lasers are then switched on to repump the ion back into the required ground state (and some Doppler cooling is performed to counteract any heating that has occurred while the lasers were off). Repeating this sequence a number of times a probability of excitation into the $D_{\frac{5}{2}}$ state for that combination of 729 nm frequency, pulse duration and laser power is found. The 729 nm laser frequency is then stepped and the process is repeated. Finally we can build up a spectrum of excitation probability as a function of the 729 nm laser frequency. It is noted that the 866 nm lasers can be left on throughout the sequence. They are required for Doppler cooling, state detection and optical pumping and do not couple to the $D_{\frac{5}{2}}$ state during the 729 nm pulse.

7.1 Electronic Setup

Figure 7.2 provides a schematic of the electronics used to perform the pulse sequence. Labview is used to communicate (via a GPIB connection) with the function generator used to produce the RF for the 729 nm laser AOM used as an optical switch. The RF start, stop and step frequencies are set by the user via the Labview interface. When the experiment is initiated Labview resets the function generator and sets its frequency to the start frequency specified. A trigger is then sent to an Arduino Mega microcontroller (§ 4.2.3). The Arduino produces the TTL pulses which toggle on and off the AOM switches (see § 4.2.5 for a description of the AOM electronics). One of the Arduino digital pins is defined as an output for each of the AOM switches. A laser pulse of a given length is produced by setting the relevant pin high and then calling a function which performs the assembler language function NOP (no operation performed) a specified number of times. Pulse lengths can be produced which are multiples of the time a NOP command takes to execute ($0.69 \mu\text{s}$). The minimum pulse time possible is that which calling the function and performing no NOP commands requires ($0.81 \mu\text{s}$). This accuracy is adequate for the $\sim \text{ms}$ pulses used in the experiment. The rise-time of a laser pulse is limited by the AOM switching speed ($\approx 10 \text{ ns}$). There is a delay between the TTL pulse and the switching on of the AOM which is limited by the distance the beam is from the AOM piezo ($\approx 1 \mu\text{s}$ - the propagation time of the acoustic wave). The pulse lengths and the number of times the pulse sequence is repeated at each 729 nm frequency is specified via the Arduino program.

Two separate multi-channel counting cards are used (described in § 4.4.2). One (card 1) is used to view the number of photons observed during the detection period of each pulse sequence. The Arduino has two further digital output triggers. One is a gate which is sent to card 1 to restrict counts to the detection part of the pulse sequence. The second trigger is sent to the bin advance of card 1 so the number of counts in each bin corresponds

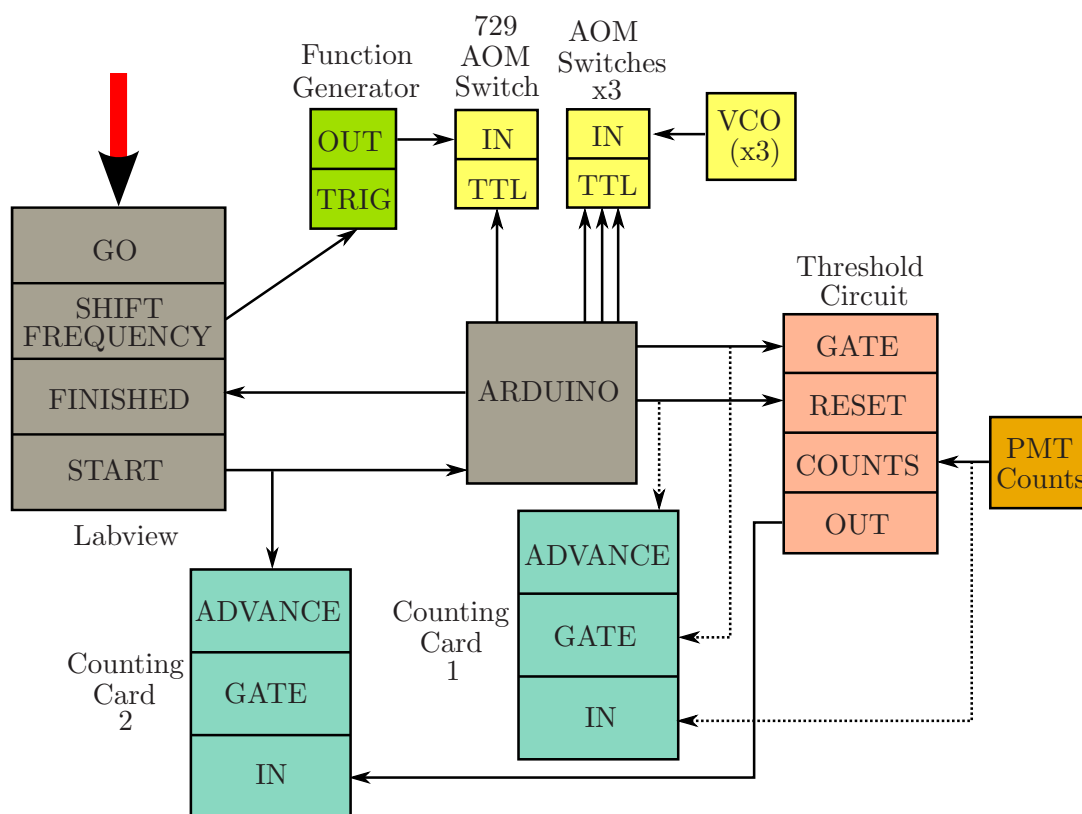


Figure 7.2: Schematic of the electronics used to perform pulsed spectroscopy. The pulse sequence itself is specified in and produced from the Arduino microcontroller. This is sent to the switches of the AOMs to create the laser pulses. Labview is used to specify and communicate to the function generator the 729 nm AOM frequencies. Triggers are sent between Labview and the Arduino to let each other know when their respective jobs are complete. Two counting cards are used. One is used for viewing the counts detected in each detection period (card 1) and the other is for counting the number of times the ion finished in the $D_{\frac{5}{2}}$ state at each 729 nm frequency (card 2). The decision of which state the ion is in is done in real-time using electronics contained in the ‘threshold detector’. This is explained in figure 7.3.

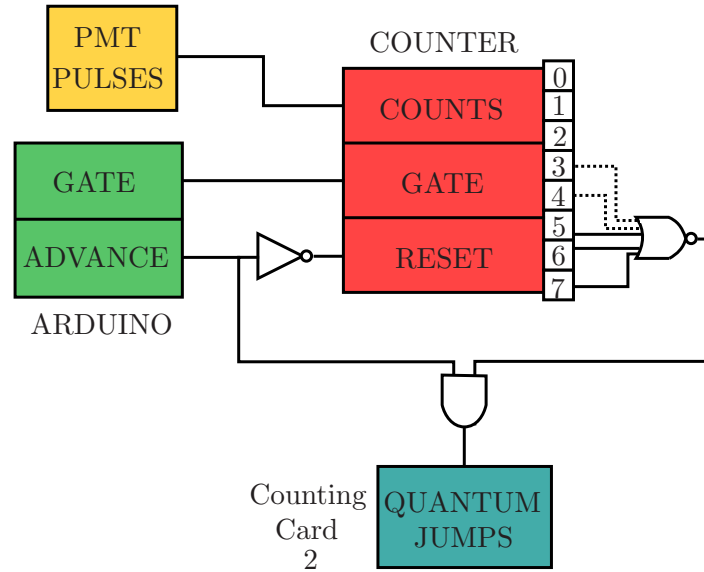


Figure 7.3: Schematic of the circuit used for deciding whether the ion is in the $S_{\frac{1}{2}}$ or $D_{\frac{5}{2}}$ state after a pulse sequence. The 8-bit counter (74HC590) counts the TTL pulses representing photons detected by the PMT. The threshold is chosen by putting a certain number of the counter's output bits into a NOR gate. A pulse is sent to the PMT counting card when the number of counts detected is below the threshold set and when the frequency is being stepped. This point in time is chosen via an AND gate (74HCT08) with the counter's output and the next frequency trigger as inputs. The NOT gate is based on a transistor. The NOR gate is made by simply connecting together the outputs from a set of these NOT gates.

to the number of counts in each detection period.

After each pulse sequence a decision must be made as to whether the number of photons detected means the ion was in the $S_{\frac{1}{2}}$ or $D_{\frac{5}{2}}$ state. This requires a threshold number of photons to be set as there will always be a background of photons detected which are from the laser beam scattering off the trap electrodes or originating from the background light. There will also be electronic dark counts giving a total background of ≈ 1 count in a 10 ms detection period. We opted to make the decision in real time rather than by post-analysing the actual number of counts. This is useful for taking preliminary results as the results of the spectroscopy can be seen in real-time and any errors noticed during the scan. A schematic of the circuit used to assess the ion's state is shown in figure 7.3.

It is based on an 8-bit counter chip. The photons detected are fed directly into this counter which is gated to only record counts in the detection part of the sequence via an Arduino trigger. The trigger from the Arduino which states that the pulse sequence has

ended is sent to the reset input of the counter. This trigger is first sent through a NOT gate to ensure the counter is reset when the trigger is high as this is also required for advancing the PMT card bin. The output from the counter is given in parallel with a pin for each bit. A high is required from this output when the number of counts is above a set threshold. To obtain this a number of the most significant bits are sent through a NOR gate. The output is thus high only if all of the chosen bits are zero. This is the equivalent of saying the output is high if the number of counts is below a certain number (the threshold). The threshold is thus set by choosing the number of bits to include in the NOR gate. This method is restrictive as the threshold cannot take any value. The maximum number of pulses that can be counted using an 8-bit counter is 255 and the threshold must equal 1, 2, 4, 8 ... 128. For the detection length used the threshold required was always low and so enough precision was available. This output is sent through an AND gate with the Arduino trigger which is resetting the counter and so a pulse can only be produced at the end of each sequence and this only occurs if the decision has been made that the ion was in the $D_{\frac{5}{2}}$ state. This is sent to a second multi-channel counting card (card 2) which counts the number of times the ion was in the $D_{\frac{5}{2}}$ state. This card moves to the next bin after receiving a trigger from the Labview program that the 729 nm frequency has been stepped. So the end result is the number of sequences in which the ion was in the $D_{\frac{5}{2}}$ state as a function of the 729 nm frequency.

A trigger from a pulse generator to the Arduino allowed the experiment to be line triggered. This will be a useful feature for future experiments where changes in the ambient magnetic field may affect the Zeeman splitting of the states. The major contributions to ambient magnetic field fluctuations come from mains noise. The Arduino would wait for this trigger before beginning each pulse sequence. No change was seen in the spectra when this was performed.

7.2 Trap and Optical Setup

The method required for state preparation is different depending on whether a Paul or Penning trap is being used. In a Penning trap the magnetic field splits the different Δm_J transitions between the $S_{\frac{1}{2}}$ and $P_{\frac{1}{2}}$ states by much more than the transition or laser linewidths and so by simply turning off one of the 397 nm lasers and keeping on the 854 nm and 866 nm repumpers the ion will eventually fall into the $S_{\frac{1}{2}}$ sub-state which is not being addressed. The situation is more difficult in the case of a Paul trap. The 397 nm transitions are overlapped and so the laser frequency cannot be used to pick a

certain transition. Instead the laser polarisation is exploitedⁱⁱ. Two separate beams are used for the σ^+ and σ^- 397 nm transitions for Doppler cooling and one of these beams is switched off for state preparation. The preliminary results presented in this thesis were conducted in a Paul trap. It was decided not to set up the optics required for state preparation as the plan would be to move to a Penning trap as soon as possible. Instead the ion would be in one of the $S_{\frac{1}{2}}$ sub-states when the 729 nm laser is switched on but which one would be unknown. Averaging over the sequences performed at a given 729 nm frequency the probability of exciting the ion up to the $D_{\frac{5}{2}}$ state would be halved if the ion was being initialised randomly into either of the two ground states.

It is also expected that even when the 729 nm laser is resonant with the correct $S_{\frac{1}{2}} \rightarrow D_{\frac{5}{2}}$ transition the probability of excitation would only be maximally $\frac{1}{2}$ due to averaging of the Rabi oscillations of different motional states of the ion. This averaging was discussed in depth in § 3.2. The results presented in this chapter were conducted in the Split Ring Trap (§ 4.3.1) acting as a Paul trap. The trap was held in the electromagnet used for the Penning trap experiments in this thesis (§ 4.4.1). The trap potential was oscillating at ≈ 1.41 MHz with a peak to peak voltage of ≈ 250 V. A lower estimate for the trap frequency would be ~ 100 kHz. At the Doppler limit the expected oscillation in the probability of being in the $S_{\frac{1}{2}}$ and $D_{\frac{5}{2}}$ states is shown in figure 3.5 at this trap frequency. The Rabi frequencies which are averaged over to create this probability are displayed in figure 3.4. In reality the ion temperature is expected to be higher. The Doppler cooling lasers have a linewidth which is of the order of the cooling transition and so it would not be expected to reach the Doppler cooling limit as the laser frequency cannot be set precisely to an optimum value (§ 3.1). There was also a lot of micromotion present as the trap was not compensated to move the ion's equilibrium position to the centre of the quadrupole field. See § 2.2 for a derivation of the micromotion amplitude and a discussion of micromotion compensation. Micromotion compensation was not conducted for the experiments discussed here as the idea would be to move to a Penning trap where it is not required. When the cooling beams were blocked for ≈ 1 second it would take on the order of seconds for the ion to cool back in so the signal level was at the same level as before. It is thus expected that the ion was hot enough so that enough different Rabi frequencies were averaged over to quickly average out the oscillations shown in figure 3.5 so the maximum probability of exciting to the $D_{\frac{5}{2}}$ state would be $\frac{1}{2}$. Thus together with the randomised state preparation we would expect the maximum probability of excitation to be $\frac{1}{4}$.

The optical setup for the 729 nm laser has been explained in § 4.2.6. The AOM used

ⁱⁱIt is possible to excite on the $S_{\frac{1}{2}} \rightarrow D_{\frac{5}{2}}$ transition for frequency dependent state preparation in a Paul trap. A small magnetic field splits the different Δm_J transitions. Exciting on one of these and then repumping the $D_{\frac{5}{2}}$ state with an 854 nm laser will prepare the ion in the other untouched $S_{\frac{1}{2}}$ sub-state [82].

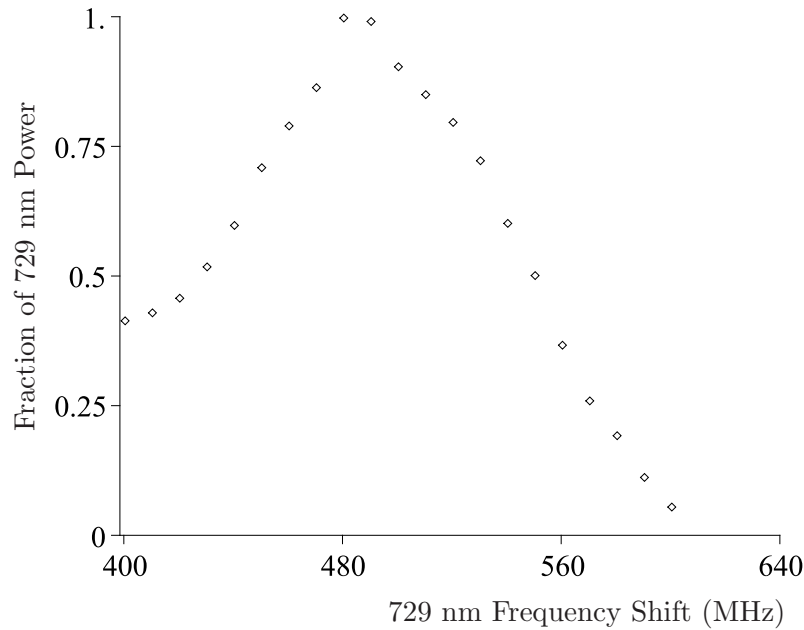


Figure 7.4: Fraction of maximum 729 nm power reaching the trapped ion as its AOM frequency is scanned. The loss is due to a combination of AOM efficiency and fibre coupling loss. The total frequency change (twice the frequency applied to the AOM) is plotted. The maximum 729 nm power at the trap is ≈ 0.5 mW. This is focused to a spot size of $\approx 85 \mu\text{m}$ at the ion.

to change the laser frequency which the ion sees is placed in a double-pass configuration before the optical fibre which transmits the light between the optical tables. The AOM was double-passed so that double the frequency change was achieved. It is preferable to have as large a scan range as possible as this will decrease the likelihood of having to lock the 729 nm laser to a high-order transverse mode of its reference cavity. Double-passing the AOM also helps to keep the beam pointing in the same direction while its frequency is scanned. The beam does however move slightly due to misalignment on the second pass of the AOM when the frequency is scanned and so becomes misaligned from the fibre. The AOM also has a peak in its frequency response. These two factors lead to the power of the 729 nm laser being a function of AOM frequency. A calibration plot is shown in figure 7.4. It is seen that an approximately 160 MHz scanning range is possible without re-optimising the fibre coupling.

7.3 Initial Experimental Results and Analysis

Initial results of pulsed spectroscopy on the $S_{\frac{1}{2}} \rightarrow D_{\frac{5}{2}}$ transition are shown in figure 7.5. The pulse sequence consisted of 5 ms of Doppler cooling, a 5 ms 729 nm pulse and then 10 ms of detection time. A threshold of 4 counts was used to distinguish whether the ion was in the $S_{\frac{1}{2}}$ or $D_{\frac{5}{2}}$ state after the 729 nm pulse (≈ 40 counts were detected when the ion was bright). The frequency shift provided by the 729 nm AOM was scanned from 400 to 560 MHz in 2 MHz steps. At each frequency 400 pulse sequences were conducted and then the probability of being in the $D_{\frac{5}{2}}$ state, $P(D_{\frac{5}{2}})$ is calculated as the fraction of the detection periods where the ion was assessed to be dark. The black and grey plots represent the 729 nm laser being locked to two different transverse modes of its stable cavity (see § 4.2.6 for a description of the lock). The black and grey plots correspond to the laser being locked to the TEM_{0,2} and TEM_{6,0} transverse modes respectively. For a symmetric cavity of length L , and mirrors with a radius of curvature R , the frequency difference of two transverse modes TEM _{l_1, m_1} , TEM _{l_2, m_2} is [83]:

$$\Delta\nu_{l,m} = \frac{c}{2\pi L} \arccos\left(1 - \frac{L}{R}\right) [(l_1 + m_1) - (l_2 + m_2)] \quad (7.1)$$

For the parameters of our cavity ($L = 0.100 \pm 0.001$ m and $R = 0.350 \pm 0.001$ m) the mode spacing is 1479 ± 21 MHz and the FSR is 1499 ± 15 MHz so the modes would be separated by 20 ± 26 MHz. Note that the two transverse modes belong to different longitudinal modes. For the ions to see the same laser frequency the AOM has to compensate for the frequency difference between the cavity modes. The shift in frequency the AOM must provide to see the same structure in the pulsed spectroscopy is seen from the plot to be ≈ 40 MHz. This is within the error of the expected shift. Although the error is large this result gives us confidence that the structure seen is not an artifact.

A number of scans were then taken at different magnetic fields. A small current was passed through the electro-magnet in which the trap is located. The results are shown in figure 7.6. As the current through the coils is decreased the feature moves towards the right of the scan and another similar feature appears from the right hand of the scan and moves left.

The $S_{\frac{1}{2}} \rightarrow D_{\frac{5}{2}}$ transition frequencies as a function of magnetic field strength are shown in figure 7.7. There are 10 transitions in total. Only the 5 with a positive frequency shift are shown in the figure as the other five behave symmetrically. It is postulated that the structure moving towards the right in the scans is made from a number of the 5 transitions with a negative magnetic field - frequency shift gradient. The structure appearing from the right is then the symmetric set which has a positive frequency shift as the magnetic

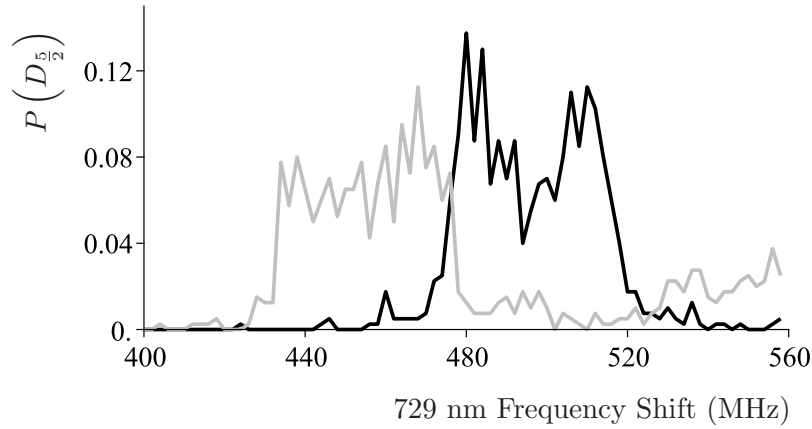


Figure 7.5: Pulsed spectroscopy on the 729 nm transition. The black and grey plots show scans of the 729 nm frequency via its AOM when the laser is locked to the $\text{TEM}_{0,2}$ and $\text{TEM}_{6,0}$ transverse modes of its external cavity respectively. The shift in the feature is ≈ 40 MHz which is within the error of the calculated distance between the modes (20 ± 26 MHz).

field strength is increased.

When conducting the experiment it proved to be impossible to change the current through the coils of the magnet such that the left and right structures overlapped. In other words it was impossible to null the magnetic field which the ion felt. This implies that there was a radial magnetic field, B_r such that the total field is $B = \sqrt{B_z^2 + B_r^2}$.

In figure 7.8 the transition frequency of the midpoint of the left structure (of the scans in figure 7.6) is plotted as a function of the total current through the magnet's coils. The position of the structure has been converted into a transition frequency by plotting its distance from the midpoint of the left and right structures (the point where $B = 0$). A calibration of the magnetic field created for a given total coil current, I at fields up to 0.5 tesla shows a linear fit [51]. Assuming that the fit is still linear at the small fields we are applying and the current only creates an axial field we have $B_z = aI + b$. A linear fit to the points is shown in figure 7.8. This would be valid if $B_r = 0$. However in reality there is a radial field. Substituting in for the total field we obtain $B = \sqrt{cI^2 + dI + e}$, where the constant radial field has been absorbed into the constant e . The Zeeman effect is linear in the magnetic field strength so the transition frequency is $\Delta\nu = m\sqrt{cI^2 + dI + e}$. This fit is shown in figure 7.8. As expected a minimum in the transition frequency is seen (21.8 MHz). A current of 39.8 mA through the coils is required to null the axial magnetic field.

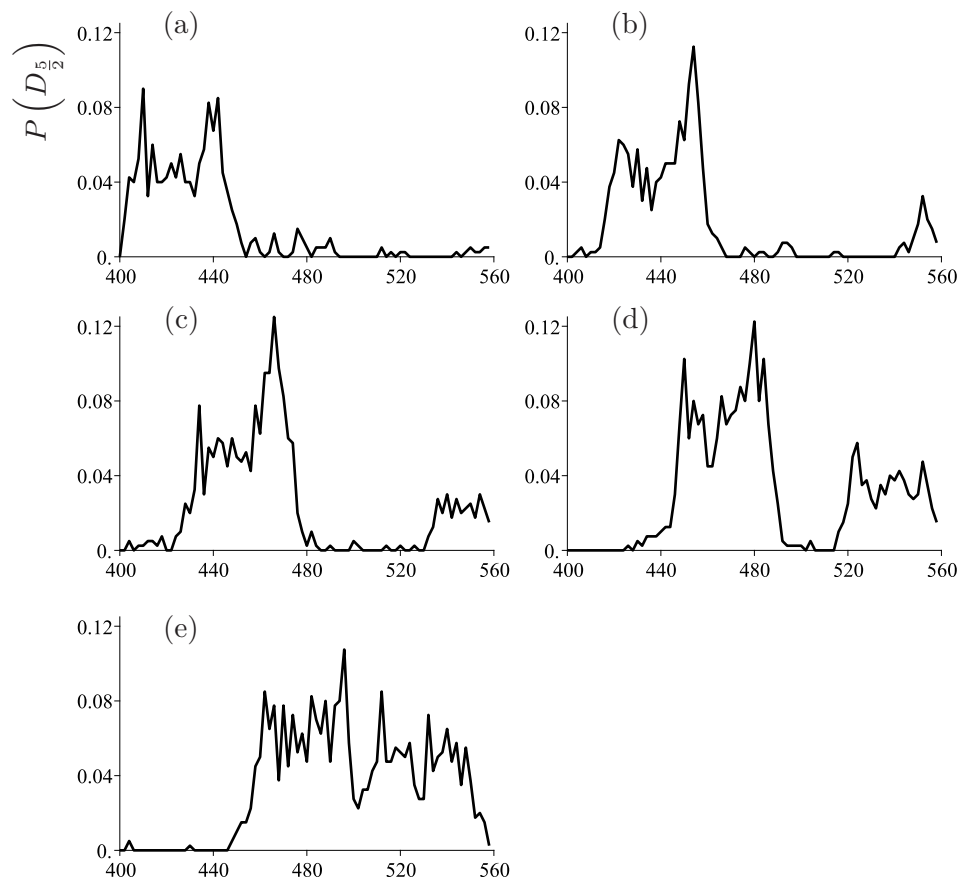


Figure 7.6: Pulsed spectroscopy scans of the 729 nm transition at different magnetic field strengths at the ion. Plots a to e are for total currents to the two coils of 90 mA to 50 mA in 10 mA steps. Two features are seen to move towards each other as the field is decreased. It is postulated that each of these features corresponds to a number of 729 nm transitions. See the text for a discussion of which transitions they may be.

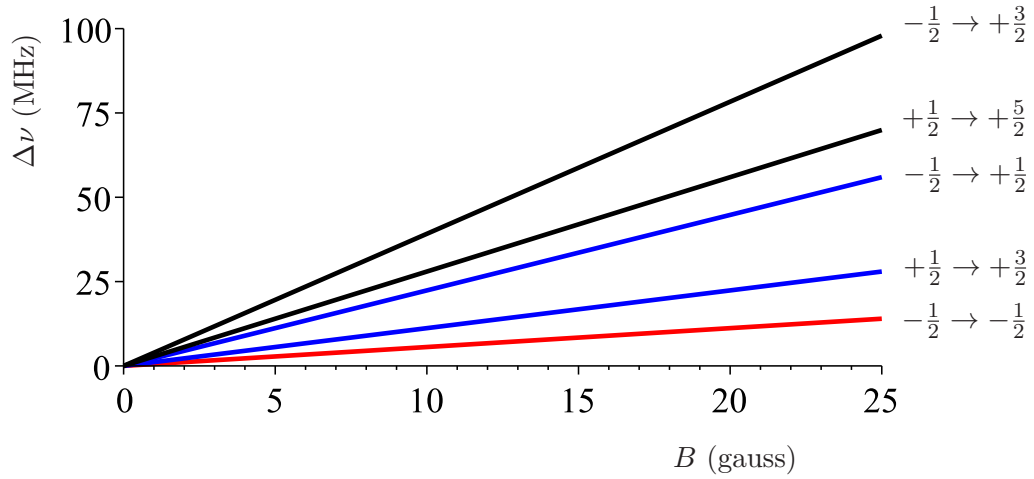


Figure 7.7: 729 nm transitions with a positive frequency shift as the magnetic field is increased. The relative transition strengths from top to bottom are: $\frac{1}{30}$, $\frac{5}{30}$, $\frac{2}{30}$, $\frac{4}{30}$ and $\frac{3}{30}$. The $|\Delta m| = 0, 1$ and 2 transitions are shown in red, blue and black respectively.

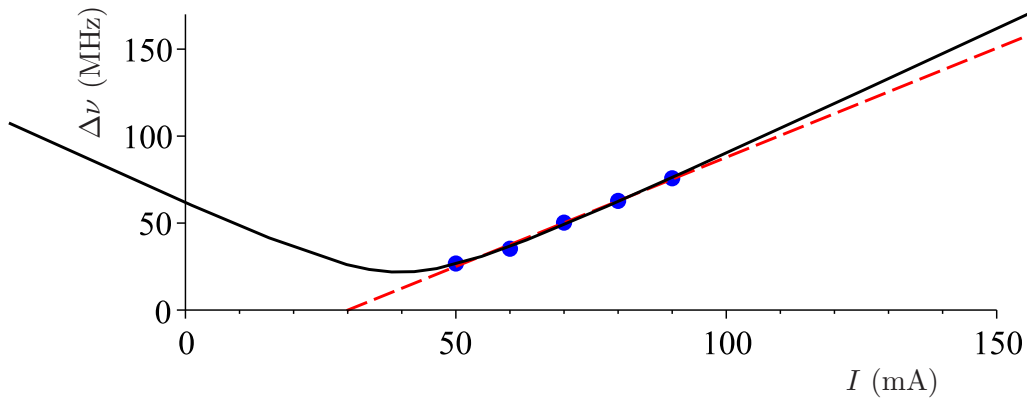


Figure 7.8: The shift of the midpoint of the left structure in the scans of figure 7.6 as a function of the total current through the magnet's coils. A linear fit is shown (dashed line). The solid line assumes a constant stray radial field and so fits to $\Delta\nu = m\sqrt{cI^2 + dI} + e$ where m , c , d and e are constants.

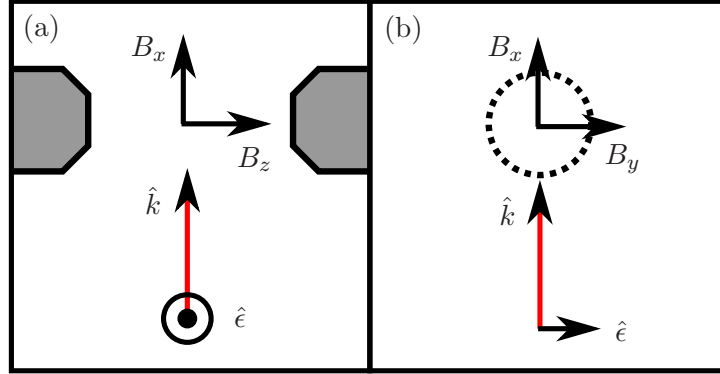


Figure 7.9: 729 nm laser propagation, \hat{k} and polarisation \hat{e} directions with respect to the magnetic field $B = B_x\hat{x} + B_y\hat{y} + B_z\hat{z}$. The shaded shapes to the left and right of (a) are the pole pieces of the magnet. In (b) the pole pieces are denoted by the dotted circle. The coils generate a magnetic field along the \hat{z} direction. The diagram on the right gives a view through the iron core.

7.3.1 Tentative Attribution of Spectral Features

The 729 nm laser polarisation is linear and its direction relative to the magnet's coils is shown in figure 7.9. The selection rules for quadrupole $|\Delta m| = 0, 1$ and 2 transitions each depend on the laser's propagation direction, \hat{k} and polarisation direction, \hat{e} (for a linearly polarised beam).

The relative transition probabilities, $g^{|\Delta m|}$ are shown in figure 7.10. These are plotted directly from the equations in reference [25]:

$$\begin{aligned}
 g^0 &= \frac{1}{2} |\cos \phi \sin 2\theta| \\
 g^1 &= \frac{1}{\sqrt{6}} |\cos \phi \cos 2\theta + i \sin \phi \cos \theta| \\
 g^2 &= \frac{1}{\sqrt{6}} |\cos \phi \sin 2\theta + i \sin \phi \sin \theta|
 \end{aligned} \tag{7.2}$$

Where θ and ϕ are the angles between the magnetic field and the laser beam and polarisation directions respectively.

Let us first consider the case where $B_r = 0$. It may be helpful to look at the left diagram of figure 7.9 with $B_x = 0$. We have $\theta = \frac{\pi}{2}$ and $\phi = \frac{\pi}{2}$ and so from figure 7.10 only the $|\Delta m| = 2$ transitions are allowed. If $B_z = 0$ then we have the situation shown in the right diagram of figure 7.9. If the magnetic field points along x then $\theta = 0$ and $\phi = \frac{\pi}{2}$. If the magnetic field points along y then $\theta = \frac{\pi}{2}$ and $\phi = 0$. In both these cases only the $|\Delta m| = 1$ transitions are allowed. If the radial field points somewhere between the x and

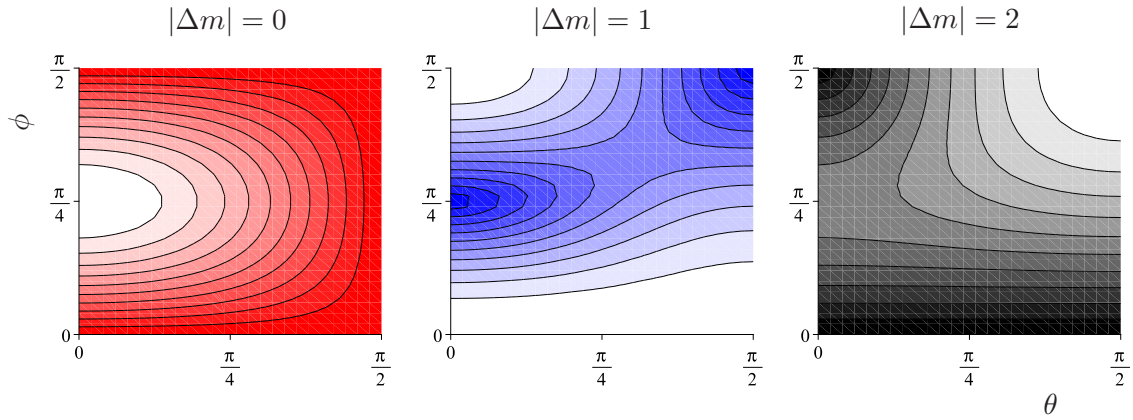


Figure 7.10: Quadrupole transition probabilities as a function of the angle between the magnetic field and the laser propagation direction, θ and its polarisation, ϕ (linear polarisation). These are plotted directly from equations 7.2. The white regions give the highest excitation probability.

y directions then we will be somewhere on a line from the bottom right to the top left of each of the plots in figure 7.10 and so it is possible all transitions are allowed.

In plot (a) of figure 7.6 it is estimated that $B_z \approx 3B_r$. The magnetic field direction should be close to being along z and so the $|\Delta m| = 2$ transitions should be strongly favored. So it is possible that when B_z is low we are observing the $|\Delta m| = 0, 1$ and 2 transitions while when it is high we only see the $|\Delta m| = 2$ transitions. There is evidence for this if we look at the spread of the structure over the different scans. It stays at ≈ 60 MHz. This wouldn't be expected if it was the same transitions being observed, they would be expected to spread out as B is increased (see figure 7.7). The frequencies of the $|\Delta m| = 0, 1$ and 2 transitions are spread over 3.36 MHz/gauss. The spread of just the $|\Delta m| = 2$ transitions is 1.12 MHz/gauss. If we assume that we are observing all the $|\Delta m| = 0, 1$ and 2 transitions when $B_z \approx 0$ and a previous calibration of the current through the coils of the electromagnet to the field of 0.53 gauss/mAmp (using a Hall probe) is valid at these low fields then B increases from 10 to 30 gauss over the scans. The spread of the $|\Delta m| = 0, 1$ and 2 transitions equals the spread of the $|\Delta m| = 2$ transitions at the higher field and the structure's width should stay constant as observed.

It is difficult to see individual transitions in the spectra taken. A possible reason for this is that the transitions are being Doppler broadened to approximately 10 MHz. This would correspond to an ion temperature of ≈ 47 mK. This compares to a Doppler limit temperature of 0.35 mK. The uncompensated micromotion described earlier could be a cause of this spectral broadening. The maximum velocity during the micromotion oscillation is given by the amplitude of the micromotion multiplied by the oscillation

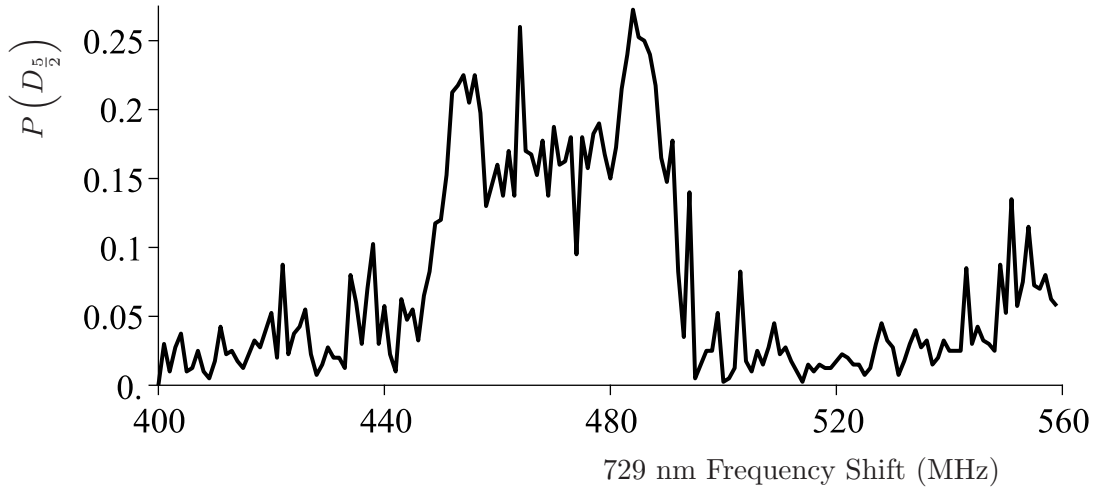


Figure 7.11: A detailed scan of the $m_J = \frac{1}{2} \rightarrow -\frac{3}{2}$ and $m_J = -\frac{1}{2} \rightarrow -\frac{5}{2}$ transitions. The 729 nm frequency is scanned in 1 MHz steps. 400 pulse sequences were conducted at each frequency and the 729 nm pulse was 10 ms. A filter was placed in the 854 nm beam to reduce light scattering into the 1st order of the AOM when its RF was turned off. It is noted that the maximum probability of excitation to the $D_{\frac{5}{2}}$ state is $\approx \frac{1}{4}$ as expected.

frequency (assumed to be the frequency of the applied trapping voltage). This velocity can be estimated by the size of the spectral feature seen to be $\approx 15 \text{ ms}^{-1}$ and hence the micromotion amplitude can be found ($\approx 2 \text{ } \mu\text{m}$). The micromotion amplitude can be linked to the ion's distance from the centre of the pseudopotential by equation 2.26. This suggests that the ion is $\approx 0.01 \text{ mm}$ from the trap centre. This is a very small distance and so could easily explain the spread of the spectral feature seen.

The fact that the structure moving towards the right is larger than the one moving towards the left is attributed to the lower 729 nm power at those AOM frequencies (as shown in figure 7.4). It is seen that the size of the two structures become more even as the magnetic field is decreased to bring them closer. Here there is a smaller differential in the 729 nm laser power.

It is noted that the probability of exciting the ion into the $D_{\frac{5}{2}}$ state never reaches the 25% expected. Another scan was taken which does reach this value (figure 7.11). Two changes were made for this new scan. Firstly the 729 nm pulse time was increased to 10 ms. Also it was noticed that some 854 nm light was leaking through the optical fibre and to the ions even when the RF to its AOM was switched off. A filter ($\approx 1\%$ transmission) was used to reduce the 854 nm power such that no light was detected when the AOM was switched off but enough light was let through when it was switched on to repump the ion.

Attempts were made to see motional sidebands by stepping the 729 nm laser by a smaller frequency (4, 10 and 20 kHz steps). No structure was seen. There are two main factors which are expected to increase the observed width of the individual sidebands. Firstly the laser linewidth and drift over the timescale of the experiment. Secondly the magnetic field instability causing a drift of the transitions.

The linewidth of the laser addressing the $S_{\frac{1}{2}} \rightarrow D_{\frac{5}{2}}$ transitions has been estimated to be less than 1 kHz relative to the stable cavity it is locked to. It may be possible that this cavity is drifting over the timescale of the experiment or additional noise is added as the laser passes through a fibre on its path to the ion.

The specified magnet supply current stability at low magnetic fields would lead to a frequency drift of ± 0.5 kHz/30mins for the 729 nm transition with the largest Zeeman shift. It was explained in § 4.4.1 that this would be a lower estimate of the magnetic field stability. The two coils of the electromagnet are connected in parallel so a relative resistance change between the two leads to a change in the current passing through each coil.

The broadening of the transitions between different m_J states resulting in them overlapping would make seeing the motional sidebands more difficult as there is a smaller separation between any two sidebands. It was explained that this broadening could be due to a combination of the high thermal state of the ion and it undergoing micromotion as it is in an uncompensated trap. Figure 7.12 shows the five $S_{\frac{1}{2}} \rightarrow D_{\frac{5}{2}}$ transitions with a positive Zeeman shift. They are shown at a magnetic field of the order of that used in obtaining the spectra in this chapter (10 gauss). A purely thermal broadening is shown. The ion temperature is chosen as 30 mK to demonstrate the overlap of the separate transitions.

Figure 7.13 shows a single transition at 0 K which is then broadened by micromotion. The ion's motion causes a frequency modulation of the laser and results in sidebands separated by the micromotion frequency. The micromotion frequency is equal to the estimated trap frequency of 100 kHz. At a high modulation index (high amplitude of the ion's motion) there are a lot of sidebands present and there are peaks corresponding to the maximum velocity of the ion during its motion. The laser and transition linewidths and jitter are assumed to be much smaller (on the timescale of the experiment) than the trap frequency such that the sidebands are easily resolved.

Figure 7.14 shows what a spectrum at a lower temperature and with no micromotion present would look like. The temperature chosen is 0.34 mK which is the theoretical Doppler limit using the $S_{\frac{1}{2}} \rightarrow P_{\frac{1}{2}}$ transition for Doppler cooling. There are now less sidebands present and it would be conceivable to take a spectra resolving the whole structure. It should then be possible to find and address the first red sideband to try and perform

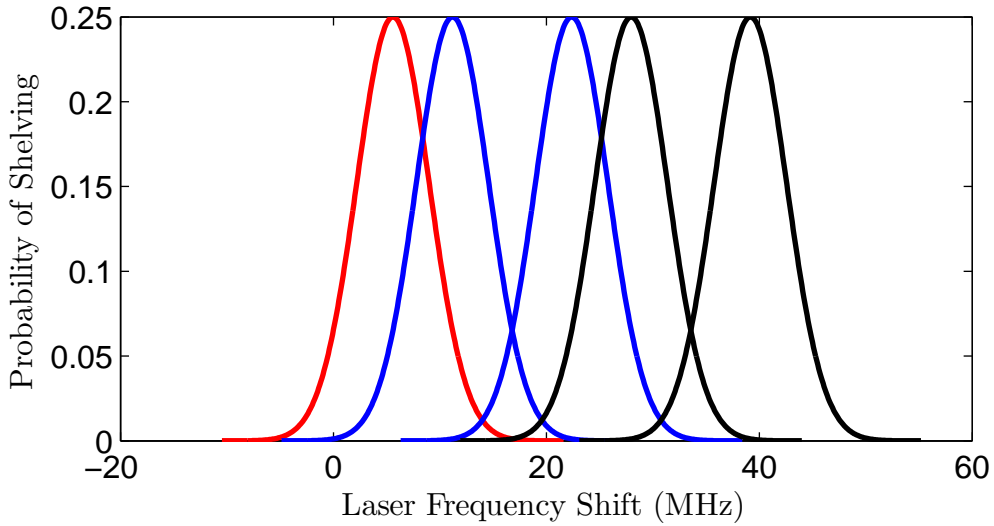


Figure 7.12: The five $S_{\frac{1}{2}} \rightarrow D_{\frac{5}{2}}$ transitions which have a positive frequency shift as the magnetic field is increased. The $\Delta m = 0, 1$ and 2 transitions are shown in red, blue and black respectively (following figure 7.7). A Gaussian spread of each transition due to an ion temperature of 30 mK is shown. The Zeeman shift of the transitions is due to a magnetic field of 10 gauss.

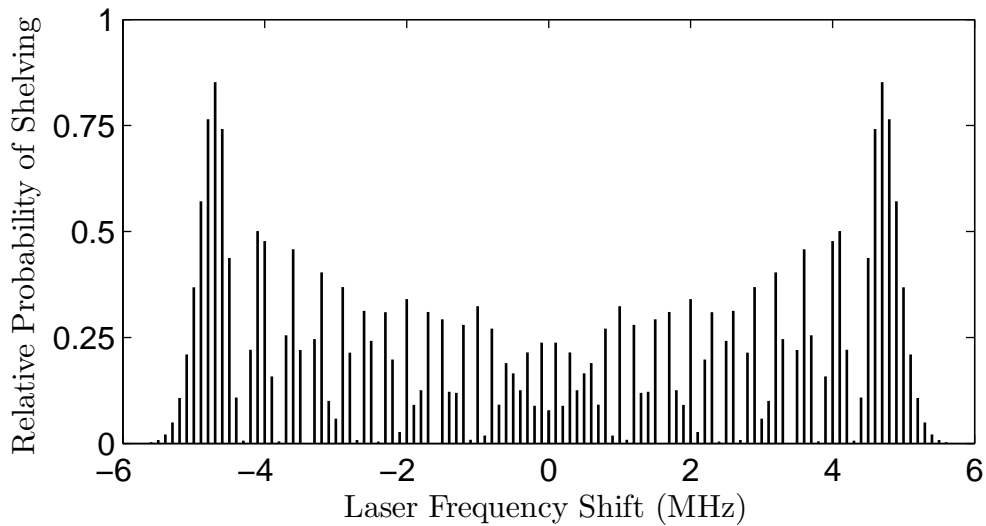


Figure 7.13: An example of the spread of an electronic transition due to micromotion. The amplitude of the motion has been chosen to produce an approximate 10 MHz spread of the single transition (originally at the origin of the x-axis). Sidebands are seen spaced at the trap frequency (0.1 MHz here). At high modulation amplitudes (as is the case here) peaks are observed at the maximum frequency shift.

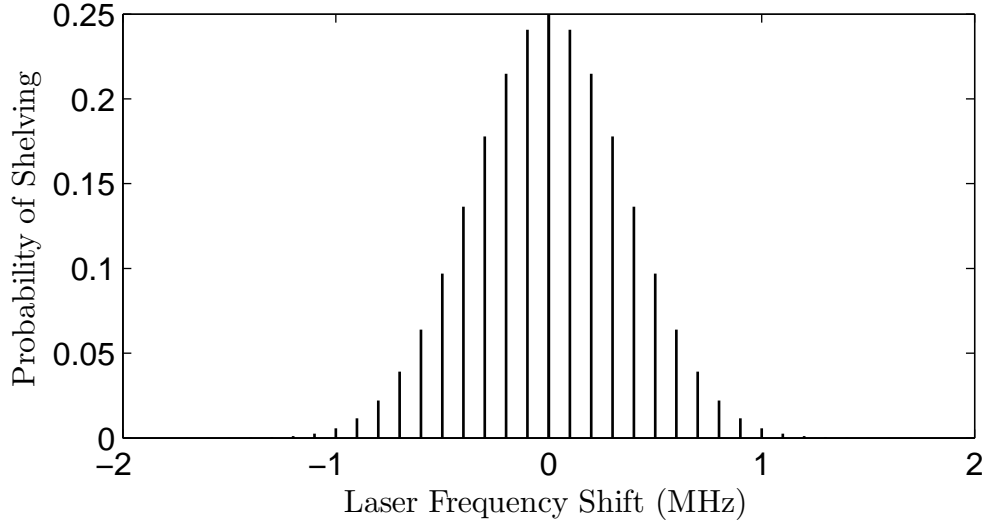


Figure 7.14: A simulated spectrum of a single $S_{\frac{1}{2}} \rightarrow D_{\frac{5}{2}}$ transition. The laser and transition linewidths and jitter over the timescale of recording the spectrum are assumed to be much smaller than the trap frequency (100 kHz). The temperature of the ion is 0.34 mK. This corresponds to the Doppler limit temperature at this trap frequency. The envelope of sidebands is a Gaussian function. At lower temperatures the sideband amplitudes deviate from this and the associated Legendre polynomials of equation 3.17 are required.

sideband cooling as described in § 3.3.

To be able to perform sideband cooling, the sidebands must be well resolved and the ion must be at a low initial temperature. An ideal first step would be to see some sideband structure. Changes can then be made to the experiment and the factor limiting the resolution can be quickly found by observing the spectra obtained. To have the best chance of seeing some structure for the first time, as high a trap frequency as possible should be used to increase the sideband separation. Using a superconducting magnet at 2.5 tesla (available in the laboratory) motional frequencies in a Penning trap of approximately 800 kHz can be obtained. The superconducting magnet will have a more stable field and will shield from external magnetic fields. The different $S_{\frac{1}{2}} \rightarrow D_{\frac{5}{2}}$ transitions will be separated by of the order of 10 GHz and so will not be overlapped. There will also be no micromotion present.

Conclusions and Future Outlook

8.1 Conclusion

In this thesis experiments using single $^{40}\text{Ca}^+$ ions in a Penning trap have been described. The experiments have been geared towards achieving sideband cooling in a Penning trap for the first time.

First the observation of magnetic field induced quantum jumps was described. This observation was explained by the ion being shelved in the $D_{\frac{5}{2}}$ state which was not being repumped. This electric-dipole forbidden transition becomes weakly allowed due to magnetic field induced mixing of states with the same S , L and m_J but with different J quantum numbers. The ion's eigenstates as a function of magnetic field were calculated and the rate of shelving in the $D_{\frac{5}{2}}$ state as a function of magnetic field was found. The experimentally observed shelving rate was shown to agree well with the calculated rate.

The magnetic field induced J-mixing causes complications in using the $S_{\frac{1}{2}} \rightarrow D_{\frac{5}{2}}$ quadrupole transition for coherent manipulation. It leads to a degradation in the readout fidelity which is at a tolerable level for a $^{40}\text{Ca}^+$ ion at 1 tesla. It also makes repumping from the $D_{\frac{5}{2}}$ state crucial for efficient Doppler cooling in a Penning trap at 1 tesla. Without repumping this state the ion is dark the majority of the time and so is not being cooled. The ion must be repumped out of all six m_J sub-levels of the $D_{\frac{5}{2}}$ state. A scheme to achieve this using a single 854 nm diode laser and a high bandwidth fibre EOM was described. A quantum-jump free signal (where jump lengths > 1 ms are detected) is seen at 1 tesla for the first time using this scheme.

The successful repumping of the $D_{\frac{5}{2}}$ state was a necessity before pulsed spectroscopy of the $S_{\frac{1}{2}} \rightarrow D_{\frac{5}{2}}$ transition could be performed even in a Paul trap. Without this repumping a time delay much greater than the ≈ 1 s lifetime of the $D_{\frac{5}{2}}$ state would be required

between each interrogation of the transition resulting in an unrealistically long experiment. Preliminary results of pulsed spectroscopy on the $S_{\frac{1}{2}} \rightarrow D_{\frac{5}{2}}$ quadrupole transition in a Paul trap have been presented. The same method developed to pulse the lasers and detect the state of the ion can be used in future experiments in the Penning trap.

As well as these specific experiments, improvements to the experimental setup have been described in this thesis. This includes the use of photoionisation loading using a pulsed, frequency-doubled YAG laser. This method has many advantages over the previous method of electron bombardment. It is more efficient so a lower calcium oven temperature can be used which results in a lower pressure at the trap and less coating of the trap electrodes. There is also less charging up of the resistive materials around the trap due to the electron beam. The charged material can modify the trap potential which the ion sees. Also there are now less restrictions on future trap geometries as no longer must a filament be included which would require a clear line of sight along the magnetic field direction to the trap centre. This method of photoionisation does not currently appear in the literature and so this will be reported when results of pulsed spectroscopy in the Penning trap are published.

A great simplification to the experimental apparatus required to laser cool a $^{40}\text{Ca}^+$ ion in a Penning trap is the reduction of the number of lasers required to repump from the $D_{\frac{3}{2}}$ state from four to one. Sidebands were put on this single laser using a fibre EOM with two RF frequencies applied to it. The stability of the RF frequencies applied to the EOM is much better than the ≈ 20 MHz transition linewidth and so does not need to be optimised from day to day. A single laser frequency therefore only needs to be set.

The method used to measure the wavelengths of the lasers has been improved. Now a ≈ 60 m fibre link to another group's laboratory enables the use of their commercial wavemeter. This wavemeter is set up to read multiple wavelengths simultaneously, it also requires less light than our previous wavemeter. This results in the ability to send some of the laser light to the wavemeter so that the laser wavelengths can be read while the ion is cooled and experiments are performed.

8.2 Future Outlook

The next logical step is to perform pulsed spectroscopy on the $S_{\frac{1}{2}} \rightarrow D_{\frac{5}{2}}$ quadrupole transition in $^{40}\text{Ca}^+$ in a Penning trap.

As well as the electromagnet used in the experiments described in this thesis the group has a superconducting magnet. The stability of the magnetic field produced by the superconducting magnet should be at least an order of magnitude better than that provided by the electromagnet. A higher stability results in a greater chance of resolving

the sidebands which are separated by the trap frequency. It will also reduce decoherence when coherently addressing the transition. The field that the superconducting magnet can produce is also higher (2.5 tesla compared to 1 tesla). A higher magnetic field leads to higher trap frequencies and hence a larger frequency separation between the carrier and sideband transitions. This means the sidebands are more easily resolved. This also reduces the amplitude of off-resonant transitions at the carrier and blue sidebands when the laser is resonant with the first red sideband during sideband cooling. It has been shown (§ 3.3) that this leads to a faster cooling rate and a lower final temperature. The amount of energy removed per sideband cooling cycle is proportional to the trap frequency. This also helps to increase the sideband cooling rate. The ion is also further into the Lamb-Dicke regime after Doppler cooling. Being in this regime is a requirement for sideband cooling and so it is more likely it will be effective.

A trap which fits inside the superconducting magnet has been developed by another student (see reference [84]) and clouds of ions have been trapped and Doppler cooled at 1.75 tesla. This trap will be modified to effectively trap and image single ions.

It has been discussed that to perform conventional sideband cooling the ion needs to be in the Lamb-Dicke regime. In this regime the ion usually does not change its phonon number when it spontaneously emits. This regime requires that both the Lamb-Dicke factor (which depends on the trap frequency and wavelength of light) and the average phonon number are small. It is important to achieve an average phonon number close to the Doppler cooling limit. It was observed that the linewidth of the Doppler cooling lasers used is comparable to the linewidth of the Doppler cooling transition. A reduction in the laser linewidth should help to reach a lower ion temperature prior to applying sideband cooling. A PDH lock to a cavity for each 397 nm laser should reduce the laser linewidth and help to reach the Doppler limit. The higher trap frequencies in the superconducting magnet trap will also lead to a lower phonon number at the Doppler cooling limit. Unlike the traps described in this thesis the superconducting magnet trap will have an axial cooling beam so the axial motion can be effectively cooled.

It has been stated that to achieve a pulsed spectroscopy spectrum of the $S_{\frac{1}{2}} \rightarrow D_{\frac{5}{2}}$ transition with the best possible resolution of the sidebands as stable a magnetic field as possible is required. The stability over the timescale which the pulsed spectroscopy takes to complete is important. This time can be reduced by increasing the 729 nm light intensity at the ion resulting in a higher Rabi frequency. One option is to use a tapered amplifier which is now available at this wavelength to increase the amount of 729 nm light available. Another option is to use a master-slave arrangement. Here two diode lasers are used. The first is an ECDL setup whose light is locked to an external stable cavity using the same

PDH lock described in this thesis. This light is then used as the seed light of the second diode. All of the light from this second diode can be used for the experiment (rather than for feedback, for locking etc) and so more light is available and higher Rabi frequencies can be achieved.

It was discussed that a possible use of sideband cooled $^{40}\text{Ca}^+$ ions in a Penning trap could be the manipulation of zigzag crystals. In previous experiments at 1 tesla it was found that two ions were the maximum number that could be lined up along the magnetic field direction [6]. The minimum number of ions required to create a zigzag crystal is three. Using a higher trapping magnetic field to create a larger radial trapping force could be the answer in achieving a three ion crystal. To align ions along the magnetic field the axial potential must be reduced below a critical fraction of the radial potential. The more ions along the trap axis, the smaller the trap depth at the outer ions of the crystal. A higher magnetic field leads to a larger possible axial trap depth and so the ions are less likely to be lost.

If the ion's sideband spectrum is observed and sideband cooling is successful then heating and decoherence rates can be accurately measured in a Penning trap. Attempts will then be made to trap and cool a 3-ion crystal along the trap axis and manipulate it.

Appendix A

Details of the $P_{\frac{1}{2}} \rightarrow D_{\frac{5}{2}}$ Transition Rate Calculation

This appendix contains some equations relating to the calculation of the $P_{\frac{1}{2}} \rightarrow D_{\frac{5}{2}}$ transition rate caused by the J-mixing effect. See § 5.2 for the rest of the calculation and further explanation.

The equations here relate to the calculation of n^{-1} defined in equation 5.21. They follow from equation 5.25. The mixed states defined by the coefficients of equation 5.15 are first substituted in. This is shown for the $P1_{+\frac{1}{2}} \rightarrow D2_{m_J}$ term as the first part of equation A.2. The coefficients are combinations of normalisation and mixing coefficients and are defined in equation A.1.

$$\begin{aligned}
 a_{m_J, m'_J} &= N_{2, m_J} N_{1, m'_J} M_{1, m'_J} \\
 b_{m_J, m'_J} &= N_{2, m_J} M_{2, m_J} N_{1, m'_J} \\
 c_{m_J, m'_J} &= N_{2, m_J} M_{2, m_J} N_{1, m'_J} M_{1, m'_J} \\
 d_{m_J} &= N_{1, m_J} M_{1, m_J} \\
 e_{m_J} &= N_{1, m_J}
 \end{aligned} \tag{A.1}$$

The Wigner-Eckart theorem (equation 5.26) is then applied. The second part of equation A.2 shows this for the $P1_{+\frac{1}{2}} \rightarrow D2_{m_J}$ term. Using the same method for the $P1_{-\frac{1}{2}} \rightarrow D2_{m_J}$ term we can obtain equation A.3. Similarly for the $P1_{+\frac{1}{2}} \rightarrow S_{m_J}$ and $P1_{-\frac{1}{2}} \rightarrow S_{m_J}$ terms we obtain equations A.4 and A.5 respectively.

The full solution for n^{-1} as a function of applied magnetic field is shown in figure 5.8.

$$\begin{aligned}
\sum_{m_J=-\frac{1}{2}}^{+\frac{1}{2}} \omega^3 \binom{P1_{+\frac{1}{2}} \rightarrow S1_{m_J}}{\left(P1_{+\frac{1}{2}} \rightarrow S1_{m_J} \right)} \left| \langle S1_{m_J} | \underline{d} | P1_{+\frac{1}{2}} \rangle \right|^2 &= \omega^3 \binom{P1_{+\frac{1}{2}} \rightarrow S_{+\frac{1}{2}}}{\left(P1_{+\frac{1}{2}} \rightarrow S_{+\frac{1}{2}} \right)} \left| \sqrt{\frac{1}{12}} d_{+\frac{1}{2}} \langle S_{\frac{1}{2}} | \underline{d} | P_{\frac{3}{2}} \rangle + \sqrt{\frac{1}{3}} e_{+\frac{1}{2}} \langle S_{\frac{1}{2}} | \underline{d} | P_{\frac{1}{2}} \rangle \right|^2 + \\
&\omega^3 \binom{P1_{+\frac{1}{2}} \rightarrow S_{-\frac{1}{2}}}{\left(P1_{+\frac{1}{2}} \rightarrow S_{-\frac{1}{2}} \right)} \left| -\sqrt{\frac{1}{6}} d_{+\frac{1}{2}} \langle S_{\frac{1}{2}} | \underline{d} | P_{\frac{3}{2}} \rangle + \sqrt{\frac{1}{6}} e_{+\frac{1}{2}} \langle S_{\frac{1}{2}} | \underline{d} | P_{\frac{1}{2}} \rangle \right|^2
\end{aligned} \tag{A.4}$$

$$\begin{aligned}
\sum_{m_J=-\frac{1}{2}}^{+\frac{1}{2}} \omega^3 \binom{P1_{-\frac{1}{2}} \rightarrow S1_{m_J}}{\left(P1_{-\frac{1}{2}} \rightarrow S1_{m_J} \right)} \left| \langle S1_{m_J} | \underline{d} | P1_{-\frac{1}{2}} \rangle \right|^2 &= \omega^3 \binom{P1_{-\frac{1}{2}} \rightarrow S_{+\frac{1}{2}}}{\left(P1_{-\frac{1}{2}} \rightarrow S_{+\frac{1}{2}} \right)} \left| -\sqrt{\frac{1}{6}} d_{-\frac{1}{2}} \langle S_{\frac{1}{2}} | \underline{d} | P_{\frac{3}{2}} \rangle - \sqrt{\frac{1}{6}} e_{-\frac{1}{2}} \langle S_{\frac{1}{2}} | \underline{d} | P_{\frac{1}{2}} \rangle \right|^2 + \\
&\omega^3 \binom{P1_{-\frac{1}{2}} \rightarrow S_{-\frac{1}{2}}}{\left(P1_{-\frac{1}{2}} \rightarrow S_{-\frac{1}{2}} \right)} \left| \sqrt{\frac{1}{12}} d_{-\frac{1}{2}} \langle S_{\frac{1}{2}} | \underline{d} | P_{\frac{3}{2}} \rangle - \sqrt{\frac{1}{3}} e_{-\frac{1}{2}} \langle S_{\frac{1}{2}} | \underline{d} | P_{\frac{1}{2}} \rangle \right|^2
\end{aligned} \tag{A.5}$$

Analytical Expressions for the RF powers required on the fibre EOM

In § 6.2 the results of a numerical calculation to find the required RF powers to put on the EOM to create light at the required frequencies were presented. An expression was written for the electric field of the laser after it has passed through the EOM as a function of the amplitude of the two RF signals and the phase between them (equation 6.5). This was sampled and the Fourier transform taken. Finding the modulus squared of this gives the resulting light spectrum.

It was mentioned that this calculation could be performed analytically by expanding the phase modulation due to both RF signals in terms of Bessel functions. The significant terms in the electric field are

$$\begin{aligned}
 E_{\nu_L} &= E_0 e^{2\pi i \nu_L t} J_0(\alpha) J_0(\beta) \\
 E_{\nu_L \pm \nu_a} &= \pm E_0 e^{2\pi i (\nu_L \pm \nu_a) t} \left[J_1(\alpha) J_0(\beta) + J_2(\alpha) J_1(\beta) e^{\pm i \phi} \right] \\
 E_{\nu_L \pm 2\nu_a} &= E_0 e^{2\pi i (\nu_L \pm 2\nu_a) t} \left[J_2(\alpha) J_0(\beta) - J_1(\alpha) J_1(\beta) e^{\pm i \phi} \right] \\
 E_{\nu_L \pm 3\nu_a} &= \pm E_0 e^{2\pi i (\nu_L \pm 3\nu_a) t} \left[J_3(\alpha) J_0(\beta) + J_0(\alpha) J_1(\beta) e^{\pm i \phi} \right] \\
 E_{\nu_L \pm 4\nu_a} &= E_0 e^{2\pi i (\nu_L \pm 4\nu_a) t} e^{\pm i \phi} \left[J_1(\alpha) J_1(\beta) + J_2(\alpha) J_2(\beta) e^{\pm i \phi} \right], \tag{B.1}
 \end{aligned}$$

where the symbols have the same meanings as in chapter 6.

Taking the modulus squared of these expressions gives the intensity at each sideband.

Chapter B

They are

$$\begin{aligned}
 I_{\nu_L} &= |E_0|^2 |J_0(\alpha) J_0(\beta)|^2 \\
 I_{\nu_L \pm \nu_a} &= |E_0|^2 \left| J_1(\alpha) J_0(\beta) + J_2(\alpha) J_1(\beta) e^{\pm i\phi} \right|^2 \\
 I_{\nu_L \pm 2\nu_a} &= |E_0|^2 \left| J_2(\alpha) J_0(\beta) - J_1(\alpha) J_1(\beta) e^{\pm i\phi} \right|^2 \\
 I_{\nu_L \pm 3\nu_a} &= |E_0|^2 \left| J_3(\alpha) J_0(\beta) + J_0(\alpha) J_1(\beta) e^{\pm i\phi} \right|^2 \\
 I_{\nu_L \pm 4\nu_a} &= |E_0|^2 \left| J_1(\alpha) J_1(\beta) + J_2(\alpha) J_2(\beta) e^{\pm i\phi} \right|^2.
 \end{aligned} \tag{B.2}$$

In the current experiment the two RF frequencies originate from different sources and so the phase will be scrambled. In this case we square the individual terms and then add to obtain the resulting intensity. We find

$$\begin{aligned}
 I_{\nu_L} &= |E_0|^2 |J_0(\alpha) J_0(\beta)|^2 \\
 I_{\nu_L \pm \nu_a} &= |E_0|^2 \left[|J_1(\alpha) J_0(\beta)|^2 + |J_2(\alpha) J_1(\beta)|^2 \right] \\
 I_{\nu_L \pm 2\nu_a} &= |E_0|^2 \left[|J_2(\alpha) J_0(\beta)|^2 + |J_1(\alpha) J_1(\beta)|^2 \right] \\
 I_{\nu_L \pm 3\nu_a} &= |E_0|^2 \left[|J_3(\alpha) J_0(\beta)|^2 + |J_0(\alpha) J_1(\beta)|^2 \right] \\
 I_{\nu_L \pm 4\nu_a} &= |E_0|^2 \left[|J_1(\alpha) J_1(\beta)|^2 + |J_2(\alpha) J_2(\beta)|^2 \right].
 \end{aligned} \tag{B.3}$$

Optimising these expressions for a required set of sidebands we obtain within the computational error the plots of figure 6.4 and 6.5.

Bibliography

- [1] I.J. Cirac and P. Zoller. Quantum Computations with Cold Trapped Ions. *Phys. Rev. Lett.*, **74**, 4091–4094, (1995).
- [2] M.P. Bradley, J.V. Porto, S. Rainville, J.K. Thompson, and D.E. Pritchard. Penning trap measurements of the masses of ^{133}Cs , ^{87}Rb , ^{85}Rb , and ^{23}Na with uncertainties ≤ 0.2 ppb. *Physical Review Letters*, **83**, 22, 4510–4513, (1999).
- [3] A Mooser, K Blaum, H Kracke, S Kreim, W Quint, C Rodeghri, S Ulmer, and J Walz. Towards a direct measurement of the g-factor of a single isolated proton. *Canadian Journal of Physics*, **89**, 1, 165–168, (2011).
- [4] Michael J. Biercuk, Hermann Uys, Aaron P. VanDevender, Nobuyasu Shiga, Wayne M. Itano, and John J. Bollinger. Optimized dynamical decoupling in a model quantum memory. *Nature*, **458**, 996–1000, (2009).
- [5] F. Diedrich, J.C. Bergquist, W.M. Itano, and D.J. Wineland. Laser Cooling to the Zero-Point Energy of Motion. *Physical Review Letters*, **62**, 4, 403–406, (1989).
- [6] D.R. Crick, H. Ohadi, I. Bhatti, R.C. Thompson, and D.M. Segal. Two-ion Coulomb crystals of Ca^+ in a Penning trap. *Opt. Express*, **16**, 4, 2351–2362, (Feb 2008).
- [7] D. R. Crick, S. Donnellan, S. Ananthamurthy, R.C. Thompson, and D.M. Segal. Fast shuttling of ions in a scalable Penning trap array. *Review of Scientific Instruments*, , 81, 013111, (2010).
- [8] J.M Amini, H. Uys, J.H Wesenberg, S. Seidelin, J. Britton, J.J Bollinger, D. Leibfried, C. Ospelkaus, A.P VanDevender, and D.J Wineland. Toward scalable ion traps for quantum information processing. *New Journal of Physics*, **12**, 3, 033031, (2010).

- [9] S. Ulmer, C.C Rodegheri, K. Blaum, H. Kracke, A. Mooser, W. Quint, and J. Walz. Observation of Spin Flips with a Single Trapped Proton. *Phys. Rev. Lett.*, **106**, 253001, (Jun 2011).
- [10] D.R. Crick, S. Donnellan, D.M. Segal, and R.C. Thompson. Magnetically induced electron shelving in a trapped Ca^+ ion. *Physical Review A*, , 81, 052503, (2010).
- [11] M. A. Nielsen and I. L. Chuang. *Quantum Computation and Quantum Information*. Cambridge, 2000.
- [12] D. Deutsch. Quantum-Theory, the Church-Turing principle and the universal Quantum computer. *Proceedings of the Royal Society of London series A-Mathematical physical and engineering sciences*, **400**, 1818, 97–117, (1985).
- [13] P.W. Shor. *Algorithms for quantum computation: discrete logarithms and factoring*. In *Foundations of Computer Science, 1994 Proceedings., 35th Annual Symposium on*, pages 124 –134, nov 1994.
- [14] P.K. Ghosh. *Ion Traps*, chapter 3. Oxford Science, 1995.
- [15] F.G. Major, V.N. Gheorghe, and G. Werth. *Charged Particle Traps - Physics and Techniques of Charged Particle Field Confinement*, chapter 2. Springer, 2005.
- [16] S. Earnshaw. On the Nature of the Molecular Forces which Regulate the Constitution of the Luminiferous Ether. *Transactions of the Cambridge Philosophical Society*, , 7, 97–112.
- [17] J. R. Castrejon-Pita, H. Ohadi, D. R. Crick, D. F. A. Winters, D. M. Segal, and R. C. Thompson. Novel designs for Penning ion traps. *Journal of Modern Optics*, **54**, 11, 1581–1594, (2007).
- [18] R.C. Thompson. Spectroscopy of Trapped Ions. *Advances in Atomic, Molecular and Optical Physics*, , 31, 63 – 136.
- [19] N.W. McLachlan. *Theory and Application of Mathieu Functions*, chapter 2. Oxford.
- [20] D.J. Bate, K. Dholakia, R.C. Thompson, and D.C. Wilson. Ion oscillation frequencies in a combined trap. *Journal of Modern Optics*, , 2, 305–316, (1992).
- [21] D Wineland and H Dehmelt. Proposed 10^{14} delta upsilon less than upsilon laser fluorescence spectroscopy on Tl^+ mono-ion oscillator III. *Bulletin of the American Physical Society*, **20**, 4, 637, (1975).

- [22] T. W. Hansch and A. L. Schawlow. Cooling of gases by laser radiation. *Optics Communications*, **13**, 68–+, (1975).
- [23] S. Scheel. Quantum Optics - Lecture 24. University Lecture, 2009.
- [24] C. Gerry and P. Knight. *Introductory Quantum Optics*, chapter 4. Cambridge, 2005.
- [25] C. Roos. *Controlling the Quantum State of Trapped Ions*. PhD thesis, 2000.
- [26] D. M. Meekhof, C. Monroe, B. E. King, W. M. Itano, and D. J. Wineland. Generation of Nonclassical Motional States of a Trapped Atom. *Phys. Rev. Lett.*, **76**, 1796–1799, (Mar 1996).
- [27] G. Morigi, J.I. Cirac, M. Lewenstein, and P. Zoller. Ground-state laser cooling beyond the Lamb-Dicke limit. *Europhys Letters*, **39**, 1, 13–18, (1997).
- [28] S. Stenholm. The Semiclassical Theory of Laser Cooling. *Reviews of Modern Physics*, **58**, 3, 699–, (1986).
- [29] I. Marzoli, J. I. Cirac, R. Blatt, and P. Zoller. Laser cooling of trapped three-level ions: Designing two-level systems for sideband cooling. *Phys. Rev. A*, **49**, 2771–2779, (Apr 1994).
- [30] C. Monroe, D.M. Meekhof, B.E. King, W.M. Itano, and D.J. Wineland. Demonstration of a Fundamental Quantum Logic Gate. *Physical Review Letters*, **75**, 25, 4714, (1995).
- [31] F. Schmidt-Kaler, H. Haffner, M. Riebe, S. Gulde, G. Lancaster, T. Deuschle, C. Becher, C. Roos, J. Eschner, and R. Blatt. Realization of the Cirac-Zoller controlled-NOT quantum gate. *Nature*, **422**, 408, (2003).
- [32] S. Gulde, M. Riebe, G. P. T. Lancaster, C. Becher, J. Eschner, H. Hffner, F. Schmidt-Kaler, I. L. Chuang, and R. Blatt. Implementation of the Deutsch Jozsa algorithm on an ion-trap quantum computer. *Nature*, **421**, 48–50, (2003).
- [33] Anders Sørensen and Klaus Mølmer. Quantum Computation with Ions in Thermal Motion. *Phys. Rev. Lett.*, **82**, 1971–1974, (Mar 1999).
- [34] G.J. Milburn, S. Schneider, and D.F.V. James. Ion Trap Quantum Computing with Warm Ions. *Fortschritte der Physik*, **48**, 9-11, 801–810, (2000).

- [35] D. Leibfried, B. DeMarco, V. Meyer, D. Lucas, M. Barrett, J. Britton, W. M. Itano, B. Jelenkovic, C. Langer, T. Rosenband, and D. J. Wineland. Experimental demonstration of a robust, high-fidelity geometric two ion-qubit phase gate. *Nature*, **422**, 412–415, (2003).
- [36] Peter W. Shor. Scheme for reducing decoherence in quantum computer memory. *Phys. Rev. A*, **52**, R2493–R2496, (Oct 1995).
- [37] A. M. Steane. Error Correcting Codes in Quantum Theory. *Phys. Rev. Lett.*, **77**, 793–797, (Jul 1996).
- [38] E. Knill. Quantum computing with realistically noisy devices. *Nature*, **434**, 39–44, (2005).
- [39] J. Labaziewicz, Y. Ge, P. Antohi, D. Leibbrandt, K. R. Brown, and I. L. Chuang. Suppression of Heating Rates in Cryogenic Surface-Electrode Ion Traps. *Phys. Rev. Lett.*, **100**, 013001, (Jan 2008).
- [40] C. Ospelkaus, U. Warring, Y. Colombe, K. R. Brown, J. M. Amini, D. Leibfried, and D. J. Wineland. Microwave quantum logic gates for trapped ions. *Nature*, **476**, 181–184, (2011).
- [41] F. Mintert and C. Wunderlich. Ion-Trap Quantum Logic Using Long-Wavelength Radiation. *Phys. Rev. Lett.*, **87**, 257904, (Nov 2001).
- [42] C Ospelkaus, C E Langer, J M Amini, K R Brown, D Leibfried, and D J Wineland. Trapped-ion quantum logic gates based on oscillating magnetic fields. *Physical Review Letters*, **101**, 9, 4, (2008).
- [43] W. C. Campbell, J. Mizrahi, Q. Quraishi, C. Senko, D. Hayes, D. Hucul, D. N. Matsukevich, P. Maunz, and C. Monroe. Ultrafast Gates for Single Atomic Qubits. *Phys. Rev. Lett.*, **105**, 090502, (Aug 2010).
- [44] J. J. Garcia-Ripoll, P. Zoller, and J. I. Cirac. Speed Optimized Two-Qubit Gates with Laser Coherent Control Techniques for Ion Trap Quantum Computing. *Phys. Rev. Lett.*, **91**, 157901, (Oct 2003).
- [45] T Monz, P Schindler, J. T. Barreiro, M. Chwalla, D. Nigg, W. A. Coish, M. Harlander, W. Hänsel, M. Hennrich, and R. Blatt. 14-Qubit Entanglement: Creation and Coherence. *Phys. Rev. Lett.*, **106**, 130506, (Mar 2011).

- [46] K. R. Brown, C. Ospelkaus, Y. Colombe, A. C. Wilson, D. Leibfried, and D. J. Wineland. Coupled quantized mechanical oscillators. *Nature*, **471**, 196–199, (2011).
- [47] M. Harlander, R. Lechner, M. Brownnutt, R. Blatt, and W. Hänsel. Trapped-ion antennae for the transmission of quantum information. *Nature*, **471**, 200–203, (2011).
- [48] A. Retzker, R. C. Thompson, D. M. Segal, and M. B. Plenio. Double Well Potentials and Quantum Phase Transitions in Ion Traps. *Phys. Rev. Lett.*, **101**, 260504, (Dec 2008).
- [49] E. Kierig, U. Schnorrberger, A. Schietinger, J. Tomkovic, and M. K. Oberthaler. Single-Particle Tunneling in Strongly Driven Double-Well Potentials. *Phys. Rev. Lett.*, **100**, 190405, (May 2008).
- [50] I. Lesanovsky, M. Müller, and P. Zoller. Trap-assisted creation of giant molecules and Rydberg-mediated coherent charge transfer in a Penning trap. *Phys. Rev. A*, **79**, 010701, (Jan 2009).
- [51] D. Crick. *Manipulation of Ca^+ Ions in Penning Traps*. PhD thesis, 2009.
- [52] H. Ohadi. *Single Ca^+ Ions in a Penning Trap for Applications in Quantum Information Processing*. PhD thesis, 2008.
- [53] C. Guet and W.R. Johnson. Relativistic many-body calculations of transition rates for Ca^+ , Sr^+ and Ba^+ . *Physical Review A*, , 44, 3.
- [54] M. Chwalla, J. Benhelm, K. Kim, G. Kirchmair, T. Monz, M. Riebe, P. Schindler, A. S. Villar, W. Hänsel, C. F. Roos, R. Blatt, M. Abgrall, G. Santarelli, G. D. Rovera, and Ph. Laurent. Absolute Frequency Measurement of the $^{40}\text{Ca}^+$ $4s^2S_{1/2} - 3d^2D_{5/2}$ Clock Transition. *Phys. Rev. Lett.*, **102**, 023002, (2009).
- [55] M. Fleming and A. Mooradian. Spectral characteristics of external-cavity controlled semiconductor lasers. *Quantum Electronics, IEEE Journal of*, **17**, 1, 44 – 59, (1981).
- [56] H. Loh, Y. Lin, I. Teper, M. Cetina, J. Simon, J.K. Thompson, and V. Vuletić. Influence of grating parameters on the linewidths of external-cavity diode lasers. *Appl. Opt.*, **45**, 36, 9191–9197, (Dec 2006).
- [57] K. Toyoda, H. Kawasaki, and T. Ikeda. Stabilization of a 729nm laser diode for high-resolution spectroscopy of calcium ions. *Japanese Journal of Applied Physics Part 1*, , 42, 1268–1271, (2003).

- [58] Y. Ralchenko, A.E. Kramida, J. Reader, and NIST ASD Team (2011). NIST Atomic Spectra Database (ver. 4.1.0), [Online].
- [59] J. Goodwin. Development of a Fast Scanning Cavity for Laser Frequency Stabilisation and Locking. Master's thesis, 2011.
- [60] E. Phillips. *Laser-Cooled Ions in a Penning Trap*. PhD thesis, 2004.
- [61] N. Seymour-Smith, P. Blythe, M. Keller, and W. Lange. Fast scanning cavity offset lock for laser frequency drift stabilization. **81**, 7, 075109, (2010).
- [62] R.V. Pound. Electronic Frequency Stabilization of Microwave Oscillators. *Rev. Scientific Instruments*, **17**, 11, 490–505, (1946).
- [63] R.W.P Drever. Laser Phase and Frequency Stabilization Using an Optical Resonator. *Appl. Phys. B*, **31**, 97–105, (1983).
- [64] E.D. Black. An Introduction to Pound-Drever-Hall Laser Frequency Stabilization. *Am. J. of Phys.*, **69**, 1, 79–87, (2000).
- [65] P.W. Milonni and J.H. Eberly. *Lasers*. 1998.
- [66] R.W. Fox, C.W. Oates, and L.W. Hollberg. Stabilizing Diode Lasers to High-Finesse Cavities. *Experimental Methods in the Physical Sciences*, , 40, 1–24.
- [67] M.E.M Storkey. *Studies of Laser Cooled Trapped Ions*. PhD thesis, 2001.
- [68] G.W.C. Kaye and T.H. Laby. *Tables of Physical and Chemical Constants*, chapter 3.6. Longman Scientific and Technical, 1986.
- [69] D.M. Lucas, A. Ramos, J.P. Home, M.J. McDonnell, S. Nakayama, J. Stacey, S.C. Webster, D.N. Stacey, and A.M. Steane. Isotope-selective photoionization for calcium ion trapping. *Phys. Rev. A*, **69**, 012711, (Jan 2004).
- [70] S. Gulde, D. Rotter, P. Barton, F. Schmidt-Kaler, R. Blatt, and W. Hogervorst. Simple and efficient photo-ionization loading of ions for precision ion-trapping experiments. *Applied Physics B*, **73**, 861–863, (Jan 2001).
- [71] D. M. Lucas, A. Ramos, J. P. Home, M. J. McDonnell, S. Nakayama, J.-P. Stacey, S. C. Webster, D. N. Stacey, and A. M. Steane. Isotope-selective photoionization for calcium ion trapping. *Phys. Rev. A*, **69**, 012711, (Jan 2004).
- [72] P. Sta anum. *Quantum Optics with Trapped Calcium Ions*. PhD thesis, 2004.

- [73] S. Mavadia. Experimental issues for consideration when trapping $^{40}\text{Ca}^+$ ions. Master's thesis, 2010.
- [74] A. Rae. *Quantum Mechanics*, chapter 6. Institute of Physics, 2002.
- [75] M. Weissbluth. *Atoms and Molecules*, chapter 1,16. Academic Press, 1978.
- [76] D. Budker, D.F. Kimball, and D.P. DeMille. *Atomic Physics*. Oxford University Press, 1998.
- [77] A.H. Myerson, D.J. Szwer, S.C. Webster, D.T.C. Allcock, M.J. Curtis, G. Imreh, J.A. Sherman, D.N. Stacey, A.M. Steane, and D.M. Lucas. High-Fidelity Readout of Trapped-Ion Qubits. *Physical Review Letters*, , 100, 200502, (2008).
- [78] K. Koo, J. Sudbery, D. M. Segal, and R. C. Thompson. Doppler cooling of Ca^+ ions in a Penning trap. *Phys. Rev. A*, **69**, 043402, (Apr 2004).
- [79] E. Wooten, K. Kissa, A. Yi-Yan, E. Murphy, D. Lafaw, P. Hallemeier, D. Maack, D. Attanasio, D. Fritz, G. McBrien, and D. Bossi. A Review of Lithium Niobate Modulators for Fiber-Optic Communication Systems. *IEEE Journal of Selected Topics in Quantum Electronics*, **6**, 69–82, (2000).
- [80] P.A. Barton, C.J.S. Donald, D.M. Lucas, D.A. Stevens, A.M. Steane, and D.N. Stacey. Measurement of the lifetime of the $3d^2D_{\frac{5}{2}}$ state in $^{40}\text{Ca}^+$. *Physical Review A*, , 62, 032503, (2000).
- [81] H Dehmelt. Proposed 10nu greater than nu laser fluorescence spectroscopy on T1 +mono-ion oscillator II. *Bulletin of the American Physical Society*, **20**, 1, 60, (1975).
- [82] H. Hffner, C. F. Roos, and R. Blatt. Quantum Computing with Trapped Ions. *Physics Reports*, **469**, 155, (2008).
- [83] O. Svelto. *Principles of Lasers*, chapter 5. Plenum.
- [84] S. Bharadia. *Dynamics of $^{40}\text{Ca}^+$ Ions in a Penning Trap*. PhD thesis, 2011.